Development, Synthesis, and Analysis of Surrogate Post-Detonation Nuclear Melt Glass

A Dissertation Presented for the

Doctor of Philosophy

Degree

The University of Tennessee, Knoxville

Andrew Vincent Giminaro

December 2016

© by Andrew Vincent Giminaro, 2016
All Rights Reserved.

For Nancy V. Giminaro,

and in loving memory of Wesley G. Ferington Sr., Eleanor J. Ferington,

and Benjamin J. Giminaro, M.D.

Acknowledgements

I would like to first start by thanking The Father, and the wonderful gifts and abilities that He has given me. Without them, this work would not be possible. It has truly been a humbling experience to be able to study, in depth, a minute portion of His creation. Next I would like to thank my family. Mom, Dad, Todd, Chris, Brittney, and Andy (yes we share a name) your love and support has made this possible and I cannot begin to describe how much you all mean to me and how much I love all of you. Dr. Howard Hall, Dr. Matt Cook, Dr. John Auxier II, Major Joshua Molgaard (and all of the FA-52 officers Ive had the pleasure of working with), Jonathan Gill, Adam Stratz, CJ Oldham, Cody Nizinski, and all of the rest of you at the University of Tennessee with whom I have worked. Additionally, I would like to recognize the Catholic community of East Tennessee. Specifically, I would like to thank His Eminence, Justin Cardinal Rigali, Archbishop Emeritus of Philadelphia, His Excellency, Richard F. Stika, Bishop of Knoxville, the Knoxville Frassati Fellowship, the Handmaids of the Precious Blood, and the clergy and parishioners of The Cathedral of the Scared Heart of Jesus and St. John XXIII Catholic Center. This work was made possible by funding from the United States Department of Energy, National Nuclear Security Administration, Stewardship Science Academic Alliances Program Grant number DE-NA0001983. Finally, I would like to thank you, dear reader. Without you, this whole effort would have been for naught.

Causa latet, vis est notissima

— Ovid: *Metamorphoses* IV, 287

Abstract

With the threats facing the world today, there is an ever-increasing need for training the the fields of radiochemistry and nuclear forensics. Training and research in these fields requires reference materials that accurately represent materials that could potentially be encountered. Unfortunately, many of the historical samples of debris from nuclear weapons tests remains classified. Because of this, there is a need for realistic surrogates. This research focuses on the development of surrogates for the bulk and particulate nuclear melt glass that is expected to be found in an urban setting after a nuclear event.

A mathematical model for the creation of surrogate melt glass precursor matrices was developed. The model was used to determine the elemental composition of melt glass precursor for the Trinity site, New York City, and Houston, Texas. The precursor matrices were used to generated surrogate bulk nuclear melt glass. While this has been previously done for the Trinity site, this study marks the first time that surrogate bulk nuclear melt glass has been produced for urban scenarios. A thermal spray coater was used to demonstrate that the precursor matrices can be used to generate surrogate particulate melt glass.

Both the bulk and particulate surrogate melt glasses were analyzed using scanning electron microscopy (SEM). Chemical differences on the surface of the samples was determined using backscatter electron analysis (BSE). Energy dispersive spectroscopy (EDS) was used to determine the elemental composition of features observed via SEM. A more complete elemental analysis of the surrogates was

conducted using inductively coupled plasma time-of-flight mass spectrometry (ICP-TOF-MS). Crystalline structure was determined using powder X-ray diffraction (P-XRD). Expected fission and activation products cause for each of the matrices were modeled. Notional uranium-fueled and plutonium-fueled improvised nuclear devices (IND) were examined in the radiological models.

Using the developed mathematical models were in conjunction with the synthesis techniques outline, it is apparent that these methods will be able to provide for and meet the current academic, training, and research needs. However, further optimization of the synthesis and analysis processes is needed before large scale production can occur.

Table of Contents

1 Introduction **1**

2 Literature review **3**

2.1 Basics of Nuclear Melt Glass 3

2.1.1 Bulk Melt Glass 4

2.1.2 Particulate Melt Glass 4

2.1.3 Conditions Found in a Nuclear Blast 5

2.2 Morphology 7

2.2.1 Bulk Melt Glass Morphology 8

2.2.2 Particulate Melt Glass Morphology 10

2.3 Composition 12

2.3.1 Bulk Melt Glass 12

2.3.2 Particulate Melt Glass 18

2.3.3 Dissolution Techniques 19

2.4 Radiological Profile 20

2.4.1 Fractionation of Radionuclides 20

2.4.2 Bulk Melt Glass 22

2.4.3 Particulate Melt Glass 27

2.5 Surrogate Development 31

2.5.1 Synthetic Bulk Melt Glass 31

2.5.2 Synthetic Particulate Melt Glass 33

3 Methodology **35**

3.1 Surrogate Precursor Matrix Development . . . 35

3.2 Surrogate Bulk Melt Glass Production . . . 45

3.2.1 Equipment . . . 45

3.2.2 Temperature Requirements . . . 47

3.2.3 Synthesis . . . 47

3.3 Surrogate Bulk Melt Glass Analysis . . . 48

3.3.1 Optical and Electron Microscopy . . . 48

3.3.2 Mass Spectrometry . . . 49

3.3.3 X-ray Diffraction . . . 50

3.4 Surrogate Particulate Melt Glass Production . . . 52

3.4.1 Equipment . . . 53

3.4.2 Synthesis . . . 55

3.5 Surrogate Particulate Melt Glass Analysis . . . 57

3.5.1 Electron Microscopy . . . 57

3.5.2 Mass Spectrometry . . . 59

3.5.3 X-ray Diffraction . . . 59

3.6 Radiological Modeling . . . 59

4 Results **61**

4.1 Surrogate Bulk Melt Glass . . . 61

4.1.1 Optical and Electron Microscopy . . . 61

4.1.2 Mass Spectrometry . . . 92

4.1.3 X-Ray Diffraction . . . 102

4.2 Surrogate Particulate Melt Glass . . . 107

4.2.1 Electron Microscopy Analysis . . . 108

4.2.2 Mass Spectrometry . . . 127

4.2.3 X-Ray Diffraction . . . 131

4.3 Radiological Modeling . . . 134

4.3.1 U-Fueled IND . . . 135
4.3.2 Pu-Fueled IND . . . 136
4.3.3 Comparison of Activity Levels Between Matrices . . . 137
4.3.4 U-Fueled IND in the STF matrix . . . 139
4.3.5 Pu-Fueled IND in the STF matrix . . . 145
4.3.6 U-Fueled IND in the NYC matrix . . . 151
4.3.7 Pu-Fueled IND in the NYC matrix . . . 156
4.3.8 U-Fueled IND in the HOU matrix . . . 162
4.3.9 Pu-Fueled IND in the HOU matrix . . . 165

5 Conclusions **172**

6 Future Work **175**

6.0.1 Determining Causes of Anomalies in the ICP-TOF-MS data . 175
6.0.2 Improvement of Dissolution Techniques . . . 175
6.0.3 Further Analysis of Surrogates via LIBS . . . 176
6.0.4 Optimization of Particulate Precursor Preparation . . . 176
6.0.5 Optimization of Torch Operational Conditions . . . 176
6.0.6 Irradiation Campaigns . . . 177
6.0.7 Further In-Depth Analysis of Radiological Models . . . 177
6.0.8 Coupling of Atmospheric Chemistry . . . 178

Bibliography **179**

Appendix **187**

A Fractionation Mass Chains **188**

B Activity Contributions Over Time **194**

Vita **197**

List of Tables

2.1 Major oxides of particulate melt glass 19
2.2 Location of some fission products post-detonation 21
2.3 α emissions of interest from published bulk nuclear melt glass data . 24
2.4 β^- emissions of interest from published bulk nuclear melt glass data . 25
2.5 γ-ray emissions of interest from published bulk nuclear melt glass data 26
2.6 β^- emissions of interest from published particulate nuclear melt glass data 29
2.7 ^{235}U fission $\gamma-$ray emissions of interest from published particulate nuclear melt glass data 31

3.1 Elemental composition of soil by weight fraction 37
3.2 Average vehicle weight by type 40
3.3 Weight fraction of various vehicular components by type 40
3.4 Fireball radius with respect to yield 42
3.5 Nuclear surface burst crater dimensions 43
3.6 Major elemental composition by weight percent for a 1-kT detonation 43
3.7 Bulk surrogate precursor matrices for a 1-kT detonation 46
3.8 Particulate surrogate precursor matrices for a 1-kT detonation 53

4.1 Ratios of major elements with respect to oxygen for precursor matrices 62
4.2 Ratios of major elements with respect to oxygen in bulk melt glass (STF matrix) 66

4.3 Ratios of major elements with respect to oxygen for bulk melt glass (NYC matrix) 78
4.4 Ratios of major elements with respect to oxygen for bulk melt glass (HOU matrix) 87
4.5 Ratios of major elements with respect to oxygen for particulate bulk melt glass (STF matrix) 117
4.6 Ratios of major elements with respect to oxygen for particulate bulk melt glass (NYC matrix) 126

List of Figures

2.1 Trinitite glass fragments typical of debris found at ground zero 4
2.2 Optical microscope images of particulate melt glass 5
2.3 Early fireball temperature and density profiles (1-MT, sea-level, air-burst at $\sim 34\mu$s) 6
2.4 Early fireball pressure and particle velocity profiles (1-MT, sea-level, air-burst $\sim 34\mu$s) 7
2.5 Fireball temperature versus radius at early times in fireball history (1-MT sea-level air-burst) 8
2.6 Regions of differing morphology within trinitite 9
2.7 SEM BSE image of a trinitite fragment 10
2.8 BSE image of dumbbell shaped particulate debris 12
2.9 SEM photomicrographs of reaction layers lining vesicles in melt glass samples 13
2.10 FeO and Na_2O vs Al_2O_3 (A, B) and FeO vs Na_2O (C) contents for trinitite. 15
2.11 Photo of "red" trinitite. Its color is caused by a high concentration of copper 16
2.12 (A,B) SEM images of PbO inclusion on the surface of trinitite glass. (C) Concentrations of Pb and Cu in trinitite melt glass 17
2.13 Correlation of (a)U and (b)Pu with respect to CaO in trinitite 18
2.14 $\gamma-$ray spectrum of trinitite 66-years post-detonation. 27

2.15 $\gamma-$ray spectra from a ^{235}U fueled air-burst test 30
2.16 Fused glass bead formation from a concrete-glass powder as a function of laser exposure time. 34

3.1 Illustration of radioactive sample mounting procedure 51
3.2 Büchi B-290 spray dryer 54
3.3 Plasma spray system control module 55
3.4 Thermal spray camera used to track particle motion and speed 56
3.5 Powder hopper used to feed precursor material into the plasma torch 57
3.6 Experimental setup for the production of synthetic particulate melt glass 58

4.1 Optical images of a typical surrogate bulk melt glass bead composed of the STF matrix 63
4.2 Micrographs and EDS of the top surface of a typical surrogate bulk melt glass bead (STF matrix) 64
4.4 Micrographs and EDS for a typical basal side of surrogate bulk melt glass (STF matrix) 64
4.3 Micrographs and EDS of crystalline structures on the surface of a surrogate bulk melt glass bead (STF matrix) 65
4.5 Micrographs and EDS for a typical thin section of surrogate bulk melt glass (STF matrix) 67
4.6 Micrographs and EDS for an homogenous region of surrogate bulk melt glass (STF matrix) 68
4.7 Micrographs and EDS for a typical granular area of surrogate bulk melt glass (STF matrix) 69
4.8 Micrographs and EDS for a typical crack found in surrogate bulk melt glass (STF matrix) 70
4.9 Micrographs and EDS for a the surface of a cavity found in surrogate bulk melt glass (STF matrix) 71

4.10 Optical images of a typical surrogate bulk melt glass bead composed of the NYC matrix 72
4.11 Micrographs and EDS of the top surface of a typical surrogate bulk melt glass bead (NYC matrix) 73
4.12 Micrographs and EDS for a typical smooth region of the top surface of a surrogate bulk melt glass bead (NYC matrix) 73
4.13 Micrographs and EDS for a typical rough region of the top surface of a surrogate bulk melt glass bead (NYC matrix) 74
4.14 Micrographs and EDS for a crystalline region of surrogate bulk melt glass (NYC matrix) 75
4.15 Micrographs and EDS for a typical basal side of a surrogate bulk melt glass (NYC matrix) 76
4.16 Micrographs and EDS for a typical thin section of surrogate bulk melt glass (NYC matrix) 78
4.17 Micrographs and EDS for a typical homogenous region of surrogate bulk melt glass (NYC matrix) 79
4.18 Micrographs and EDS for a typical granular area of surrogate bulk melt glass (NYC matrix) 80
4.19 Micrographs and EDS for a the surface of a cavity found in surrogate bulk melt glass (NYC matrix) 81
4.20 Micrographs and EDS of a typical crack found in bulk melt glass (NYC matrix) 82
4.21 Optical images of a typical surrogate bulk melt glass bead composed of the HOU matrix 83
4.22 Micrographs and EDS of the top surface of a typical surrogate bulk melt glass bead (HOU matrix) 84
4.23 Micrographs and EDS for a typical protrusion on the surface of a surrogate bulk melt glass bead (HOU matrix) 85

4.24 Micrographs and EDS for the basal side of a typical surrogate bulk melt glass (HOU matrix) 85
4.25 Micrographs and EDS for beads found on the basal side of a typical surrogate bulk melt glass (HOU matrix) 86
4.26 Micrographs and EDS for a typical thin section of surrogate bulk melt glass (HOU matrix) 88
4.27 Micrographs and EDS for a typical homogenous region of surrogate bulk melt glass (HOU matrix) 89
4.28 Micrographs and EDS for a typical granular region of surrogate bulk melt glass (HOU matrix) 90
4.30 Micrographs and EDS for a typical crack found in surrogate bulk melt glass (HOU matrix) 90
4.29 Micrographs and EDS for a the surface of a cavity found in surrogate bulk melt glass (HOU matrix) 91
4.31 Comparison of ICP-TOF-MS results for the STF matrix 94
4.32 Comparison of ICP-TOF-MS results for the NYC matrix 96
4.33 Comparison of ICP-TOF-MS results for the HOU matrix 98
4.34 Comparison of ICP-TOF-MS results between all three matrices . . . 100
4.35 XRD patterns for precursor material compared to a powdered surrogate bulk melt glass bead (STF matrix) 102
4.36 XRD patterns for three powdered surrogate bulk melt glass beads (STF matrix) 103
4.37 XRD patterns for precursor material compared to a powdered surrogate bulk melt glass bead (NYC matrix) 104
4.38 XRD patterns for three powdered surrogate bulk melt glass beads (NYC matrix) 105
4.39 XRD patterns for precursor material compared to a powdered surrogate bulk melt glass bead (HOU matrix) 105

4.40 XRD patterns for three powdered surrogate bulk melt glass beads (HOU matrix) . . . 106
4.41 Comparison of XRD patterns for all three bulk melt glass matrices . . 107
4.42 Micrographs and EDS of surrogate particulate melt glass precursor (STF matrix) . . . 109
4.44 Micrographs and EDS for a typical clump found in surrogate particulate melt glass precursor (STF matrix) . . . 109
4.43 Micrographs and EDS of granules found in surrogate particulate melt glass precursor (STF matrix) . . . 110
4.45 Micrographs and EDS of spray-dried surrogate particulate melt glass precursor (STF matrix) . . . 111
4.46 Micrographs and EDS of granules found in spray-dried surrogate particulate melt glass precursor (STF matrix) . . . 112
4.47 Micrographs and EDS for a typical clump found in spray-dried surrogate particulate melt glass precursor (STF matrix) . . . 113
4.48 Micrographs and EDS of heat-treated surrogate particulate melt glass precursor (STF matrix) . . . 114
4.49 Micrographs and EDS for a typical globule found in heat-treated surrogate particulate melt glass (STF matrix) . . . 115
4.50 Micrographs and an EDS spectrum of fused SiO_2 granules found in heat-treated surrogate particulate melt glass (STF matrix) . . . 116
4.51 Micrographs and an EDS spectrum for a spherical particle found in surrogate particulate melt glass (STF matrix) . . . 117
4.52 Micrographs and EDS of surrogate particulate melt glass precursor (NYC matrix) . . . 119
4.53 Micrographs and EDS of granules found in surrogate particulate melt glass precursor (NYC matrix) . . . 119
4.54 Micrographs and EDS for a typical clump found in surrogate bulk melt glass (NYC matrix) . . . 120

4.55 Micrographs and EDS of spray-dried surrogate particulate melt glass precursor (NYC matrix) . . . 121
4.56 Micrographs and EDS spectrum of typical granules found in spray-dried surrogate particulate melt glass precursor (NYC matrix) 122
4.57 Micrographs and EDS for a typical example of the fine powder found in spray-dried surrogate particulate melt glass precursor (NYC matrix) 123
4.58 Micrographs and EDS of heat-treated surrogate particulate melt glass precursor (NYC matrix) . . . 124
4.59 Micrographs and an EDS spectrum of fused SiO_2 granules found in heat-treated surrogate particulate melt glass (NYC matrix) 125
4.60 Micrographs and an EDS spectrum for a spherical particle found in surrogate particulate melt glass (NYC matrix) 125
4.61 Comparison of particulate melt glass ICP-TOF-MS results for the STF matrix . . . 128
4.62 Comparison of particulate melt glass ICP-TOF-MS results for the NYC matrix . . . 130
4.63 XRD patterns for untreated, spray-dried, and heat treated particulate surrogate melt glass (STF matrix) 132
4.64 XRD patterns for untreated, spray-dried, and heat treated particulate surrogate melt glass (NYC matrix) 133
4.65 Comparison of XRD results for the STF and NYC matrices 134
4.66 Total modeled activity over time generated by a notional U-fueled IND in a STF matrix . . . 136
4.67 Total modeled activity over time generated by a notional Pu-fueled IND 137
4.68 Comparison of total activity over time for all radiological models . . . 138
4.69 Activity of α-emitting radionuclides for a notional U-fueled IND in an STF matrix . . . 140
4.70 Activity of β-emitting radionuclides for a notional U-fueled IND in an STF matrix expected to be found near ground-zero 141

4.71 Activity of β-emitting radionuclides for a notional U-fueled IND in an STF matrix that are expected to be found away from ground-zero . . 142
4.72 Activity of γ-emitting radionuclides expected to be found at ground-zero after the detonation on a notional U-fueled IND in an STF matrix 143
4.73 Activity of γ-emitting radionuclides for a notional U-fueled IND in an STF matrix expected to be found in a location away from ground-zero 144
4.74 Activity of α-emitting radionuclides for a notional Pu-fueled IND in an STF matrix 146
4.75 Activity of β-emitting radionuclides for a notional Pu-fueled IND in an STF matrix expected to be found at ground-zero 147
4.76 Activity of β-emitting radionuclides for a notional Pu-fueled IND in an STF matrix expected to be found in areas away from ground-zero 148
4.77 Activity of γ-emitting radionuclides for a notional Pu-fueled IND in an STF matrix expected to be found near ground-zero 149
4.78 Activity of γ-emitting radionuclides for a notional Pu-fueled IND in an STF matrix expected to be found away from ground-zero 150
4.79 Activity of α-emitting radionuclides for an notional U-fueled IND in an NYC matrix 152
4.80 Activity of β-emitting radionuclides for a notional U-fueled IND in an NYC matrix expected to be found near ground-zero 153
4.81 Activity of β-emitting radionuclides for a notional U-fueled IND in an NYC matrix expected to be found away from ground-zero 154
4.82 Activity of γ-emitting radionuclides for a notional U-fueled IND in an NYC matrix expected to be found near ground-zero 155
4.83 Activity of γ-emitting radionuclides for a notional U-fueled IND in an NYC matrix expected to be found away from ground-zero 156
4.84 Activity of α-emitting radionuclides for an notional Pu-fueled IND in a NYC matrix 157

4.85 Activity of β-emitting radionuclides for a notional Pu-fueled IND in an NYC matrix expected to be found in areas near ground-zero . . . 158
4.86 Activity of β-emitting radionuclides for a notional Pu-fueled IND in an NYC matrix expected to be found in areas away from ground-zero 159
4.87 Activity of γ-emitting radionuclides for a notional Pu-fueled IND in an NYC matrix expected to be found in areas away from ground-zero . . 160
4.88 Activity of γ-emitting radionuclides for a notional Pu-fueled IND in an NYC matrix near ground-zero 161
4.89 Activity of α-emitting radionuclides for an notional U-fueled IND in a HOU matrix 162
4.90 Activity of β-emitting radionuclides for a notional U-fueled IND in a HOU matrix expected to be found in the vicinity of ground-zero . . . 163
4.91 Activity of β-emitting radionuclides for a notional U-fueled IND in a HOU matrix expected to be found in areas away from ground-zero . . 164
4.92 Activity of γ-emitting radionuclides expected to be found near ground zero after the detonation of a notional U-fueled IND in a HOU matrix 165
4.93 Activity of γ-emitting radionuclides for a notional U-fueled IND in a HOU matrix that are expected to be found in areas away from ground-zero 166
4.94 Activity of α-emitting radionuclides for an notional Pu-fueled IND in a HOU matrix 166
4.95 Activity of β-emitting radionuclides for a notional Pu-fueled IND in a HOU matrix expected to be found in areas away from ground zero . . 167
4.96 Activity of β-emitting radionuclides for a notional Pu-fueled IND in a HOU matrix expected to be found in areas away from ground-zero . . 168
4.97 Activity of γ-emitting radionuclides generated by a notional Pu-fueled IND in a HOU matrix that are expected to be found in areas near ground-zero 170

4.98 Activity of γ-emitting radionuclides generated by a notional Pu-fueled IND in a HOU matrix, and expected to be found in areas away from ground-zero 171

A.1 Mass chains 85-88 189
A.2 Mass chains 89-92 190
A.3 Mass chains 93-95 191
A.4 Mass chains 101-104 192
A.5 Mass chains 105-108 193

B.1 Activity contribution by mass number (A) over time for a modeled notional U-fueled IND detonation 195
B.2 Activity contribution by mass number (A) over time for a modeled notional Pu-fueled IND detonation in a STF matrix 196

Chapter 1

Introduction

The threat of a nuclear attack is nothing new. Since the dawn of the Atomic Age, many people around the world have found themselves fearful of such an attack. While this threat may not seem as real today as it did during the Cold War, the threat of nuclear proliferation and nuclear terrorism is a continued and growing concern. While countries once had to worry about megaton scale weapons delivered by missiles launched halfway around the world by large nuclear-capable nations, the major concern today comes from the use of small improvised nuclear devices (IND) by a non-state actor. Unlike their more powerful counterparts, INDs are more likely to be detonated at ground level rather than at altitude. When a nuclear device is detonated at ground level, surrounding materials will be irradiated and drawn into the ensuing fireball. Typically, what is left behind at ground zero is a glassy, highly radioactive substance known as nuclear melt glass.

The most commonly recognized and studied example of nuclear melt glass is trinitite, the material left on the floor of the Jornada del Muerto desert following the Trinity test. Numerous studies have been conducted on the physical, chemical, and radiological properties of trinitite, some even going so far as to produce an accurate non-radiological surrogate (1) However, it is highly unlikely that a malicious actor would carry out an attack in an environment similar to those of nuclear weapon test

sites. Instead, the most probable locations are considered to be high-density urban areas. Because the only two historical uses of nuclear weapons on urban environments were both altitude bursts, no examples of nuclear melt glass generated in an urban setting exist.

A major point of concern for analytical methods development is the expected disparity between the morphology and elemental composition of the desert trinitite versus the post-detonation debris generated in an urban setting. Forensically analyzing urban samples in a post-detonation scenario using techniques optimized for trinitite would likely produce analytical challenges when applied to urban debris with dissimilar chemical features. Rapid sample analysis is essential during a post-detonation situation, and minimizing any hindrances to the process is essential. It is therefore beneficial to develop a means to synthesize melt glass debris materials characteristic of urban environments in order to allow for the development and optimization of forensic techniques.

This project investigates the development of accurate nuclear melt glass surrogates. The focus of the work is four-fold: 1) to develop a mathematical model that can be used to create a matrix of materials that will serve as the basis of urban surrogate nuclear melt glass, 2) to synthesize various surrogate nuclear melt glasses using both a New York City and Houston, TX matrix, 3) to compare the morphology and composition of the surrogates to previously developed synthetic trinitite, and 4) to model the effects of a notional uranium and plutonium fission spectra on the reactivity and speciation of the matrices over time. The development, synthesis, and analysis of surrogate nuclear melt glass will provide a reference material that can support radiochemical and nuclear forensic education programs, help to improve validation and verification techniques for fallout modeling, and allow for the development and optimization of analytical techniques. Supporting and strengthening these areas allows for improved attribution capabilities, leading to a safer, more secure future.

Chapter 2

Literature review

2.1 Basics of Nuclear Melt Glass

Nuclear melt glass is the vitreous material produced in the detonation of a nuclear weapon. In the field of post-detonation nuclear forensics, nuclear melt glass that has been formed via a surface burst — any nuclear explosion which originates on or near the surface of the Earth and results in the displacement, melting, or even vaporization of local soil(2) — is of particular interest. Nuclear melt glass is formed when the fireball from the detonation contacts the ground, vaporizing and incorporating material. After this incorporation, the vaporized material rapidly cools to its vaporization point and transitions to a liquidus phase a few seconds after detonation. As the material continues to cool, partially molten droplets will begin to fall back to the earth or will be carried away via atmospheric phenomena(3; 4; 5). It should be noted that not all material will return to ground zero, with some studies estimating the lost mass as high as 80%(4). The nuclear melt glass that returns to the earth following a surface burst can be sub-categorized into either bulk(>2-mm with a flat, pancake-like shape), or particulate melt glass(<2-mm and predominately spheroid in shape).

2.1.1 Bulk Melt Glass

Bulk nuclear melt glass is the debris that typically comes to mind when post-detonation materials located at or near ground-zero are discussed. Examples of bulk nuclear melt glass from weapons tests at a variety of locations all exhibit vitreous, highly vesicular morphology, and have a largely amorphous crystalline structure. Usually extremely heterogenous, these materials typically hold refractory elements, including fission and activation products. After a detonation, bulk melt glass is found in a "lake" surrounding ground zero. In the case of the Trinity test, the lake had a roughly circular shape, and a radius of 500 m(6) Bulk melt glass (trinitite) in the area had an average thickness of 0.5 cm, with thickness inversely correlated to radial location from ground-zero(4). Composition of trinitite was found to have a chemical composition very similar to the surrounding soil(3). An example of bulk melt glass can be seen in Figure: 2.1.



Figure 2.1: Trinitite glass fragments typical of debris found at ground zero (7)

2.1.2 Particulate Melt Glass

In addition to bulk debris, small-diameter spheroids (<2 mm) have been found at the Trinity site(4). These particulates tend to take either a spheroid or oblong shape

which occasionally resembles a dumbbell. The particulates are typically of an overall higher specific activity (measured in $^{dpm}/_{g}$) than bulk melt glass specimens(7; 8). Additionally, particulate melt glass tends to be more widely distributed than bulk melt glass, a result of smaller molten droplets being carried downwind before deposition(7). Multiple examples of particulate melt glass can be seen in Figure: 2.2.

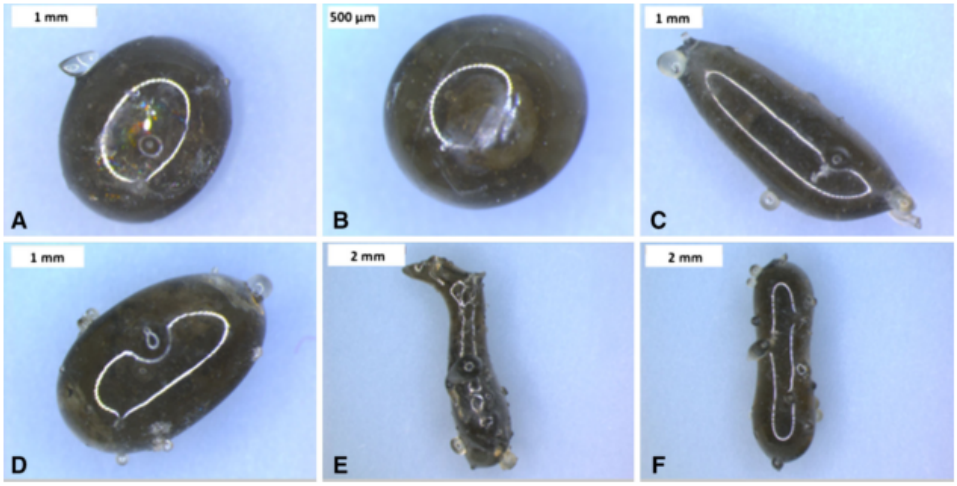


Figure 2.2: Optical microscope images of particulate melt glass
Panels A and B are representative of spheroid shaped debris, and panels C-F are representative of oblong shaped debris. (8)

2.1.3 Conditions Found in a Nuclear Blast

A typical temperature and density profile for a nuclear fireball is illustrated in Figure: 2.3. The highest temperature within the sphere is less than twice that of the outer edge. The density curve shows relatively little change in the air from its ambient condition beyond 10-m (9). In fact, at this time shown in the figure, there is only a slight compression at the front of the fireball and a slight rarefaction, or reduction in density, in the interior (10). The figure shows a high compression, also known as a shock, of the bomb materials which, at the time shown in the graph, have expanded out to a thin shell of 10m radius.

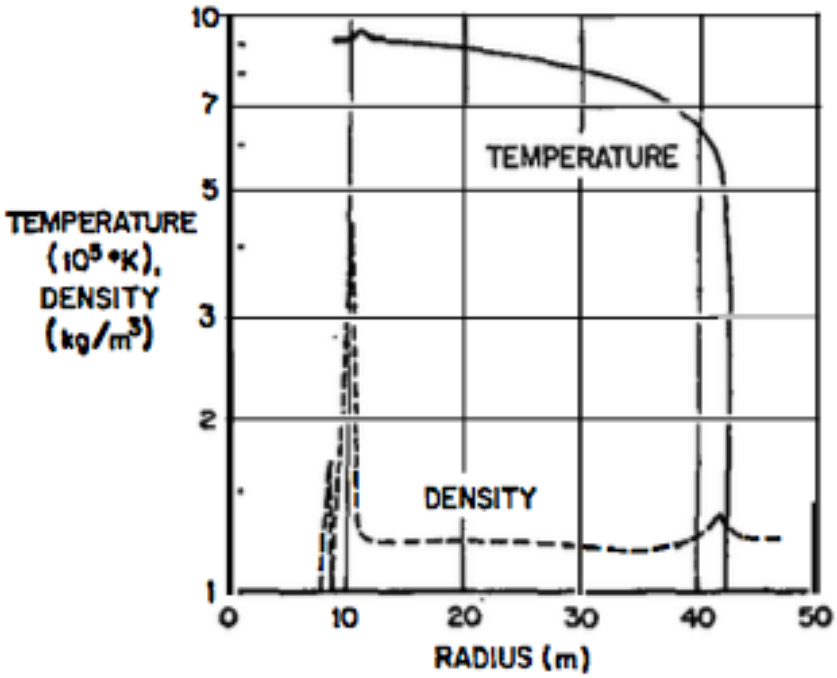


Figure 2.3: Early fireball temperature and density profiles (1-MT, sea-level, air-burst at $\sim 34\mu$s)

(9)

Figure:2.4 illustrates the distribution of pressure and of velocity. The pressure profile is similar to the temperature profile within the hot air, but shows much higher pressure in the bomb vapor shock wave. Similarly, the bomb material can be seen expanding at an extremely high velocity, while the air out in the front of the fireball is just beginning to move (9). This rapidly expanding sphere of bomb vapors compresses the adjacent air in a nonadiabatic, nearly isothermal shock. The expanding wave front can compress air to many times the density achievable in a classical adiabatic shock because most of the energy (and pressure) the compressed air acquires during the shock is immediately radiated ahead through the transparent fireball interior (10).

Figure: 2.5 shows subsequent temperature profiles as the the early fireball ceases to expand solely by radiation diffusion and begins to "shock up," and to grow by compressing do work (in the physics sense) on the surrounding air (2). In Figure: 2.5, one sees at the earliest indicated time the temperature of the radiation diffusion

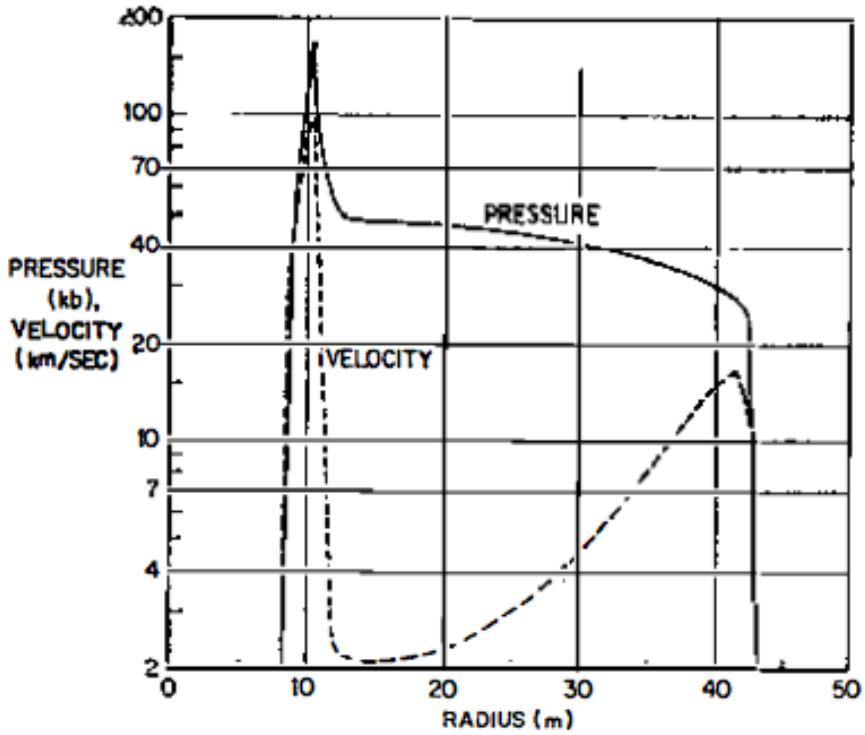


Figure 2.4: Early fireball pressure and particle velocity profiles (1-MT, sea-level, air-burst $\sim 34\mu$s)

(9)

sphere. At subsequent times, this radiatively heated region is shown to expand and cool as it follows the shock wave. One can also see the shock-heated air as a region of steep temperature gradient beyond the hot interior. At these times, the lowest temperature of the fireball are found at the surface, or in the outer shock front itself (9). The visible fireball radius becomes coincident with this shock front after the first ms.

2.2 Morphology

The textures and morphology of trinitite, and the positions of inclusions within trinitite suggest a two-stage formation process. In the first stage of this process, arkosic sand is incorporated into the fireball, and subsequently rained down along

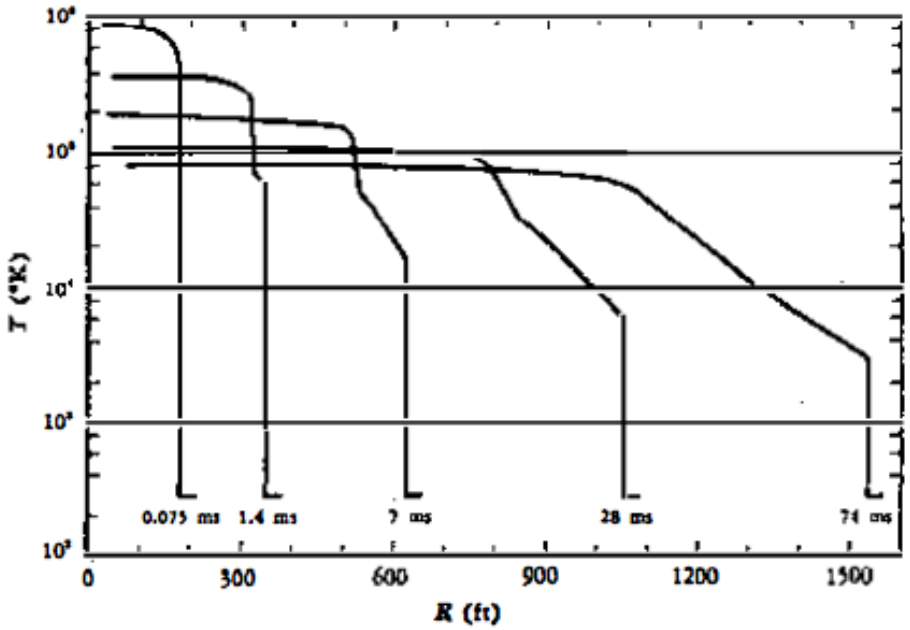


Figure 2.5: Fireball temperature versus radius at early times in fireball history (1-MT sea-level air-burst)

(9)

with nuclear device, geological, and site material. This liquid fell to the ground and fused into trinitite, the second stage(4). Bellucci argues that precipitation of material occurs at a point later in time, as this would permit cooling and solidification of the trinitite matrix prior to the incorporation of solid-type inclusions. The argument is also made that sustained precipitation of debris would be required for the two-stage formation model to be viable(11).

2.2.1 Bulk Melt Glass Morphology

Because of its unclassified nature, numerous studies have been conducted on the morphology of trinitite. For this reason, trinitite provides an excellent benchmark against which other bulk melt glass samples, specifically surrogates, can be compared. Trinitite morphology can be broken into three basic regions:1) the blast side (top of the sample); 2) the basal side (bottom); and 3) the interior(3; 4; 5; 1; 12) These three

distinct morphological regions can be seen in Figure 2.6 below. The blast side of trinitite exhibits a glassy, almost smooth surface; whereas the basal side of trinitite is characterized by the loose adhesion of unmelted, naturally occurring geological comppounds(7; 13). Both the blast side and the ground side are outside of the scope of this research, and thus will not be covered in this discussion.

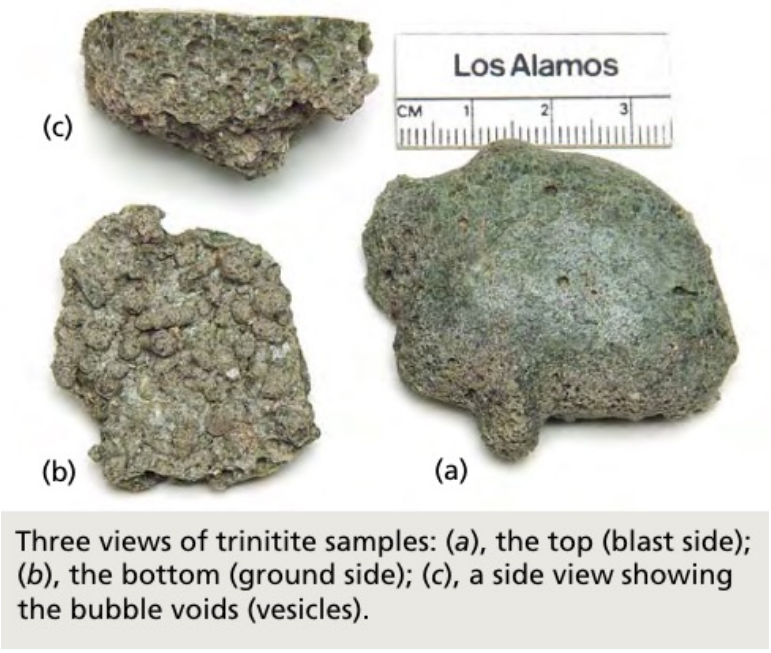


Figure 2.6: Regions of differing morphology within trinitite (5)

The interior of trinitite appears glassy and vesicular, similar to scoria (a volcanic rock) in appearance. This morphological similarity would suggest that these vesicles were formed when volatilized elements and compounds were captured within the rapidly cooling molten arkosic sand after the event(3; 7). Extensive morphological studies have shown that heterogeneities within trinitite can provide information about post-detonation conditions at ground zero. As seen in Figure 2.7, the quartz grains within trinitite take on a rounded shape indicating incomplete melting, and rapid cooling. These characteristics are indicative of a partial melting of quartz in the arkosic sand at the test site(3; 7).

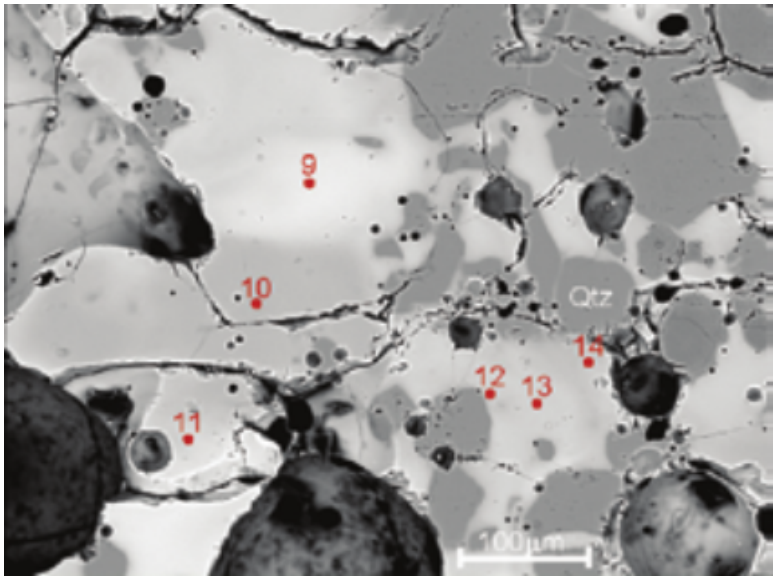


Figure 2.7: SEM BSE image of a trinitite fragment (7)

Numerous X-ray diffraction studies have corroborated the findings of SEM/EDS studies(1) X-ray diffraction of trinitite has shown that the only crystalline phase present is α-quartz, suggesting that all other compounds in the sand were completely melted and did not recrystalize(7; 1; 14). Additionally, the presence of quartz in only the α phase (a low-temperature/low-pressure phase) allows for the assumption that the over-temperature and over-pressure of the detonation was not sufficient enough to produce any other stable polymorphs of quartz. Many of these properties are exhibited not only in trinitite, but also in bulk melt glass from underground tests(15). These findings would seem to indicate that the processes driving the formation of bulk nuclear melt glass are similar (though certainly not identical) in both surface and subsurface scenarios.

2.2.2 Particulate Melt Glass Morphology

After a nuclear detonation particulate debris produced in the fireball will either be dispersed into the atmosphere where it may be transported for great distances(16; 17),

or it will return to the earth in the general vicinity of ground zero. Particle size distribution has been examined extensively for the purpose of radionuclide transport and plume modeling studies but unfortunately extensive research has not been conducted on the size distribution of all particles produced in a surface/near-surface nuclear detonation(18; 19). However, melt glass particles collected from area surrounding ground-zero of surface-burst tests are usually no larger than a few hundred μm(7; 8; 18; 19). Given what is known about debris formation, it is reasonable to assume this value as an upper limit. Particulate melt glass sapmles with sizes down to a few μm have been collected and identified. Particles in this size range are difficult to prepare for in-depth analysis via SEM/EDS, and thus have not yielded much information on their composition and structure. However, cursory physical inspection of these specimens revealed that they do not differ in physical appearance from larger particles except in size(18).

Particulate melt glass is generally opaque, and greenish black in color, and usually takes an either a spheroid or oblong shape(7; 8; 19). The differences in shape can be seen in Figure: 2.2. The morphology of the particulate melt glass bears a striking similarity to tekitites, the debris formed from meteor impacts(7). The spheroids have very smooth surfaces with no obvious top or bottom(8). While oblong particles also display no discernible top or basal orientation, their surfaces tend to be distorted by smaller particulates that appear to have agglomerated on the surface, indicating that their oblong/dumbbell shape is a result of multiple particles fusing together after they have formed(7; 8). Unlike bulk debris, particulates appear to have no discernible reaction layer(8).

SEM, BSE, and EDS analyses indicate a high degree of heterogeneity within the debris, with many particles showing a swirly texture indicative of intimate mixing of various liquidous compunds on the 10 to 100μm scale(7; 8; 18). The primary constituent of the particles is amorphous silica. Inclusions of α-quartz and K-feldspar can be observed in some particles. Additionally, Mg-rich amphibole can be observed

on the surface of some particles(7; 8). Textural heterogeneity and the presence of α-quartz inclusions can be seen in Figure: 2.8.

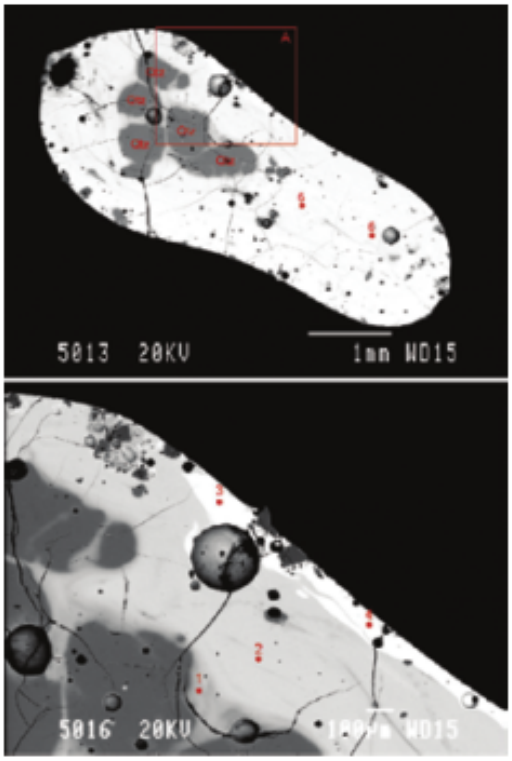


Figure 2.8: BSE image of dumbbell shaped particulate debris
The bottom image illustrates diffuse margins around a quartz inclusion. Mg-rich amphibole is indicated by the brightest region. (7)

Morphological studies, while informative, can only provide information on the structure of bulk melt glass. Because of this, it is necessary to examine specimens with a variety of other techniques.

2.3 Composition

2.3.1 Bulk Melt Glass

Elemental composition of bulk melt glass is highly variable from sample to sample. However, even with this variation, a replicable average can be determined by

examining multiple samples, provided that the samples are chosen at random (7; 20; 21). Techniques used to examine chemical composition and distribution of bulk melt glass are the same as those commonly used for geochemical measurements (SEM, EDS, BSE, XRD, and mass spectrometry)(21). In addition to these techniques, autoradiography is also commonly used to determine the location of radioactive species.

EDS analysis of trinitite has revealed the presence of a reaction layer lining both the exterior of the samples and the interior of some vesicles(22). An abrupt transition between this reaction layer and the remainder of the sample can be seen in photomicrographs such as those seen in Figure: 2.9. The presence of the reaction layer varies greatly between vesicles. At times, it can completely encapsulate the void space, while at other times it may only be partially present, if at all(22).

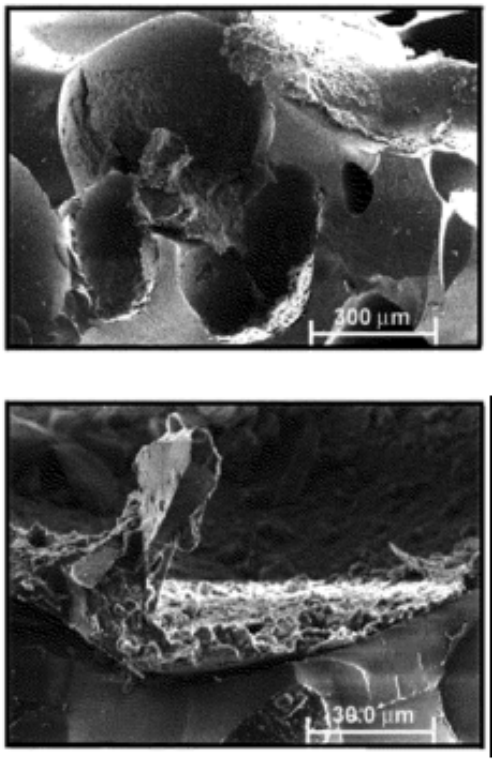


Figure 2.9: SEM photomicrographs of reaction layers lining vesicles in melt glass samples

(22)

Silicon

As previously stated, the vast majority of trinitite has been found to be composed of silicon, primarily α-quartz, though minor grains of other silicon bearing minerals, such as plagioclase, have been observed(3). Silicon occurs throughout trinitite in high concentrations, though some inclusions may show lower abundance. It has also been hypothesized that urban melt glass will contain a large quantity of silicon due to the vast quantity of aggregates found in structural and infrastructural materials in cities such as concrete, brick, and paving asphalt(23).

Aluminium

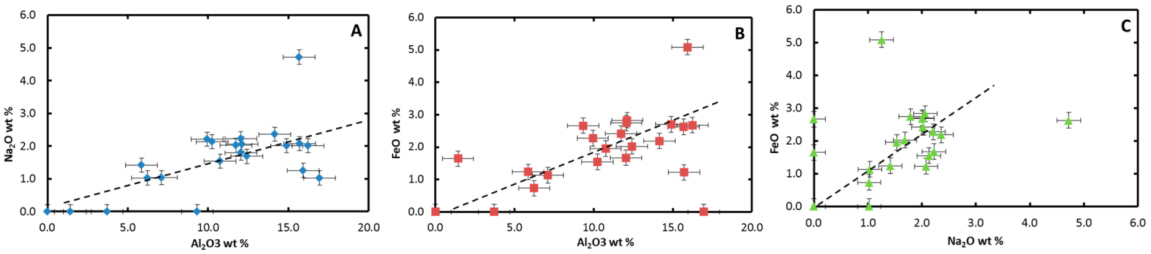
Aluminum abundances in trinitite positively correlate with both iron and sodium content (as Al:Fe and Al:Na), as demonstrated in Figures 2.10a and 2.10b (13). Several analyses of trinitite have shown an Al_2O_3 content of greater than 18 wt.%. According to Bellucci, the major aluminum bearing phases found in arkosic sand are K-feldspar and plagioclase, both of which contain at most 18wt.% of Al_2O_3, before dilution from other mineral phases are taken into account. These findings would indicate that the aluminum content within trinitite partially comes from an anthropogenic source, possibly the aluminum shells within the nuclear device(20).

Iron

Melt glass that contains a high concentration of iron (experimentally determined at >5wt.% FeO) tends to appear very dark in plane-polarized light(24). High iron concentrations tend to positively correlate with aluminum and sodium abundance, which is expected, due to the coexistence of these three elements in the naturally occurring compounds present at the trinity site(20). Areas of iron-rich trinitite that lack sodium likely indicate an anthropogenic origin(13).

Sodium

Sodium content in trinitite has been found to positively correlate with both iron and aluminum content. This can most likely be attributed to a varying proportion of amphibole — dark-colored inosilicate materials composed of linked SiO_4 tetrahedra, generally containing iron, aluminum, and/or sodium/magnesium — in the arkosic sand at the Trinity site (13). These correlations can be seen in Figure 2.10a and 2.10c.



(a) Al_2O_3 vs Na_2O **(b)** Al_2O_3 vs FeO **(c)** Na_2O vs FeO

Figure 2.10: FeO and Na_2O vs Al_2O_3 (A, B) and FeO vs Na_2O (C) contents for trinitite.

Error bars are reported at the 1σ level (13)

Copper

Because of the red color it imparts to melt glass, the presence of copper metal in trinitite can be observed with the naked eye, as seen in Figure 2.11. Upon closer inspection with both optical microscopy and scanning electron microscopy, it is revealed that the copper is in the form of metallic chondrules. BSE analysis further shows the occasional incorporation of metallic iron globules within the copper chondrules, indicating that at one point, both the iron and copper occurred as two immiscible liquids(7). As arkosic sand does not contain copper-bearing compounds, the copper in these samples originated from the "gadget", as copper wiring was used extensively in its assembly(3; 25).

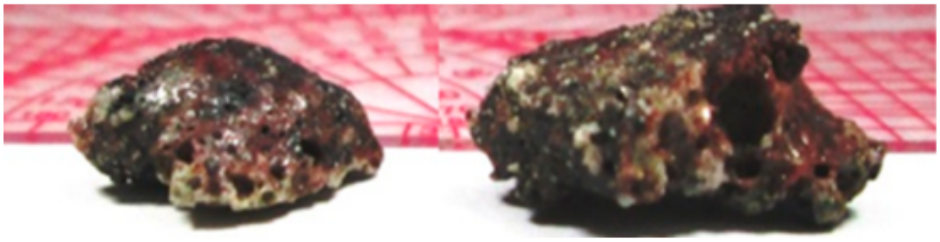


Figure 2.11: Photo of "red" trinitite. Its color is caused by a high concentration of copper

(26)

Lead

Lead oxide inclusions are not always observed in trinitite, though when they do occur, they are commonly found in concentrations positively correlated with copper. Figure 2.12 demonstrates this correlation. LA-ICPMS analysis indicates that lead concentrations occur between ∼500 and ∼27,000 $^{\mu g}/_{g}$(26). While this is a large variation in concentration, it is interesting to note that it is well above the ∼40 $^{\mu g}/_{g}$ concentrations found in the arkosic sand at the trinity site. It is also notable that the highest concentrations of lead found in green trinitite are around 1735 $^{\mu g}/_{g}$, quantitatively supporting the correlation between lead and copper concentrations(20). Because of the low concentrations of lead in the natural soil, the majority of lead trinitite can be assumed to come from the "gadget" and the support structure at the trinity site.

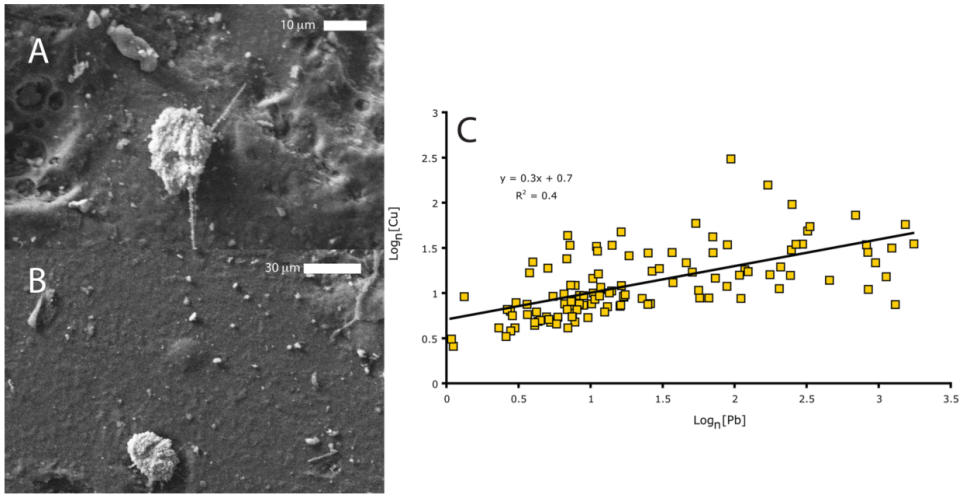


Figure 2.12: (*A*,*B*) SEM images of PbO inclusion on the surface of trinitite glass. (*C*) Concentrations of Pb and Cu in trinitite melt glass

(27)

Titanium

An SEM-EDS analysis of the blast side of trinitite by Koeman revealed the presence of Fe-Ti oxide inclusions on the scale of 10-100 μm (13). The presence of these inclusions confirms the findings of Eby, Bellucci, and Fahey, all of whom have deemed the inclusions anthropogenic in origin (7; 21; 25)

Calcium

While they themselves are not necessarily useful as forensic indicators, calcium-rich areas of melt glass can yield invaluable information when trying to generate a source-term for nuclear debris. Regions of nuclear melt glass that with a higher than 10 wt.% composition of CaO generally contain larger concentrations of uranium and plutonium as compared to regions with a lower concentration of calcium. These trends can be observed in Figure 2.13. It should be noted that the concentrations of uranium found in areas of high-calcium concentrations in trinitite are consistent with the natural uranium content found in the soil of Alamogordo, NM(3.2ppm)(14; 21; 24). This

information can be used as an investigative tool to differentiate between natural and anthropogenic sources of uranium.

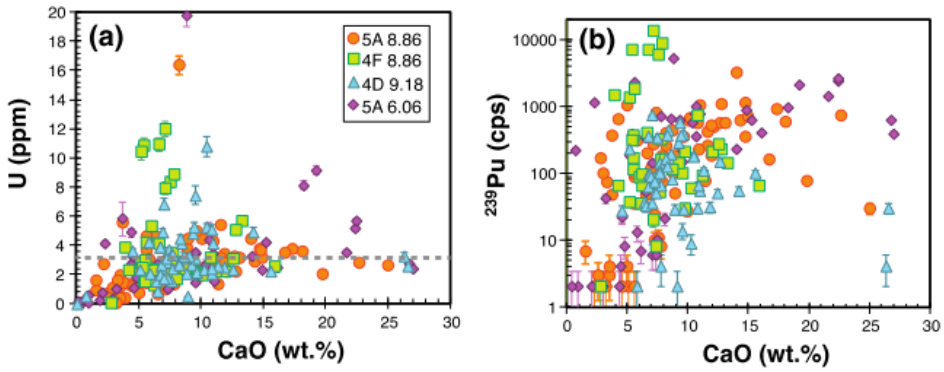


Figure 2.13: Correlation of (*a*)U and (*b*)Pu with respect to CaO in trinitite (24)

2.3.2 Particulate Melt Glass

While research on various bulk melt glass samples has yielded a plethora of elemental composition data, investigations of particulate debris have primarily been concerned with the fractionation and transport of various radioactive species. The presence and correlation between radioactive nuclides in particulate melt glass is discussed in subsection: 2.4.3. Because of the limited amount of research conducted, there is no information on either the colocation of chemical species or correlation between the presence of elements. Quantitative data is available, however, on the major oxides present in particulate melt glass found at the Trinity site. These values can be found in Table: 2.1 as representative oxide species.

Table 2.1: Major oxides of particulate melt glass

Oxide	Average wt.%
SiO_2[a]	61.29±2.49
TiO_2[a]	0.62±0.63
Al_2O_3[b]	11.25±0.42
FeO[b]	2.99±0.13
MnO[a]	0.09±0.02
CaO[b]	1.65±0.41
MgO[b]	0.57±0.06
Na_2O[b]	3.29±0.17
K_2O[b]	4.58±0.48

a- Reported by Eby et al.(7)

b- Reported by Eppich et al.(8)

SiO_2 (in no particular form) is the predominant oxide found in particulate debris. The concentration of SiO_2 is six times larger than the concentration of the next most abundant oxide (Al_2O_3), which is expected due to the large mass of silica-based soil and geological material consumed by the fireball. The presence of TiO_2, while claimed by Eby, is suspect at best due to the large error. The presence of the other identified oxides is expected based on the soil chemistry of the Trinity site.

2.3.3 Dissolution Techniques

The metalo-silicate nature of nuclear melt glass presents unique challenges when attempting to dissolve samples for isotopic analysis. Geochemical dissolutions are typically the favored method, though their long digestion and preparation times make them unsuitable for the rapid isotopic determination that would be needed in a post-detonation scenario. Typically, these methods involve either an acid or alkaline fusion to separate elements of interest from the rest of the sample(28; 29; 30). Work

performed at the University of Tennessee by Gill, involved investigations of various dissolution techniques in order to determine the most effective way to both rapidly and effectively analyze nuclear melt glass(31). Four methods were analyzed and compared against each other: a multi-stage acid digestion(8); a modified version of the acid digestion designed to use a microwave digestion vessel in order to decrease preparation time(31); a lithium flux method(32); and an alkaline flux method(33). The modified HF acid digestion was found to be the most effective in terms of both time and precision(31). It should be noted, however, that the formation of SiF_4 (boiling point -65 °) during this process leads to a loss of silicon. For the purpose of nuclear melt glass analysis, this is an acceptable loss, as radioactive silicon isotopes are, for the most part, short lived (half-life on the order of seconds or minutes), and do not provide any useful forensic signature.

2.4 Radiological Profile

2.4.1 Fractionation of Radionuclides

In order to properly determine the radioactive species present in nuclear melt glass, it is important to understand what happens to various elements when they are exposed to the extreme conditions within the fireball. The dispersion of material after a nuclear explosion is heavily dependent on the boiling point of its constituent materials. Isotopic concentrations have no bearing on material fractionation. Refractory compounds, those with high melting points, can be found in enriched concentrations in the area surrounding ground zero and in depleted concentrations in atmospherically transported particulate fallout. These compounds tend to be highly stationary, remaining in the vicinity of ground zero. Conversely, volatile compounds, those possessing lower melting points, can be found in depleted concentrations in the area surrounding round zero and in enriched concentrations in atmospherically transported particulate fallout(34; 35; 36; 37; 16). These compounds tend to be highly migratory,

as they are transported away from ground zero via atmospheric conditions. The most likely location of fission products and their daughters are listed in Table: 2.2. It should be noted that some elements found in the vicinity of ground zero are volatile in nature and some found away from ground-zero are refractory. This is because their parent nuclides were either deposited and ground-zero, or transported in the fallout plume. Decay of these parent nuclides is the cause for the presence of refractory or volatile fission products in areas that they may not be expected to occur. Activation products are scenario dependent, and thus are not listed in this review.

Table 2.2: Location of some fission products post-detonation

Elements Found at Ground Zero	Ge As Se Br Rb Mo Ru Pd Ag Cd In
Elements Found Away from Ground Zero	Ga Kr Sr Y Zr Nb Tc Rh Cs U

A variety of computer codes such as FAT, SCALE, and ORIGEN can be used in conjunction with one another to model the production, decay, and dispersion of radionuclides post-detonation(38; 39). Using these codes to model fallout shows that while the general rules of refractory vs volatile elements allows for a good first order approximation. However, they also reveal that it is important to account for the decay of the radionuclides in question. Elements that are incorporated into particulate fallout sometimes decay into refractory elements and vice versa. Careful attention needs to be paid to the time scale on which debris is analyzed in order to glean the most pertinent information. Decay chains highlighting the fission and daughter products and their locations post-detonation can be seen in Figures: A.1-A.5.

2.4.2 Bulk Melt Glass

Activity levels and distribution

Multiple studies have been conducted over the years on the radiological profile of various nuclear melt glasses. Activity distribution widely varies not just in samples of trinitite, but in the vast majority of atomsite found at nuclear test sites. Beta radioactivity accounts for the a large portion of these variations, with numerous samples showing top/bottom surface ratios ranging between 2.6 and 22.9(40). This would strongly correlate with the fractionation of Sr (^{90}Sr) being a beta-particle emitting fission product), which would have fallen to the ground as a particulate and adhered to the bulk melt glass already present and cooling on the surface.(6) Alpha activity also varies throughout samples. Eaton reports that darker areas of melt glass obtained from the Nevada Nation Security Site tend to have higher alpha activity than lighter regions, with alpha-track radiography indicating a high level of homogeneity of alpha-emitters in darker regions(22). Additionally, it is noteworthy that areas of high alpha activity are strongly correlated with calcium concentrations(21). It is unknown whether or not exposure of these samples to environmental aqueous solutions influenced these findings. Naturally occurring nuclides such as ^{40}K, ^{238}U, and ^{232}Th were examined by Schlauf, and their contributions to activity have been accounted for in subsequent studies(41).

α-emitters of interest in bulk nuclear melt glass

Alpha-emitters found in nuclear melt glass primarily come from anthropogenic sources such as the fuel or tamper of the weapon. Alpha-emitting nuclides that are not anthropogenic in nature are usually either products of neutron capture events that occured during the detonation (^{229}Th), or daughters products of nuclides generated via capture events (^{241}Am being produced by β-decay of ^{241}Pu). Table 2.3 lists the published alpha emissions of interest from bulk nuclear melt glass. Uranium can be found in two of the major components of a nuclear weapon, the fuel, and

the tamper. Both ^{233}U and ^{235}U are viable for use as the fissionable material in a device, however current infrastructure of the nuclear industry makes the use of ^{235}U much more likely. ^{238}U can potentially be used in the tamper of the weapon. With the implementation and development of implosion-type devices, identification and characterization of isotopes of plutonium and their sources became a very important forensic indication. ^{239}Pu is in many ways the most desirable fuel source for an implosion type device. This nuclide is most commonly produced in a nuclear reactor via a (n,γ) reaction. Subsequently, further neutron bombardment of ^{239}Pu can lead to the production of ^{238}Pu, ^{240}Pu, ^{241}Pu, which are simultaneously produced in situ via (n,2n), (n,γ), and (2n,γ) reactions, respectively(6). It stands to reason that ^{239}Pu Isolated from spent fuel will contain ^{238}Pu, ^{240}Pu, ^{241}Pu, albeit in small amounts. Large quantities of ^{240}Pu are considered highly undesirable in nuclear weapon pits due to its high propensity of spontaneous fission, and subsequent safety concerns when a weapon is fully assembled. Because of this, a common prerequisite in the production of weapon-grade plutonium is that the concentration of ^{240}Pu be <7% by weight, while super-grade plutonium contains <3% 240Pu. Concentrations of ^{240}Pu found in bulk melt glass can lead to valuable information about the types of reactors used for production, and their operations (42). These results could narrow the number of potential production site, and origin of a device. However, because of the nature of the reactions, it is likely that plutonium isotopes (other than ^{239}Pu) could be produced during detonation, necessitating additional forensic analyses before a source could be determined. ^{241}Am is produced via β-decay of ^{241}Pu. It has been reported by Rhodes that the Hanford plutonium was separated from uranium and fission products using a bismuth phosphate carrier, followed by a lanthanum fluoride carrier, and finally by oxidation of plutonium to transfer it to the solution. In this process, trivalent actinides, such as americium, would have remained with the lanthanum fluoride carrier(10). Therefore, the ^{241}Am measured after a nuclear event would reflect only the ^{241}Pu which was produced in a reactor and did not decay during the production, as well as the ^{241}Pu which was produced during the explosion(43).

Table 2.3: α emissions of interest from published bulk nuclear melt glass data

Nuclide	**Half-life** (yr)	**Energy** (MeV)
^{229}Th	7.4E3	5.168
^{233}U	1.59E5	4.909
^{234}U	2.46E5	4.859
^{235}U	7.04E8	4.679
^{236}U	2.34E7	4.572, 7.322
^{238}U	4.47E9	4.267
^{238}Pu	87.7	5.499
^{239}Pu	2.41E5	5.156
^{240}Pu	6.56E3	5.168
^{242}Pu	3.73E5	4.984
^{241}Am	432.7	5.486

β^- emitters of interest in bulk nuclear melt glass

β^--emitting nuclides in bulk nuclear melt glass come primarily from the fission products of ^{235}U and ^{239}Pu. Fission products tend to be neutron-rich, and hence favor β^- as their decay mode. Additionally, many of these decays are accompanied by characteristic γ-rays. Because of the continuous nature of the energy emitted by β^- decay spectra can sometimes become very complicated and difficult to deconvolute. Because of these, the accompanying characteristic γ-rays can be used for isotopic identification. Table 2.4 lists common β^--emitters that can be found in bulk nuclear melt glass. Half-life, total β^- decay energy, and energy of accompanying γ-rays are also listed. The vast majority of these nuclides have short half-lives (less than a year), and will therefore be highly radioactive. ^{90}Sr, and ^{241}Pu are the only two nuclides that would be useful for identification after any appreciable amount of time.

Table 2.4: β^- emissions of interest from published bulk nuclear melt glass data

Nuclide	Half-life (yr)	β^- Energy (MeV)	γ Energy (keV)
^{89}Sr	1.39E-01	1.488	909.1
^{90}Sr	2.88E+01	0.546	—
^{95}Zr	1.75E-01	0.368, 0.400	724.2, 756.7
^{97}Zr	1.91E-03	1.92	743.3
^{140}Ba	3.49E-02	0.48, 1.00, 1.02	29.97, 537.26
^{141}Ce	8.90E-02	0.436, 0.581	145.4
^{144}Ce	3.77E-03	1.110, 1.404	80.1, 133.5
^{91}Y	1.60E-01	1.545	1205
^{156}Eu	4.16E-02	0.49, 2.45	89.0, 811.8, 1230.7
^{147}Nd	3.01E-02	0.805	91.1, 531.0
^{231}Th	2.91E-03	0.305	25.64, 84.21
^{239}Np	3.72E-03	0.341, 0.438	106.1, 228.2, 277.6
^{241}Pu	1.43E+01	0.0208	103.7

γ-ray emitters of interest in bulk nuclear melt glass

Gamma-emitting nuclides found in bulk nuclear melt glass can come from a variety of sources, including both fission and activation products. Table 2.5 lists several gamma-ray emissions of interest from bulk melt glass that have been discussed in the literature, while Figure 2.14 shows a typical gamma-ray spectrum of trinitite. The literature has shown a significant positive correlation in trinitite for ^{152}Eu and ^{154}Eu concentrations, which seems to indicate the activation of stable europium isotopes from the soil at the trinity site(4; 11; 44) As for ^{155}Eu, there is significant disagreement in the literature as to whether or not it should even be detectable in trinitite after thirteen half-lives. Both Pittauerova(40) and Bellucci(11) report correlation with ^{239}Pu measurements, while Parekh(6), Schlauf(41), and Cook(45) report no finding whatsoever of ^{155}Eu. ^{133}Ba was found in numerous studies and

displayed a fairly uniform distribution in numerous atomsite samples, indicating a low degree of fractionation(6; 41) The presence of barium in melt glass samples indicates the use of the compound baratol in the explosive lenses of a device.

Table 2.5: γ-ray emissions of interest from published bulk nuclear melt glass data

Nuclide	**Origin**	**Half-life (yr)**	**Energies (keV)**
^{40}K	Natural	1.25E9	1461
^{60}Co	Activation	5.3	1173, 1333
^{133}Ba	Activation	10.5	81, 303, 356, 384
^{137}Cs	Fission	30.2	662
^{152}Eu	Activation	13.2	122, 245, 344, 779, 964, 1086, 1112, 1408
^{154}Eu	Activation	8.6	123, 723, 873, 996, 1005, 1275
^{208}Tl	Th daughter	5.81E-6*	583, 2615
^{212}Pb	Th daughter	1.21E-3*	238
^{214}Pb	U-Ra daughter	1.6E3	395, 352
^{228}Ac	Th daughter	7.02E-4*	339, 911, 969
^{239}Pu	Transuranic	2.4E4	129
^{241}Am	Pu daughter	432	59

*These nuclides are seen in the decay chain of ^{232}Th ($t_{1/2}$=1.4E10)

Due to the stochastic nature of radioactive decay, multifarious sample sizes, and systematic errors, variation can always be expected in radionuclide activity measurements. Additionally, when analyzing bulk melt glass, it is important to note that variation in measurements can also come from the sample's location(43). Studies performed by both Semkow and Pittauerova found a power-law dependence between ^{152}Eu inventory, and the slant range between sample location and the nuclear explosion center(40; 43). This locational dependency appears to only have an effect on activation products as the same specimens showed no correlation between ^{137}Cs

(a fission product) and slant range(40). Pittauerova additionally notes that while site clean-up activities may affect these models, evidence found during a 2006 survey indicates that the specimens measured were probably within a meter or two of their original location(6; 43)

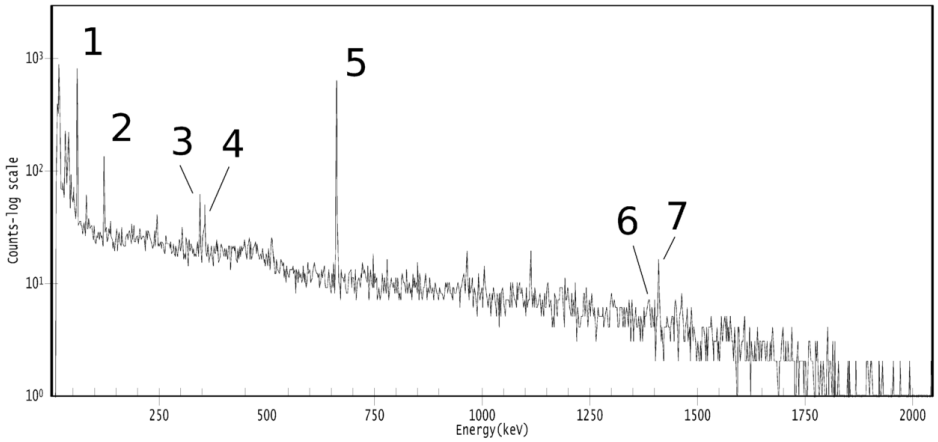


Figure 2.14: $\gamma-$ray spectrum of trinitite 66-years post-detonation. Noteworthy peaks are numbered: 1) 59.5 keV, ^{241}Am; 2) 121.8 keV, ^{152}Eu; 3) 344.3 keV, ^{152}Eu; 4) 356.0 keV, ^{133}Ba; 5) 661.6 keV, ^{137}Cs; 6) 1408 keV, ^{152}Eu; 7) 1461 keV, ^{40}K (4)

2.4.3 Particulate Melt Glass

Activity Levels and Distribution

While particulate melt glass contains some of the same radionuclides found in bulk melt glass, fractionation effects during the cooling of the fireball ultimately dictate both the presence and concentration of elements(18; 35). Volatile radionuclides are interspersed throughout the particles, while refractory radionuclides tend to be concentrated on the outer layers(8). Total specific activity levels ($^{dpm}/_{g}$) of particulate melt glass tend to be higher than those of bulk melt glass, with spherical particles having a higher specific activity than oblong particles(7; 8; 16; 46).

α emitters of interest in particulate nuclear melt glass

The alpha emitters present in particulate nuclear melt glass can be attributed to either anthropogenic sources (discussed in subsection: 2.4.2), actinides, activation products, or daughter products. The alpha-emitting nuclides of interest in particulate melt glass are the same as those in bulk melt glass. A list of the alpa-emitters of interest can be found in Table: 2.3. As with any melt glass, the alpha-emitting nuclides present will vary depending on weapon specifications.

Eppich et al. investigated various isotopic ratios from debris generated at the NNSS(8). This investigation found that concentrations of U can be 3-12 times higher than the concentrations found in bulk melt glass. Particulate melt glass is also enriched in other alpha-emitters such as Pu, Am, and Pa, which all have elemental boiling points either lower than or comparable to U(35; 47). Th concentrations in particulate melt glass are similar to those found in bulk samples, which is expected due to its higher elemental boiling point. Isotopically, the ratio of two isotopes of the same element should not differ between particulate and bulk melt glass.

β^- emitters of interest in particulate nuclear melt glass

Again, β^--emitters tend to be neutron-rich fission products with short half-lives. Nuclides of interest found in particulate melt glass are ^{137}Cs, ^{24}Na, and ^{99}Mo. ^{137}Cs is an important contributor to dose and one of the main causes of concern after a nuclear detonation from a health physics perspective. ^{24}Na concentrations can assist in calculating total neutron exposure in an area of interest. Finally, ^{99}Mo can be used to compare isotopic fractionation between events (^{99}Mo yield is fairly independent of both neutron spectrum and fuel type). Because ^{99}Mo is very shot-lived, its daughter product ^{99}Tc can also be used for this purpose. A complete list of β^--emitters that are commonly found in particulate melt glass can be found in Table 2.6 along with their half-lives, decay energies, and the energies of the accompanying γ-rays.

Table 2.6: β^- emissions of interest from published particulate nuclear melt glass data

Nuclide	**Half-life (yr)**	β^- **Energy** (MeV)	γ **Energy** (keV)
^{99}Mo	7.53E-03	1.214	140.5, 181,1, 739.5
^{111}Ag	2.05E-02	1.035	342.1
^{115m}Cd	1.22E-01	1.62	933.8, 1290.6
^{115}Cd	6.10E-03	0.593, 1.11	336, 527.9
^{103}Ru	1.08E-01	0.223	497.1
^{106}Ru	1.02E+00	0.0394	—
^{136}Cs	3.59E-02	0.341	340.5, 818.5, 1048.1
^{137}Cs	3.01E+01	0.514	661.7
^{24}Na	1.71E-03	1.391	1368.6, 2754.0
^{64}Cu	1.45E-03	0.578	1345.8
^{67}Cu	7.07E-03	0.39, 0.48, 0.58	93.3, 184.6
^{187}W	2.73E-03	0.622, 1.312	479.6, 685.7
^{237}U	1.85E-02	0.24, 0.25	59.5, 208.0
^{240}U	1.61E-03	0.36	44.1

γ-ray emitters of interest in particulate nuclear melt glass

Gamma-emitting nuclides found in particulate nuclear melt glass can come from a variety of sources, including both fission and activation products. While fission products vary solely based on the weapon fuel, the presence of specific activation products is directly related to the materials present at the site of detonation. Figure: 2.15 shows overlaid time-dependent $\gamma-$ray spectra from a ^{235}U fueled air-burst detonation(19).

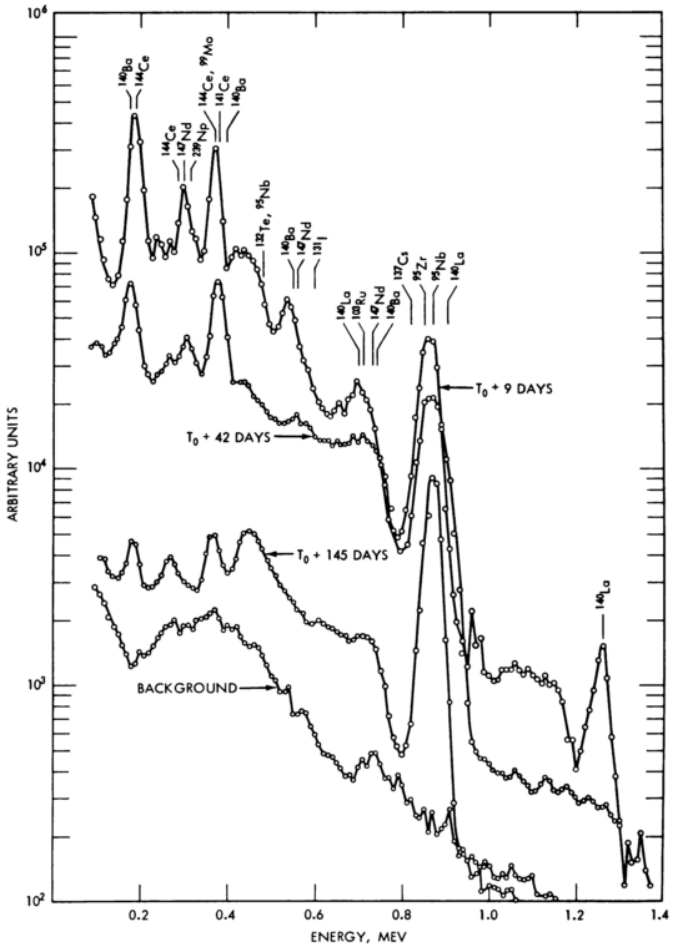


Figure 2.15: $\gamma-$ray spectra from a ^{235}U fueled air-burst test (19)

As expected, particulate melt glass has been found to be enriched in volatile nuclides, while depleted in refractory nuclides. The exception to this rule would be in the case of refractory daughter products such as ^{95}Nb and ^{103m}Rh(19). These nuclides were not present during the formation of the particles, but instead grew-in from the decay of their parent nuclides which were volatile in nature. A list of fission $\gamma-$ray signatures expected in particulate debris can be found in Table: 2.7.

Table 2.7: ^{235}U fission $\gamma-$ray emissions of interest from published particulate nuclear melt glass data

Nuclide	Activity (γ-emissions/min)	Energies (keV)
^{95}Zr-^{95}Nb	55.67	235, 717, 745
^{99}Mo-^{99m}Tc	1,401.5	41, 141, 180, 740, 780
^{103}Ru-^{103m}Rh	74	40, 498
^{131}I	138	364
^{132}Te-^{132}I	2,206	231, 528, 673, 777, 960, 1,400
^{137}Cs-^{137m}Ba	0.27	661
^{140}Ba-^{140}La	724	30, 160, 300, 490, 540, 815, 1,600
^{141}Ce	60	145
^{143}Ce	2,130	126, 289, 356, 660
^{144}Ce-^{144}Pr	55.67	34, 81, 134, 695, 1,480
^{147}Nd	86.5	92, 318, 532

(19)

2.5 Surrogate Development

2.5.1 Synthetic Bulk Melt Glass

Synthetic Trinitite

The heat generated by a nuclear explosion will produce temperatures as high as 8,430 °C leaving most materials near ground zero in a plasma state(14). This environment cannot be easily recreated with standard equipment in a laboratory. However, because the critical parameters of nuclear melt glass formation such as the soil solidification temperature and corresponding solidification time are independent of heating rate

and the means of heating, it is possible to create viable surrogates, specifically by replicating the conditions existing at the moment of soil solidification(1).

Research conducted by Molgaard determined that if a mixture of oxides was combined in a high purity graphite crucible and heated until a liquidous state was reached, the resulting molten material could then be poured onto a bed of room temperature sand where it quickly vitrified. Samples were characterized using P-XRD, SEM, EDS and gamma spectroscopy. and it was shown that a reasonable set of processing parameters could be employed to produce synthetic melt glass with chemical and morphological properties very similar to trinitite(1). Specifically, it was shown that a high degree of vitrification can be achieved at temperatures between 1400 °C and 1500 °C and melt times between 30 and 60 minutes(1). Samples were cool enough to handle without thermal protective equipment within 10 to 15 minutes.

Synthetic Urban Debris

Building upon the research conducted by Molgaard et al. for the synthesis of surrogate trinitite, a method of developing matrix formulations for the creation of synthetic urban nuclear melt glass was developed, and examples were for two different cities (New York, NY, and Houston, TX)(23). Giminaro et al. determined that given appropriate data sets and assumptions, it could be possible to use a formulated methodology to model any city or site-specific location worldwide(23). The method can be used to analyze other areas that could be potential target areas for non-state actors. The research showed that it is also possible to scale the nuclear weapon yield as well as the fuel and tamper components for added verisimilitude in the resulting synthetic debris. Using approach outlined by Giminaro et al. in combination with the techniques outlined by Molgaard et al. it is possible to develop a realistic urban debris surrogate that is comparable to an expected actual post-detonation material, thus providing a pathway for synthesis and preparation of melt glasses for a variety of scenarios for methods development and procedural quality control. These methods are further outlined in section: 3.1.

2.5.2 Synthetic Particulate Melt Glass

While static furnaces are suitable for the production of synthetic bulk surrogates, the production of synthetic particulate debris poses a unique challenge because of particle size.

Currently, PNNL has been focusing research efforts on the use of various porous chromatographic materials (PCM) loaded with the chemical species that are expected to be found in a post-detonation scenario(48). The loaded PCM serves as a precursor material for the synthesis of complex nuclear explosion debris form.

A CO_2 laser is used to rapidly heat the surface of the loaded PCM to temperatures >2500K. Particles several mm in diameter have been produced using matrices resembling trinitite and a hybrid trinitite/concrete/iron matrix(49) The glasses produced were similar in appearance to trinitite and other nuclear melt glasses produced by both French tests in Algeria, and Russian tests at the Semipalatinsk site. Pictures of debris as a function of laser exposure time can be seen in Figure:2.16. Additional research by Liezeres et al. has been successful in loading these glasses with isotopically altered Xe before laser treatment, and succesfully generating debris enriched in ^{129}Xe(49). While the techniques currently employed by PNNL do show promise for particulate debris production, refinement of the process is needed in order to produce particulate debris of appropriate size.

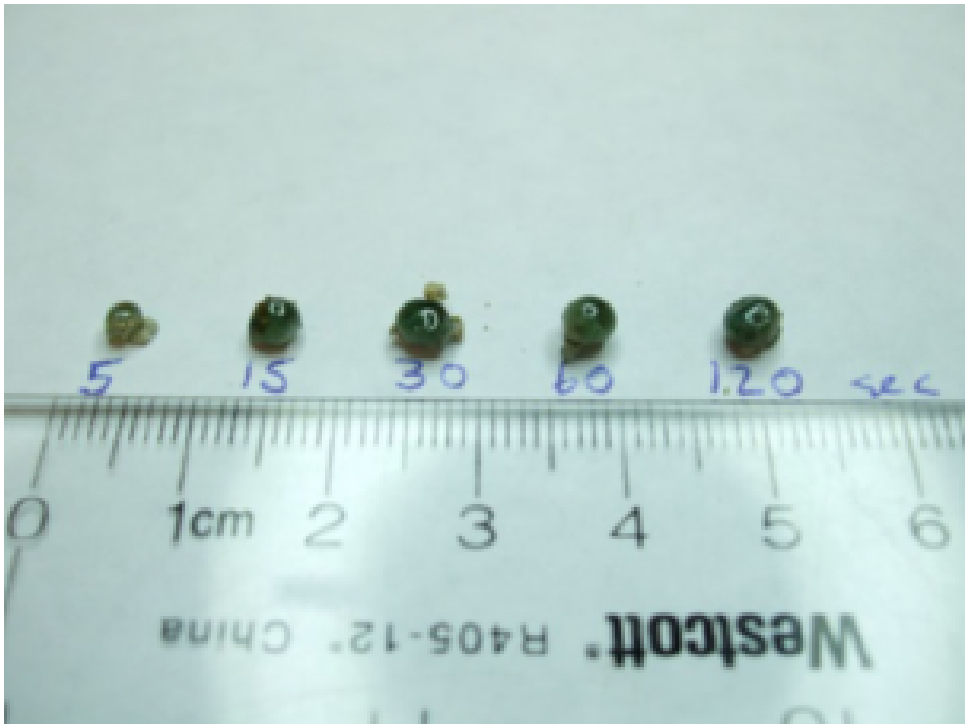


Figure 2.16: Fused glass bead formation from a concrete-glass powder as a function of laser exposure time.

(49)

Chapter 3

Methodology

3.1 Surrogate Precursor Matrix Development

Urban areas can be modeled as a three-component system comprised of: (1) a soil layer; (2) an infrastructural layer consisting principally of buildings, bridges, roads, rail lines, etc.; and (3) a vehicular layer, comprised of public, private, and industrial modes of transportation: cars, buses, trains, etc. Generic formulae for the determination of urban matrix compositions have been developed. Specific examples for Houston (Texas, USA) and New York City (New York, USA) were developed to illustrate the variability in resulting debris. Data for these scenarios was taken from the borough of Manhattan and the city limits of Houston, TX.

Soil Layer

Soil data were obtained from the United States Geological Survey (USGS)(50). The data presented in the study gave mineralogical data sampled from approximately 5000 sites in the conterminous United States (1 site per 1600 km^2). Coordinates for NYC and Houston,TX were determined, and all USGS data points for the C horizon – the layer of soil that extends from at most, 1 m below the surface to bedrock – that fell within a 34,000 km^2 area around the point of interest (in the conterminous U.S.,

this equates to roughly $\pm 1^{\circ}$ latitude/longitude) were averaged and used as the soil composition for the city. The organic layers were not used for comparison due to an expectation that organic layers will volatilize in the extreme temperatures exhibited in a nuclear event, and hence not be highly incorporated in the resulting melt glasses. Deeper soil layers will constitute the majority of the soil contribution(2). The USGS data were presented in the form of mineralogical composition by weight percentage, and it was necessary to convert them to an elemental composition in order to properly formulate the desired precursor matrices, as shown by 3.1.

$$S_x = \sum_i [S_i w_x] \tag{3.1}$$

S_i is the total percent by weight of element i found in the soil, S_x is the percent by weight of mineral i as found within the soil sample, and w_x is the weight fraction of the element x in mineral i. The weight fraction w_x is determined by equation 3.2,

$$w_x = \frac{m_x n_i}{m_i} \tag{3.2}$$

Where m_x is the mass of a single atom of element x in amu, n_i is the number of atoms of element x in a single formula unit of mineral i, and m_i is the mass of a single formula unit of mineral i in amu.

Elemental soil compositions were calculated for both New York City and Houston, and the weight fractions of the twelve most prevalent elements, excluding oxygen, are reported in Table 3.1.

Infrastructure Layer

Analyzing permanent structures and roads requires knowledge of land use, regional construction specifications, fundamental building materials, and infrastructure age. Land use data were readily available in the open source literature for many urban locations. Based on land use data, the prevalence of structures and undeveloped

Table 3.1: Elemental composition of soil by weight fraction

Element	NYC(%)	Houston(%)
Si	60.5 ± 5.4	63.8 ± 5.7
K	3.55 ± 0.2	2.20 ± 0.2
Al	15.1 ± 1.4	17.9 ± 1.6
Ca	6.35 ± 0.7	7.48 ± 0.7
Na	3.23 ± 0.3	0.75 ± 0.07
Fe	7.63 ± 0.6	6.23 ± 0.6
Mg	2.65 ± 0.2	0.87 ± 0.08
S	0.06 ± 0.01	0.07 ± 0.01
Ba	0.06 ± 0.01	0.09 ± 0.01
Mn	0.12 ± 0.01	0.06 ± 0.01
P	0.10 ± 0.01	0.03 ± 0.01
Ti	0.61 ± 0.05	0.60 ± 0.05

areas within a city can be determined. Structures required further material and elemental breakdown, whereas undeveloped areas were considered to have a negligible contribution to the overall infrastructural composition of the city. Internal, non-construction materials of most structures were assumed to be primarily wood and plastics. The elemental contribution of these organic materials was considered to be negligible, again using the assumption that organics would be lost due to combustion, vaporization, etc. In order to estimate the elemental composition of urban post-detonation debris for each city, the primary construction materials of each type of structure must be known, and elemental fractions of each material must be evaluated. The effective height of a structure, h, or the height the structure when reduced to rubble while occupying the same footprint, must also be considered. For example, the relative percentage of concrete used in commercial buildings must be known; however, concrete itself has several components: aggregate, cementitious materials, etc., all of which may have some level of regional variation. Construction material variances can be substantial depending on land use(51). Each of these components in turn must be analyzed for their elemental constituents. The elemental composition of the infrastructural layer was calculated using equation 3.3.

$$I_x = \sum_l [v_l l_x] \tag{3.3}$$

I_x is the total percent by weight of element x found in the infrastructural layer, v_l is a volumetric fraction of structure type l in the area of interest, and l_x is the weight fraction of element x in structure type l. Equation 3.4 shows the volumetric fraction calculations used.

$$v_l = a_l \frac{h_l}{\sum_l h_l} \tag{3.4}$$

In equation 3.4, a_l is percentage of the area of interest covered by structure type l, and h_l is the effective height of structure type l. It should be noted that this equation does not result in a volumetric quantity, but rather a volumetric material fraction of structure type l with respect to total material volume.

$$l_x = \sum_j [j_x l_j] \tag{3.5}$$

Equation 3.5 shows the calculation of elemental weight fraction for structure type l, where j_x is the elemental composition of material type j (asphalt, steel, concrete, drywall, etc.), and l_j the weight fraction of material type j in structure type l.

Vehicle Layer

The elemental composition of the vehicle layer can be determined using equation 3.6:

$$V_x = \sum_p [f_p w_p p_x] \tag{3.6}$$

where V_x is the weight fraction of element x in the vehicle layer, w_p is a weight correction factor that accounts for different vehicle types (p), and can be calculated using equation 3.7; f_p is the percentage of vehicle type p as compared to the total number of vehicles in the area of interest, and can be calculated using equation 3.8;

p_x is the weight fraction of element x found in vehicle type p, and can be calculated using equation 3.9:

$$w_p = \frac{m_p}{\sum_p n_p} \tag{3.7}$$

where m_p is the average mass of vehicle type p. A list of the average vehicle masses per type and their weight corrections can be found in Table 3.2. The percentage of vehicle type is calculated as

$$f_p = \frac{n_p}{\sum_p n_p} \tag{3.8}$$

where n_p is the number of vehicles of type p in the area of interest. This number can usually be found in national transportation statistics [11]. Finally, the elemental weight fraction from vehicles, p_x, is calculated as

$$p_x = \sum_k [k_x p_k] \tag{3.9}$$

where k_x is the weight fraction of element x in constituent k (as presented in Table:3.2), and p is the weight fraction of constituent k found in vehicle type p, as calculated in equation 3.10.

$$p_k = \frac{m_x n_k}{m_k} \tag{3.10}$$

n_k is defined as the number of atoms of element x in a molecule of constituent k, and m_k is the mass of a single molecule of constituent k in amu. Vehicle composition data was obtained from Cheah(52), and was found to vary primarily by the type of vehicle (gasoline, hybrid, diesel), and can be seen in Table 3.3. Because of the tendency for plastic, rubber and fluids to vaporize or combust in the extreme conditions found in a nuclear blast, their contribution is assumed to be negligible. The other portion of the composition can be considered as principally trace amounts of semi-conductor materials, in addition to organic materials, contributed by seat stuffing, insulation, interior liners, carpets, etc. These contributions can also be neglected in the elemental calculations because of either their small contributions to the total vehicle mass, or

their propensity for volatilization (i.e. organic materials). Compositions of buses and trains were modeled as diesel vehicles.

Table 3.2: Average vehicle weight by type

Type	Avg. weight (lbs)	Weight Fraction (w_p)
Gasoline	1,854	0.082
Diesel	19,536	0.860
Hybrid	1,325	0.058

(52)

Table 3.3: Weight fraction of various vehicular components by type

Constituent(k)	Gasoline(%)	Diesel(%)	Hybrid(%)
Iron	12.8 ± 0.9	11.9 ± 0.8	6.38 ± 0.4
High Strength Steel	12.8 ± 0.9	12.90 ± 0.9	17.0 ± 1.2
Other Steel	31.9 ± 2.2	31.7 ± 2.2	36.2 ± 2.5
Aluminium	10.6 ± 0.7	9.90 ± 0.7	8.51 ± 0.6
Plastics	10.6 ± 0.7	11.9 ± 0.8	14.9 ± 1.0
Rubber	4.26 ± 0.3	4.95 ± 0.3	2.13 ± 0.1
Glass	2.13 ± 0.1	1.98 ± 0.1	2.13 ± 0.1
Fluids	7.45 ± 0.5	6.93 ± 0.5	10.6 ± 0.7
Other	7.45 ± 0.5	7.92 ± 0.6	2.13 ± 0.1

(52)

Debris Mass Calculations

In addition to elemental compositions, it is important to know what contribution each of the three components of the model makes to the the total mass of debris consumed by the fireball. In order to make this determination, it is necessary to calculate the total mass of each component that is consumed by the fireball, and normalize to the total mass consumed. The total weight fraction of any element x can be calculated using equation 3.11.

$$T_x = (M_S S_x) + (M_I I_x) + (M_V V_x) \tag{3.11}$$

Where T_x is the total weight fraction of element x in the matrix being formulated, M_S is the fraction of the total mass consumed by the fireball that is contributed by soil, M_I is the fraction of total mass consumed contributed by infrastructure, and M_V is the fraction of total mass consumed contributed by vehicles. The mass fractions M_S, M_I, and M_V can be calculated using equations 3.12, 3.13, and 3.14 respectively.

$$M_S = \frac{S_m}{S_m + I_m + V_m} \tag{3.12}$$

$$M_I = \frac{I_m}{S_m + I_m + V_m} \tag{3.13}$$

$$M_V = \frac{V_m}{S_m + I_m + V_m} \tag{3.14}$$

The mass of soil, infrastructure, and vehicles consumed by the fireball are S_m, I_m, and V_m respectively. The mass of soil consumed S_m can be calculated using equation 3.15.

$$S_m = S_v \sum_i [\rho_i S_i] \tag{3.15}$$

The mass calculations for the infrastructural layer can be seen in equation 3.16.

$$I_m = I_v \sum_j \left[\rho_j \sum_l (l_j a_l) \right] \tag{3.16}$$

I_v is the effective volume (volume of material without void space) of infrastructure consumed, and is calculated in equation 3.17, using A to represent the area of the blast, again calculated using Glasstone(2). Finally, ρ_j is the average density of component j.

$$I_v = A \sum_l [a_l h_l] \tag{3.17}$$

The vehicle mass contribution, V_m can be calculated as:

$$V_m = \sum_p [m_p n_p] \tag{3.18}$$

The volume of urban material that is vaporized by the weapon was determined by calculating the volume affected by the fireball. Table: 3.4 shows effected area of the fireball radius for different weapon yields up to 10 kT. The thermal radius is the blast radius of the bomb before the energy of the weapon is reflected off of the ground, and the breakaway radius is the blast radius of the weapon after ground reflection is accounted for.

Table 3.4: Fireball radius with respect to yield

Yield(kT)	**Thermal Radius(m)**	**Breakaway Radius(m)**
0.10	11	18
0.20	14	23
0.50	21	34
1.00	27	44
2.00	36	58
5.00	52	84
10.00	69	111

(2)

Table: 3.5 shows the dimensions of the crater that is formed for differing yields of a nuclear weapon surface burst up to 10kT. The values in the table were tabulated using equations found in Glasstone and Dolan (2). The soil is assumed to be a mixture of compact soil and hard rock. In an urban environment, the soil has been tamped, and also contains concrete for the foundations of the building; therefore, the soil mixture and density was calculated. By determining the average density of the soil, the total volume of of the crater was multiplied by the calculated density. The result is the mass of soil displaced and possibly melted/vaporized during a nuclear detonation.

After calculating the mass of soil, infrastructural material, and vehicles that are vaporized; the aforementioned equations were used to calculate mass ratios. These mass ratios were used to create precursor matrices for creating synthetic urban nuclear

Table 3.5: Nuclear surface burst crater dimensions

Yield(kT)	**Diameter**(m)	**Depth**(m)	**Volume**(m^3)
0.10	14.6	3.35	2.89E+02
0.20	21.20	4.89	9.29E+02
0.50	25.3	5.76	1.44E+03
1.00	34.7	7.31	2.88E+03
2.00	40.0	9.14	5.78E+03
5.00	54.3	12.5	1.44E+04
10.00	68.3	15.8	2.89E+04

(2)

melt glass. Table 3.6 highlights the differences between the precursor matrices for NYC and Houston as generated by a 1 kT nuclear device.

Table 3.6: Major elemental composition by weight percent for a 1-kT detonation

Element	**NYC(%)**	**Houston(%)**
Fe	9.88	6.55
Si	58.08	63.30
Ca	6.64	7.56
N	0.01	N/A
S	0.06	0.07
C	0.01	N/A
O	0.55	0.14
Al	14.55	17.80
Mg	2.68	0.90
K	3.39	0.22
Ba	0.05	0.09
Na	3.08	0.74
Mn	0.11	0.06
P	0.09	0.03
Ti	0.58	0.60

Unburned Fuel and Fission Products

The preceding calculations are used to determine the composition of precursor matrices that will constitute the bulk of any surrogate nuclear melt glass sample. A small remaining fraction of the samples will include unburned weapon fuel, while

an even smaller fraction will consist of fission products. The mass contributions for fission products and unburned fuel can be calculated using the method below.

It has been estimated that the complete fission of 57 grams of ^{235}U will produce a nuclear explosion with a yield equivalent to 1 kiloton of TNT(50). It has also been estimated that approximately 375 metric tons (375,000 kilograms) of melt glass are produced per kiloton of nuclear yield(53). This implies a fission product mass fraction for a surface burst of 1.5x10^{-7} grams of fission products per gram of nuclear melt glass and, while this is scenario dependent, this fraction is treated as independent of yield.

In the case of synthetic debris formulations, fission products are generated during irradiation (necessarily post-synthesis) and the fraction reported here is an upper limit. The IAEA definition of the significant quantity of HEU is 25 kilograms(54). If this is taken as the assumed device fuel load, i.e. mass is assumed to be a fixed quantity and the yield of the weapon depends solely on the efficiency, then the fraction of unburned uranium fuel can be calculated by dividing the 25 kilograms of fuel by the 375,000 kilograms of melt glass produced per kiloton of nuclear yield (which gives 6.67x10^{-5}), leading to equation 3.19.

$$m_U = \frac{6.67x10^{-5}}{\gamma} \tag{3.19}$$

Here, γ represents the nuclear yield of the weapon and m_U is the uranium mass fraction. A similar equation can be derived for a plutonium-fueled device. The IAEA significant quantity of weapons grade plutonium is 8 kilograms(54). Again, dividing this fuel mass by the mass of melt glass produced per kiloton of nuclear yield (which gives 2.13x10^{-5}) leads to the development of equation 3.20.

$$m_{Pu} = \frac{2.13x10^{-5}}{\gamma} \tag{3.20}$$

Here m_{Pu} represents the plutonium mass fraction. Equations 3.19 and 3.20 give the mass fractions of fuel (uranium or plutonium) to be incorporated into a synthetic

sample prior to irradiation. The actual fractions of ^{235}U and ^{239}Pu depend on both the actual amount and the grade of the fuel used. For the purposes of this study, deliberate simplifying assumptions concerning the grade and quantity of fuel are made. A small fraction of the fuel is reduced to fission products during the irradiation process. It is presumed here that the fuel is vaporized by the fireball and distributed uniformly along with the carrier material. The mass of the carrier material is determined using equations 3.15-3.18, and the total mass is adjusted to include the appropriate fraction of fuel based on the yield of the device.

3.2 Surrogate Bulk Melt Glass Production

Surrogate bulk melt glass can be synthesized with relative ease using only a few pieces of equipment. Using the equipment and methods described by Molgaard, surrogate trinitite was reproduced(53). Urban surrogates for NYC and Houston were also produced. The subsections below describe both the equipment and procedures used to synthesize surrogate bulk nuclear melt glass.

3.2.1 Equipment

Raw Materials

The bulk melt glass surrogates were comprised of minerals and metal oxide powders procured from Sigma-Aldrich and Fisher Scientific. The reagents used were a minimum of 99.9% pure, and were used without further purification. The mineral and oxide powders were mixed according to the matrices developed in Section: 3.1. Additionally, the Synthetic Trinitite Formulation (STF) matrix developed by Molgaard et al. was produced to be used as a benchmark for comparison. A full breakdown of the precursor matrices can be seen in Table: 3.7. All constituents were measured to the $^{1}/_{10{,}000}{}^{th}$ of a gram, and mixed together using a ceramic mortar and pestle.

Table 3.7: Bulk surrogate precursor matrices for a 1-kT detonation

Consituent	**STF(%)**	**NYC(%)**	**Houston(%)**
SiO_2	64.21	60.49	63.71
Al_2O_3	14.27	15.10	17.88
Fe_2O_3	2.20	7.63	6.22
CaO	9.64	6.35	7.47
Na_2O	1.25	3.23	0.75
KOH	6.12	3.55	2.20
MgO	1.15	2.65	0.87
S	0	0.06	0.07
BaO	0	0.06	0.09
MnO	0.05	0.12	0.06
$Ca_3(PO_4)_2$	0	0.10	0.03
TiO_2	0.42	0.61	0.60
UNH	0.06	0.06	0.06

Furnace

The furnace used to synthesize the surrogate bulk melt glass was a Carbolite 18/4 High Temperature Furnace (HTF). The furnace is rated with a maximum temperature of 1800 °C and a recommended working temperature range of 1400-1650 °C. The furnace has a small chamber with a height of 5.5 inches, width of 5.5 inches, and a depth of 7.5 inches. The chamber is heavily insulated and the heating elements are made of molybdenum disilicide. The unit is programmable and capable of supporting rapid ramp rates and extended dwell times at elevated temperatures. The internal temperature of the furnace is monitored using two high-temperature thermocouples, which are estimated to keep the temperature range within ± 15°C under normal operating conditions.

Crucibles

High purity graphite crucibles were chosen as the best candidates for use in the HTF. The high melting point of graphite (∼4000°C) allows for the crucibles to withstand the temperatures needed to produce the surrogate melt glasses. However,

the graphite will oxidize readily at the temperatures used (forming CO_2), leading to an increased incorporation of carbon in the samples in the form of silicon and iron carbides. Crucibles of other materials such as alumina, zirconia, and platinum, were either unable to withstand the thermal shock of introduction to the furnace, or had a tendency to react with the constituents of the matrices. For these reasons, graphite crucibles were used in surrogate bulk nuclear melt glass production.

3.2.2 Temperature Requirements

The temperature needed to transform the precursor matrices from a solid to a liquidus phase is highly dependent on composition. Typically, complex phase diagrams are consulted in order to determine appropriate melting temperatures for complex soil and mineral mixtures. Because these phase diagrams are not available for the specific matrices used, the appropriate melting temperatures were calculated by using disconnected peak functions, as was done by Molgaard et al(1; 55). Similarly to Molgaard, a temperature of 50°C higher than the calculated melting temperature was chosen as the production temperature (1500°C for the STF matrix, and 1600°C for the NYC and Houston matricies)

3.2.3 Synthesis

Approximately 1g of precursor matrix was placed in a new, clean graphite crucible. Using a pair of steel tongs, the graphite crucible was placed in the HTF in air. After 30 minutes, the graphite crucible was removed. The crucible was emptied upside down over a bowl filled with SiO_2, allowing the molten bead of glass to quickly vitrify. While the STF matrix was easily released from the crucible, the NYC and Houston matrices would only release when the crucible was tapped with blunt object. A total of 7 bulk melt glass samples of each matrix were produced for this study.

3.3 Surrogate Bulk Melt Glass Analysis

3.3.1 Optical and Electron Microscopy

Sample Preparation

12 melt glass beads were analyzed via scanning electron microscopy techniques (4 beads each of the STF, NYC, and Houston matrices). 6 beads (2 beads of each matrix type) were left unprepared so that the surface could analyzed via electron microscopy. Each of the 6 remaining beads was placed on a pane of glass, and surrounded by a 0.5 inch high, 1 inch diameter mold made from a phenolic paper tube. A degassed acrylic resin was poured into the molds until the samples were completely covered. Once the acrylic resin was cured, the mounted samples were cut into wafers of approximately 1.5-mm thickness using an Allied Techcut4 wafering saw. The wafers were released from the resin by applying gentle pressure, and remounted in degassed acrylic resin. Care was taken to ensure that the location of each wafer within the bead was recorded. After the acrylic was cured, the surfaces of the mounted wafers were ground and polished so that the maximum variation in surface height was 1-μm. This was done using an MTI EQ-Unipol-800-LD rotary lap polisher with SiC lapping paper of various grit size. Between polishing steps, the samples were inspected via a stereo microscope to ensure there were no irregularities on the surface. Once it was determined that there were no irregularities, the samples were cleaned using a mixture of soap and deionized water, and then rinsed with methanol.

Electron Microscopy

The samples were first analyzed using a LEO 1525 electron microscope and Zeiss SmartSEM software. Unsectioned, unmounted samples were used to observe surface characteristics, while sectioned, mounted samples were used to observe interior characteristics. Morphology and topography of the samples were observed via type-II

secondary electron (SE2) detection with an Everhart-Thornley (ET) detector.Back-scatter electron (BSE) analysis was performed to determine variation of chemical composition throughout the sample. All samples were imaged using a beam current of 300.0-nA and an accelerating voltage of 10-kV

EDS was performed on a JEOL JXA-840 electron microscope equipped with an EDAX APOLLO X energy dispersive spectrometer manufactured by AMATEK. The EDS was used in conjunction with the EDAX Genesis software in order to qualitatively identify the elemental species present in the samples. Areas of interest identified via optical microscopy, SE2, and BSE imaging were investigated using EDS. EDS results from these areas were compared to the EDS results of typical sample areas. All samples were analyzed using a beam current of 1.0-μA and an accelerating voltage of 20-kV. The JEOL SEM was used for EDS because of the superior sensitivity and resolution of the attached EDAX detector.

3.3.2 Mass Spectrometry

Sample Preparation

A total of 9 melt glass beads (3 each of the STF, NYC, and Houston matrices), and the 3 unmelted precursor matrices were analyzed using ICP-TOF-MS. Each bead was individually crushed, first using a steel mortar and pestle to fracture it into smaller pieces, followed by a ceramic mortar and pestle which was used to grind the smaller pieces into a fine powder. No preparation was used to prepare the precursor matricies for dissolution. The mortar and pestles were cleaned thoroughly after crushing each bead in order to prevent cross contamination. The steel mortar and pestle was cleaned using methanol and clean Kimwipe®, while the ceramic mortar and pestle were cleaned using concentrated HNO_3 followed by methanol and clean Kimwipes®. No further preparation was required for the precursor matrices.

Dissolution

An aliquot of approximately 10 mg was measured from a sample (a single ∼1.0-g melt glass bead) and placed into a 32 mL Parr microwave bomb with 14 mL of a 5:2 mixture of 28.9 M HF and 15.6 M HNO_3. The bomb was heated in a conventional microwave for 35 seconds at 700 watts. The bomb was allowed to cool in air for approximately 20 minutes before being opened. Once cooled, the solution was transferred to a clean teflon container and placed on a hot plate to evaporate. Once evaporated, the sample was rehydrated with 10-mL of a 1:1:38 mixture of HF, HNO_3, and 18.2-MΩ water. The resulting solution was placed in a 20-mL PTFE sample vial.

Sample Dilution and Analysis

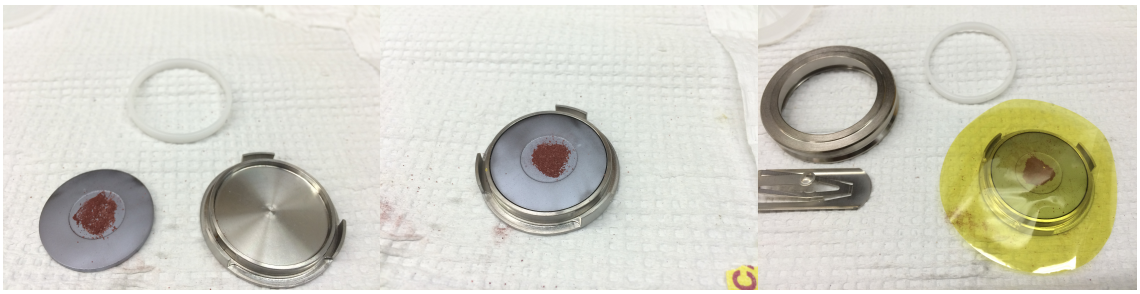
Using a 1:1:38 (by volume) mixture of HF, HNO_3, and 18.2-MΩ water. The resulting solution was diluted to concentrations of 1-ppm and 100-ppt (total) so that the both the abundant and trace elements could be analyzed. The diluted samples were analyzed using an OptiMass 9500 ICP-TOFMS. Rare-earth, multi-element (REME) standards were mixed to concentrations of 10-ppt, 100-ppt, and 1-ppb in order to provide a calibration curve for the data. Si, and Ti standards were added in order to account for elements not present in the REME standards.

18.2-MΩ water was introduced to the mass-spectrometer to make sure that any artifacts from previous analyses did not cause interference in the data. Three prepared aliquots from each sample were analyzed in succession. 100-ppt aliquots were run before the 1-ppm aliquots. 18.2-MΩ water was run through the mass-spectrometer between analyzing aliquots from different samples, or between aliquots of differing concentrations.

3.3.3 X-ray Diffraction

Powder X-ray Diffraction (P-XRD) analysis was performed on synthetic trinitite, NYC, and Houston bulk melt glass samples. The samples used for analysis were the

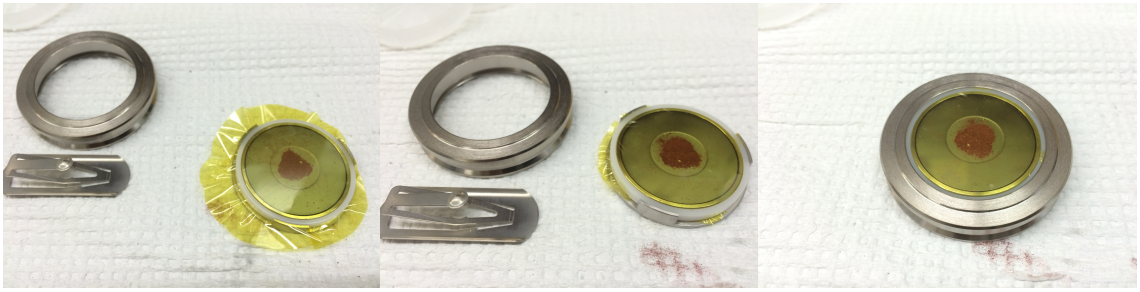
same samples that were ground and powdered for ICP-TOF-MS analysis. A total of three samples were analyzed for each matrix type. Additionally, each of the three precursor matrices was analyzed so that differences in crystalline structure caused during synthesis could be determined. Samples were prepared for analysis by placing them on a silicon (001) zero-background sample holder. Between runs, the sample holder was cleaned using isopropanol. In order to prevent radiological contamination of the X-ray diffractometer, a 35-μm thick mylar sheet was placed over the sample and secured with an O-ring and trimmed. A background measurement using a blank sample holder covered by a mylar sheet was taken as well. Figure: 3.1 shows a step by step process of this technique.



(a) Sample on a zero-background stage

(b) Stage placed in sample holder

(c) Covered with mylar sheet



(d) Mylar sheet secured with O-ring

(e) Trimmed mylar sheet

(f) Fully assembled sample holder

Figure 3.1: Illustration of radioactive sample mounting procedure

After the sample was properly mounted to avoid contamination, analysis was performed using a PANalytical Empryean X-ray diffractometer with a Pixcel 3D detector. The X-ray source was a Cu anode set at a 40-mA and 45-kV. A slit window

of 0.25° 2θ was used along with a 0.125° 2θ anti-scatter diffraction grating. Samples were set to spin at 4-revolutions/sec. All spectra were acquired from 10° 2θ to 90° 2θ with a 0.1° 2θ step size and 4.5-s time step.

To analyze the data, the background spectrum was first subtracted from each of the sample spectra. Each sample spectrum was normalized to the highest peak in the background-corrected diffraction pattern. Comparisons were made between samples of the same precursor matrix in order to confirm reproducibility. The three spectra from each precursor matrix were then averaged together to that comparison between precursor matrices could be made. PANalytical HighScore Plus was used to fit known diffraction patterns to the obtained spectra so that crystalline species could be identified. These known diffraction patterns were superimposed on the acquired spectra to aid in analysis.

3.4 Surrogate Particulate Melt Glass Production

Surrogate particulate melt glass was synthesized using a commercial-off-the-shelf plasma spray torch. It was necessary to spray-dry the the precursor matrix so that a uniform particle size could be introduced to the plasma torch. By using taking the precursor matrices and introducing them into a slurry containing polyvinyl acetate which is then spray-dried, it was thought that a precursor of uniform particulate size (90-150 μm) could be created. This is necessary because particles of differing sizes have different dwell times in the plasma. Using a uniformly sized precursor matrix, allows for a consistent dwell time among particles, and thus eliminates one source of process error. Surrogate particulate melt glass was produced using the STF, NYC and Houston matrices. The equipment used, and the synthesis process is described in the subsections below.

3.4.1 Equipment

Raw Materials

The particulate melt glass surrogates were comprised of minerals, metal oxide powders, and metal hydroxide powders procured from Sigma-Aldrich and Fisher Scientific. It is important to note that many of these components contained waters of hydration. The reagents used were a minimum of 99.9% pure, and were used without further purification. The mineral and oxide powders were mixed according to the matrices developed in Section: 3.1. Additionally, the STF matrix developed by Molgaard et al. was produced to be used as a benchmark for comparison. A full breakdown of the precursor matrices can be seen in Table: 3.8. All constituents were measured to ±0.0001 g

Table 3.8: Particulate surrogate precursor matrices for a 1-kT detonation

Consituent	STF(%)	NYC(%)	Houston(%)
SiO_2	63.82	63.42	68.66
Al_2O_3	14.19	14.03	17.05
Fe_2O_3	0.98	7.22	4.75
$Ca(OH)_2{\cdot}nH_2O$	12.66	6.06	7.02
$NaOH{\cdot}nH_2O$	1.60	2.73	0.65
$KOH{\cdot}nH_2O$	6.08	2.48	0.16
$Mg(OH)_2$	1.65	3.28	1.10
MnO	0.05	0.07	0.04
$Ca_3(PO_4)_2$	0	0.0.20	0.07
TiO_2	0.42	0.49	0.51

Spray Dryer

A Büchi B-290 spray dryer was used to ensure that the precursor was a uniform size before being run through the plasma torch. Uniform precursor size allows for uniform dwell time within the plasma, and thus consistent and reproducible results. Unfortunately, the spray-drying process was not as effective as anticipated, and

particles of many different sizes could be seen in the precursor matrix when examined using an electron microscope. A picture of the spray dryer can be seen in Figure: 3.2



Figure 3.2: Büchi B-290 spray dryer

Plasma Torch

The precursor matrices were fed through an AMTag Series 80 Thermal Spray System. The system was able to be fed with a mixture of H_2 and Ar gases. For this study, only pure Ar gas was used in order to demonstrate the proof-of-concept of using a plasma spray torch to synthesize synthetic particulate nuclear melt glass. Temperature of the plasma was controlled by varying the H_2/Ar ratio, with a higher ratio producing a higher temperature. By varying the flow rate of the gases, the dwell time of the precursor in the plasma could be varied. A picture of the plasma spray control module can be seen in Figure: 3.3.



Figure 3.3: Plasma spray system control module

Thermal Spray Camera

A Control Vision Inc. Spraycam thermal spray camera was purchased to track particle movement through the torch. The camera is able to track particles $>20\mu m$ in diameter traveling at velocities up to $500^{m}/_{s}$. Because the camera is capable of continuous process monitoring, adjustments can be made to gas flow rates and particle feed rates, allowing the particle dwell time to be varied in real time. This was useful when adjusting the plasma spray system to allow for maximum dwell time of the precursor matrix in the plasma. A picture of the thermal spray camera can be seen in Figure: 3.4.

3.4.2 Synthesis

The precursor matrix was poured into a beaker filled with 1-L of 18.2 MΩ water. 88% hydrolyzed polyvinyl alcohol(PVA) was added to the solution to serve as a thickener.

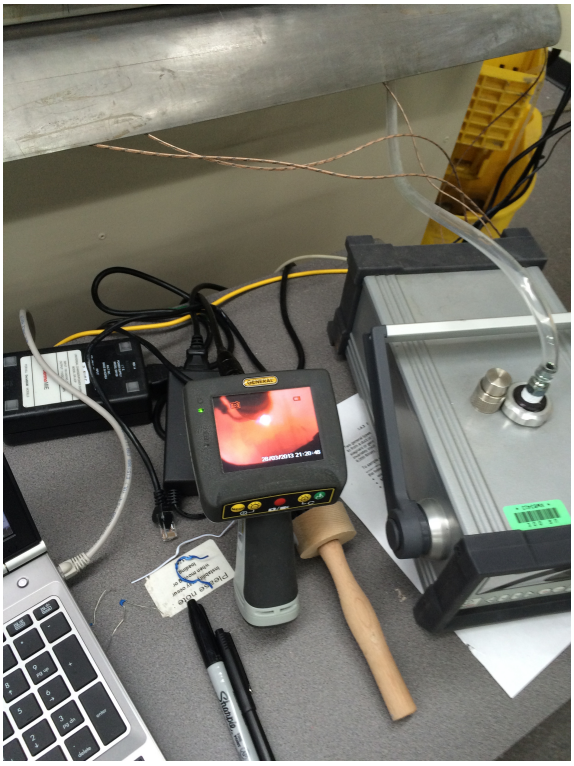


Figure 3.4: Thermal spray camera used to track particle motion and speed

The mixture was placed on a magnetic stirrer to keep the particulates suspended in solution. The mass of PVA added to solution was 2% of the precursor matrix mass for the trinitite precursor matrix, and 4% of the precursor matrix mass for the NYC precursor matrix. The solution was then spray dried and placed in the powder hopper of the AMTag Series 80 thermal spray system. The matrix was injected into the center-line of the torch while running a pure Ar plasma (≈6000-K). The torch was placed at the opening of a 6 ft length of 8 in diameter stainless steel duct. A 75-μm screen was placed at the other end of the duct to catch the generated surrogates. After several torch runs, the debris was collected from the mesh screen and the interior of the duct. The duct and powder hopper were thoroughly cleaned and the powder feed lines were bled between runs in order to prevent cross contamination between matrices.



(a) Powder hopper (side view)

(b) Powder hopper (top view)

Figure 3.5: Powder hopper used to feed precursor material into the plasma torch

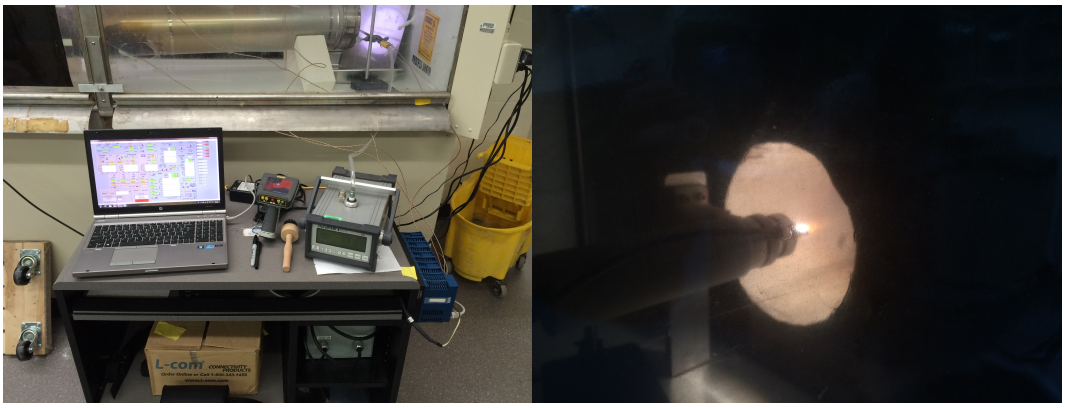
3.5 Surrogate Particulate Melt Glass Analysis

Samples of surrogate particulate melt glass were created using both a synthetic trinitite, and a NYC matrix. A single 10-g sample was taken from each of the following: 1) the untreated precursor material; 2) the spray-dried precursor material; and 3) material that had been run through the plasma torch. Samples were taken for both matrix types for a total of 6 10-g samples (three samples each from two matrices).

3.5.1 Electron Microscopy

Sample Preparation

Particulate melt glass samples were analyzed via scanning electron microscopy techniques. Approximately 10-mg of sample was dispersed evenly in a petri dish. The particulate melt glass was mounted on an SEM stub covered with carbon tape by gently pressed the stub on the bottom of the dish and then removed. This technique allowed for the imaging and analysis of both individual, and a random sampling of particles. Analysis of individual particles was deemed necessary in order to determine variation in size, composition, and morphology. Samples were also heavily loaded on



(a) Experimental setup **(b)** Location of plasma torch in duct

Figure 3.6: Experimental setup for the production of synthetic particulate melt glass

to carbon tape covered SEM stubs so that the average characteristics of the sample could be observed.

Electron Microscopy

The samples were first analyzed using a LEO 1525 electron microscope and Zeiss SmartSEM software. Morphology of the samples was observed via type-II secondary electron (SE2) detection with an Everhart-Thornley (ET) detector. BSE analysis was performed to determine variation of chemical composition throughout the sample. All samples were imaged using a beam current of 300-nA and an accelerating voltage of 10-kV

EDS was performed on a JEOL JXA-840 electron microscope equipped with an EDAX APOLLO X energy dispersive spectrometer manufactured my AMATEK. The EDS was used in conjunction with the EDAX Genesis software in order to qualitatively identify the elemental species present in the samples. Areas of interest identified via optical microscopy, SE2, and BSE imaging were investigated using EDS. EDS results from these areas was compared to the EDS results of typical sample areas. All samples were analyzed using a beam current of 1.0-nA and an accelerating voltage

of 20-kV. Again, the JEOL SEM was used for EDS because of the superior sensitivity and resolution of the attached EDAX detector.

3.5.2 Mass Spectrometry

Dissolution

3 aliquots of each sample were analyzed. With the exception of powdering the material using a mortar and pestle, sample preparation, dissolution, and analysis techniques/instrument settings were the same as what is described for the surrogate bulk melt glass analysis.

3.5.3 X-ray Diffraction

Powder X-ray Diffraction (P-XRD) analysis was performed on synthetic trinitite and NYCparticulate melt glass samples. A total of three samples were analyzed for each of the two matrix types. The three samples analyzed came from the 10 grams each of material taken from the untreated precursor, the spray-dried precursor, and the heat-treated precursor that had been subjected to the plasma spray system. All instrument settings and treatment of data remained the same as those used in the analysis of the surrogate bulk melt glass.

3.6 Radiological Modeling

Radiological modeling of both the bulk and particulate surrogate melt glass samples was conducted using the Fallout Analysis Tool. Each of the three matrices was entered into the program in appropriate isotopic mass ratios. Naturally occurring isotopic fractions were used for each element. Two analyses were run for each matrix, one for a ^{235}U fueled weapon and one for a ^{239}Pu fueled weapon. The U fueled weapon was modeled at a 90%-enrichment of ^{235}U with the balance being comprised of ^{238}U. The mass of fuel in the U device was modeled as 25-kg. The Pu fueled weapon was

modeled at a ^{239}Pu enrichment of 93%, with the balance being comprised of ^{240}Pu. The mass of fuel in the Pu device was modeled as 8-kg.

Each case was estimated as a 1-kT detonation, with the time from initiation to mechanical disassembly taking 100 shakes (1-ms). Using data from the Trinity test, it was estimated that 375,000-kg of melt glass would be produced per 1-kT of energy released. Therefore, 375,000-kg of precursor matrix was used in each model in order to provide proper elemental and isotopic ratios. Fission and activation product inventories were calculated in from the point of initiation until 100-years post-detonation.

Chapter 4

Results

4.1 Surrogate Bulk Melt Glass

The results from the analysis of the surrogate bulk nuclear melt glass synthesized in this study is discussed first. The results from the optical and electron microscopy studies are discussed first, followed by the ICP-TOF-MS results. Finally, the measured P-XRD diffraction patterns are discussed. In each section, the three matrices are described in order as follows: 1) the synthetic trinitite formulation (STF), 2) a mathematical model of the major elemental constituents of New York City (NYC), and 3) a mathematical model of the major elemental constituents of Houston, TX (HOU). The order that the matrices are examined corresponds to the order in which they were originally modeled.

4.1.1 Optical and Electron Microscopy

Optical images of unsectioned surrogate bulk melt glass beads are shown and described first. SEM images of the top and basal sides of the beads are shown. Chemical composition is examined via EDS, and unique features are described. Thin sections of the beads are then shown, common features are analyzed and described

via BSE and EDS. EDS intensity ratios for the major elements with respect to O are listed in Table: 4.1.

Table 4.1: Ratios of major elements with respect to oxygen for precursor matrices

Element	STF	NYC	HOU
Si	1.96	1.09	1.22
Al	0.13	0.13	0.16
Mg	0.1	0.28	0.10
Ca	0.41	0.24	0.29
Fe	0.02	0.23	0.20
K	0.02	N/A	N/A

Synthetic Trinitite Matrix

Top, side, and basal views of an STF surrogate bulk melt glass bead are shown in Figure: 4.1. The bead is round in shape and is light green in color on the top and sides. The light green coloration is punctuated by darker green spots that are unevenly distributed across the surface. The radius of the bead is approximately 6-mm and the maximum height is also around 6-mm. The top and sides of the bead appear smooth and free of any major imperfections. Unlike the top and sides of the bead, which are rounded, the bottom is flat. The bottom of the bead is dark gray in color and rough in nature. The rough textures on the bottom of the bead look like the surface of the graphite crucible used for synthesis. This would make sense, as the basal side of the melt glass bead was in contact with the crucible during the heat-treatment of the sample.

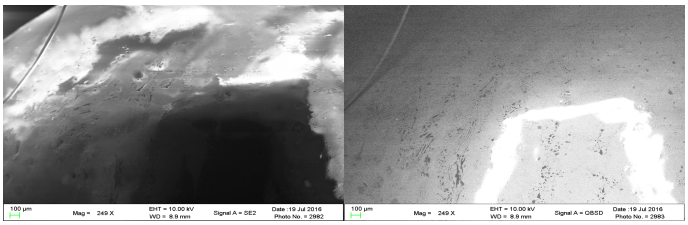


(a) Top view **(b)** Side view **(c)** Basal view

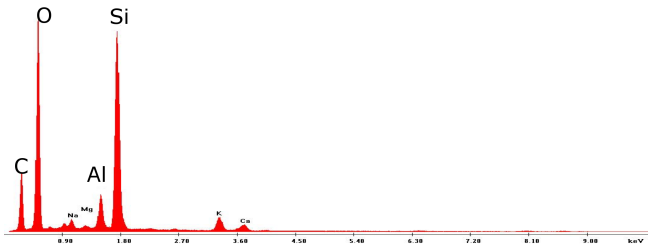
Figure 4.1: Optical images of a typical surrogate bulk melt glass bead composed of the STF matrix

Surface Analysis Figure: 4.2 shows micrographs and an EDS spectrum for a typical bead of surrogate bulk melt glass composed of the STF matrix. Under SEM, the surface of a typical STF melt glass bead appears to be mostly smooth with with exception of a few small pits and indentations that measure on the order of μm. Occasionally, scratches similar to the one seen in the upper left hand corner of the figure are observed. BSE imaging reveals these pits to be chemically composed of lighter elements than the rest of the surface. EDS analysis shows the surface to be composed of C, O, Na, Mg, Al, Si, K, and Si.

An unusual dendritic crystal structure can be seen in Figure: 4.3. The individual crystals are less than 15-μm at their widest point, and appear to have a thickness on the scale of hundreds of nm. The structures appear brighter than the surrounding melt glass in the BSE image, indicating larger concentrations of the heavier elements found in the matrix. EDS analysis shows the presence of C, O, Fe, Na, Mg, Al, Si, K, Ca, and Ti. The intensity of the Fe peak in the spectrum is much higher than that observed when analyzing the surface of the bead. However, the true composition of the crystalline structures cannot be identified for certain with this technique. Because of the thinness of the structures, it is possible that the some of the elements present in the EDS spectrum are present due to interactions with the bulk melt glass bead and not the crystal structures themselves.

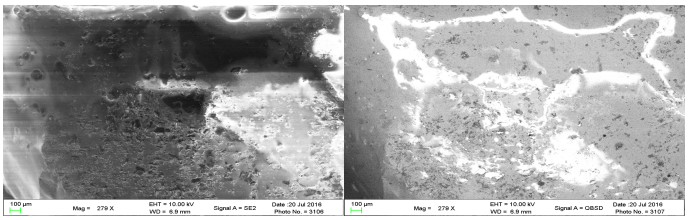


(a) STF SE2 surface **(b)** STF BSE surface

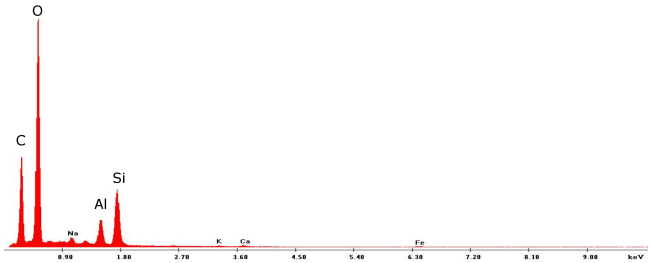


(c) STF EDS surface

Figure 4.2: Micrographs and EDS of the top surface of a typical surrogate bulk melt glass bead (STF matrix)

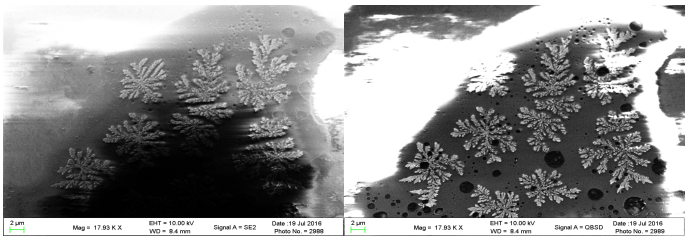


(a) STF SE2 basal side **(b)** STF BSE basal side



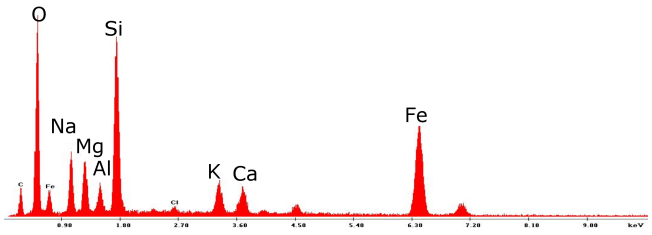
(c) EDS basal side

Figure 4.4: Micrographs and EDS for a typical basal side of surrogate bulk melt glass (STF matrix)



(a) STF SE2 crystalline structure

(b) STF BSE crystalline structure



(c) STF EDS crystalline structure

Figure 4.3: Micrographs and EDS of crystalline structures on the surface of a surrogate bulk melt glass bead (STF matrix)

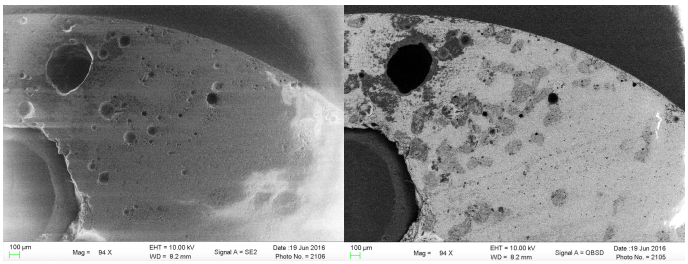
The basal side of a typical STF surrogate bulk melt glass bead is rough with many pits and indentations, which are possibly caused by contact with the graphite crucibles used for synthesis. These pits and indentations vary in size, but are all roughly on the order of tens of μm at their widest dimension. BSE imaging reveals the chemical composition to be fairly homogenous, with the exception of the pits which are concentrated in lighter elements. EDS analysis reveals the presence of C, O, Na, Al, Si, K, Ca, and Fe. The intensity of the carbon peak is higher for the basal side than the top side. This is possibly due to the contact of the basal side of the bead with the graphite crucible during the synthesis process. Contact with the crucible allows for the formation for carbide compounds during synthesis. Figure: 4.4 shows micrographs and an EDS spectrum of a typical basal side of a bulk STF surrogate melt glass bead.

Thin section analysis Figure: 4.5 shows a typical thin section of a STF bulk melt glass bead. The thin sections had many voids of varying sizes, ranging from tens of

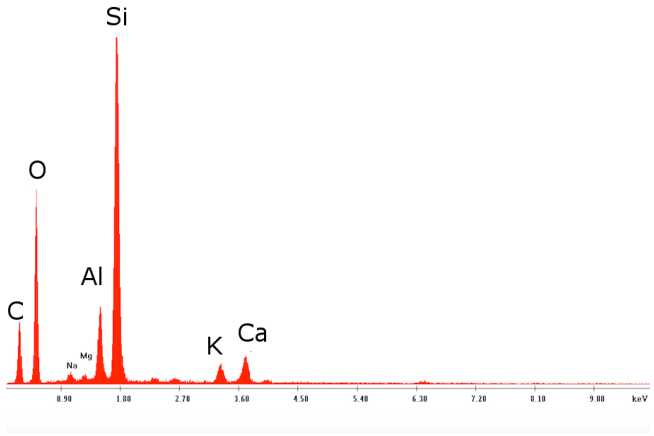
μm to several mm. BSE imaging reveals a fair degree of chemical heterogeneity with the samples, with several dark spots appearing throughout the section. It should be noted that while these spots appear in the upper left hand corner of the sample shown, no general pattern or distribution could be discerned when all samples were taken into account. The areas that are not covered in dark spots appear to be fairly chemically homogenous in nature. EDS shows that the thin sections were predominantly comprised of Si, Al, K, Ca, Mg, Na, and O, with some C present. It is believed that the elements identified exist in the form of complex oxides, thus explaining the large amount of oxygen present. The source of C in the spectrum is thought to be predominately from the acrylic resin seen in the upper right hand corner of the images. EDS intensity ratios for the major elements with respect to O are listed in Table: 4.2. The ratios of Si:O, Mg:O, Ca:O, and Fe:O all show a decrease compared to the elemental ratios observed in the precursor. The decrease in the Si ratio is the largest in terms of the total decrease, while the Ca:O ratio shows the largest decrease in terms of percentage. The Al:O and K:O ratios both in comparison to the precursor. Both show an increase of approximately 300%, with the Fe:O ratio showing the largest overall increase.

Table 4.2: Ratios of major elements with respect to oxygen in bulk melt glass (STF matrix)

Element	**Ratio**
Si	1.78
Al	0.40
Mg	0.04
Ca	0.14
Fe	0.01
K	0.09



(a) STF SE2 thin section **(b)** STF BSE thin section

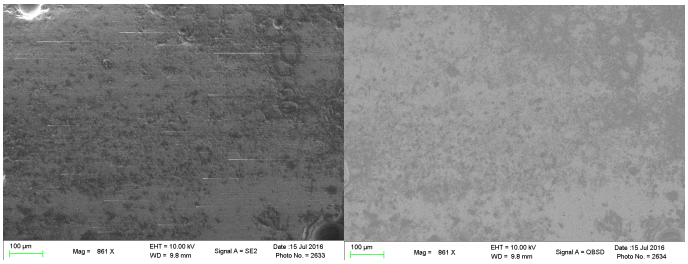


(c) STF EDS thin section

Figure 4.5: Micrographs and EDS for a typical thin section of surrogate bulk melt glass (STF matrix)

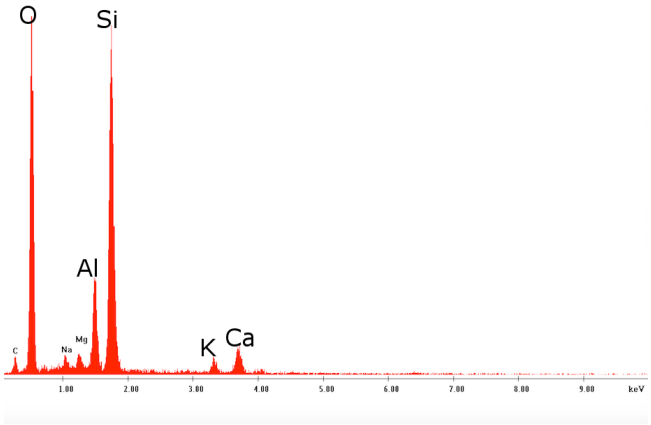
The first specific area of the sections targeted for further analysis was the relatively homogenous region. SE2 imaging shows some surface roughness, but no distinct crystalline patterns, suggesting that the more homogenous regions are amorphous in nature. After analyzing the elements present in the EDS spectrum and how they tend to interact with one another, it is thought that the melt glass beads are primarily composed of aluminosilicate compounds containing small amounts of Mg, Na, K, and Ca. Micrographs and an EDS spectrum for this region can be seen in Figure: 4.6.

Figure: 4.7 shows micrographs and an EDS spectrum for the dark spots seen in Figure: 4.5. The dark regions showed a complex topography compared to the amorphous regions when analyzed using SE2 imaging. BSE images show a uniform chemical composition in the region. It should be noted that the dark spot at the



(a) STF SE2 homogenous region

(b) STF BSE homogenous region

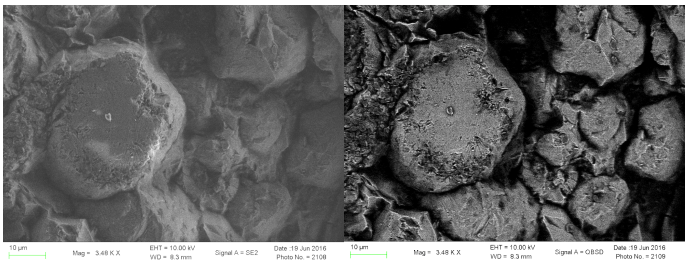


(c) EDS homogenous region

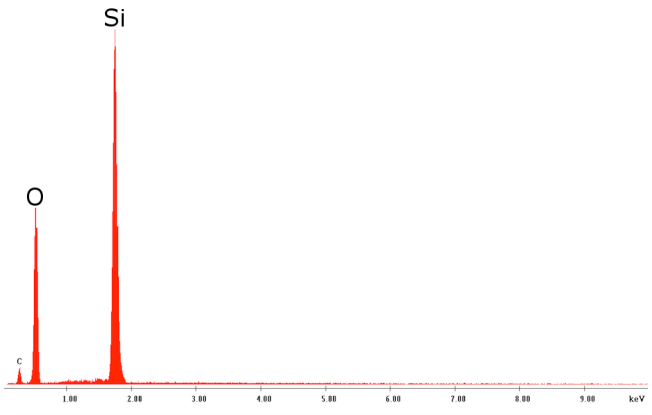
Figure 4.6: Micrographs and EDS for an homogenous region of surrogate bulk melt glass (STF matrix)

top of the BSE image is an image artifact created by the topography of the sample, and not indicative of a different chemical composition. EDS showed that these dark regions were composed of Si and O. Morphology and chemical composition suggest that the darker regions are caused by incomplete transition of SiO_2 to an amorphous phase during synthesis.

Each thin section showed on average 1-2 cracks, though they were not prevalent in the morphology of the sample. The cracks were narrow (<10 μm in width) and therefore unable to be seen at lower magnifications. The cracks were typically found to either originate from or travel near cavities in the sample. Figure: 4.8 shows micrographs and an EDS spectrum of a typical crack for the surrogate bulk STF matrix. EDS results showed that the composition of cracks tends to be extremely



(a) STF SE2 granular region **(b)** STF BSE granular region

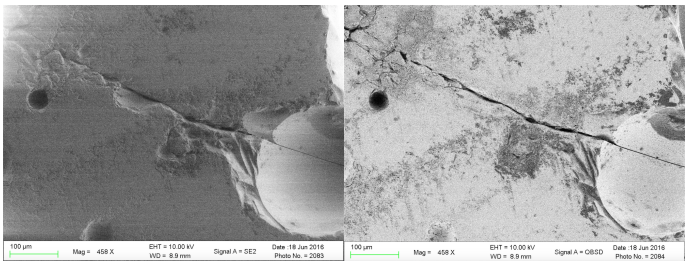


(c) STF EDS granular region

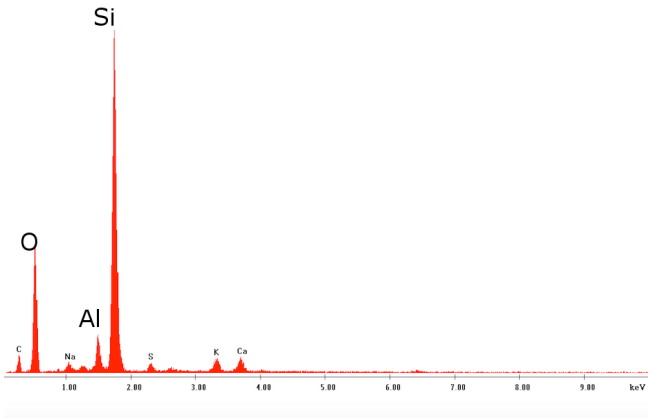
Figure 4.7: Micrographs and EDS for a typical granular area of surrogate bulk melt glass (STF matrix)

similar to both the total and amorphous regions consisting of O, Si, Al, S, K, Ca, and a small amount of C. BSE imaging shows that while there may be some chemical differences in the areas around the crack, there is no correlation between crack location and chemical composition in the sample. Because of this, crack formation in surrogate bulk STF melt glass beads is very possibly a product of thermal and mechanical stresses that occurred during synthesis. This is similar to what can be seen in historical melt glass samples.

Figure: 4.9 shows micrographs and an EDS spectrum for the surface of a typical cavity found in a surrogate bulk STF melt glass bead. The cavity surface shown in the bottom of image has a diameter of $\approx$ 500-μm. The typical surface of a vesicle appears relatively smooth and amorphous in nature. BSE imaging shows areas of



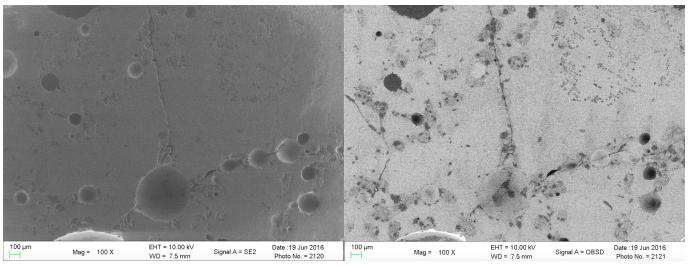
(a) STF SE2 crack **(b)** STF BSE crack



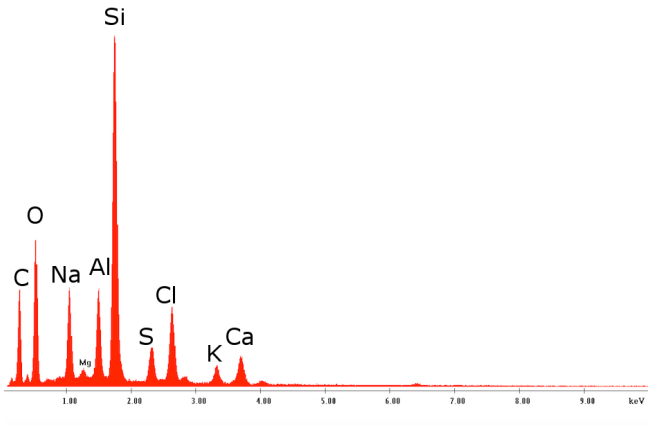
(c) STF EDS crack

Figure 4.8: Micrographs and EDS for a typical crack found in surrogate bulk melt glass (STF matrix)

lighter elements on the cavity surface indicating the presence of a reaction layer similar to those found on the surface cavities found in trinitite. EDS analysis revealed the presence of C, O, Na, Mg, Al, Si, S, Cl, K and Ca. These elements are the same as those used to develop the precursor matrices. Their presence and relative spectral intensities indicate that the process used to generate surrogate bulk nuclear melt glass does not produce a reaction rind on the surface of the cavities present in the samples. The presence of Cl is thought to be caused by either contamination introduced by the water used during grinding and polishing, or from acrylic not being completely removed from the cavity.



(a) STF SE2 void **(b)** STF BSE void



(c) STF EDS void

Figure 4.9: Micrographs and EDS for a the surface of a cavity found in surrogate bulk melt glass (STF matrix)

New York City Matrix

Figure: 4.10 shows optical images of the top, side, and basal views of a typical surrogate nuclear melt glass bead composed of the NYC matrix. From the top view, the bead is generally round in shape, with a radius of approximately 6-mm. The surface appears unevenly pitted. The side view shows that unlike the typical STF bead, the NYC bead does not have a hemispherical profile, but is instead somewhat flattened. The average hight of the bead appears to be between 4 and 5-mm. The basal side of the bead has a large cavity in the center. The area of the bead that was in contact with the graphite crucible during synthesis shows many large voids. All three views of the bead show that it is dark green, to the point of almost appearing black. The top and sides of the bead show red speckling that is possibly indicative of

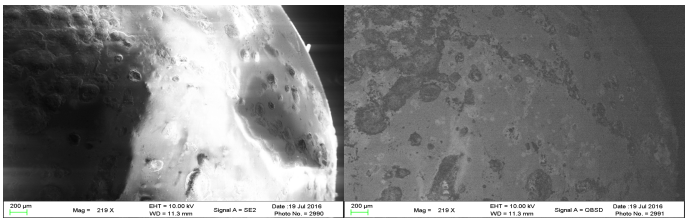
differences in chemical composition at the surface. The basal side of the bead does not have any uniquely colored features.



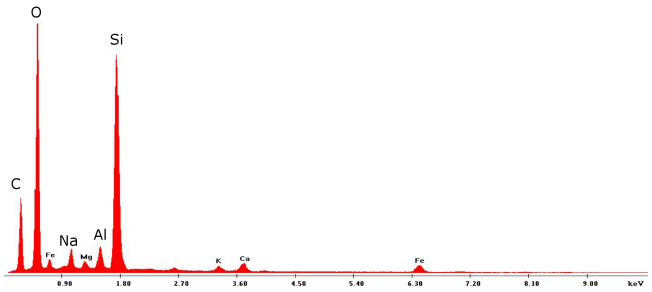
(a) Top view **(b)** Side view **(c)** Basal view

Figure 4.10: Optical images of a typical surrogate bulk melt glass bead composed of the NYC matrix

Surface analysis Figure: 4.11 shows micrographs and an EDS spectrum of a typical NYC surrogate bulk melt glass bead. The surface of the bead has a combination of both smooth and rough areas, with the rough areas containing a large number of protrusions. BSE imaging shows that the rough areas have higher concentration of lighter elements, while smooth areas have a higher concentration of heavier elements. The EDS spectrum reveals that the sample is composed of C, O, Fe, Na, Mg, Al, Si, K, and Ca.

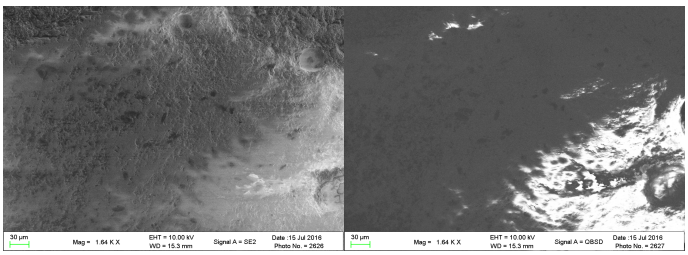


(a) NYC SE2 surface **(b)** NYC BSE surface

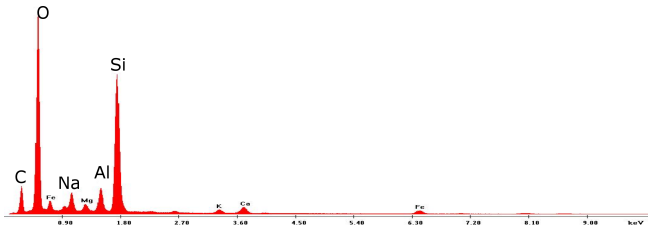


(c) NYC EDS surface

Figure 4.11: Micrographs and EDS of the top surface of a typical surrogate bulk melt glass bead (NYC matrix)



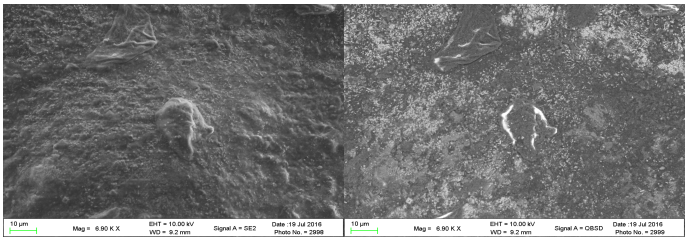
(a) NYC SE2 smooth region **(b)** NYC BSE smooth region



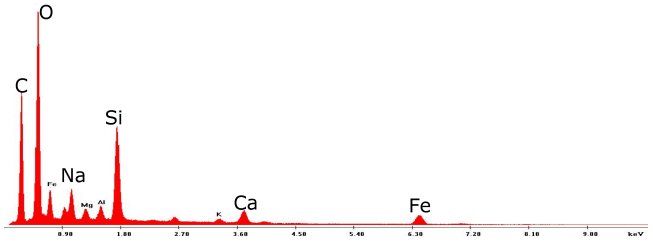
(c) NYC EDS smooth region

Figure 4.12: Micrographs and EDS for a typical smooth region of the top surface of a surrogate bulk melt glass bead (NYC matrix)

Closer inspection at higher magnifications reveals that the smooth region is actually finely textured, with maximum variation in topography appearing no larger than several hundred nm. BSE imaging reveals that the region is chemically heterogeneous, although there does not appear to be a correlation between morphology and composition. The EDS spectrum shows that the smooth regions of the surface have a chemical composition nearly identical to that of the surface as a whole. Figure: 4.12 depicts micrographs and an EDS spectrum of a typical smooth region of the surface of a surrogate bulk melt glass bead comprised of the NYC matrix. It should be noted that the bright region in the lower right hand corner of the micrographs is indicative of sample charging, and of not morphological or chemical differences.



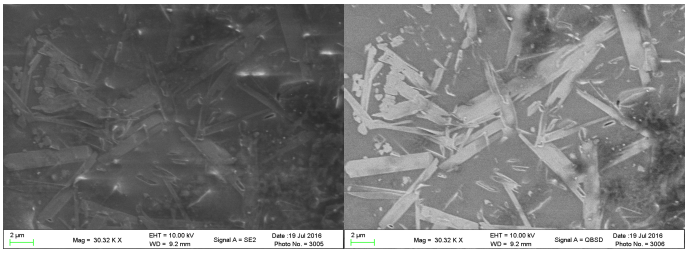
(a) NYC SE2 rough region **(b)** NYC BSE rough region



(c) NYC EDS rough region

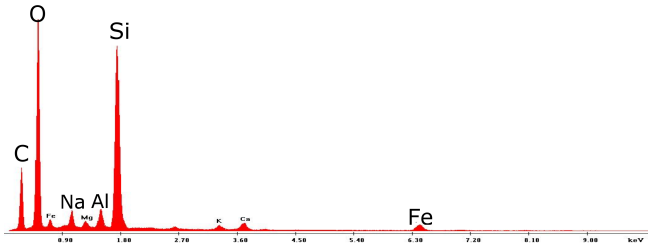
Figure 4.13: Micrographs and EDS for a typical rough region of the top surface of a surrogate bulk melt glass bead (NYC matrix)

Figure: 4.13 shows micrographs and an EDS spectrum for a typical NYC surrogate bulk melt glass bead. The region shows an extremely varied topography, with maximum surface topography varying by several μm. Chemical composition of the region is extremely heterogeneous, and appears to be enriched with the heavier elements of the matrix. EDS analysis shows the presence of C, O, Fe, Mg, Al, Si, K, and Ca. Additionally, the intensity of the Fe peak is higher than that of both the total surface and the smooth region, indicating a higher than normal concentration in the rough region.



(a) NYC SE2 crystalline structure

(b) NYC BSE crystalline structure

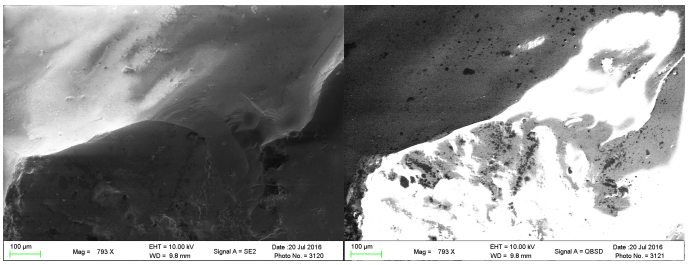


(c) NYC EDS crystalline structure

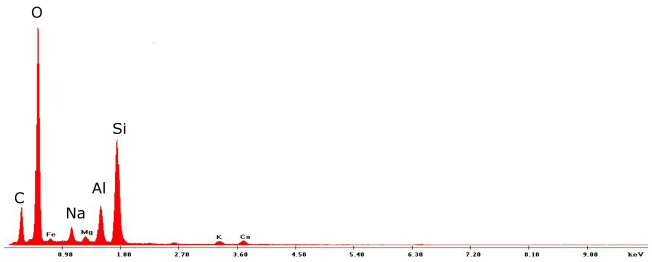
Figure 4.14: Micrographs and EDS for a crystalline region of surrogate bulk melt glass (NYC matrix)

Inspection of the smooth region at high magnification sometimes reveals the presence of crystalline formations. Unlike with the STF matrix, these formations appear to be within the melt glass bead, not on the surface. The crystals are at most 2-μm in width and 6-μm in length, though they are usually smaller. The unorganized arrangement of the crystals suggests that they formed fairly quickly.

They were possibly formed during the synthesis process. BSE imaging reveals that the crystalline structures are of a different chemical composition than the rest of the surrounding area. EDS results show the presence of C, O, Fe, Na, Mg, Al, Si, K, and Ca. Because of the small size of the crystals, it is possible that the spectrum shows a combination of the elemental composition of both the crystals and the non-crystalline region of the melt glass bead. SEM micrographs and and EDS spectrum of a crystalline region of a NYC bulk surrogate melt glass bead can be seen in Figure: 4.14.



(a) NYC SE2 basal side **(b)** NYC BSE basal side



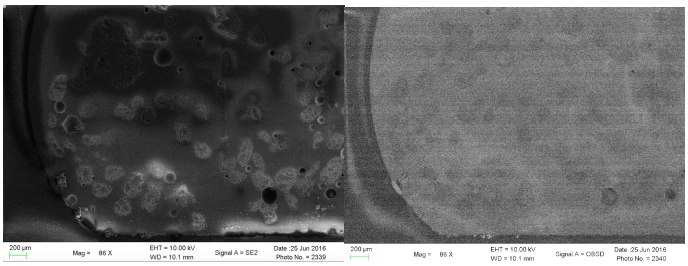
(c) NYC EDS basal side

Figure 4.15: Micrographs and EDS for a typical basal side of a surrogate bulk melt glass (NYC matrix)

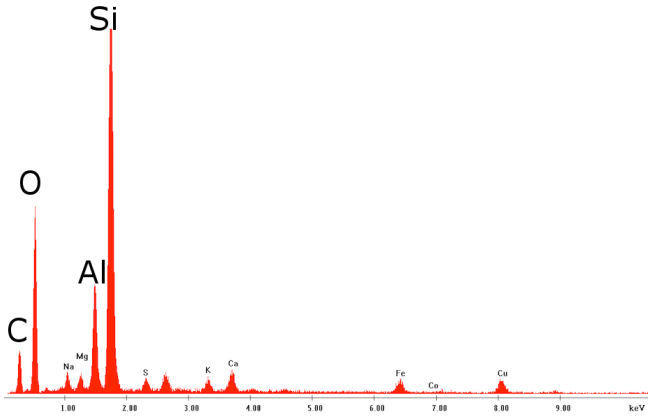
Figure: 4.15 depicts micrographs and an EDS spectrum for the basal side of a typical NYC surrogate bulk melt glass bead. The portion of the bead that was in contact with the graphite crucible used during synthesis can be seen in the lower right hand corner of the micrographs, while the concave region identified in Figure: 4.10 can be seen in the upper left hand corner. The concave region appears smooth and untextured in contrast to the region that was in contact with the graphite

crucible, which has significant variation in its surface. BSE imaging of the basal side is inconclusive due to severe charging of the sample. EDS analysis indicates the presence of C, O, Fe, Na, Mg, Al, Si, K, and Ca. The intensities of the peaks are similar to those observed on the surface of the sample, albeit with a higher C content. Again, the higher C content is indicative of sample contact with th graphite crucible during synthesis.

Thin section analysis Figure: 4.16 shows micrographs an EDS spectra for a typical thin section for bulk surrogate nuclear melt glass modeled for New York City. The thin section shows the presence of many small cavities, and a large number of granular areas. Cavity size in the NYC sections are smaller on average than those found in the STF with the maximum diameter typically around 200 μm. Darker, granular areas appear to be very prominent throughout the samples, even in the SE2 image. The BSE image indicates a large degree of chemical homogeneity in the sample. Major elements in the sample identified by EDS were C, O, Na, Mg, Al, Si, S, K, Ca, Fe, Co, and Cu. In conjunction with BSE images, the EDS data indicates that the melt glass beads are comprised predominately of a ferro-aluminum silicate, with lighter elements dispersed fairly evenly. The presence of Cu in the spectrum is due to the copper tape placed on the sample to reduce charging of the thin section during analysis. The speak for Co in the spectrum is not visible, and therefore is considered a mis-identification by the EDS software. EDS intensity ratios for the major elements with respect to O are listed in Table: 4.3. The Si:O, Al:O, Fe:O, and K:O ratios all showed increases compared to the precursor. The most interesting result is that the intensity of K is visible in the fired sample, where it was not in the precursor spectrum. The Mg:O, Ca:O, and Fe:O ratios all showed a decrease compared to the precursor. The decrease in the Fe:O ratio is possibly caused by the migration of Fe to the surface of the bead. As the thin section analyzed is a cross-sectional analysis of the bead, Fe would appear to be depleted.



(a) NYC SE2 thin section **(b)** NYC BSE thin section



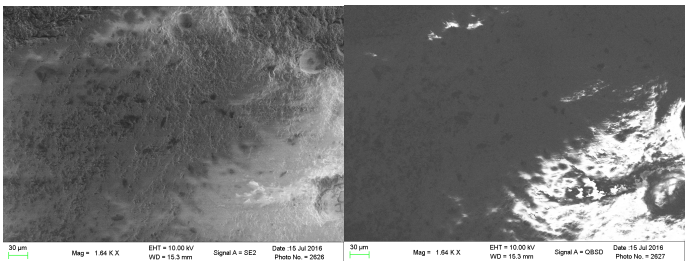
(c) EDS thin section

Figure 4.16: Micrographs and EDS for a typical thin section of surrogate bulk melt glass (NYC matrix)

Table 4.3: Ratios of major elements with respect to oxygen for bulk melt glass (NYC matrix)

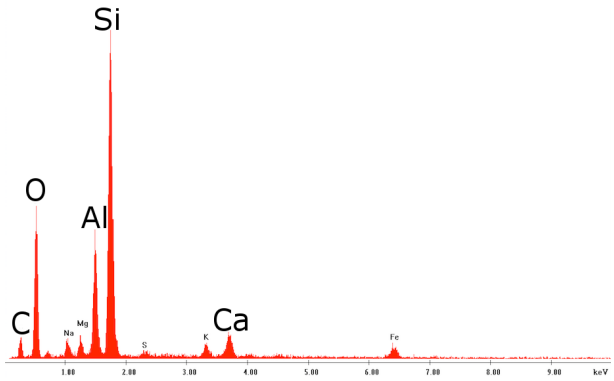
Element	Ratio
Si	1.94
Al	0.58
Mg	0.11
Ca	0.12
Fe	0.08
K	0.09

As with the STF matrix, the first area to be analyzed in detail for the NYC matrix was the homogenous region. Figure: 4.17 shows SE2/BSE micrographs and an EDS spectrum for a typical homogenous region. Inspection using SE2 imaging reveals a



(a) NYC SE2 homogenous region

(b) NYC BSE homogenous region



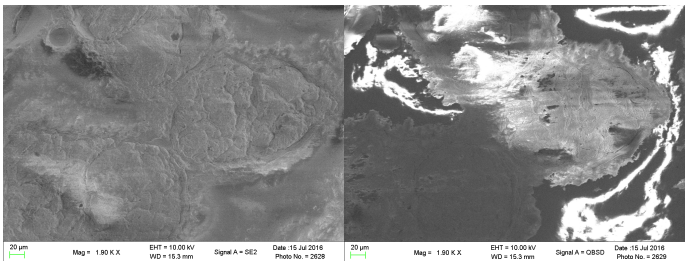
(c) EDS homogenous region

Figure 4.17: Micrographs and EDS for a typical homogenous region of surrogate bulk melt glass (NYC matrix)

rough, irregular surface. EDS analysis revealed that the typical homogenous region is composed of predominately Si, Al, and O with C, Na, Mg, S, K, Ca, and Fe also present. The small dark spots visible on the BSE images are caused due to C contamination from either the graphite crucible used during synthesis, or by the acrylic resin used to mount the sample. The lighter region in the lower right of the images is an image artifact indicative of sample charging.

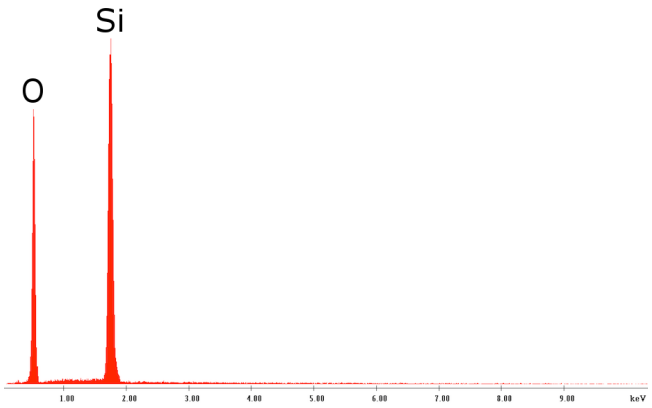
The second areas of the NYC thin sections analyzed in detail were the dark regions of Figure: 4.16. As with the STF matrix, these regions are rough and granular in appearance and show little chemical heterogeneity. EDS results indicate that these regions are composed of Si and O. Again, these areas are indicative of an incomplete melting of SiO_2 during synthesis. Micrographs and an EDS spectrum of a typical granular region of bulk NYC surrogate melt glass are shown in Figure: 4.18. The

lighter region in the upper right hand corner of the BSE image is a result of sample charging, and is not indicative of a varying chemical composition.



(a) NYC SE2 granular region

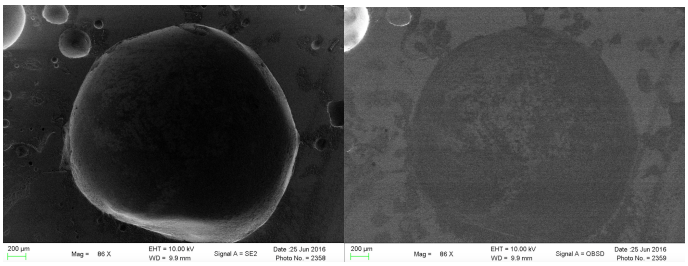
(b) NYC BSE granular region



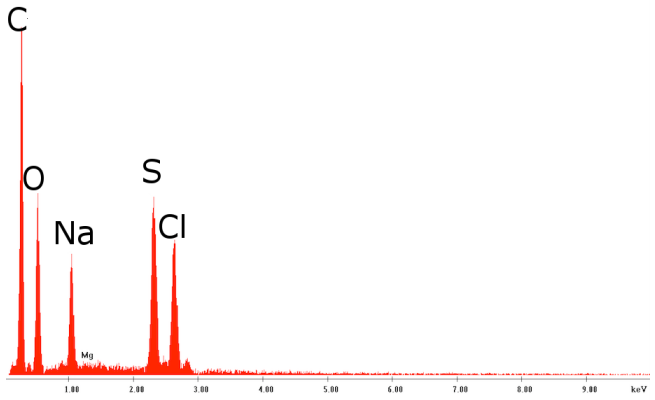
(c) EDS granular region

Figure 4.18: Micrographs and EDS for a typical granular area of surrogate bulk melt glass (NYC matrix)

Figure: 4.19 shows micrographs and an EDS spectrum of a large cavity of ≈2-mm found in a thin section of bulk NYC surrogate melt glass. Though the cavity pictured is larger than the typical cavities found in the NYC matrix, the morphological and chemical characteristics are the same. The vesicle surface is smooth and free of debris. BSE analysis shows regions of distinct chemical composition. When compared with the EDS spectrum, the darker areas can be identified as C-rich, while the lighter areas have high concentrations of Na, S, and Cl. The absence of Si from the spectrum indicates a reaction layer several μm thick on the cavity surface. The presence of a reaction layer would inhibit the ability for any Si present to be identified by EDS. It



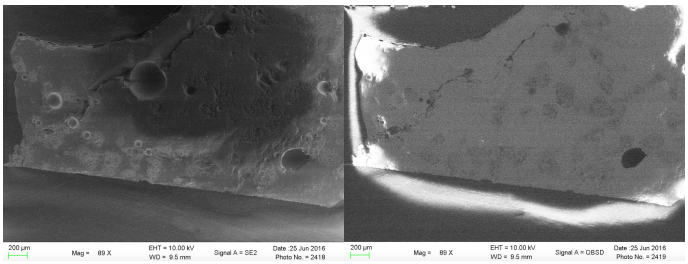
(a) NYC SE2 void **(b)** NYC BSE void



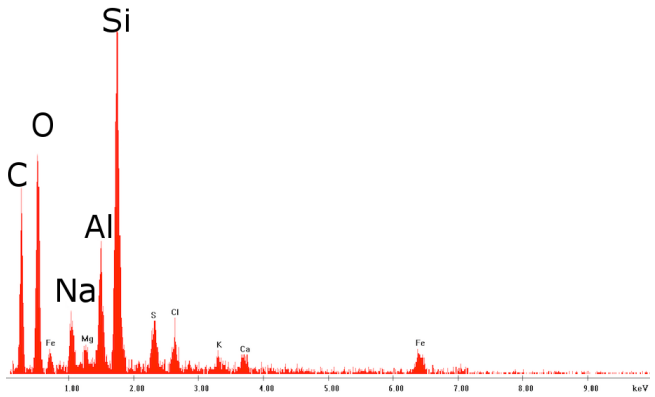
(c) NYC EDS void

Figure 4.19: Micrographs and EDS for a the surface of a cavity found in surrogate bulk melt glass (NYC matrix)

is believed that the presence of Cl is a result of contamination by the water used for grinding and polishing.



(a) NYC SE2 crack **(b)** NYC BSE crack



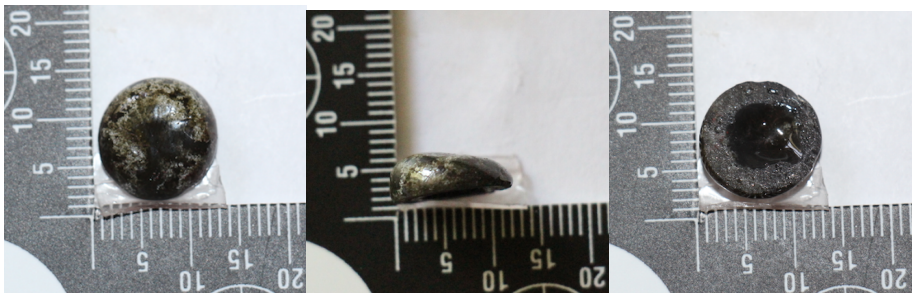
(c) NYC EDS crack

Figure 4.20: Micrographs and EDS of a typical crack found in bulk melt glass (NYC matrix)

Figure: 4.20 shows micrographs and and EDS spectrum of a typical crack found in bulk NYC surrogate melt glass. Again, the cracks either original from or travel through cavities in the thin sections. BSE analysis shows that there is no difference in the chemical composition of the cracks and the chemical composition of the thin section as a whole. C, O, Fe, Na, Mg, Al, Si, S, Cl, K, and Ca were all found to be present in the crack. The cracks found in samples comprised of the NYC matrix are also formed due to thermal and mechanical stresses experienced during the synthesis process.

Houston Matrix

A typical surrogate bulk melt glass bead composed of the HOU matrix can be seen from a top, side, and basal view in Figure: 4.21. The bead is dark green in color with a a few lighter colored patches near the sides. It is not thought that the lighter colored patched represent any differences in chemical composition. From the top, the bead is round and has a radius of 6-mm. A small depression is visible in the center of the top of the bead. The texture of the bead on both the top and side surfaces is smooth and free from imperfections or small agglomerated particulates. The side view of the bead reveals that it is uneven in height. The height of the bead ranges from 3-mm at its minimum, to 6-mm at its maximum. Like the melt glass bead seen in the NYC matrix, this bead has a large cavity in the center of its basal surface.

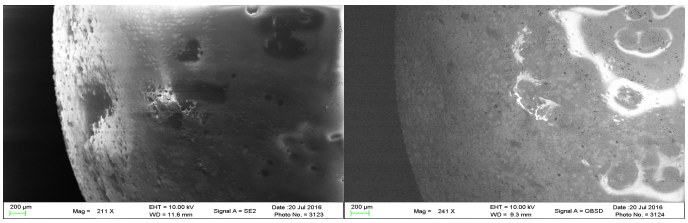


(a) Top view **(b)** Side view **(c)** Basal View

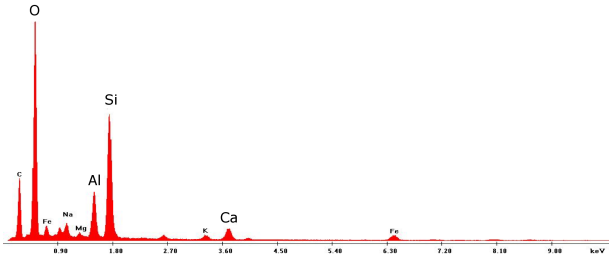
Figure 4.21: Optical images of a typical surrogate bulk melt glass bead composed of the HOU matrix

Surface analysis Figure: 4.22 shows SEM micrographs and an EDS spectrum for the surface of a typical surrogate bulk melt glass bead of the HOU matrix. The surface of the sample has many small pits and irregularities, including several protrusions. Unlike the previous matrices, there are no fully smooth regions of the surface. BSE imaging reveals that the small pits are concentrated in the heavier elements of the matrix. The protrusions do not appear to have a different chemical composition when compared to the non-pitted portions of the surface. The bright rings on the right hand side of the BSE image are artifacts from charging of the sample. EDS

analysis indicates the presence of C, O, Fe, Na, Mg, Al, Si, K, and Ca on the surface of the sample.



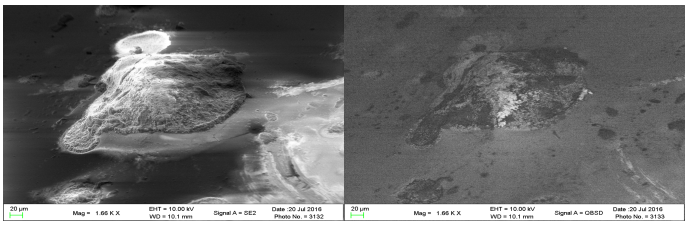
(a) HOU SE2 surface **(b)** HOU BSE surface



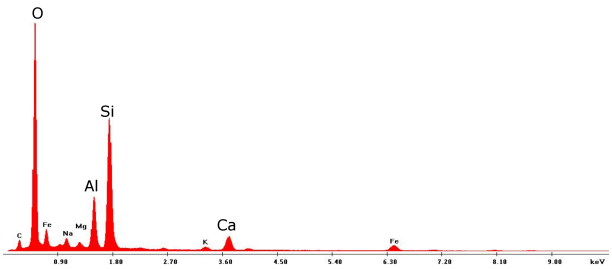
(c) HOU EDS surface

Figure 4.22: Micrographs and EDS of the top surface of a typical surrogate bulk melt glass bead (HOU matrix)

Upon closer inspection, the protrusions were found to be extremely textured when compared to the surrounding surface. A distinct boundary resembling glacial moraine can be seen at the edges of the protrusion. The protrusions are on the order of hundreds of μm wide at their widest point. BSE imaging shows chemical heterogeneity of the protrusions. However, there is no correlation between location and chemical composition. EDS analysis indicated the presence of C, O, Fe, Na, Mg, Al, Si, K, and Ca.

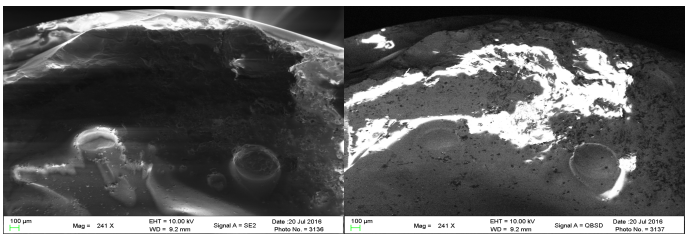


(a) HOU SE2 protrustion **(b)** HOU BSE protrustion

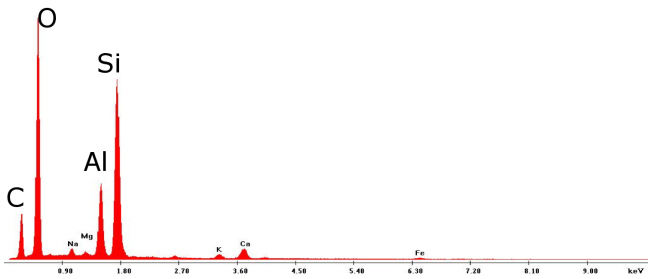


(c) HOU EDS protrustion

Figure 4.23: Micrographs and EDS for a typical protrusion on the surface of a surrogate bulk melt glass bead (HOU matrix)



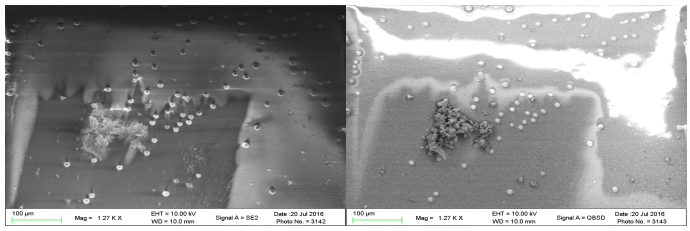
(a) HOU SE2 basal side **(b)** HOU BSE basal side



(c) HOU EDS basal side

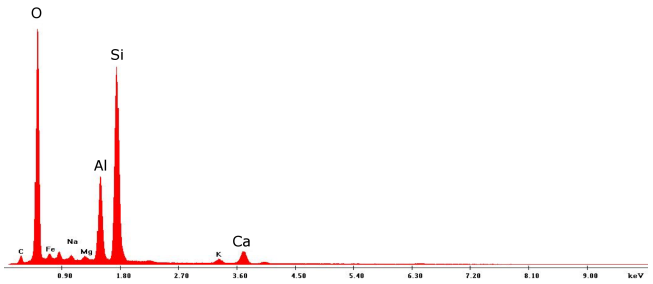
Figure 4.24: Micrographs and EDS for the basal side of a typical surrogate bulk melt glass (HOU matrix)

Figure: 4.24 shows micrographs and an EDS spectrum of the basal side of a typical HOU surrogate bulk melt glass bead. Two distinct regions can be observed on the bottom of the bead. The first region is the outer edges of the bead where contact was made with the graphite crucible during synthesis. This region is rough and highly textured with the maximum variation in topography on the order of hundreds of μm. The second region the can be seen is the concave region in the center of the bead. The region has a smooth surface that is covered in several small beads $\approx$10-μm in diameter. BSE imaging reveals a large degree of heterogeneity on the basal side of the sample, specifically in the region that came into contact with the graphite crucible. EDS analysis indicates the presence of C, O, Na, Mg, Al, Si, K, and Ca. With information, it is possible to conclude that the dark spots seen in the rough region are C inclusions.



(a) HOU SE2 basal side beads

(b) HOU BSE basal side beads



(c) HOU EDS thin section beads

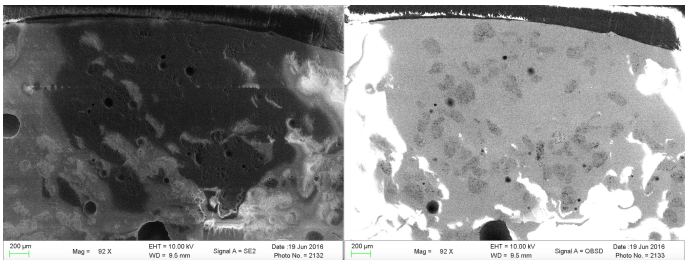
Figure 4.25: Micrographs and EDS for beads found on the basal side of a typical surrogate bulk melt glass (HOU matrix)

Further inspection of the small beads first seen in Figure: 4.24 reveals that the beads are almost perfectly spherical in shape. BSE imaging reveals that these small beads have a higher concentration of the heavier elements in the matrix than the surface of the concave region of the sample. EDS analysis reveals the presence of C, O, Fe, Na, Mg, Al, Si, K, and Ca. Unfortunately, when compared to the EDS spectrum for the total basal side of the sample, there is not enough of a difference in the intensity of the peaks to determine the elemental composition for these structures.

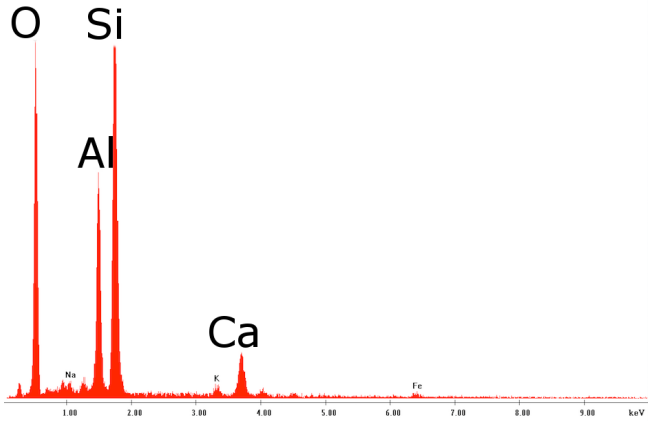
Thin section analysis Figure: 4.26 shows micrographs and an EDS spectrum of a typical thin section from a bead of bulk surrogate melt glass modeled for Houston, TX. The surface of the section is fairly smooth, with multiple sized voids ranging in diameter from tens to hundreds of μm. The BSE image shows dark, granular areas similar to those found in the thin sections of the STF and NYC matrices. The thin section appears to be chemically homogenous with the exception of these regions. EDS analysis shows the presence of O, Na, Al, Si, K, Ca, and Fe. As with the two prior matrices, it is highly possible that the thin section is primarily composed of aluminosilicate compounds. EDS intensity ratios for the major elements with respect to O are listed in Table: 4.4. The ratios that decreased wth respect to the precursor are Si:O, Al,:O, and Ca:O. The behavior of the Si:O and Al:O ratios is unexpected, as they were found to increase for the NYC matrix. The Mg:O, Fe:O, and K:O ratios all show increases from what was observed in the precursor.

Table 4.4: Ratios of major elements with respect to oxygen for bulk melt glass (HOU matrix)

Element	Ratio
Si	0.99
Al	0.63
Mg	0.05
Ca	0.12
Fe	0.01
K	0.04



(a) HOU SE2 thin section **(b)** HOU BSE thin section

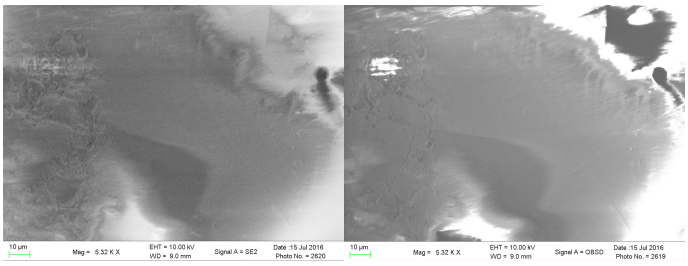


(c) HOU EDS thin section

Figure 4.26: Micrographs and EDS for a typical thin section of surrogate bulk melt glass (HOU matrix)

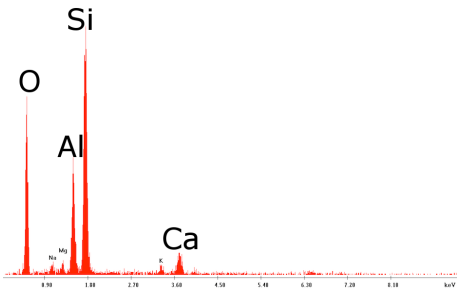
A typical homogenous region of a HOU matrix thin section is extremely smooth with very few features. BSE imaging reveals the region as extremely homogenous. Lack of readily discernible features and crystalline structures indicates that the region is possibly amorphous in nature. EDS reveals that the chemical composition of the region is nearly identical to the composition of the total thin section, with the only difference being the absence of Fe in the homogenous region. SEM micrographs and an EDS spectrum of a typical homogenous region for a thin section of a HOU bulk surrogate melt glass bead can be seen in Figure: 4.27.

Figure: 4.28 shows SEM micrographs and an EDS spectrum of a typical granular region of a thin section of a bulk HOU surrogate melt glass bead. SE2 imaging reveals many cracks and fissures which contrast sharply with the smooth surface of the surrounding homogenous regions. BSE imaging once again shows the granular



(a) HOU SE2 homogenous region

(b) HOU BSE homogenous region

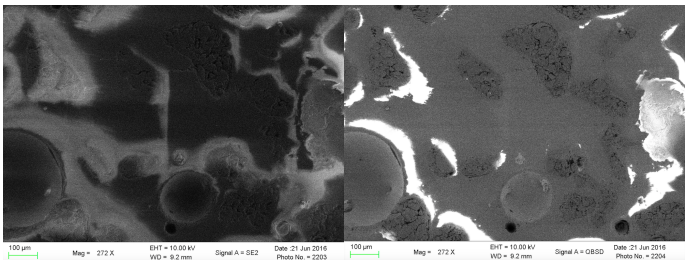


(c) HOU EDS homogenous region

Figure 4.27: Micrographs and EDS for a typical homogenous region of surrogate bulk melt glass (HOU matrix)

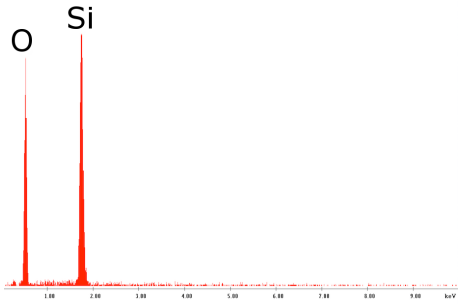
regions are chemically different from the surrounding regions. EDS analysis confirms that these regions are composed of Si and O, indicating an incomplete melt of SiO_2 during synthesis.

Figure: 4.29 depicts SEM micrographs and an EDS spectrum for a vesicle typical of those found in bulk surrogate HOU melt glass. Unlike the cavities found in the STF and NYC matrices, the cavities found in the HOU matrix thin sections have rough, uneven surfaces. BSE imaging indicates a fair degree of chemical heterogeneity, with lighter elements concentrated on the sides of the vesicle. EDS analysis shows the presence of C, O, Fe, Cu, Al, and Si. The presence of Cu in the spectrum is an artifact of the Cu-tape used to help reduce sample charging. Unfortunately, charging is apparent in the upper right hand corner of the micrographs.



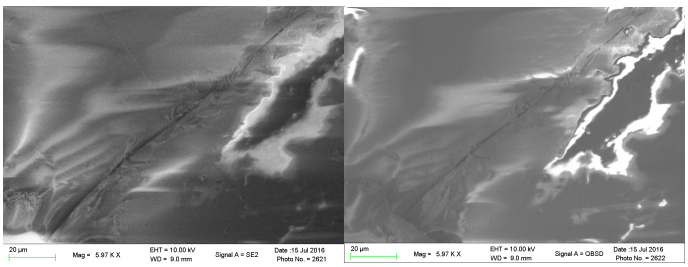
(a) HOU SE2 granular region

(b) HOU BSE granular region



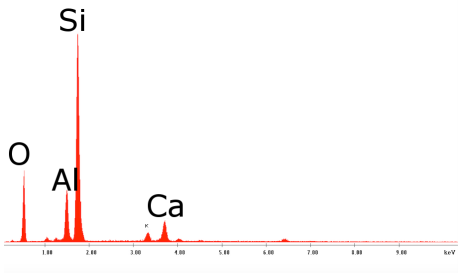
(c) HOU EDS granular region

Figure 4.28: Micrographs and EDS for a typical granular region of surrogate bulk melt glass (HOU matrix)



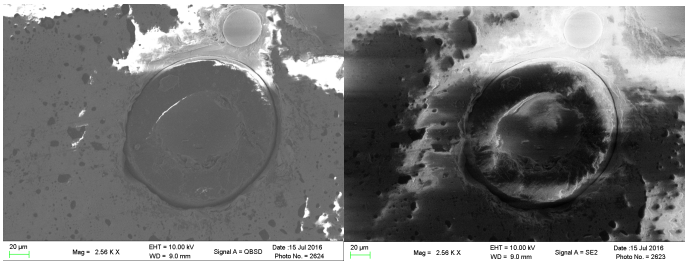
(a) HOU SE2 crack

(b) HOU BSE crack

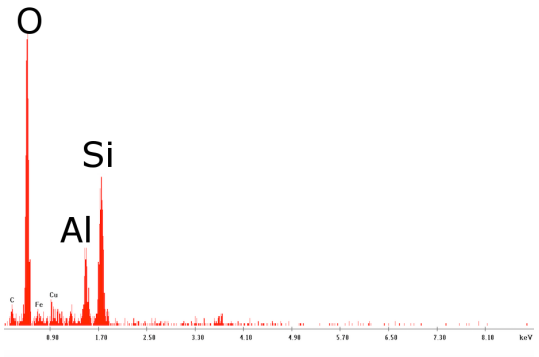


(c) HOU EDS crack

Figure 4.30: Micrographs and EDS for a typical crack found in surrogate bulk melt glass (HOU matrix)



(a) HOU SE2 void **(b)** HOU BSE void



(c) HOU EDS void

Figure 4.29: Micrographs and EDS for a the surface of a cavity found in surrogate bulk melt glass (HOU matrix)

Unlike with the STF and NYC matrices, cracks in the thin sections of surrogate HOU melt glass beads do not always originate in or travel through cavities. This is apparent in the micrographs found in Figure: 4.30. BSE imaging shows chemical homogeneity in the region around the crack, indicating that the crack was formed by thermal and mechanical stresses during synthesis. EDS analysis indicates the presence of O, Al, Si, K, and Ca. With the exception of Fe and Na, these are the same elements found in the homogenous region.

Comparison of Matrices

The three matrices show many of the same features. The surfaces all show smooth areas, though the NYC and HOU matrices do show textured regions. The basal side of the STF matrix shows large carbon deposits, and it is posited that these come from the graphite crucible used during synthesis. Beads composed of the NYC and HOU matrices show large depressions on the basal side which have small spherical particles attached. The three matrices display similar features in the thin sections. Crystalline granules characteristic of incomplete melting are visible in the SEM images of all three matrices. Voids of varying size and frequency are seen in the thin sections, as are crack indicative of mechanical stress during cooling. Though they each show some unique characteristics, each of three matrices display similarities to historical samples of bulk nuclear melt glass. This shows that the process used in this study to produce synthetic bulk nuclear melt glass is effective for both urban and non-urban surrogates.

4.1.2 Mass Spectrometry

The results for the analysis of the surrogate bulk melt glass samples via inductively-coupled time-of-flight mass-spectrometry (ICP-TOF-MS) are discussed in the sections below. Elements analyzed are Na, Mg, Al, Ca, Mn, Fe, Be, U, and Ti. Because of interference results with the flow gas used in the mass spectrometer with common

elements found in the atmosphere, Si, P, S, and K are not able to be analyzed. All uncertainties are given at a 2σ. Again, the matrices are examined in the order that they were modeled (STF, NYC, HOU).

Synthetic Trinitite Matrix

Figure: 4.31 shows a comparison of ICP-TOF-MS results for STF matrix surrogate bulk melt glass precursor, and three identical STF matrix surrogate bulk melt glass beads (labeled as STF A, B, and C in the figure). With the exception of STF B, all samples have similar Na concentrations. The precursor has a Na concentration of 111±24 ppm, which is less than the concentrations of Na found in samples A (151±81 ppm) and C (121±81 ppm). The Na concentration for Sample B is undetectable. Mg concentrations for the precursor material are 14±1 ppm, while the concentrations for samples A, B, and C are 26±2 ppm, 42±7 ppm, and 38±14 ppm respectively, with all three surrogate bulk melt glass bead samples having a higher concentration of Mg than the precursor material. Al concentrations also follow this pattern, albeit in a much more extreme way. The precursor Al concentration is 9±1 ppm while the three samples are 341±18 ppm, 516±102 ppm, and 482±44 ppm for rounds A, B, and C. The reason for the extreme difference in the Al concentration for the precursor and the samples is unknown based solely on the data gleaned from samples obtained from the STF matrix.

With the exception of sample B, concentration of Ca is similar in the precursor and samples A and B. Sample A has a Ca concentration of 139±29 ppm, sample B has a Ca concentration of 516±102 ppm, sample C has a Ca concentration of 89±25 ppm, and the precursor has a Ca concentration of 100±8 ppm. As with the discrepancy in the Na concentration for sample B, there is no theory to explain the large difference in the concentration found in sample B. Additionally, there is no evidence to suggest that the anomalies are linked in any way, and to do so would only be speculation. Mn and Ba levels remain fairly consistent through the different samples. Concentration of Mn is 2±1 ppm, 2±1 ppm, 4±1 ppm, and 4±1 ppm respectively for the precursor

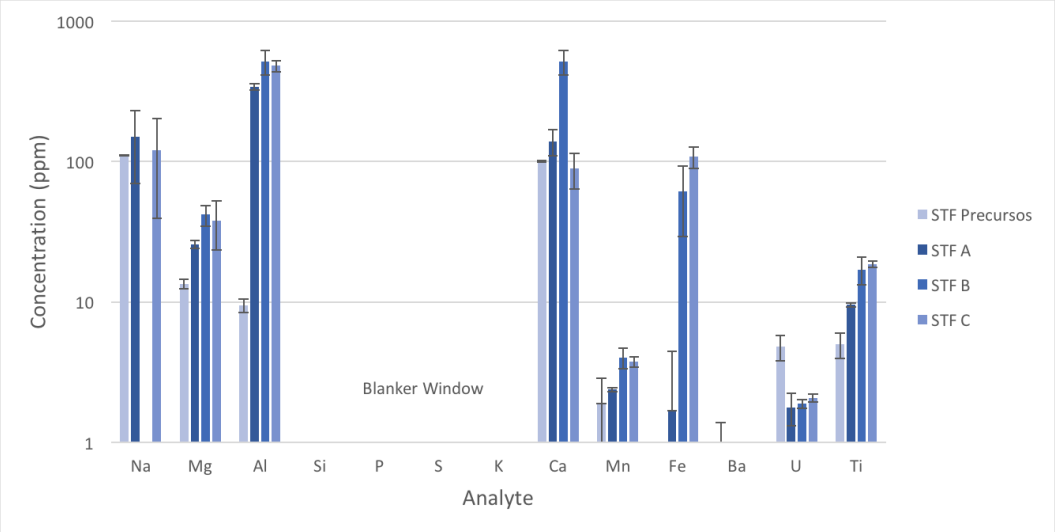


Figure 4.31: Comparison of ICP-TOF-MS results for the STF matrix

and samples A, B, and C. Concentration of Ba is 397±420 ppt, 130±7 ppt, 576±109 ppt, and 273±45 ppt respectively for the precursor and samples A, B, and C.

The concentration of Fe in the precursor matrix is not measurable, possibly due to an error by the experimentalist during the dissolution process. This is further supported by the inconsistent levels of Fe found in the three samples. Sample A had an Fe concentration of 2±3 ppm; sample B, 61±32 ppm; and sample C, 108±19 ppm. This drastic increase between the three samples coupled with the calculated error values indicates that once again, systematic error is a possible cause for discrepancies in the data. The precursor matrix has a U concentration of 5±1 ppm, while the concentrations found in samples A, B, and C are approximately half of that at 1700±400 ppt, 1900±100 ppt, and 2100±100 ppt respectively. The cause for the lower concentration of U in the surrogate bulk melt glass beads is possibly due to loss during the synthesis process via unaccounted for side reactions. Ti concentrations follow a similar pattern to those seen in Fe concentrations, albeit not as extremely. Concentrations found in the precursor are not as high as those seen in the samples. Concentration of Ti is 5±1 ppm, 19±1 ppm, 17±4 ppm, and 10±1 ppm respectively for the precursor and samples A, B, and C.

For the STF matrix of surrogate bulk melt glass, it is possible to get consistent ICP-TOF-MS results for Mn, Ba, and U. As for the other elements analyzed, no assumptions can be made about the reproducibility of the synthesis techniques based solely on the ICP-TOF-MS data. When the inconsistencies in the data are compared to the range of error in the measurements made, it appears that systematic error is responsible for some of the discrepancies seen as opposed to random error.

New York City Matrix

Figure: 4.32 shows a comparison of ICP-TOF-MS results for NYC matrix surrogate bulk melt glass precursor, and three identical STF matrix surrogate bulk melt glass beads. The three surrogate melt glass beads labeled as NYC A, B, and C in the figure. Na concentrations are similar for the precursor and sample C, measuring at 455±131 ppm and 453±83 ppm respectively. Na concentrations for samples A and B are higher, measuring 613±291 ppm and 762±475 ppm. Mg concentrations are fairly consistent between the four samples analyzed, though the concentration of Mg in the three melt glass beads is slightly higher than the concentration in the precursor. The Mg concentration in the precursor is 136±16 ppm; the Mg concentration in sample A is 213±132 ppm; the Mg concentration in sample B is 178±19 ppm; and the Mg concentration in sample C is 189±11 ppm. The pattern seen in Al concentration for the NYC matrix is very similar to that of the STF matrix. Samples A, B, and C all have significantly higher concentrations of Al than the precursor matrix. The precursor Al concentration is 44±4 ppm while the three samples are 1335±517 ppm, 1182±145 ppm, and 1245±100 ppm for rounds A, B, and C. The repeat of this pattern does not appear coincidental, and points to a systematic error. The data suggests that the samples were not accidently contaminated with additional Al, but rather exposed to Al during the synthesis process. As the hearth and insulation of the high-temperature furnace used to synthesize the bulk surrogate melt glass beads is insulated with low-density refractory bricks, the furnace is a possible source of

the contamination. Additionally, the ceramic mortar and pestle used to powder the samples could have been the cause of aluminum contamination.

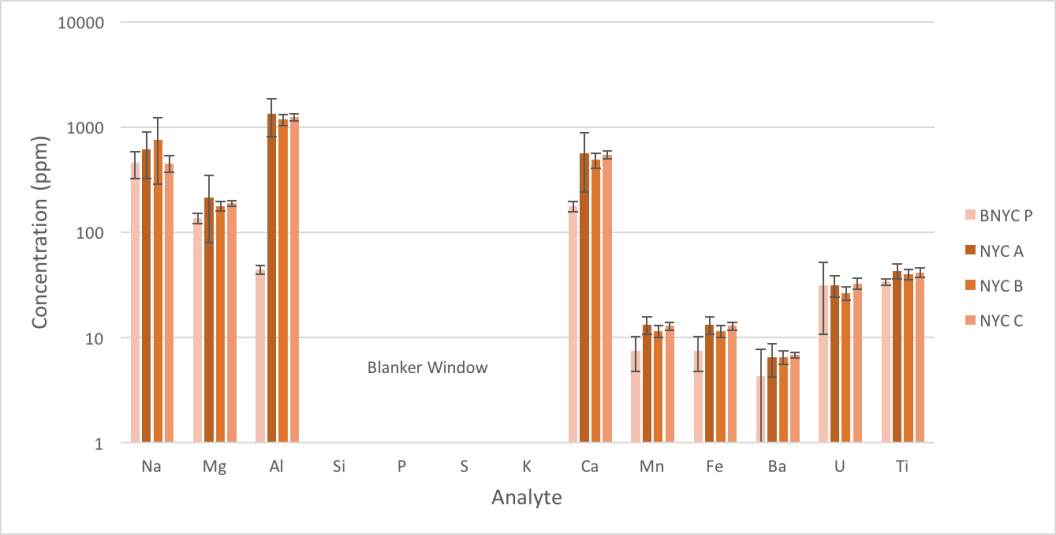


Figure 4.32: Comparison of ICP-TOF-MS results for the NYC matrix

The results for the concentration of Ca are similar to what is observed for Al concentrations, albeit to a smaller extent. The three samples all have a higher concentration of Ca than the precursor, but are all within the range of error compared to one another. Ca concentrations for samples A, B, and C are 566±324 ppm, 488±79 ppm, and 545±44 ppm respectively while the Ca concentration for the precursor is 176±19 ppm. Mn concentrations for the samples are roughly double the concentration found in the precursor. The concentration in the precursor is 7±3 ppm. Sample A shows a concentration of 13±2 ppm, sample B shows a concentration of 11±1 ppm, and sample C shows a concentration of 13±1 ppm.

Fe concentrations are unexpectedly low in the precursor and in the samples. The sample has an Fe concentration of 7±3 ppm, while the samples have Fe concentrations of 13±2 ppm, 11±1 ppm, and 13±1 ppm respectively for samples A, B, and C. The measured Fe concentrations are significantly lower than those observed in the STF matrix, when they should be higher. The cause of the low concentrations could be due to Ar-Ar interference in the mass spectrometer, though why these effects were

not observed in the STF matrix is unknown. Ba concentrations are consistent with one another across the samples and the precursor. Ba concentrations in the precursor are 4±3 ppm. The concentration in samples are 6±2 ppm for sample A, 6±1 ppm for sample B, and 7±1 ppm for sample C. U concentrations are consistent between the samples and the precursor. U concentration in the precursor is 31±21 ppm, while the samples have U concentrations of 31±7 ppm, 26±4 ppm, and 33±4 ppm for samples A, B, and C respectively. There is no discrepancy in the U concentration between the samples and the precursor like that seen in the STF matrix, other than the slightly lower concentration seen in sample B. The Ti concentration displays a similar behavior for the NYC matrix. Ti concentrations in the samples are 43±7 ppm for sample A, 40±4 ppm for sample B, 42±4 ppm for sample C. These concentrations are all similar to one another and to the Ti concentration of 34±2 ppm found in the precursor.

For the NYC matrix of surrogate bulk melt glass, it is possible to get consistent ICP-TOF-MS results for Mg, Mn, Fe, Ba, and U. An argument can be made that it is possible to obtain consistent results for Al, as the measured concentrations for the samples were all within an acceptable range when accounting for random error. As for the other elements analyzed, no assumptions can be made about the reproducibility of the synthesis techniques based solely on the ICP-TOF-MS data. When the inconsistencies in the data are compared to the range of error in the measurements made, it appears that systematic error is responsible for most of the discrepancies seen as opposed to random error.

Houston Matrix

Figure: 4.33 shows a comparison of ICP-TOF-MS results for NYC matrix surrogate bulk melt glass precursor, and three identical STF matrix surrogate bulk melt glass beads. The three surrogate melt glass beads labeled as NYC A, B, and C in the figure. Na concentrations are undetectable by the mass spectrometer for the precursor and the three samples. Because the STF and the NYC matrix both had detectable

quantities of Na, the absence of Na in the HOU matrix is possibly due to an error in the digestion process. Mg concentrations are higher in the samples then in the precursor. Mg concentration in the precursor is 39±16 ppm, while the concentration in the samples are 1.25-1.5 times higher at 63±11 ppm, 62±7 ppm, and 54±6 ppm for samples A, B, and C respectively. As seen in the STF and NYC matrices, the Al concentration in the HOU samples is significantly higher than that in precursor. The concentration of Al in the samples is 1114±259 ppm for sample A, 1211±34 ppm for sample B, and 1005±164 ppm for sample C. These values are all two orders of magnitude higher than the Al concentration of 47±22 ppm for the precursor. These results further strengthen the hypothesis that samples are contaminated with Al during the synthesis process.

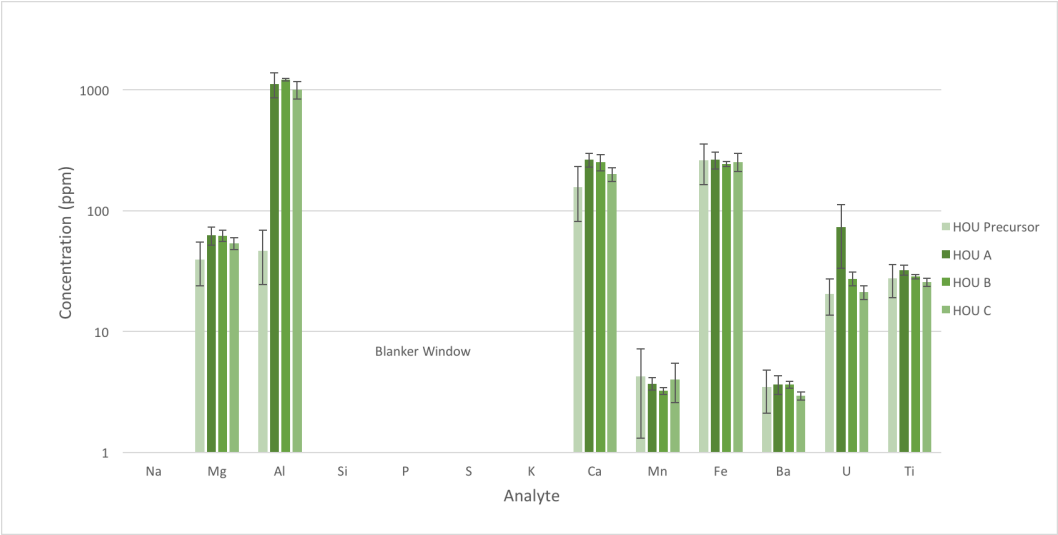


Figure 4.33: Comparison of ICP-TOF-MS results for the HOU matrix

Again, the pattern of Ca concentration is similar, albeit not as extreme as the pattern witnessed for Al concentration, with the samples having only a slightly higher concentration of Ca than the precursor. Ca concentration in the precursor is 156±75 ppm, while the Ca concentration in the samples are 263±35 ppm, 253±39 ppm, and 201±26 ppm for samples A, B, and C respectively. Mn concentrations in the HOU samples and precursor are similar to those found in the STF and NYC matrices.

The HOU precursor has a Mn concentration of 4±3 ppm while sample A has a concentration of 4±1 ppm, sample B has a concentration of 3±1 ppm, and sample C has a concentration of 4±1 ppm.

With the exception of sample C, the HOU precursor and samples have Fe concentrations that are in agreement with one another. The precursor and samples A and B have Fe concentrations of 261±97 ppm, 263±41 ppm, and 243±11 ppm respectively. Sample C has a concentration of 225±5 ppm, which is consistent with the concentrations measured for the HOU precursor and samples A and B. Ba concentrations are consistent between the precursor and the three samples, with the precursor having a Ba concentration of 3±1 ppm, and the samples having concentrations of 4±1 ppm, 4±1 ppm, and 3±1 ppm for samples A, B, and C respectively. For the precursor, the U concentration was found to be 21±7 ppm. This value is consistent with the concentrations of samples B and C, which are 27±4 ppm and 21±3 ppm respectively. The U concentration of sample A is 73±39 ppm, slightly over twice the concentrations of precursor and samples B and C. The concentration of Ti in the precursor is similar to that of the three samples. The precursor has a concentration of 27±8 ppm, while the samples A, B, and C have concentrations of 32±3 ppm, 28±1 ppm, and 26±2 ppm respectively.

For the HOU matrix of surrogate bulk melt glass, it is possible to get consistent ICP-TOF-MS results for Mg, Mn, Ba, and Ti. As with the NYC matrix, an argument can be made that it is possible to obtain consistent results for Al. Additionally, when not considering the offending data point it is possible to obtain consistent results for Fe. As for Ca, no assumptions can be made about the reproducibility of the synthesis techniques based solely on the ICP-TOF-MS data. The NYC matrix shows the least amount of error in the measurement of individual samples and the most consistency between samples. It is not known whether this is a result of the matrix, ambient laboratory/equipment conditions, or simply an increase in proficiency of the analyst.

Comparison of Matrices

The calculated and measured elemental concentrations in the three matrices have been compared to one another in order to determine whether or not the synthesis and analysis processes have the same effect when matrix composition is varied. All ratios are given in terms of STF:NYC:HOU. Table: 3.6 shows the expected elemental concentrations for each of the three matrices, while Figure: 4.34 shows the measured elemental concentrations for each of the three matrices.

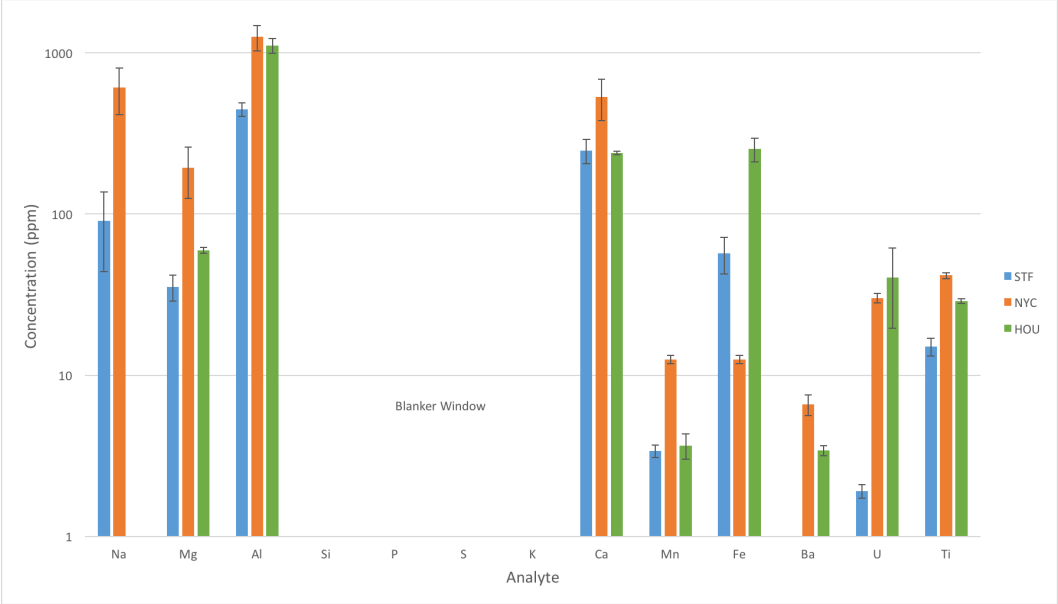


Figure 4.34: Comparison of ICP-TOF-MS results between all three matrices

Na concentrations are highest in the NYC matrix with the calculated concentration ratio being 1.67:4.31:1 and the measured ratio being 0.15:1:0. Unfortunately, because Na concentrations are not detectable in the HOU matrix, it is not possible to get a comparison of Na levels between all three matrices. Mg concentration ratios are 1.32:3.05:1 for the calculated values, and 0.59:3.25:1 for the measured values. The STF matrix is depleted in Mg in the synthesized samples, while the NYC and HOU matrices show Mg ratios close to their expected values. Because of the high levels of expected Al contamination in the synthesized surrogate melt glass beads, Al ratios will not be compared. Any information gleaned from the measured Al

concentration values will be suspect at best. Ca concentration ratios are slightly lower than expected for the STF matrix, and much higher than expected for the NYC matrix in the synthesized samples. Expected Al concentration ratios are 1.29:0.85:1, while the ratios for the synthesized samples are 1.04:2.23:1.

The STF matrix has a close to expected Mn concentration when compared to the Mn concentration of the HOU matrix. The concentration of Mn in the NYC matrix is much higher than expected when compared to the other two matrices. The expected Mn ratio for the three matrices is 0.83:2:1, while the actual ratio is 0.93:3.42:1. Examining the Fe concentrations shows that the STF matrix once again has a close to expected concentration when compared to the HOU matrix. The Fe concentration ratios are 0.35:1.23:1 for the calculated ratios, and 0.23:0.05:1 for the Fe ratios. The NYC matrix shows a much lower than expected concentration of Fe when compared to the other two matrices. Ba concentration ratios are very inconsistent among the three matrices. The expected Ba concentration is 0:0.67:1, while the measured ratio is 0.10:1.93:1. U concentration ratios are lower than expected for the STF and NYC matrices. The U concentration ratio is expected to be 1:1:1, as all three matrices had the same mass of U. However, the measured U concentration ratio is 0.05:0.74:1.00. The STF matrix has a slightly lower than expected Ti concentration when compared to the HOU matrix, while the NYC matrix shows a higher than expected concentration. The calculated Ti concentration ratio is 0.70:1.02:1, while the measured ratio is 0.52:1.45:1. The compared concentration ratios show that the synthesis and dissolution processes do play a large role in the final concentration values of the elements present in the matrices. In order to produce a sample of synthetic nuclear met glass with the appropriate elemental concentrations, further experimentation and analyses is required so that the responsible phenomena can be identified, and corrections to the the synthesis and analysis processes can be made.

4.1.3 X-Ray Diffraction

Crystallinity of the samples is examined via X-Ray Diffraction (XRD). Measured diffraction patterns were compared against a library of known crystalline phases and those with the best matches were chosen. The total number of patterns was limited to those phases containing at least one of the elements present in the matrix. All spectra shown are background corrected.

Synthetic Trinitite Matrix

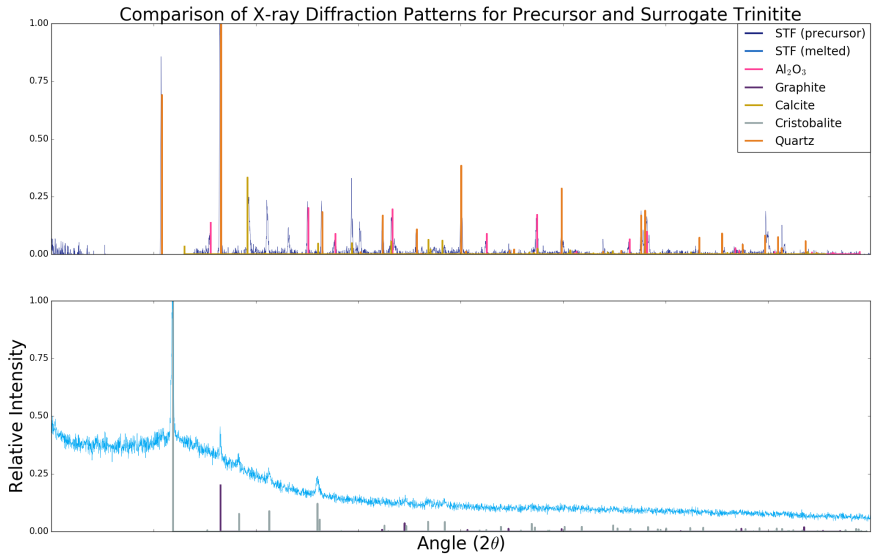


Figure 4.35: XRD patterns for precursor material compared to a powdered surrogate bulk melt glass bead (STF matrix)

A comparison of the STF precursor matrix and an average X-ray diffraction (XRD) pattern for a powdered STF melt glass bead can be seen in Figure: 4.35. The precursor shows large concentrations of quartz, alumina, and calcite. There is very little amorphous material in the precursor matrix, indicating that the compounds used for synthesis were crystalline in nature. After synthesis, the XRD pattern shows a high degree of amorphous character, with only cristobalite appearing as a crystalline

phase. As cristobalite is a high temperature polymorph of quartz, it appears that the quartz present in the precursor matrix was transformed during synthesis. With these additional data, the granular regions can be identified as cristobalite, while the smooth regions can be identified as amorphous. It should be noted that the presence of the amorphous region indicates that not all quartz was converted to cristobalite. Graphite from the crucibles used during synthesis can also be identified in average XRD pattern for powdered melt glass beads (STF matrix).

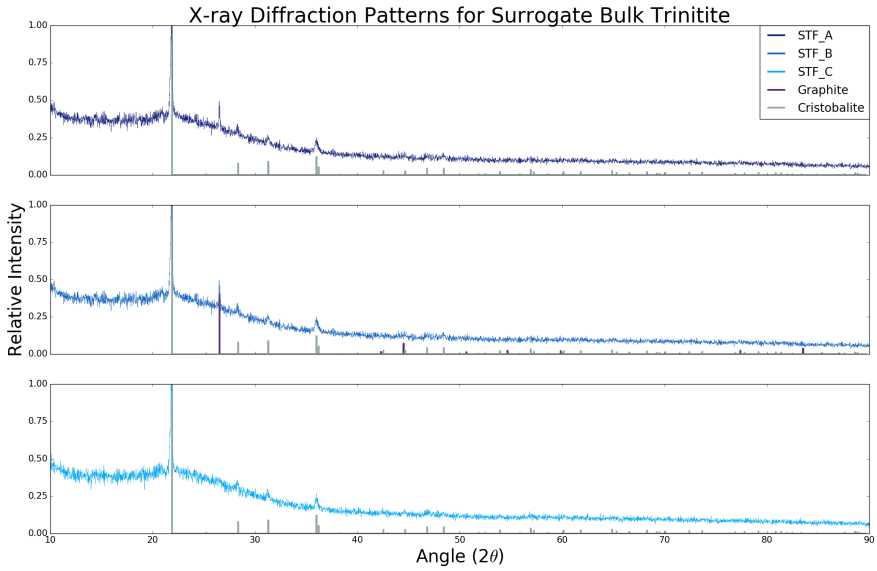


Figure 4.36: XRD patterns for three powdered surrogate bulk melt glass beads (STF matrix)

Figure: 4.36 shows XRD patterns for three powdered surrogate melt glass beads composed of the STF matrix. All three samples show cristobalite as the major crystalline phase present. The only major difference in the three patterns is the presence of graphite in the second sample. The near identical patterns of the three samples indicates that the synthesis process can create samples with reproducible crystalline structures for surrogate melt glass beads using the STF matrix.

New York City Matrix

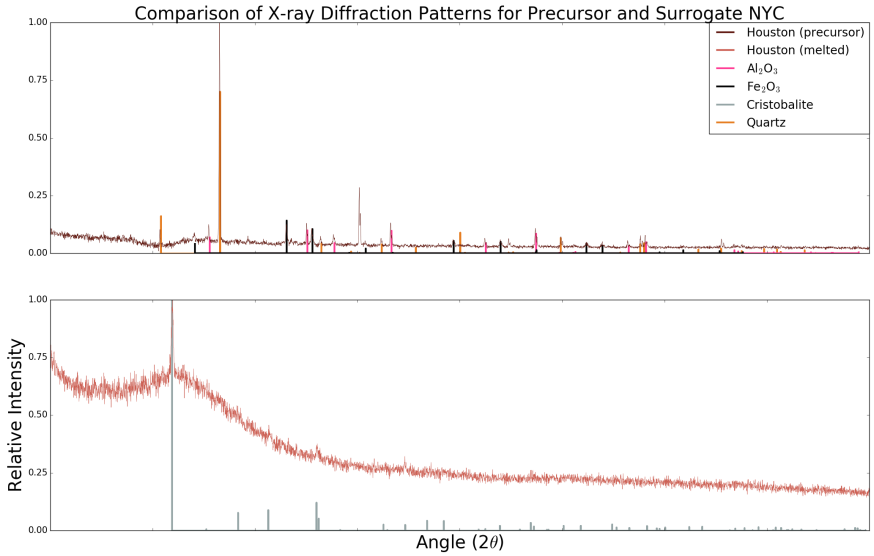


Figure 4.37: XRD patterns for precursor material compared to a powdered surrogate bulk melt glass bead (NYC matrix)

A comparison of the NYC precursor matrix and an average XRD pattern for a powdered NYC melt glass bead can be seen in Figure: 4.37. The XRD pattern for the precursor shows a large degree of quartz, alumina, and hematite. After heat treatment, the XRD pattern only displays cristobalite. Again, it is believed that the quartz present in the sample was transformed into cristobalite during synthesis. The absence of diffraction patterns for alumina and hematite in the second diffraction pattern indicates that these species were completely melted and exist in the surrogate melt glass beads in an amorphous form.

XRD patterns for three powdered surrogate melt glass beads composed of the NYC matrix can bee seen in Figure: 4.38. As with the STF matrix, all three samples exhibit cristobalite as their only crystalline phase. The three samples all display similar amorphous regions, albeit at varying intensities. The cause for the variation in intensity of the patterns is unknown.

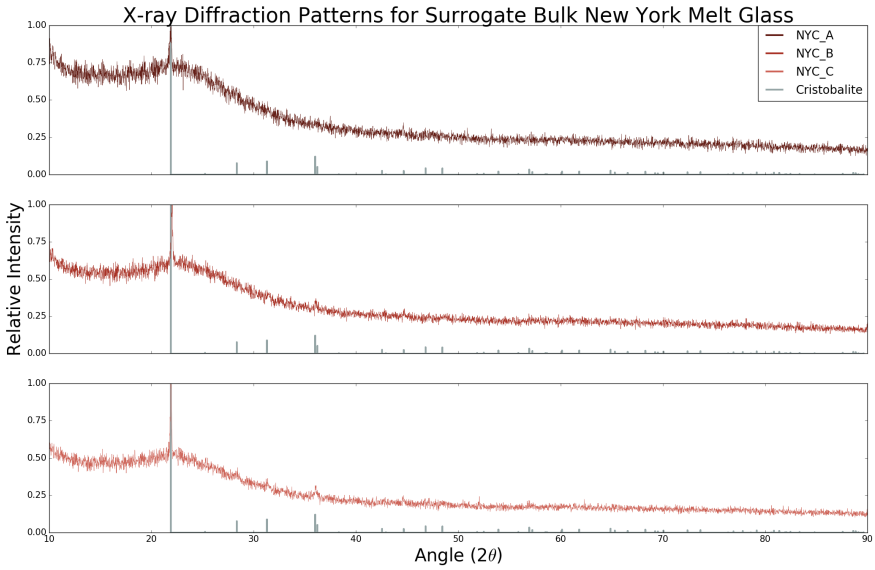


Figure 4.38: XRD patterns for three powdered surrogate bulk melt glass beads (NYC matrix)

Houston Matrix

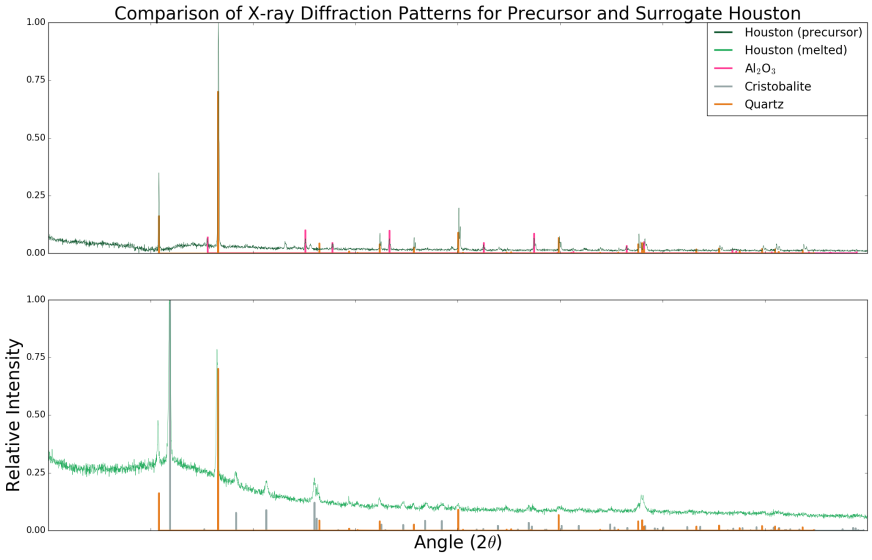


Figure 4.39: XRD patterns for precursor material compared to a powdered surrogate bulk melt glass bead (HOU matrix)

Figure: 4.39 shows a comparison of XRD patterns for the HOU precursor matrix and an average powdered HOU melt glass bead. The XRD pattern for the precursor matrix indicates the presence of quartz and alumina, and shows a very high crystallinity. The XRD pattern of the powdered melt glass bead shows the presence of both quartz and cristobalite. It can be seen that after synthesis, quartz is no longer the dominant crystalline species. This again indicates that the high temperatures used during synthesis causes the quartz present in the precursor materials to reorder into cristobalite. The fired sample also shows an increase in amorphous character.

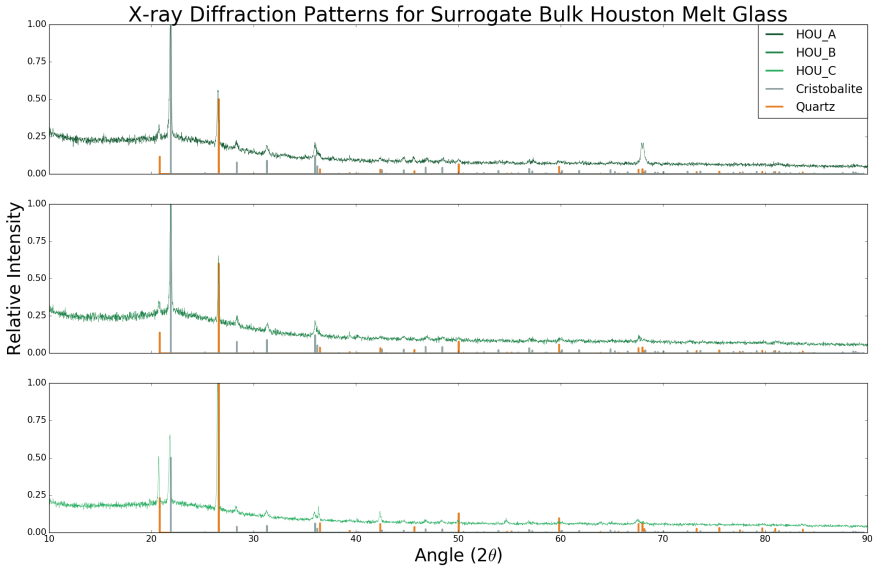


Figure 4.40: XRD patterns for three powdered surrogate bulk melt glass beads (HOU matrix)

XRD patterns for three powdered surrogate melt glass beads composed of the HOU matrix can be seen in Figure: 4.40. The three patterns all show the presence of both cristobalite and quartz. With the exception of the third pattern, cristobalite is the dominant crystalline phase. All three patterns exhibit a similar degree of crystallinity.

Comparison of Matrices

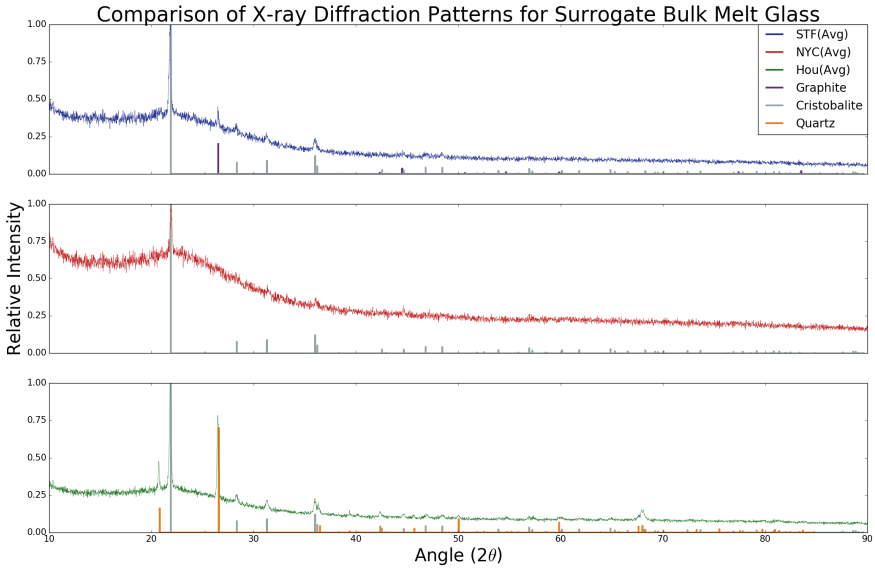


Figure 4.41: Comparison of XRD patterns for all three bulk melt glass matrices

Figure: 4.41 shows a comparison of XRD patterns for powdered beads of the three matrices of surrogate bulk melt glass. All three matrices show cristobalite as the dominant crystalline phase, with only the HOU matrix showing the presence of quartz. Looking at the relative intensity of the peaks, the NYC matrix shows the lowest degree of crystallinity while the HOU matrix shows the highest. The STF matrix is the only matrix that shows the presence of graphite, which as previously noted is a byproduct of the synthesis process. In all, though similar, the three matrices have distinct and unique crystalline properties. All matrices show a decrease in crystallinity after heat treatment.

4.2 Surrogate Particulate Melt Glass

Surrogate particulate melt glass and its precursors are discussed below. The three 'stages' discussed are the untreated precursor, the spray-dried precursor, and the

heat-treated precursor also known as surrogate particulate melt glass. Two matrices, the STF and NYC matrices, are examined. The surrogate particulate melt glass results for electron microscopy, ICP-TOF-MS, and XRD analyses are discussed.

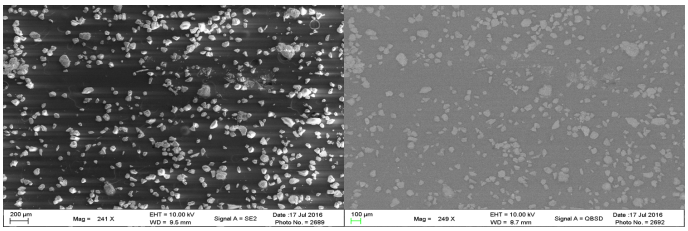
4.2.1 Electron Microscopy Analysis

SEM and EDS analysis of surrogate particulate melt glass and it precursors is discussed below. Major physical characteristics such as silica granules, fine particulates, and fused material are discussed.

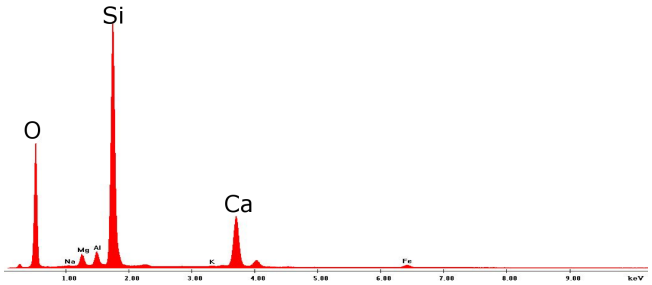
Synthetic Trinitite Matrix

Untreated Precursor SEM micrographs and an EDS spectrum of a typical sample of STF matrix surrogate particulate melt glass precursor can be seen in Figure: 4.42. At 241x magnification, it is clear that the precursor is made up of many granules ranging in size from tens of μm to hundreds of μm at their largest dimension. The granules have sharp edges and are very angular in appearance. Additionally, clumps of powder also appear in the sample. The maximum dimension of these clump is usually around 100 μm. Chemically the precursor is homogenous, with O, Na, Mg, Al, Si, K, Ca, and Fe all appearing in the sample.

Figure: 4.43 provides an in-depth analysis of the granules seen in Figure: 4.42. At closer magnification, the granules appear to be crystalline in nature with very pronounced, angular features. BSE imaging reveals a lack of chemical differences both within and between particles. The particles are composed of predominately Si and O, though trace amounts of Na, Mg, Al, and Ca are present. Because of the significantly larger quantities of Si and O present, it is very possible that these granules are the SiO_2 gel used to create the precursor matrix. The presence of C in the sample is thought to come from the carbon tape used to mount the precursor for analysis, and not from the precursor itself.

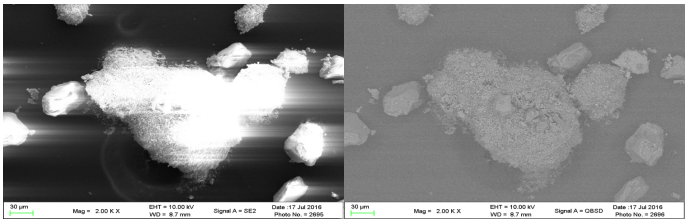


(a) STF SE2 precursor **(b)** STF BSE precursor

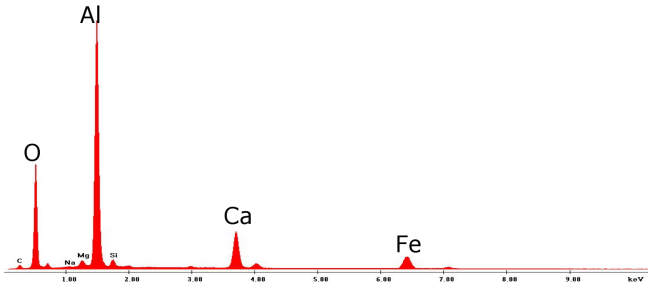


(c) STF EDS precursor

Figure 4.42: Micrographs and EDS of surrogate particulate melt glass precursor (STF matrix)

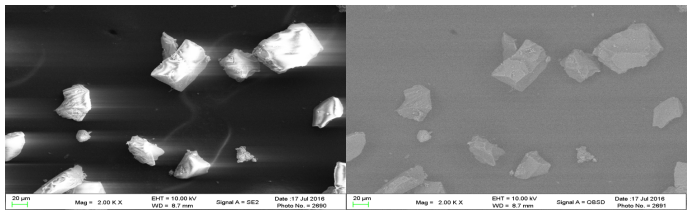


(a) STF SE2 clump **(b)** STF BSE clump

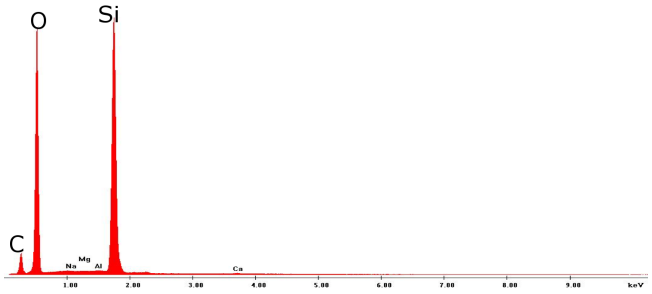


(c) STF EDS clump

Figure 4.44: Micrographs and EDS for a typical clump found in surrogate particulate melt glass precursor (STF matrix)



(a) STF SE2 granules **(b)** STF BSE granules

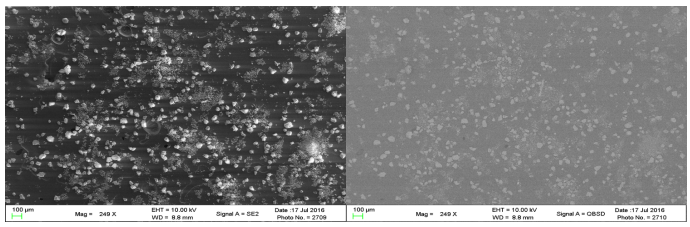


(c) STF EDS granules

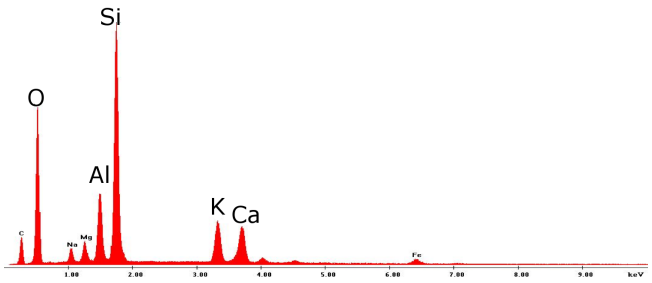
Figure 4.43: Micrographs and EDS of granules found in surrogate particulate melt glass precursor (STF matrix)

Figure: 4.44 shows SEM micrographs and an EDS spectrum for typical clump of material found in surrogate STF particulate melt glass precursor matrix. The clump appears to be comprised of small particles that have agglomerated together, many of which are smaller than a μm in diameter. Because of this, the surface of the clump is rough and uneven, with the edges appearing rounded. However, the outline of the clump is clearly defined, indicting that it is indeed an agglomeration of particles and not a region of high particle density. BSE analysis shows chemical homogeneity in the clump, while EDS reveals the presence of O, Na, Mg, Al, Si, Ca, and Fe. When the EDS spectrum of the clump is compared to that of the granules found in Figure: 4.43, it becomes obvious that they are chemically different. The clump is comprised of high levels of Al, O, and Ca. Other elements such as Na, Mg, and Fe appear in larger quantities than in the granules, which are composed of SiO_2. This indicates a physical separation, and hence chemical heterogeneity, of the compounds used to create the precursor matrix.

Spray-dried Precursor SEM micrographs and an EDS spectrum of a typical sample of spray-dried STF matrix surrogate particulate melt glass precursor can be seen in Figure: 4.45. Like untreated precursor, the spray-dried precursor consists of many granules, all appearing to be on the order of tens of μm in their largest dimension. Clumps of material are not visible in the sample. Instead, a fine powder is present. BSE analysis indicates that the granules are comprised of heavier heavier elements than the powder. EDS indicated the strong presence of O, Na, Mg, Al, Si, K, Ca, and Fe in the sample, all of which were also present in the untreated precursor. Because EDS is not a suitable method for quantitative analysis of these samples, ICP-TOF-MS must be used to determine if the ratios of the elements present are the same as those in the untreated precursor.

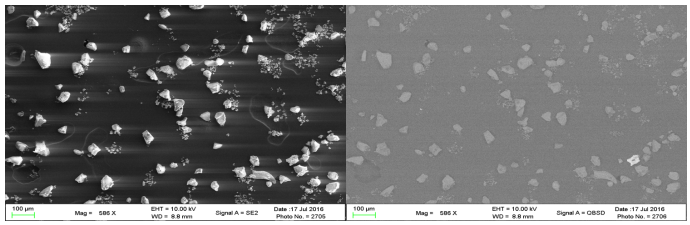


(a) STF SE2 spray-dried **(b)** STF BSE spray-dried



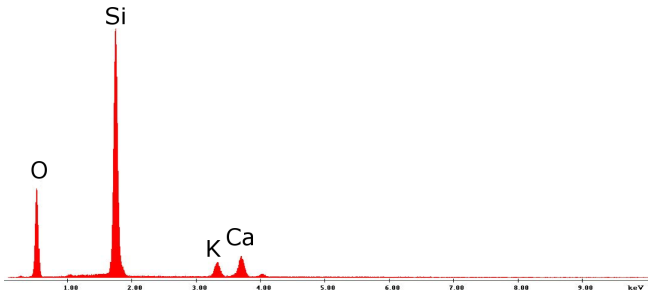
(c) STF EDS spray-dried

Figure 4.45: Micrographs and EDS of spray-dried surrogate particulate melt glass precursor (STF matrix)



(a) STF SE2 spray-dried granule

(b) STF BSE spray-dried granule

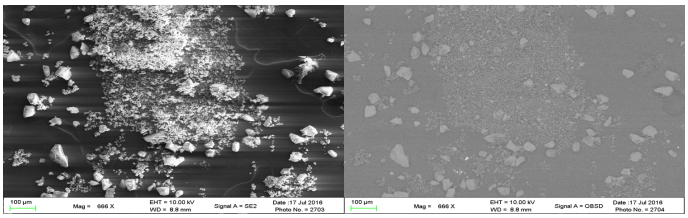


(c) STF EDS spray-dried granule

Figure 4.46: Micrographs and EDS of granules found in spray-dried surrogate particulate melt glass precursor (STF matrix)

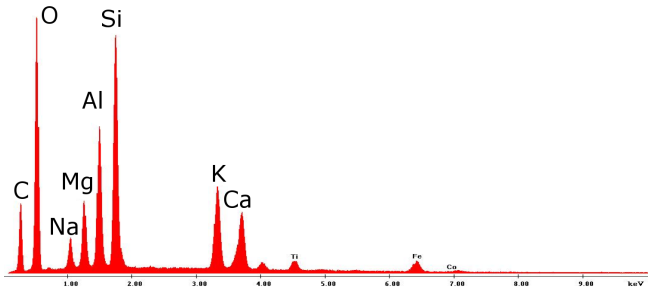
Closer inspection of the granules in the spray-dried STF particulate bulk glass matrix shows that they are no larger than 100-μm in their largest dimension, which is smaller than their size before the spray drying process. Additionally, it appears that the granules retain their angular shape. BSE imaging shows no obvious chemical differences between particles. The presence of O, Si, K, and Ca were confirmed using EDS. As with the untreated STF granules, Si, and O are the primary elements present. SEM micrographs and an EDS spectrum for granules found in a spray-dried STF particulate precursor can be seen in Figure: 4.46

Figure: 4.47 shows micrographs and a EDS spectrum for a typical 'clump' of material found in spray-dried STF particulate precursor. Unlike in the non-treated precursor, this clump does not have clearly defined edges, and the small constituents do not appear to be as tightly packed together. There appears to be minimal variation in the size of the small particles making up the clump, however BSE imaging shows



(a) STF SE2 spray-dried clump

(b) STF BSE spray-dried clump



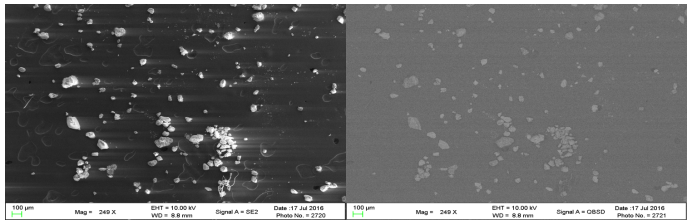
(c) STF EDS spray-dried clump

Figure 4.47: Micrographs and EDS for a typical clump found in spray-dried surrogate particulate melt glass precursor (STF matrix)

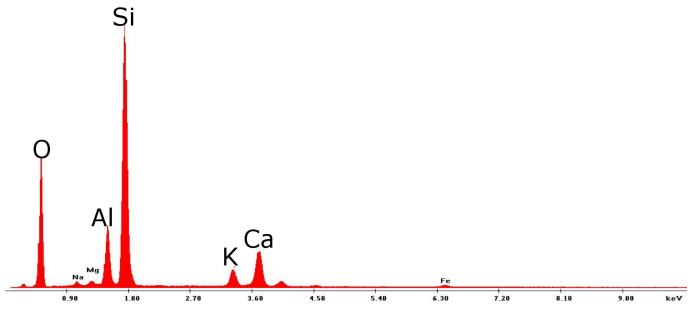
that there does appear to be some chemical variation. EDS shows the presence of C, O, Na, Mg, Al, Si, K, Ca, Ti, and Fe. It is thought that the presence of carbon in the spectrum is caused by the carbon tape used in mounting. The large presence of oxygen indicates that the constituents are possibly in an oxide form in the sample. The intensity of the signals for Al, Ma, Na, K, and Ca are al higher than those found in the spray-dried granules, again indicating a degree of chemical heterogeneity in the precursor matrix.

Heat-Treated Precursor SEM micrographs and an EDS spectrum of a typical sample of heat-treated STF matrix surrogate particulate melt glass precursor can be seen in Figure: 4.48. The sample shows a large variation in of the surrogate particulate debris, with individual particles ranging from hundreds of nm to hundreds of μm in their largest dimension. Additionally, morphology is greatly variable throughout the sample. Some particles have smooth edges and corners, appearing to be partially

melted. Others are clearly comprised of several fused granules, and retain their jagged rough features. The clumps seen in the micrographs of the precursor and the spray-dried material seem to have fused into solid masses. Larger sized particles appear to be composed of heavier elements than the smaller particles, which are darker in appearance when analyzed using BSE. EDS indicates the presence of O, Na, Mg, Al, Si, K, Ca, and Fe. Si is the most prominent element, followed by O, Al, and Ca. These results are expected given the elemental compositions of the precursor matrix used.



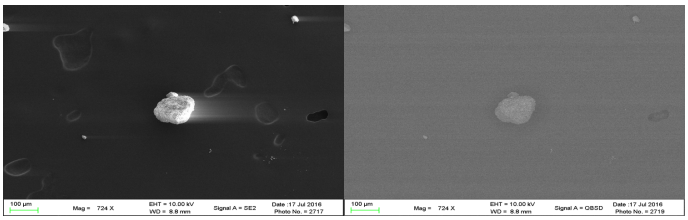
(a) STF SE2 heat-treated **(b)** STF BSE heat-treated



(c) STF EDS heat-treated

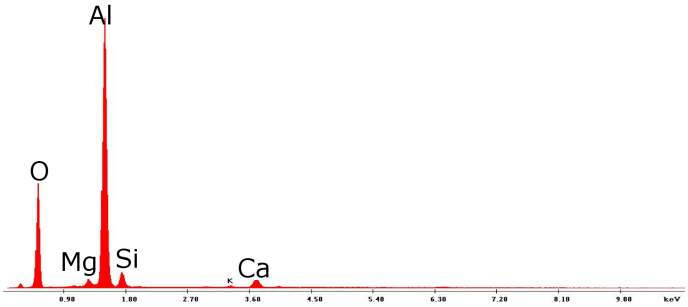
Figure 4.48: Micrographs and EDS of heat-treated surrogate particulate melt glass precursor (STF matrix)

Globules in the surrogate particulate melt glass have well defined boundaries and edges, unlike the spray-dried precursor. Their appearance indicates that the constituents were fused together when exposed to the plasma torch. Size of the globules varies, but typically the largest dimension is approximately 100-μm in length. The surface of the globules appears speckled when analyzed using BSE, suggesting that while the spray-dried precursor has been fused neither a full melt, or mixing



(a) STF SE2 heat-treated globule

(b) STF BSE heat-treated globule

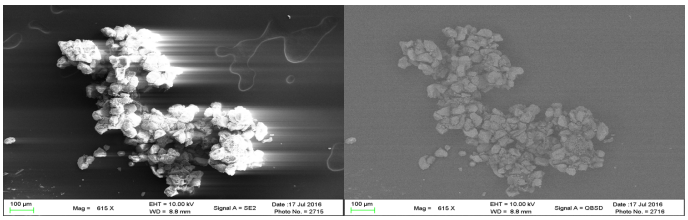


(c) STF EDS heat-treated globule

Figure 4.49: Micrographs and EDS for a typical globule found in heat-treated surrogate particulate melt glass (STF matrix)

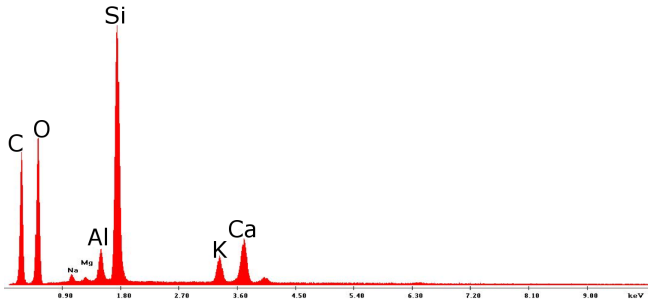
of the elements present occurred during heat-treatment. The globules are composed primarily of Al and O, possibly as Al_2O_3. Other elements present are O, Mg, Si, K, and Ca. SEM micrographs and an EDS Spectrum for typical globules found in heat-treated surrogate particulate melt glass composed of the STF matrix can be found in Figure: 4.49.

Heat-treatment of the spray-dried precursor resulted in the fusing and agglomeration of many SiO_2 granules. The size of the fused granules varies greatly, but is usually on the scale of several hundred μm in the largest dimension. The shape of the agglomerated granules also varies greatly from particle to particle. The surface is very rough, and individual granules can be distinguished from one another. BSE analysis indicates that there is a large degree of chemical heterogeneity. O, Na, Mg, Al, Si, K, and Ca are all present. The intensity of the peaks indicated that Si is present in the highest concentration of all the observed elements. This is a stark contrast to the heat-treated clumps, which contained high levels of Al.



(a) STF SE2 heat-treated fused granules

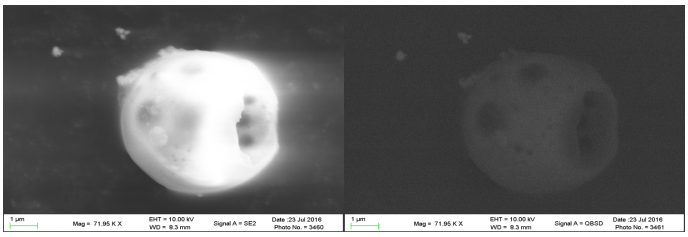
(b) STF BSE heat-treated fused granules



(c) STF EDS heat-treated fused granules

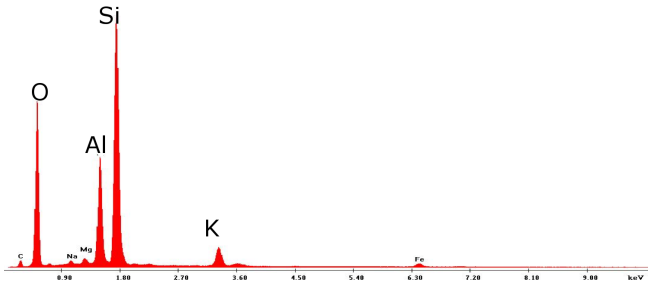
Figure 4.50: Micrographs and an EDS spectrum of fused SiO_2 granules found in heat-treated surrogate particulate melt glass (STF matrix)

Figure: 4.51 shows SEM micrographs and an EDS spectrum for a spherical particle found in surrogate particulate melt glass formed from the STF matrix. The sphere in the figure has a diameter of roughly 4 μm. The surface of the sphere is covered in pockmarks and bumps in the upper right hand of the photo, and is relatively smooth in the lower left hand of the photo. The topography of the sphere makes it difficult to discern chemical differences via BSE due to shadowing effects. However, the smooth region appears to be chemically homogenous. Homogeneity in the sphere indicates a thorough melting and mixing of the precursor during heat-treatment. EDS analysis shows the presence of O, Na, Mg, Al, C, Si, K, and Fe. The intensities of the peaks for these elements are what is expected for the STF matrix. Surprisingly, Ca is absent from the spectrum without explanation.



(a) STF SE2 heat-treated sphere

(b) STF BSE heat-treated sphere



(c) STF EDS heat-treated sphere

Figure 4.51: Micrographs and an EDS spectrum for a spherical particle found in surrogate particulate melt glass (STF matrix)

Table 4.5: Ratios of major elements with respect to oxygen for particulate bulk melt glass (STF matrix)

Element	Heat-treated precursor	Fused granules	Particulate spheres
Si	2.05	1.56	1.49
Al	0.49	0.21	0.66
Mg	0.04	0.04	0.06
Ca	0.28	0.27	n/a
Fe	0.02	n/a	0.02
K	0.13	0.17	0.11

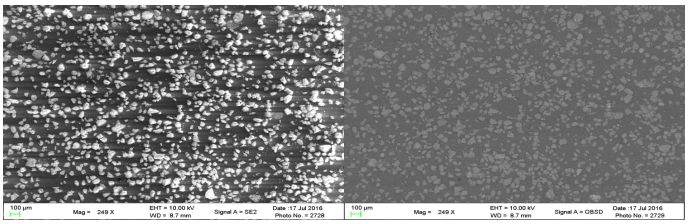
The ratios of the major elements with respect to O found in various particulate melt glass features can be seen in Table: 4.5. Analyzing the heat-treated precursor as a whole, the ratios for Si, Al, and K were all found to increase, while the ratios for Mg and Ca were found to decrease. The Fe:O ratio is the same as that of the untreated precursor.

The fused granules and particulate spheres have a lower Si:O ratio than the total heat-treated precursor. The Al:O ratio is lower for the fused granules, but higher for the particulate spheres. The ratio for Mg:O is identical for the total precursor and the granules, while the spheres show a slight increase in the ratio. No Ca peak was found for the spheres, but the Ca:O ratio was almost identical for the fused granules. Similarly, the total precursor and the spheres show an identical Fe:O ratio, while the fused granules did not have an Fe peak for their EDS spectrum. The K:O ratios are increased for the fused globules, and decreased for the spheres.

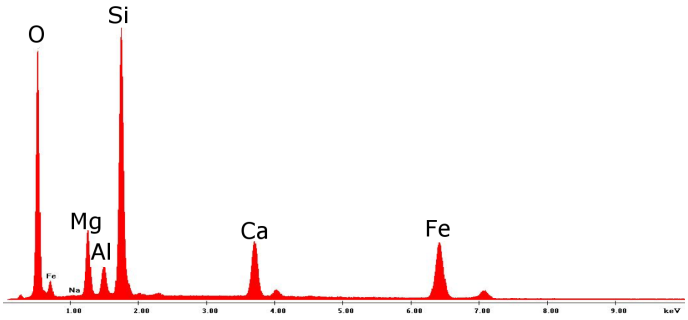
New York City Matrix

Untreated Precursor SEM micrographs and an EDS spectrum of a typical sample of NYC matrix surrogate particulate melt glass precursor can be seen in Figure: 4.52. The sample contains many different constituents, from large grains to fine powdery clumps. Chemically, the grains appear to be composed of heavier elements than the clumps. EDS analysis shows that the sample contains O, Fe, Na, Mg, Al, Si, and Ca. The intensity of the Fe peak is higher than that found in samples of the STF matrix. This is expected due to the higher Fe content in the NYC sample.

Closer inspection of the granules reveals that they are identical in size and morphology to those found in the untreated STF precursor matrix. Again, the granules appear very angular and crystalline in shape, and are chemically homogenous. EDS analysis shows only the presence of Si and O, again indicating that the granules are composed of SiO_2 gel. Figure: 4.53 shows SEM micrographs and an EDS spectrum of typical granules found in surrogate particulate melt glass NYC precursor matrix.

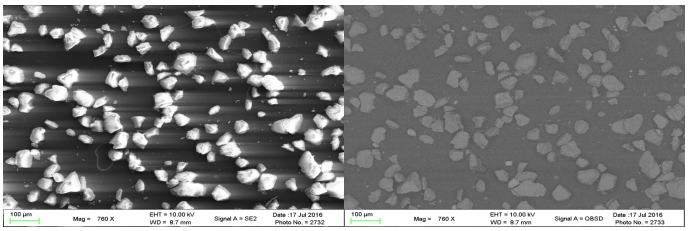


(a) NYC SE2 precursor **(b)** NYC BSE precursor

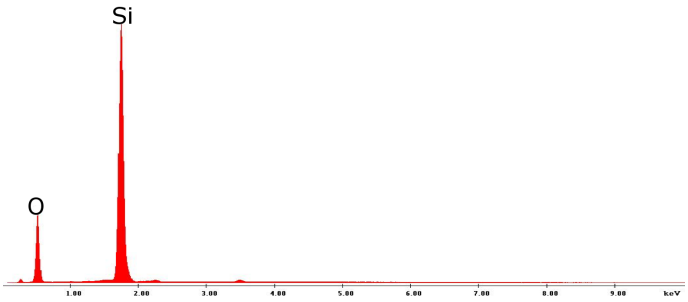


(c) NYC EDS precursor

Figure 4.52: Micrographs and EDS of surrogate particulate melt glass precursor (NYC matrix)

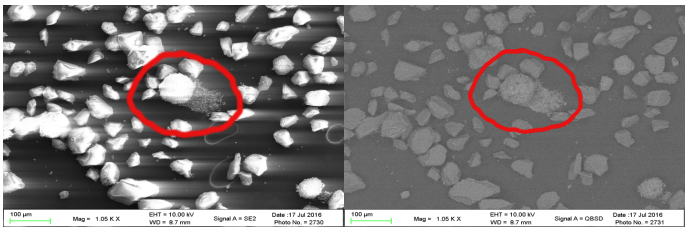


(a) NYC SE2 granule **(b)** NYC BSE granule

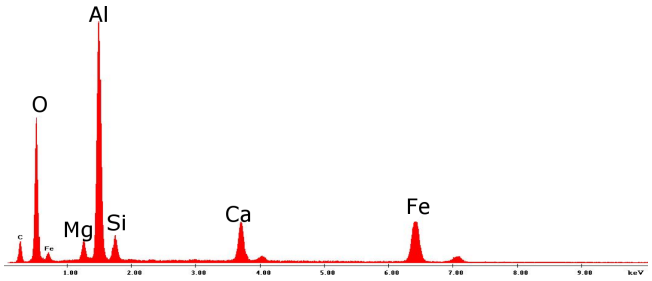


(c) NYC EDS granule

Figure 4.53: Micrographs and EDS of granules found in surrogate particulate melt glass precursor (NYC matrix)



(a) NYC SE2 clump **(b)** NYC BSE clump



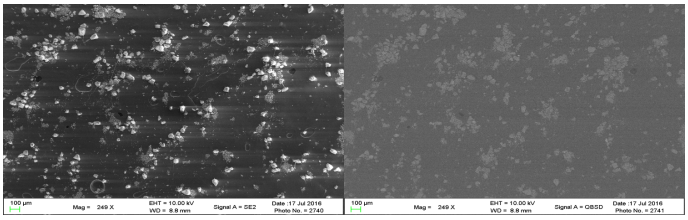
(c) NYC EDS clump

Figure 4.54: Micrographs and EDS for a typical clump found in surrogate bulk melt glass (NYC matrix)

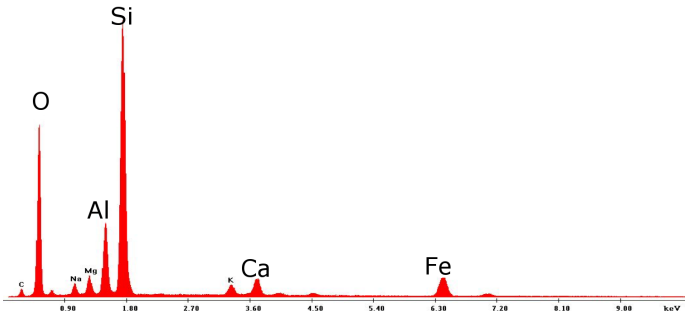
Figure: 4.54 hows SEM micrographs and an EDS spectrum for typical clump of material found in surrogate NYC particulate melt glass precursor matrix. The clumps observed in the NYC precursor are smaller than those seen in the STF precursor, measuring only tens of μm in their largest dimension. As with the other clumps observed, it appears that they are composed of many small constituent particles agglomerated together. The 'smearing' on the lower right hand side of the clump in the figure indicates that it is only loosely held together. BSE analysis shows chemical heterogeneity in the clump. Elements identified by EDS are C, O, Fe, Mg, Al, Si, and Ca. The vast majority of the clump appears to be composed of Al (possibly Al_2O_3), followed by Ca and Fe. This indicated that the non-silicon compounds in the matrix tend to agglomerate together in the precursor mixing process.

Spray-Dried Precursor After spray drying the precursor matrix still shows two major features, granules and clumps of smaller material. SEM micrographs and an EDS spectrum of the spray-dried NYC precursor matrix can be seen in Figure: 4.55.

When compared to the untreated NYC precursor matrix, there does not appear to be a large difference between the granules. However, the non-silicon compounds of the matrix appear not as clumps but as patches of micron scale particles. The patches of small particles were too thin for useful BSE analysis at a working distance of 8.8-mm (the working distance used in Figure: 4.55). What could be resolved by the backscatter detector did not show any differences in chemical composition. EDS analysis showed O, Na, Mg, Al, Si, K, Ca, and Fe in roughly the ratios expected for the NYC matrix.



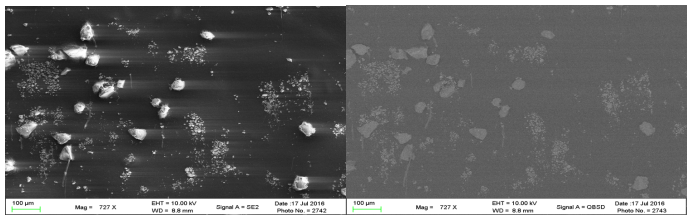
(a) NYC SE2 spray-dried **(b)** NYC BSE spray-dried



(c) NYC EDS spray-dried

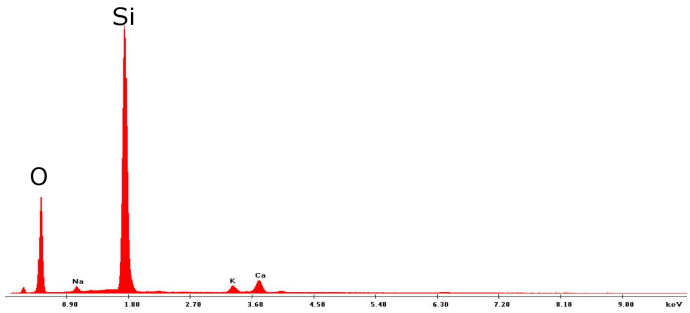
Figure 4.55: Micrographs and EDS of spray-dried surrogate particulate melt glass precursor (NYC matrix)

Figure: 4.56 shows SEM micrographs and an EDS spectrum of typical granules found in spray-dried surrogate NYC particulate melt glass precursor. The granules appear to be coated in strands of what is possibly PVA. Otherwise, their morphology and size remains unchanged. Interestingly, backscatter analysis shows no disparity in chemical composition for any constituents. The heavy coating of PVA on the precursor material could explain the lack of observed chemical differences in both



(a) NYC SE2 spray-dried granule

(b) NYC BSE spray-dried granule

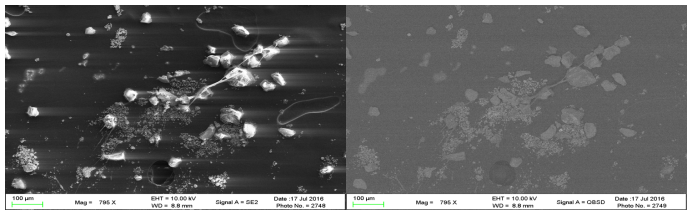


(c) NYC EDS spray-dried granule

Figure 4.56: Micrographs and EDS spectrum of typical granules found in spray-dried surrogate particulate melt glass precursor (NYC matrix)

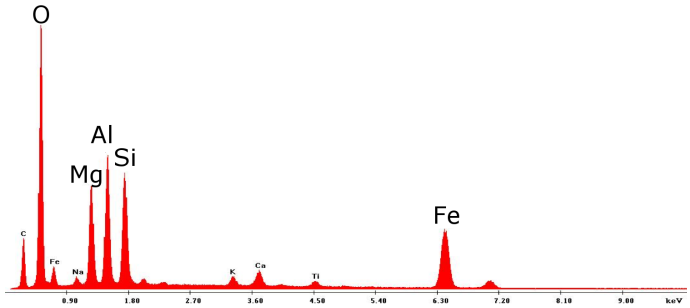
Figure: 4.56 and Figure: 4.55. EDS analysis shows high Si and O intensities, while Na, K, and Ca are also present albeit at much lower levels.

SEM micrographs and an EDS spectrum of the fine powder found in the spray-dried NYC particulate melt glass precursor can be seen in Figure: 4.57. Inspection of the powder with SEM imaging confirms that the fine powder is comprised of many small micron scale particles. Strings of PVA are easily seen in the sample. Again, BSE analysis is unable to distinguish differences in chemical composition. EDS analysis shows the presence of C, Ti, O, Na, Mg, Al, Si, K, Ca, and Fe. The presence of C is from either the carbon tape used to mount the sample, of the large quantities of PVA present. Though Ti has a large l-α intensity, inspection of the k-α intensity indicates that the majority of the peak intensity is due to the presence of O. Peak intensities for Mg, Al, and Si are all similar. Na, K, and Ca intensities are relatively small.



(a) NYC SE2 spray-dried fine powder

(b) NYC BSE spray-dried fine powder

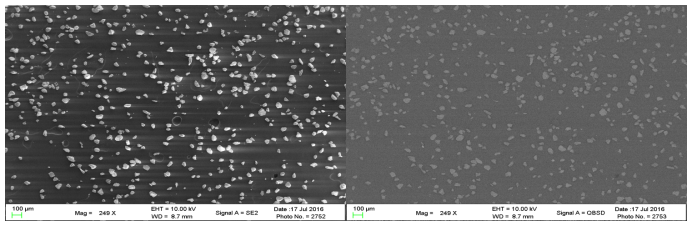


(c) NYC EDS spray-dried fine powder

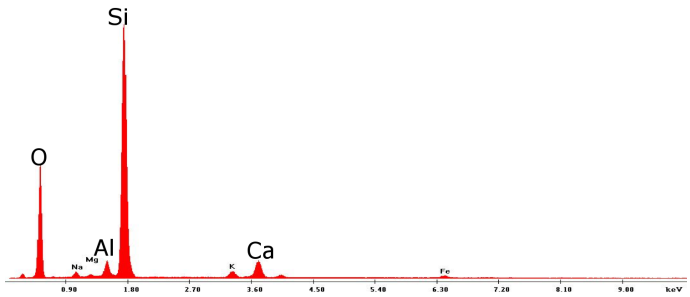
Figure 4.57: Micrographs and EDS for a typical example of the fine powder found in spray-dried surrogate particulate melt glass precursor (NYC matrix)

Heat-Treated Precursor Inspection of the heat treated NYC particulate matrix reveals a distinct lack of the fine powder present in both the untreated and the spray-dried precursors. SEM micrographs and an EDS spectrum of the heat treated NYC precursor matrix can be seen in Figure: 4.58. Granules are still present, with a maximum dimension of 100 μm, which is comparable to the dimensions found in both the NYC and STF spray-dried precursors and the heat treated STF precursor. Some granules appear to have fused together during the heat treatment. No strands of PVA are visible in the sample. It is thought that the PVA was vaporized during hear treatment. BSE analysis shows no difference in chemical composition in the figure above. EDS reveals the presence of O, Na, Mg, Al, Si, K, Ca, and Fe. The intensities of the peaks found on the EDS spectrum indicates that the vast majority of the fired NYC particulate matrix is composed of SiO_2, which is expected.

Figure: 4.59 shows SEM micrographs and an EDS spectrum of a typical fused granule found in heat-treated surrogate NYC particulate melt glass precursor.As



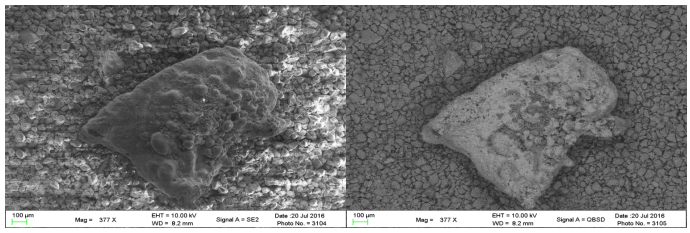
(a) NYC SE2 heat-treated **(b)** NYC BSE heat-treated



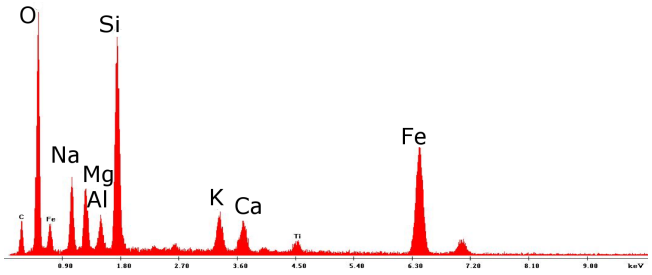
(c) NYC EDS heat-treated

Figure 4.58: Micrographs and EDS of heat-treated surrogate particulate melt glass precursor (NYC matrix)

with the STF precursor, many granules appear to have fused together to form a large globule of material. The globule in the figure is one of the larger ones found. Other than in its size, it is characteristic of a typical globule found in NYC surrogate particulate debris. The globule measures ∼1.5-mm x 1-mm. The surface suggests a two-stage formation process where first a large mass of material was completely melted in the flame of the torch. As it began to cool, smaller molten globules agglomerated onto the surface, thus forming the warty texture seen on the surface. BSE imaging shows a very chemical heterogeneous surface, with many dark streaks present in the warty region. Dark spots are frequently present in other areas on the surface. EDS analysis shows the presence of C, O, Fe, Na, Mg, Al, Si, K, Ca, and Ti. Though Si shows the highest intensity (other than O), it does not have the dominance as it does in other spectra examined. Surprisingly, the intensity of the Al peak is lower than those of the Na and Mg peaks, and on par with the K and Ca peaks. Fe shows a higher than expected intensity. The reasons for the unexpected intensity values is unknown, and no informed explanation is available at this time.

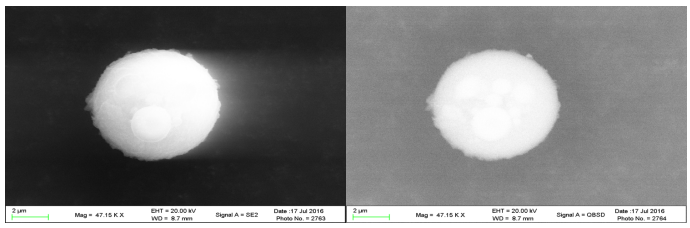


(a) NYC SE2 heat-treated fused granules **(b)** NYC BSE heat-treated fused granules

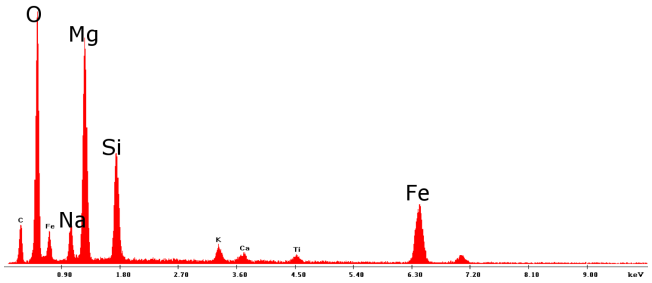


(c) NYC EDS heat-treated fused granules

Figure 4.59: Micrographs and an EDS spectrum of fused SiO_2 granules found in heat-treated surrogate particulate melt glass (NYC matrix)



(a) NYC SE2 heat-treated sphere **(b)** NYC BSE heat-treated sphere



(c) NYC EDS heat-treated sphere

Figure 4.60: Micrographs and an EDS spectrum for a spherical particle found in surrogate particulate melt glass (NYC matrix)

Small spherical particles can be seen in the fired NYC precursor, just as they were seen in the fired STF precursor. The spheres measure roughly 4 μm in diameter with smaller spheroid protrusions on the surface. As with the globules, it appears that the larger spheroid formed first, and the smaller protrusions agglomerated on the surface during cooling. The smaller protrusions appear lighter when analyzed using BSE, thus indicating a heavier chemical composition. EDS indicates the presence of C, O, Fe, Na, Mg, Si, K, Ca, and Ti. Other than O, Mg shows the highest intensity in the spectrum, followed by Si. Fe and Na also have appreciable intensities. The presence of C in the spectrum is thought to come from the carbon tape used in mounting the sample. SEM micrographs and an EDS spectrum of a spherical particle found in the heat-treated NYC particulate melt glass precursor can be seen in Figure: 4.60.

Table 4.6: Ratios of major elements with respect to oxygen for particulate bulk melt glass (NYC matrix)

Element	Heat-treated precursor	Fused granules	Particulate spheres
Si	2.19	0.89	0.43
Al	0.14	0.16	n/a
Mg	0.03	0.27	0.90
Ca	0.16	0.13	0.04
Fe	0.02	0.45	0.22
K	0.06	0.18	n/a

Table: 4.6 lists the ratios of the major elements with respect to O found in various particulate melt glass features. Analyzing the heat-treated precursor as a whole, the ratios for Si, Mg, and K were all found to increase, while the ratios for Fe and Ca were found to decrease. The Al:O ratio is roughly the same as that of the untreated precursor.

The fused granules and particulate spheres have a lower Si:O ratio than the total heat-treated precursor. The Al:O ratio is slightly higher for the fused granules, but non-existent for the particulate spheres. The ratio for Mg:O is substantially larger for

both the granules and the spheres, with the spheres showing the largest ratio. The Ca:O ratio is lower for both the granules and the spheres, with the spheres showing the lowest ratio. It is worth noting that the spheres had both the highest Mg:O ratio and the lowest Ca:O ratio. This behavior is possibly caused by the replacement of Ca with Mg (both are in the alkaline earth group and thus have similar chemical properties). The fused granules show an approximately 2000% increase in the Fe:O ratio, twice that of what is seen for the spheres. The K:O ratios are increased for the fused globules, and non-existent for the spheres.

4.2.2 Mass Spectrometry

Results from ICP-TOF-MS of surrogate particulate melt glass and its precursors is discussed. Elements analyzed are the same as those for the surrogate bulk melt glass with the exception of U, which was not used in the precursor matrices, because the laboratory in which the synthesis took place was not cleared for radiological work at the time of this study. Again, Si, P, S, and K are not analyzed due to interference effects within the mass spectrometer. All values are reported with a 2σ confidence interval.

Synthetic Trinitite Matrix

Figure: 4.61 shows a comparison of ICP-TOF-MS results for untreated, spray-dried, and heat-treated STF matrix surrogate particulate melt glass precursor. A quick glance at the graph shows that Ca is by far the most prominent element that can be detected. Concentrations of Ca vary between 322±142 ppm for the heat-treated (PSTF F) and 389±261 ppm for the untreated precursor (PSTF P). Ca levels appear at first to show a downward trend through the various synthesis processes. However, the range of error for the untreated and heat-treated samples is too large to confirm the apparent trend. Na levels are similar for the untreated and spray-dried precursor (104±45 ppm and 97±11 ppm respectively), but lower for the heat-treated samples

(63±19 ppm). Like Ca, Na shows a downward trend as the precursor goes further through the synthesis process. This similarity is not surprising due to the similar chemistry of Ca and Na.

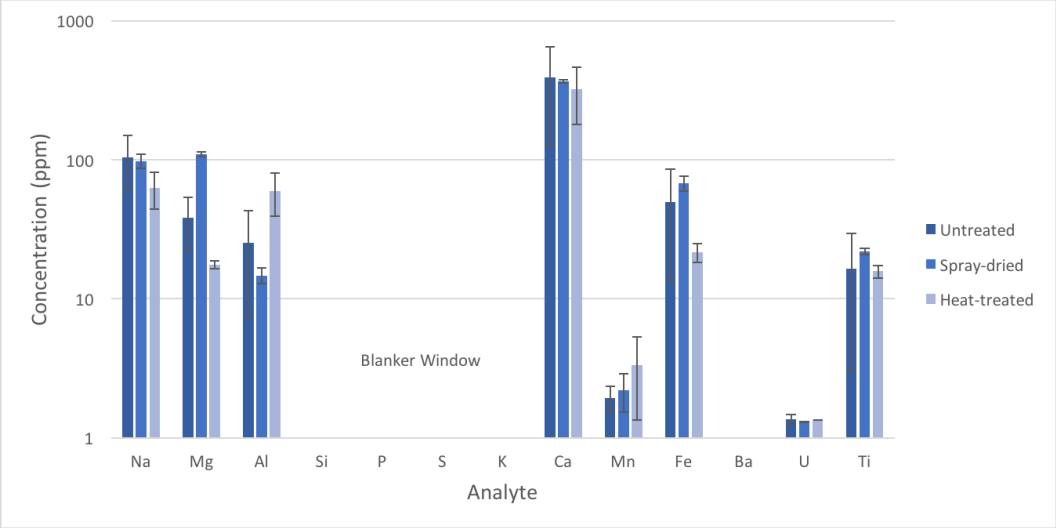


Figure 4.61: Comparison of particulate melt glass ICP-TOF-MS results for the STF matrix

Mg levels fluctuate between 38±16 ppm in the untreated samples, 109±4 ppm in the spray-dried samples, and 17±1 ppm in the heat-treated samples. The cause for the large disparity in the concentration of Mg in the spray-dried samples is unknown. Fe and Ti concentrations also follow a similar pattern as the Mg concentrations, with the spray-dried samples showing higher concentrations than either the untreated or the heat-treated samples. However, it should be noted the average concentration values for the average spray-dried samples for both Fe and Ti are within the error of the concentration measurements for their respective untreated samples. Because of this, a definitive conclusion cannot be made about the trends in concentration for these two elements.

Mn levels show a steady increase through the synthesis process, going from 1.9±0.4 ppm to 2.2±0.7 ppm between the untreated and the spray-dried runs, before ending at 3.3±2 ppm for the heat-treated samples. The concentration values for Al are perhaps the most confusing of all of the elements analyzed. The untreated samples

average a concentration of 25±18 ppm. Concentration values decrease to 14±2 ppm in the spray-dried sample before increasing again to 60±20 ppm for the heat-treated samples. The lack of trend, coupled with the sudden increase in concentration points to a systematic error as opposed to a random error. Possible sources of error could include contamination from previous dissolutions, contamination from other components in the plasma torch/ collection vessel, or even the leaching of elements from glassware in the lab.

New York City Matrix

A comparison of the concentrations of elements of interest for the untreated, spray-dried, and heat-treated NYC matrix surrogate particulate melt glass can be seen in Figure: 4.62. Ca concentrations are consistent between the untreated and spray-dried samples, measuring at 176±6 ppm and 177±10 ppm respectively. This concentration increases to 226±21 ppm for the heat-treated samples. The increase in Ca concentration for the heat-treated samples is inconsistent with what was observed in the STF matrix. Concentrations of Na are consistent across the three stages of synthesis. The untreated samples average a Na concentration of 103±10 ppm, the spray-dried samples average 90±14 ppm, and the heat-treated samples average 101±10 ppm. All measurements are within the error ranges of each other, and seem to point to a consistent level of Na throughout the various synthesis processes.

Like the concentrations of Ca, the concentrations of Mg remain approximately the same for the untreated and spray-dried samples, with respective values of 100±12 ppm and 116±26 ppm. However, there is a large decrease in concentration of Mg measured for the heat-treated samples (17±1 ppm). This decrease is similar to the decrease seen from the spray-dried to the heat treated samples for the STF matrix, and may be due to a large amount of Mg being fractionated within the torch during heat-treatment. Al concentrations follow the same pattern as the one seen for the STF matrix. Untreated samples average an Al concentration of 26±3 ppm, spray-dried samples have an average concentration of 10±2 ppm, and heat-treated samples

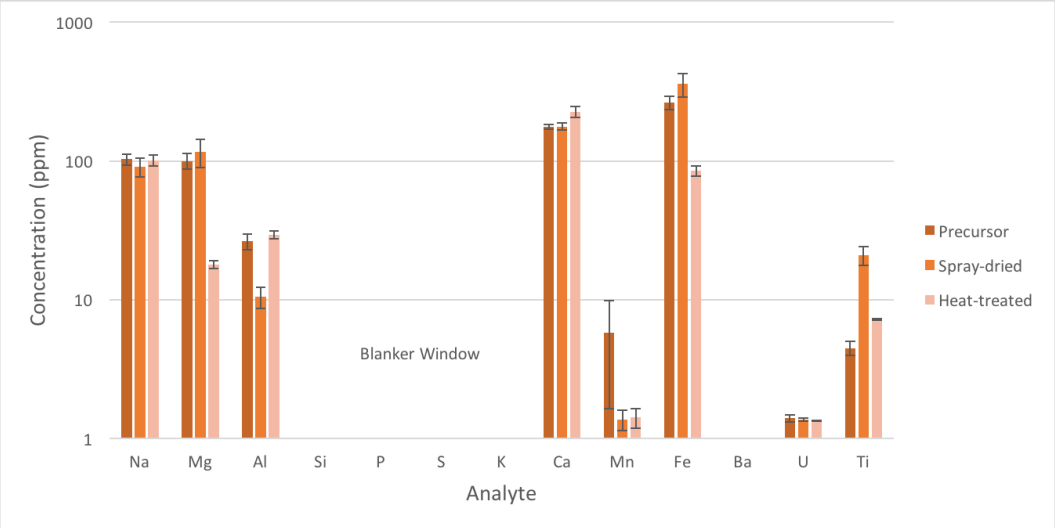


Figure 4.62: Comparison of particulate melt glass ICP-TOF-MS results for the NYC matrix

have an average Al concentration of 29±2 ppm. The low error of these measurements indicates that the differences in the concentration of Al comes from systematic, as opposed to random error.

Fe concentration patterns for the NYC matrix mimic those in the STF matrix with the spray-dried samples having the highest average concentration (358±69 ppm), and the heat-treated samples having the lowest average concentration 85±7 ppm. The untreated samples have an average concentration of 263±27 ppm. Ti concentrations follow the same pattern as Fe. Untreated samples have an average concentration of 5±1 ppm, the spray dried samples have an average concentration of 21±3 ppm, and the heat-treated samples have an average concentration of 7±1 ppm. In all, Fe concentrations are the highest of all elements examined, which is to be expected given the composition of the matrix. Na, Al, Ca, and Ti concentrations are roughly the same between synthesis steps, while the concentrations of Mg and Fe change drastically.

4.2.3 X-Ray Diffraction

Crystallinity of the three surrogate particulte melt glass precursor types for each of the two matrices is examined via X-Ray Diffraction (XRD). As with the surrogate bulk melt glass analysis, measured diffraction patterns were compared against a library of known crystalline phases and those with the best matches were chosen. Once again, the total number of patterns was limited to those phases containing at least one of the elements present in the matrix, and all spectra show have had their background subtracted.

Synthetic Trinitite Matrix

Figure: 4.63 shows XRD patterns for untreated, spray-dried, and heat treated particulate surrogate melt glass composed of the STF matrix. When viewed together, the three spectra show how the various techniques used to synthesize particulate melt glass can affect the crystalline structure of the matrix. The untreated STF matrix gives off a strong signal for Al_2O_3 and CaMg(IV). Additionally, SiO_2 has an appreciable intensity in the spectrum. A significantly sized amorphous region is present in the spectrum, indicating that not all of constituent oxides are purely crystalline in nature.

Spray drying of the matrix results in the disappearance of most signals from the spectrum. However, Al_2O_3 still shows the highest intensity in the spectrum. Noteworthily, NaOH appears in the spectrum. This is caused by the addition of NaOH to the slurry during spray drying. As discussed in Chapter 3, NaOH was added to the slurry as the primary source of Na in the matrix.

The heat-treated precursor again shows Al_2O_3 as having the highest intensity. The only other identifiable phase in the heat-treated precursor is calcite. The implications of this data are that the SiO_2 present in the matrix has a very low degree of crystallinity. Additionally, very few compounds are able to survive the extreme conditions of the plasma torch and retain their crystalline nature. For these

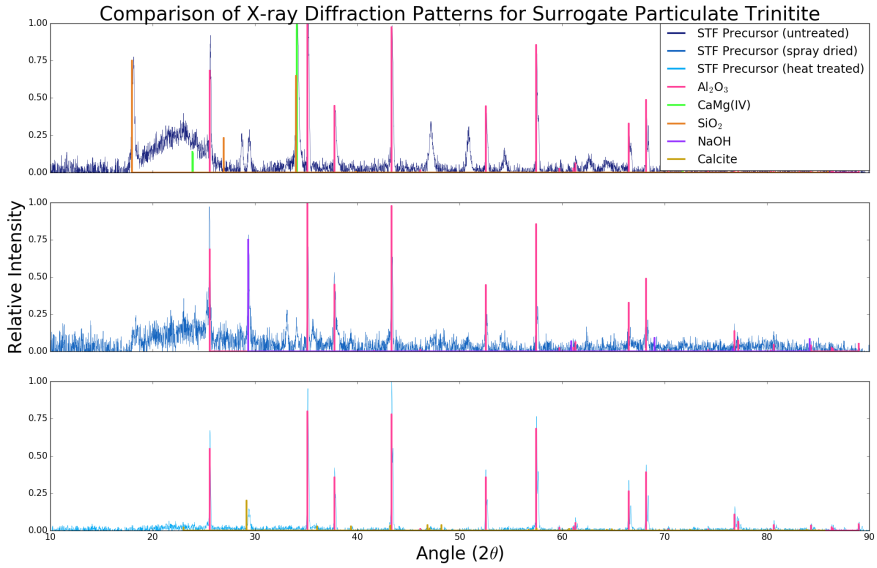


Figure 4.63: XRD patterns for untreated, spray-dried, and heat treated particulate surrogate melt glass (STF matrix)

reasons, it is possible to conclude that surrogate particulate melt glass of the STF matrix will be extremely amorphous in nature.

New York City Matrix

XRD patterns for untreated, spray-dried, and heat treated particulate surrogate melt glass composed of the NYC matrix can be seen in Figure: 4.64. The untreated matrix shows a large amorphous hump, roughly half of the relative intensity of the spectrum. SiO_2, Al_2O_3, and Fe_2O_3 are the major crystalline phases identified. The presence of these three phases is not expected, as they are three of the most prominent compounds present in the NYC precursor matrix.

As with the spray-dried STF precursor, the spray-dried NYC precursor shows a lack of SiO_2. Additionally, Fe_2O_3 is the dominant phase in the spectrum as opposed to Al_2O_3, which was the dominant phase in the spray-dried STF matrix. The intensity of the amorphous hump is lower than the intensity of the hump in the untreated precursor. This phenomenon was also observed with the STF matrix.

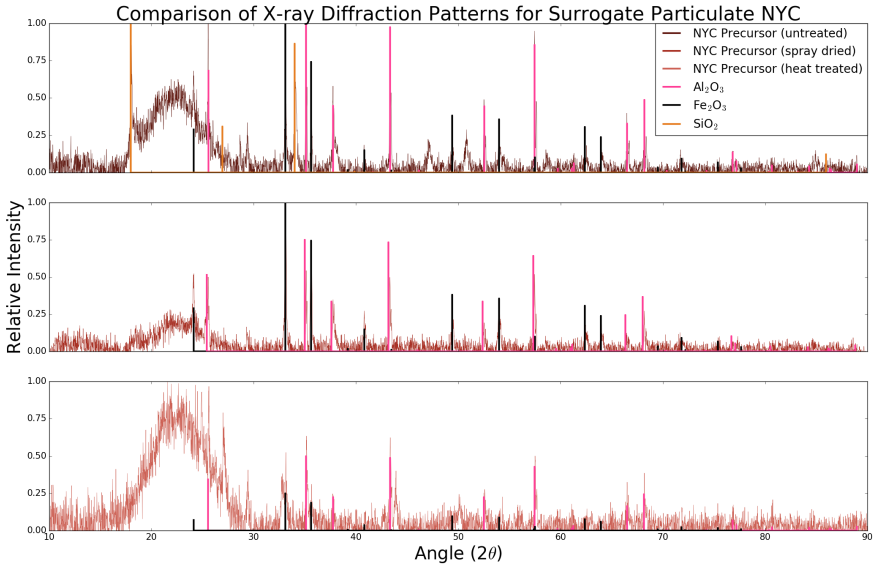


Figure 4.64: XRD patterns for untreated, spray-dried, and heat treated particulate surrogate melt glass (NYC matrix)

The dominant feature of the heat-treated spectrum is the amorphous hump. Al_2O_3 and Fe_2O_3 are the only two crystalline phases identified in the heat-treated matrix. Again, it appears that the compounds in the matrix are unable to stand up to the extreme conditions found in the plasma torch. For these reasons, it can be concluded that surrogate NYC matrix particulate melt glass will tend to be amorphous in nature.

Comparison of Matrices

A comparison of surrogate particulate melt glass XRD spectra for the STF and NYC matrices can be seen in Figure: 4.65. Both patterns reveal the presence of Al_2O_3 as a major crystalline phase. As discussed, silica is not present in either matrix, and with the exception of Fe_2O_3 in the NYC matrix and calcite in the STF matrix alumina is the only crystalline phase that is present in both matrices. The high melting point of alumina (~2100°C) allows it to better withstand the intense conditions of the plasma torch during heat treatment, and therefore retain its crystalline structure. Interpreting the XRD data, it is clear that Al_2O_3 is the only crystalline phase that

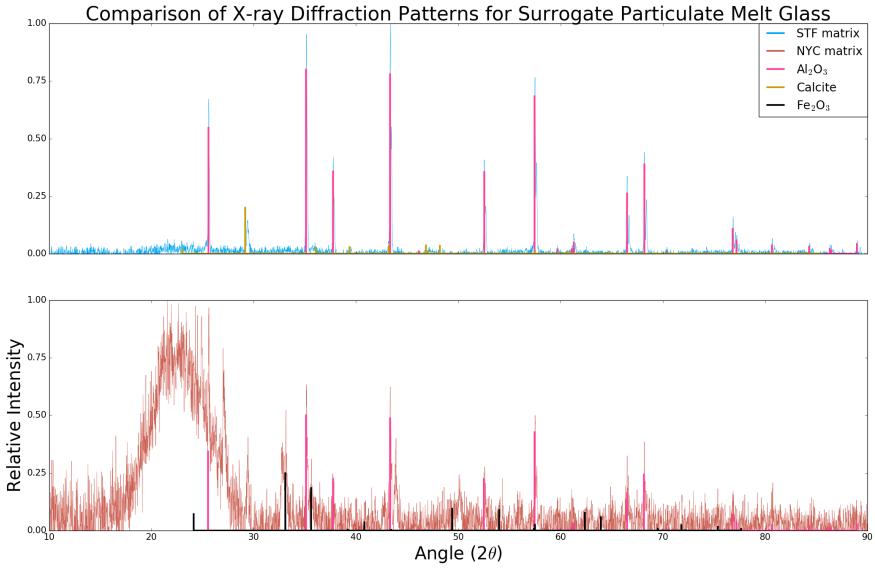


Figure 4.65: Comparison of XRD results for the STF and NYC matrices

can be reliably predicted to be present when generating surrogate particulate melt glass using the methods and materials outlined in this dissertation.

4.3 Radiological Modeling

Modeled activity levels over time for a U-fueled and a Pu-Fueld notional improvised nuclear device (IND) are examined for each of the three matrices (STF, NYC, and HOU). Total activity contribution by mass number is examined over time for the two notional INDs examined. Total activity over time for all models are compared against one another. Contribution to total activity by radionuclides typically analyzed in historical nuclear melt glass samples is examined. It should be noted that because only the historically analyzed nuclides are discussed, this is not a comprehensive list of all radioactive species present.

Radionuclides are grouped into five categories: 1) alpha-emitters, beta-emitters found near ground-zero, beta-emitters found away from ground-zero, gamma-emitters found near ground zero, and gamma-emitters found away from ground-zero. Nuclides

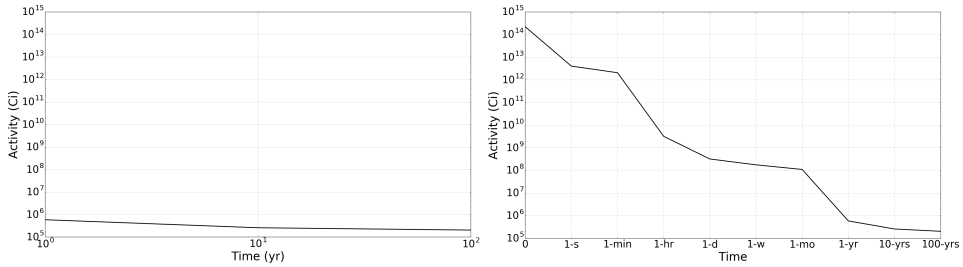
that ate beta-gamma emitters are defined as beta-emitters for the purposes of this study. The rationale for grouping the radionuclides in this ways is that the radionuclides found away from ground zero will tend to be found in higher concentrations in particulate melt glass while the radionuclides found near ground-zero will tend to found in higher concentrations in the bulk nuclear melt glass. The radionuclides are examined for each of the six models.

4.3.1 U-Fueled IND

Activity contribution by mass number (A) over time for a modeled notional U-fueled IND detonation can be seen in Figure: B.1. Immediately after detonation, lighter activation products (nuclides with a mass number between 20 and 55) are the largest generators of activity by several orders of magnitude. However, within several seconds the activity contribution from these nuclides becomes roughly equivalent to the contribution from the fission products (nuclides with mass numbers between 70 and 170). After a day, the lighter activation products and the fission products both contribute similar levels of activity, and decay on roughly the same time scale as a whole. One month after detonation, activity levels have dropped nearly three orders of magnitude for these two groups. One year after the event, the two groups have activity levels that are 10^8 times lower than they originally were. After 100-yrs, only a few nuclides contribute to the residual radiation, with most only contributing on the order of tens of mCi.

The activity contribution from the heavier radionuclides (mass numbers between 205 and 250) is limited to only the unfissioned fuel and its contaminants in the first few hours after detonation. Unlike the lighter activation products and fission products, some of these nuclides show an increase in inventory over time. Nuclides with mass numbers between 205 and 230 start to grow in immediately after detonation, and have a visible presence on the graph after only one day. Over time, the inventories of nuclides with mass numbers between 205 and 230 continue to increase, while those

with mass numbers between 230 and 250 decrease. Because of the long half-lives of many of the nuclides in these ranges, these changes are not immediately apparent, and it is not until 100-yrs post event that the activity levels of the two groups are even similar.



(a) Logarithmic time scale **(b)** Custom time scale

Figure 4.66: Total modeled activity over time generated by a notional U-fueled IND in a STF matrix

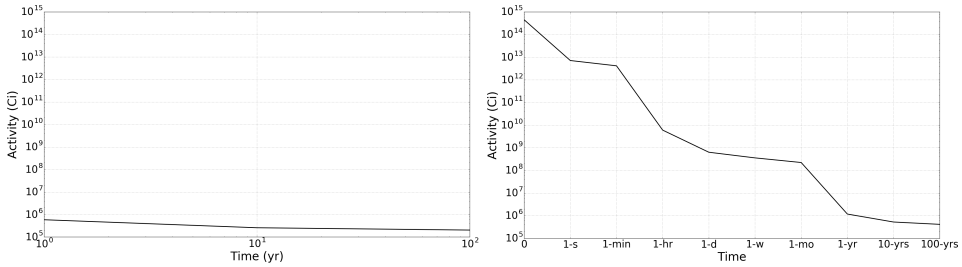
The total activity over time due to the U-fueled IND can be seen in Figure: 4.66. Within a day after the event, the total activity drops by six orders of magnitude, activity levels continue to fall in an exponential manner until the end of the time frame examined in the model. After 100-yrs, activity levels drop by a factor of one-billion. This response is expected, and fits the natural behavior of radionuclides.

4.3.2 Pu-Fueled IND

Figure: B.2 shows the activity contribution by mass number over time for a modeled notional Pu-fueled IND detonation. Like what is seen in the model for the U-fueled IND, the lighter activation products contribute the majority of the activity in the first few seconds following detonation of the IND. In the ensuing weeks and months following the event, the light activation products and the fission products follow the same pattern as they did for the U-fueled IND, eventually reaching activity levels one-billion times less than those present immediately after detonation.

Initially, the activity contribution from the heavier radionuclides is only constrained to those with mass numbers between 230 and 250. Again, nuclides with

mass numbers between 205 and 230 start to grow in immediately after detonation. As with the U-fueled IND, nuclides with mass numbers between 205 and 230 increase with time, while nuclides with mass numbers between 230 and 250 decrease. The activity contributions of two groups of heavy nuclides do not ever get as close to one another as they did with the U-fueled IND. The closest that the two groups gets to one another is a factor of almost ten-billion after 100-yrs has passed. The reason for the higher activity of the nuclides with mass number between 230 and 250 is that they tend to have shorter half-lives than the nuclides in the same mass range generated by the U-fueled IND.



(a) Logarithmic time scale **(b)** Custom time scale

Figure 4.67: Total modeled activity over time generated by a notional Pu-fueled IND

The total activity over time due to the Pu-fueled IND can be seen in Figure: 4.67. Total activity drops by six orders of magnitude in the first day fallowing the event. Again, activity levels fall in an exponential manner until they reach a magnitude of hundreds of thousands of Ci. Again, this response is expected, and fits the behavior of the radionuclides examined. Activity levels for the Pu-fueled IND are almost twice of that of the U-fueled IND.

4.3.3 Comparison of Activity Levels Between Matrices

A comparison of total activity levels over time for all of the models generated can be seen below in Figure: 4.68. All six models show the same general behavior over time. The U-fueled IND models begin to diverge approximately one day post-event.

Though the NYC matrix shows the highest activity for a brief period of time around the one-year mark, the STF matrix shows the highest activity long-term, followed by the NYC matrix and finally the HOU matrix. The activity levels shown for the U-fueled IND models tend to be lower than those for the Pu-fueled models. The exception to this observation is the STF matrix, which has a higher activity than the Pu-fueled HOU matrix after approximately ten-years post-detonation.

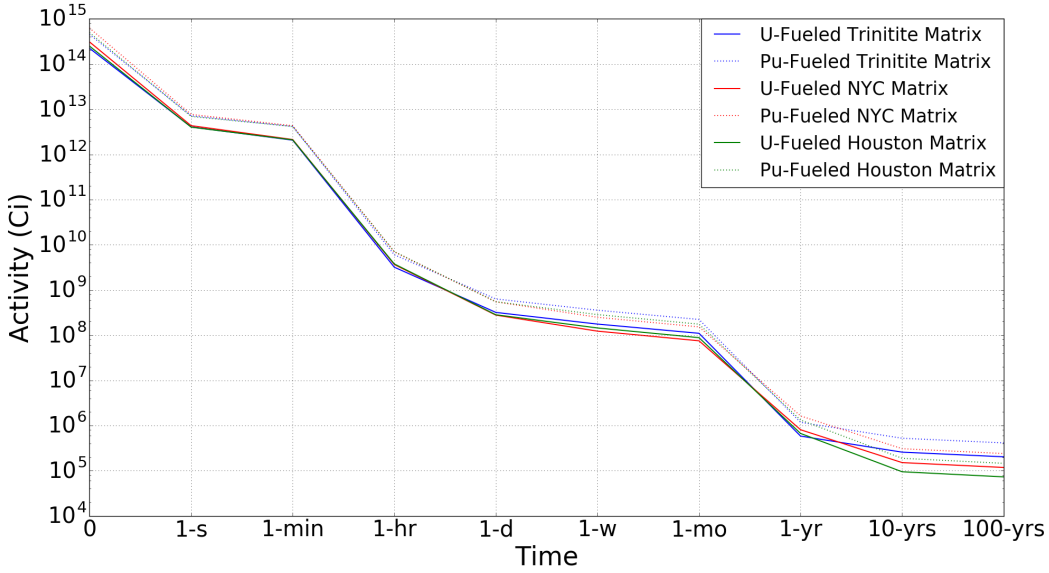


Figure 4.68: Comparison of total activity over time for all radiological models

The three models utilizing the Pu-fueled IND show approximately the same activity until one day post event. At this point the activity levels begin to diverge, with the STF matrix showing the highest activity followed by the HOU and NYC matrices. One-year post detonation, the NYC matrix shows the highest activity, but by the ten-year mark the STF matrix again shows the highest activity. The HOU matrix shows the lowest levels of activity between the three at this point, lower than those seen in the U-fueled STF model.

As expected, INDs fueled with the same fissile material will have the same general trends in activity post-detonation. Pu-fueled devices have higher levels of activity than their U-fueled counterparts. This is again due to the shorter half-lives of the

heavy elements that are left post-fission. If the time scale of the models were extended to hundreds of thousands of years, it is very possible that the activity levels of the U-fueled devices would overtake those of the Pu-fueled devices. From the models, it appears that activation products play a large role in total activity over time, as evidenced by the differences in the activity levels of the three matrices. The STF matrix shows the highest levels of activity followed by the NYC matrix, with the HOU matrix showing the lowest levels of activity. This pattern is the same, regardless of the fissionable material in the IND. The effect of historically examined radionuclides on the total activity of each of the six models is examined in further detail in the sections below.

4.3.4 U-Fueled IND in the STF matrix

The activity over time of historically examined alpha-emitting radionuclides found in nuclear melt glass (both bulk and particulate) from an area similar to that modeled by the STF matrix can be seen in Figure: 4.69. The nuclear melt glass is assumed to be created by the detonation of a notional U-fueled improvised nuclear device (IND). Unfissioned ^{235}U is the largest contributor to radioactivity from the moment of detonation, through the entire 100 years modeled after the event. The second largest contributor to total alpha-activity is ^{239}Pu, which quickly grows in, reaching equilibrium approximately two week after the event. Other U species present (^{233}U, ^{234}U, ^{236}U, and ^{238}U) remain in equilibrium once the fission-chain reaction of the IND has completed. Both ^{241}Am and ^{229}Th have substantial ingrowth but fail to majorly contribute to the total activity. ^{238}Pu shows steady growth before peaking at approximately two weeks post-event. Alpha-emitting radionuclides are expected to contribute around 100-mCi of activity to the overall inventory of a U-fueled IND device well past 100 years post-detonation. For forensic purposes, these nuclides can be examined at any time as long as they are properly separated and prepared for alpha spectrometry.

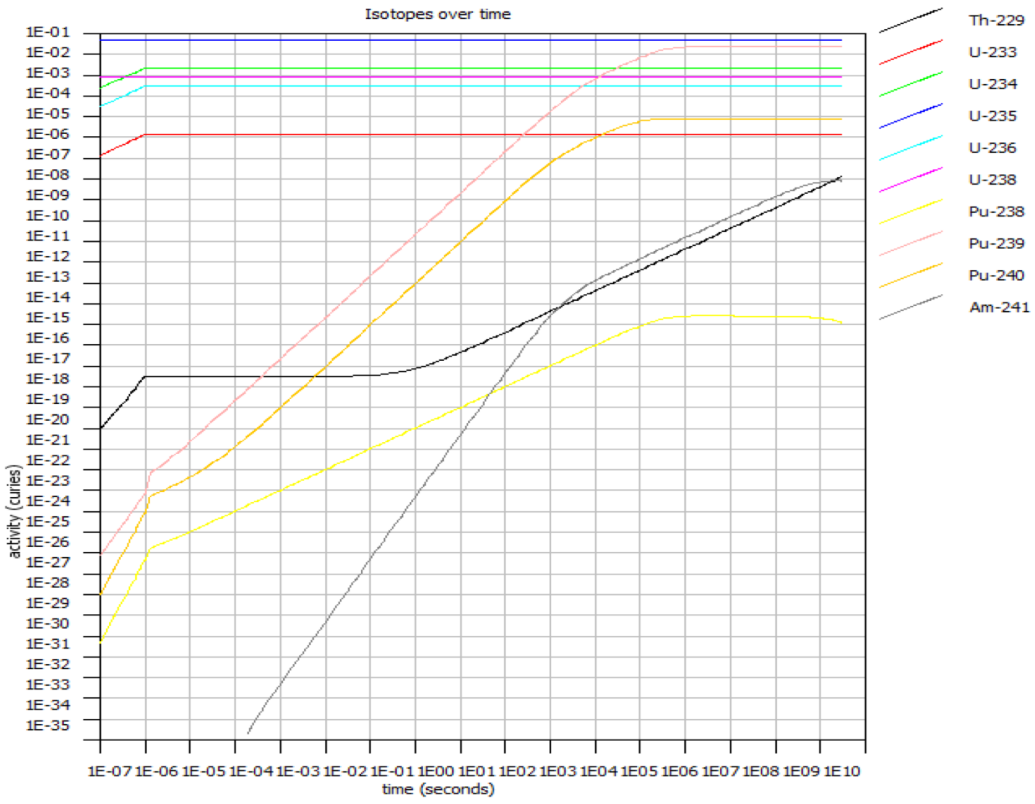


Figure 4.69: Activity of α-emitting radionuclides for a notional U-fueled IND in an STF matrix

Figure: 4.70 shows the activity contributions over time for the beta-emitting radionuclides expected to be found near ground-zero in bulk nuclear melt glass formed from a U-fueled IND in a an area similar to that modeled by the STF matrix. The first few hours following an event, ^{97}Zr is expected to contribute several MCi of activity before decaying away, briefly leaving ^{140}Ba as the primary source of activity. Approximately two months post-detonation, both ^{140}Ba and ^{147}Nd activity contributions decrease enough to allow for $^{Y}91$ and ^{89}Sr to become the major contributors. At this point, ^{144}Ce is the major contributor to activity for these beta-emitting radionuclides and remains so for several years. Once enough ^{144}Ce decays, ^{90}Sr becomes the major contributor to activity for several decades. Though it shows a substantial ingrowth ^{241}Pu never reaches a point where it contributes an appreciable amount of activity as its activity always at least 7 orders of magnitude less than the

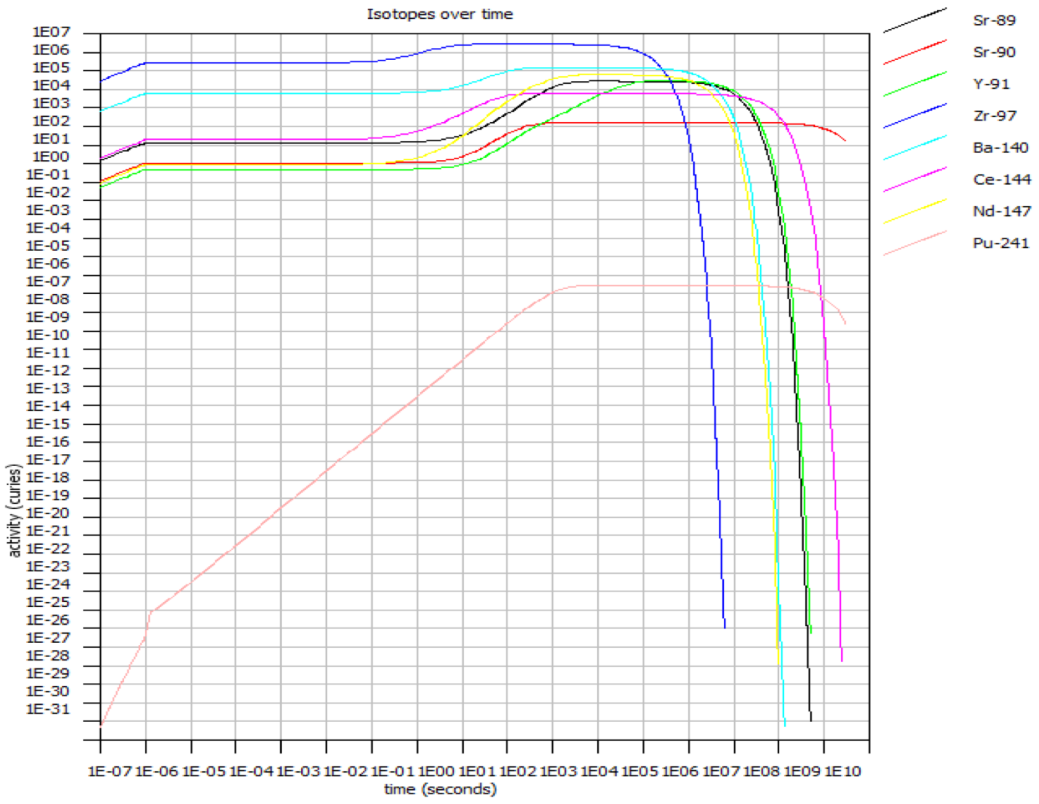


Figure 4.70: Activity of β-emitting radionuclides for a notional U-fueled IND in an STF matrix expected to be found near ground-zero

next-lowest radionuclide. Beta-emitters found near ground-zero (with the exception of ^{90}Sr) should be analyzed within the first few days to months following a detonation due to their relatively short half-lives. Because of interference from other high-activity species, radiochemical separation is necessary in order to obtain reliable results.

Activity contributions over time for the beta-emitting radionuclides expected to be found in areas away from ground zero and formed from a U-fueled IND in a an area similar to that modeled by the STF matrix can be seen in Figure: 4.71. Early on, these nuclides contribute substantially more to the overall activity than the beta-emitters found near ground zero. In the first week post-event ^{24}Na is the highest contributor, with several hundred MCi of activity. As the inventory of ^{24}Na declines, ^{103}Ru dominates the total activity contribution with several kCi of activity. After approximately eight to nine months, ^{106}Ru becomes the largest contributor to

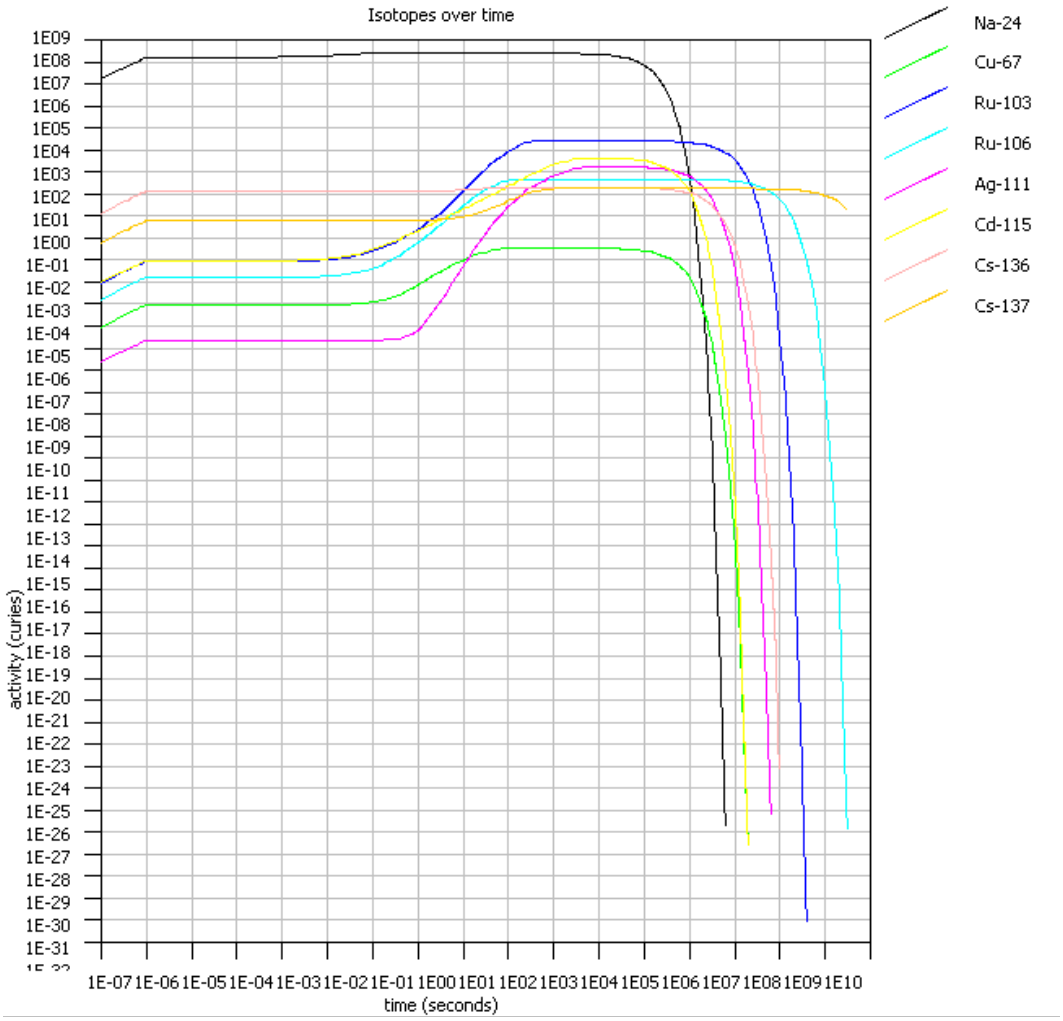


Figure 4.71: Activity of β-emitting radionuclides for a notional U-fueled IND in an STF matrix that are expected to be found away from ground-zero

activity before being overtaken by ^{137}Cs which contributes roughly 100-Ci (and is the nuclide which contributes the largest activity of the beta-emitters expected to be found away from the vicintiy of the blast), dropping off at the outer bound of the model (100 years). ^{115}Cd and ^{111}Ag, while at their maximums several hundred Ci of activity, are both dwarfed by other radionuclides present. ^{136} Cs levels remain stable for two weeks post-detonation before sharply decaying away. Though ^{67}Cu emits several hundred mCi of beta radiation, its contribution to activity can be considered negligible when compared to the other nuclides present. For forensic

purposes, it would optimal to examine debris any time between a few days, to a few months post-detonation. However, the orders of magnitude between activity levels of the radionuclides examined necessitates that radiochemical separations be performed before analysis. Additionally, after several months, it may be necessary to use mass-spectrometry to determine the presence of some of the short-lived radionuclides.

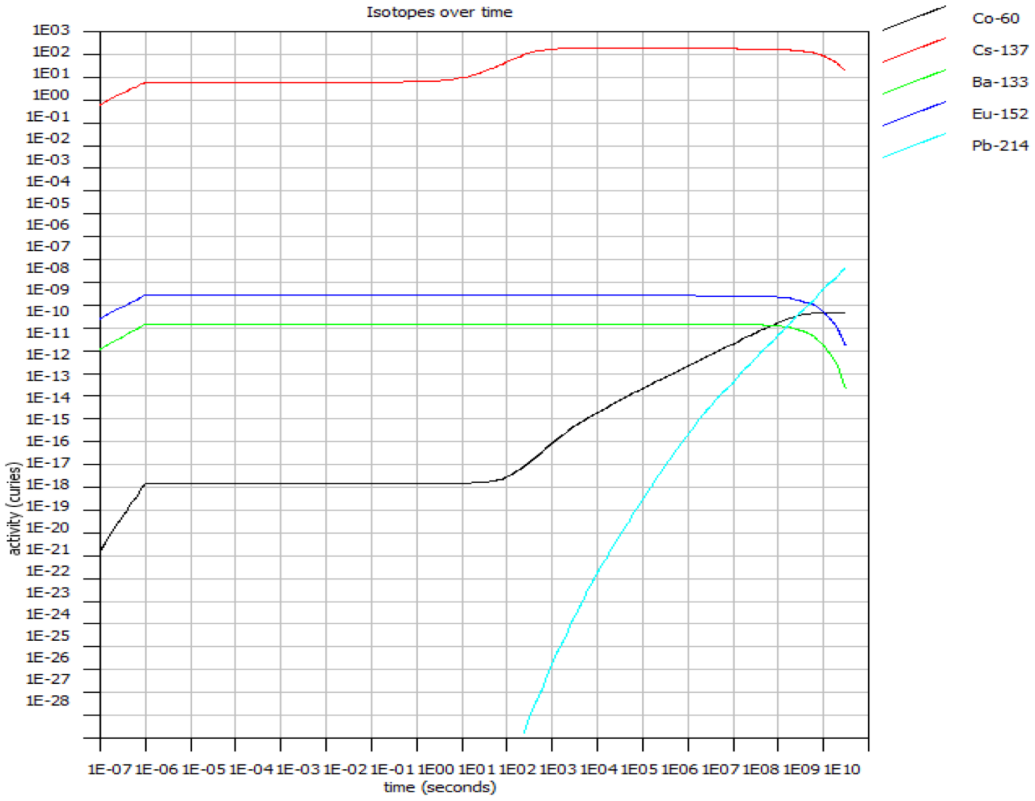


Figure 4.72: Activity of γ-emitting radionuclides expected to be found at ground-zero after the detonation on a notional U-fueled IND in an STF matrix

Activity contributions over time for the gamma-emitting radionuclides expected to be found near ground-zero in bulk nuclear melt glass formed from a U-fueled IND in a an area similar to that modeled by the STF matrix can be seen in Figure: 4.72. These gamma-emitting nuclides emit hundreds of Ci of activity at their maximum. The major contributor to this value is ^{137}Cs. The activity contribution from ^{137}Cs starts at roughly 10-Ci and reaches its maximum value roughly fifteen minutes post-detonation. ^{152}Eu and ^{133}Ba activity levels are in equilibrium until they both begin to

drop off several years post-detonation. Throughout this time, ^{152}Eu activity remains approximately 1.5 orders of magnitude higher than ^{133}Ba activity. A few minutes post-event, the activity contribution from ^{60}Co begins increasing until it reaches equilibrium after approximately 150-years. ^{214}Pb begins growing in around 3-hours after the detonation, and appears to continue increasing well after the times modeled have passed. Though they may not be the largest contributors to activity, the gamma-emitting nuclides expected to be found near ground zero that have been examined remain present for extended periods of time, making them all ideal candidates to examine for forensic purposes. Additionally, the long half-lives of these nuclides make them of particular interest for health-physics and species migration studies.

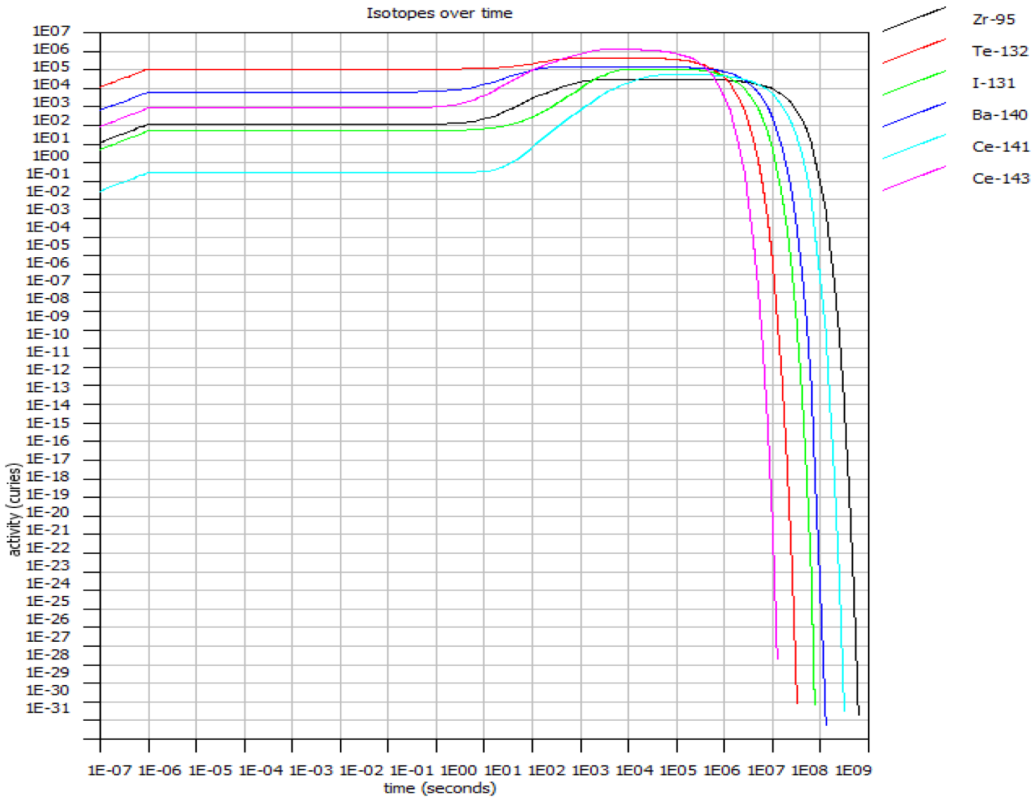


Figure 4.73: Activity of γ-emitting radionuclides for a notional U-fueled IND in an STF matrix expected to be found in a location away from ground-zero

Figure: 4.73 shows the activity contributions over time for the gamma-emitting radionuclides expected to be found away from ground-zero in particulate nuclear

melt glass formed from a U-fueled IND in a an area similar to that modeled by the STF matrix. Though they contribute several MCi of activity to the total activity following a detonation, these gamma-emitting nuclides all tend to substantially decay away between a few days and months post-event. In the first few minutes, ^{132}Te is the most prominent nuclide before being overtaken by the ingrowth of ^{143}Ce which quickly falls out of equilibrium. ^{95}Zr, ^{140}Ba and ^{141}Ce are the longest living nuclides of those examined, and thus are the largest contributors to activity in the long term before their decay (several months to approximately five years post-event). Interestingly, all of these gamma-emitting nuclides have significant ingrowth before they decay. If one were to want to try to find these nuclides easily, the optimal time for analysis would be between several hours and several weeks after detonation of the notional IND. Air sampling would be ideal for many of these nuclides in the hours after the event. Any analysis after several weeks would best be performed using mass-spectrometry.

4.3.5 Pu-Fueled IND in the STF matrix

Figure: 4.74 shows the activity contributions over time for alpha-emitting radionuclides that are expected to be found in both bulk and particulate nuclear melt glass formed from a Pu-fueled IND in an area similar to that modeled with the STF matrix. The largest contributor to activity is the ^{239}Pu that was not fissioned during detonation, followed closely by the ^{240}Pu that was present as a contaminant. ^{238}Pu is generated during detonation, and remains the third largest contributor to activity until the ingrowth of ^{241}Am reaches equilibrium at t=1E10 seconds ($\sim$100 years). The other alpha-emitting nuclides present do not contribute greatly to the total activity. ^{233}U, ^{234}U, ^{235}U, and ^{229}Th inventories begin growing around t=1 second post-detonation and continue increasing, with only ^{233}U reaching a brief equilibrium between t=3 months and t=3 years. Overall, the greatest alpha-emitting contributors to the total activity inventory are expected to be the ^{239}Pu and ^{240}Pu that remained

unfissioned after detonation. These radionuclides would possibly be found in nuclear melt glass samples at any reasonable time post-event.

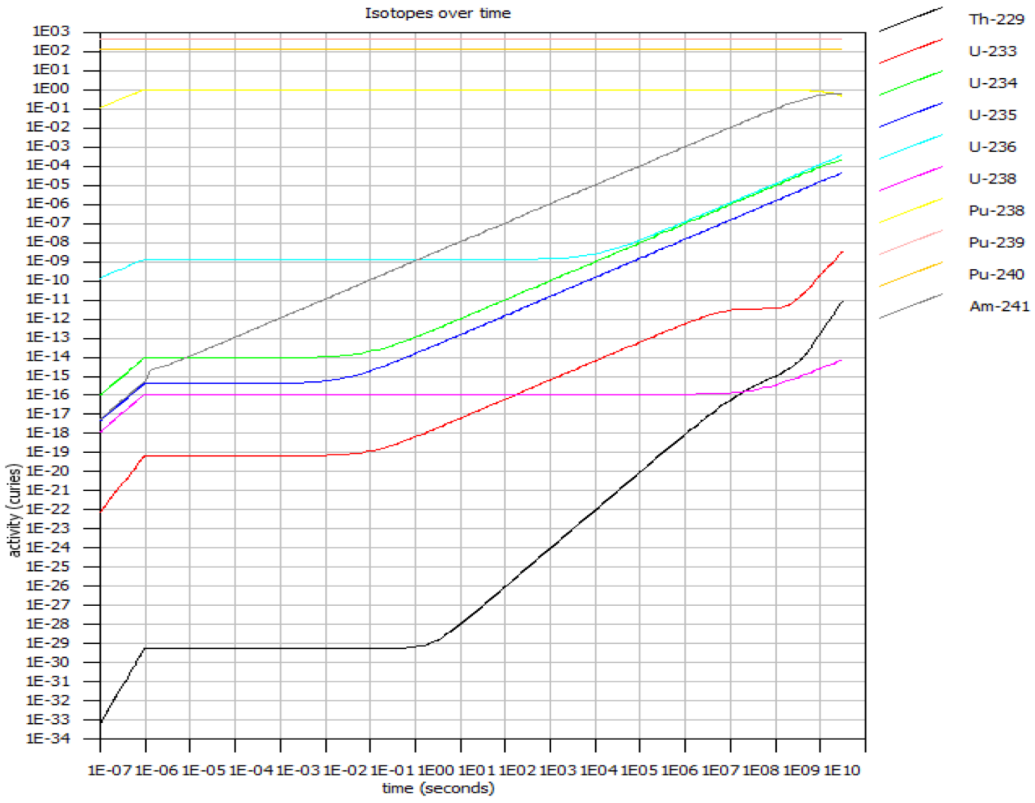


Figure 4.74: Activity of α-emitting radionuclides for a notional Pu-fueled IND in an STF matrix

Activity contributions over time for the beta-emitting radionuclides expected to be found near ground-zero in bulk nuclear melt glass formed from a Pu-fueled IND in a an area similar to that modeled by the STF matrix can be seen in Figure: 4.75. Initially, the beta-emitting nuclides contribute to the overall activity much more than the alpha emitters. For the first three months post-event, ^{97}Zr is the largest contributor to total activity (on the order of MCi) followed by ^{140}Ba, which is briefly the largest contributor from 3 months post event until 1.5 years post event (several hundred kCi). ^{147}Nd activity closely follows that of ^{140}Ba, contributing tens of kCi to the total activity. ^{241}Pu and ^{90}Sr closely follow each other in terms of contribution to total activity. They become the largest contributors to activity approximately 100

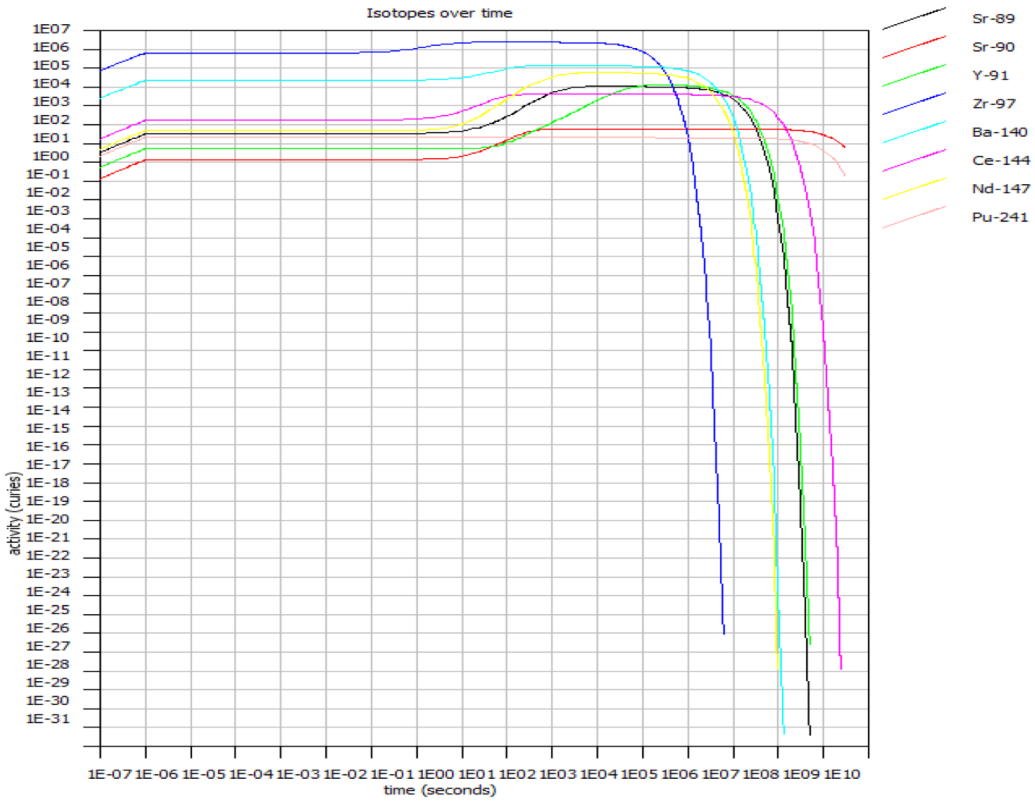


Figure 4.75: Activity of β-emitting radionuclides for a notional Pu-fueled IND in an STF matrix expected to be found at ground-zero

years post detonation. ^{91}Y, ^{89}Sr, ^{144}Ce, ^{147}Nd all contribute the same amount of activity, within 2 orders of magnitude once a few hours have passed. Though these beta-emitting nuclides contribute more to total activity, they do not remain in the environment as long as the alpha-emitting radionuclides because of their shorter half-lives. The best time to examine bulk nuclear melt glass samples for the presence of these radionuclides would be between the first few days and a year post-detonation.

Figure: 4.76 shows the activity contributions over time for the beta-emitting radionuclides expected to be found in particular nuclear melt glass formed from a Pu-fueled IND in a an area similar to that modeled by the STF matrix, and found in areas away from ground-zero. The total activity contribution for the beta-emitting nuclides found in expected to be found in particulate melt glass is almost six orders of magnitude less than the contribution from the beta-emitting radionuclides

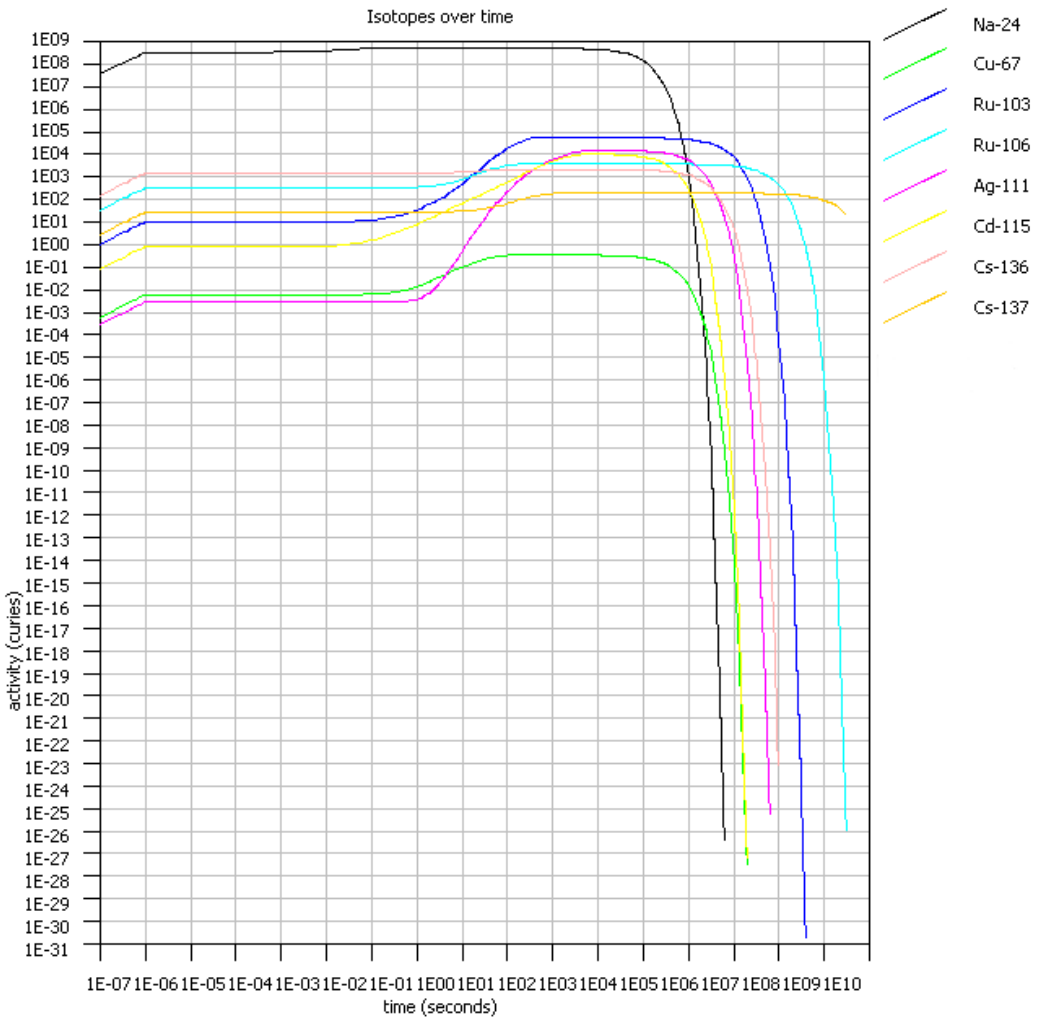


Figure 4.76: Activity of β-emitting radionuclides for a notional Pu-fueled IND in an STF matrix expected to be found in areas away from ground-zero

expected to be found near ground-zero. The activation product ^{24}Na is the largest contributor for the first 10 days. At that point ^{103}Ru, ^{106}Ru, and ^{137}Cs all contribute approximately the same amount to the total activity inventory before ^{103}Ru inventory falls out of equilibrium at 3 months post-event, and ^{106}Ru begins to decay away shortly afterwards. ^{111}Ag shows a sharp increase in inventory several seconds after the event, only to decay sharply after a few weeks. As seen in the graph, these beta-emitting nuclides to not contribute much activity when compared to their counterparts found near ground-zero. Additionally, they do not exist as long as other beta-emitting

radionuclides that have been identified in the historical literature. Because of this, the optimal time for collection and analysis would be from a few days to a few months post-event.

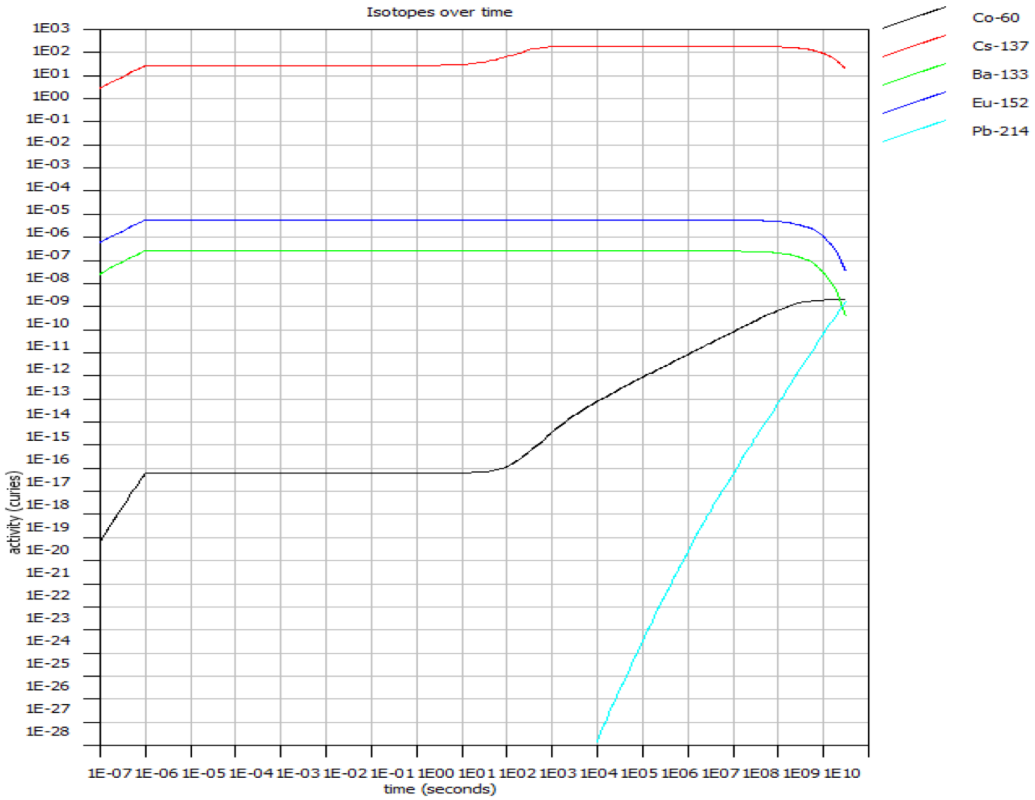


Figure 4.77: Activity of γ-emitting radionuclides for a notional Pu-fueled IND in an STF matrix expected to be found near ground-zero

Activity contributions over time for gamma-emitting radionuclides expected to be found near ground-zero in bulk nuclear melt glass formed from a Pu-fueled IND in a an area similar to that modeled by the STF matrix can be seen in Figure: 4.77. These nuclides do not contribute as much activity as the beta-emitting nuclides expected to be found near ground-zero, but do contribute more than the beta-emitting nuclides expected to be found away from ground zero. The largest contributor to activity is ^{137}Cs, which remains in equilibrium from roughly 20 minutes post-detonation, until approximately 3 years post-detonation. The radionuclide with the second highest activity is ^{152}Eu, which has a gamma activity roughly seven orders of magnitude less

than ^{137}Cs. Other contributors to gamma activity near ground-zero are ^{133}Ba, ^{60}Co, and ^{214}Pb. These radio nuclides do not contribute highly to the radioactivity present, and their signatures would possibly be lost in the noise of a gamma spectrum is they were not properly separated. The nuclides examined in Figure: 4.77 are all present for a significant period of time post-event, and none of them appear to fall out of equilibrium until a minimum of several years post-event. For this reason, the optimal time to attempt to identify these nuclides would be any time a few weeks/months post event. The rationale for waiting is to allow for the decay of any high-activity fission/activation products.

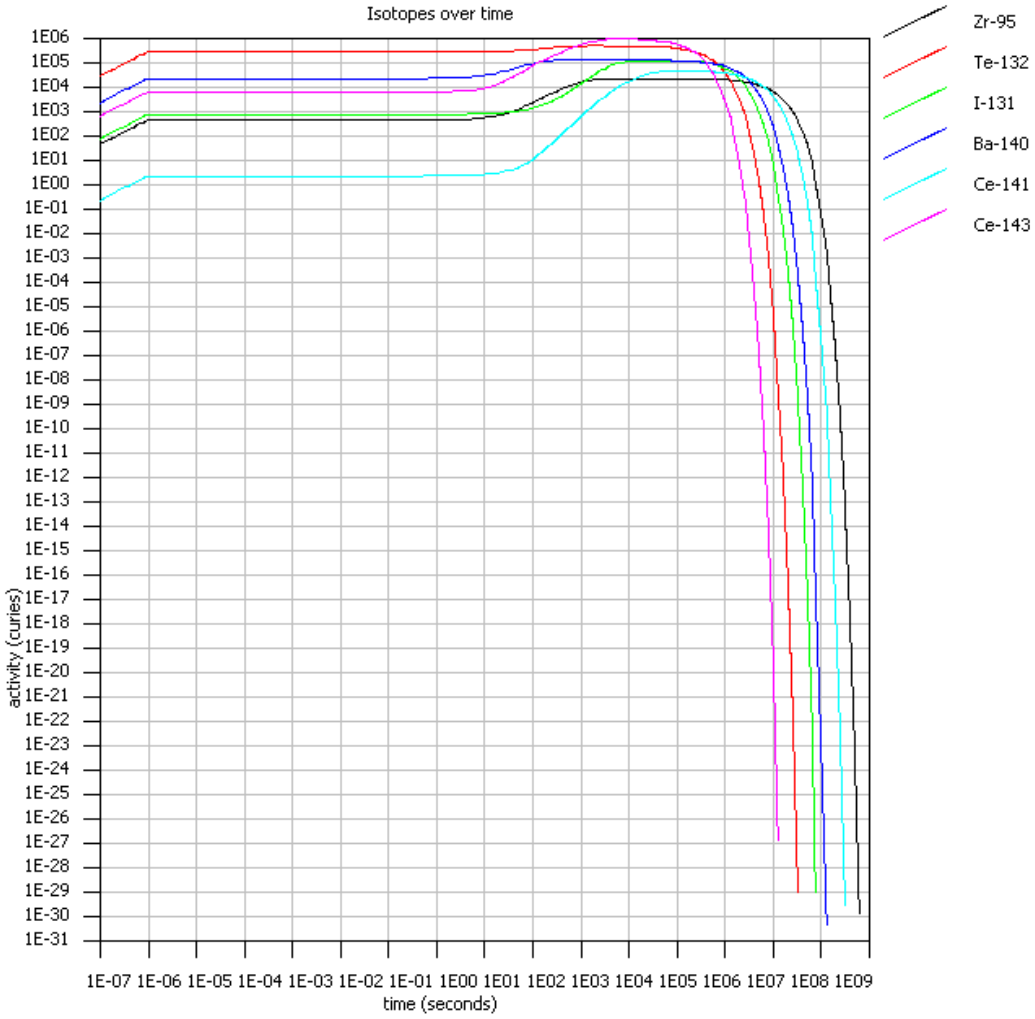


Figure 4.78: Activity of γ-emitting radionuclides for a notional Pu-fueled IND in an STF matrix expected to be found away from ground-zero

Figure: 4.78 shows the activity contributions over time for the gamma-emitting radionuclides expected to be found away from ground-zero in particulate nuclear melt glass formed from a Pu-fueled IND in a an area similar to that modeled by the STF matrix. Like the gamma-emitting nuclides examined in Figure: 4.73, the nuclides examined are extremely radioactive, but tend to decay away quickly between a few days and months post-event. Again, ^{132}Te is the most prominent nuclide before being overtaken by the ingrowth of ^{143}Ce. The other nuclides examined exhibit the same behavior seen for the non-local gamma-emitters generated by a notional U-fueled IND. Specifically, all of the nuclides (with the exception of ^{132}Te) show a significant ingrowth before rapidly decaying away. Similarly, the optimal time to analyze any debris for the presence of these species would be several hours to several weeks post-detonation. The same challenges faced when considering a U-fueled IND are also present in this scenario.

4.3.6 U-Fueled IND in the NYC matrix

The modeled activity over time of alpha-emitting radionuclides created by the detonation of a notional U-fueled IND an area similar to that modeled by the NYC matrix can be seen in Figure: 4.79. When compared to the results from a notional U-fueled IND in the STF matrix, both the alpha-emitting radionuclides present and their activity levels over time are identical. These results are not surprising, as the alpha-emitting nuclides are either unburned fuel, generated by neutron capture reactions during detonation, or a daughter product of one of the two. Because the only difference in the two scenarios was the surrounding matrix, the results both makes sense and are expected. Ideal times for analysis and sample preparation remain the same.

Figure: 4.80 shows the modeled activity over time for beta-emitting radionuclides expected to be found at ground-zero in bulk nuclear melt glass generated from a notional U-fueled IND detonated in an NYC matrix. As with the alpha-emitting

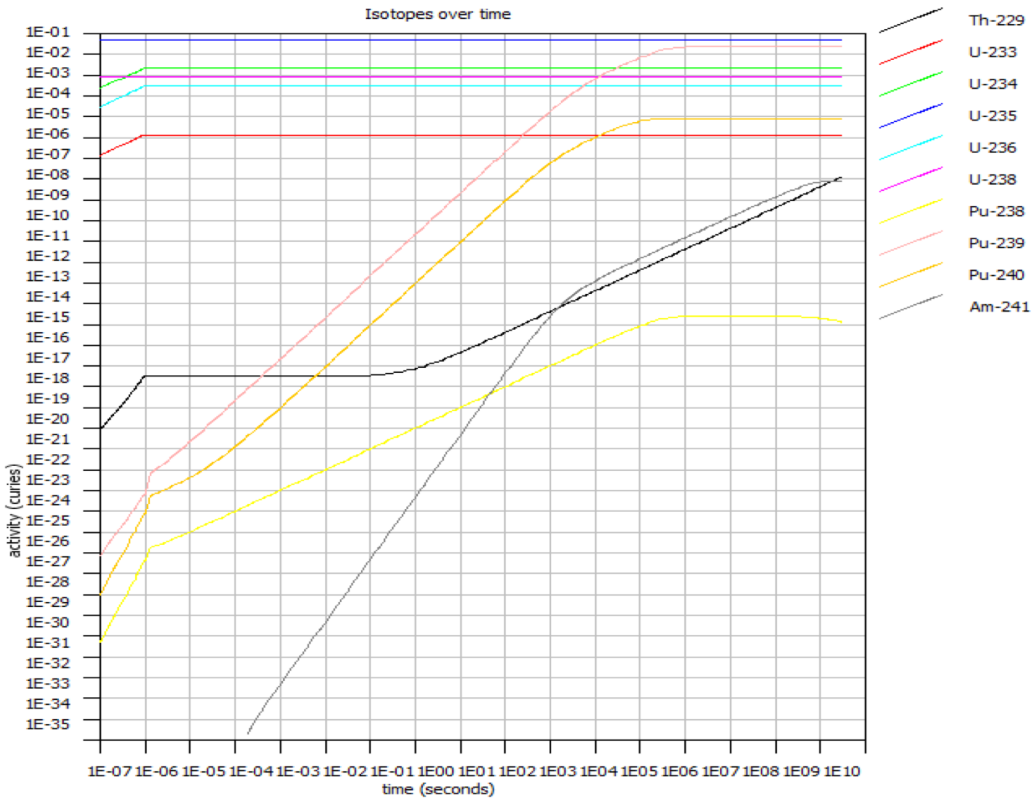


Figure 4.79: Activity of α-emitting radionuclides for an notional U-fueled IND in an NYC matrix

nuclides, with respect to time, the activity of the beta-emitting nuclides expected near ground-zero are identical to those examined in the STF matrix. With the exception of ^{241}Pu (which in this case is generated from multiple n-capture events) all of the beta-emitters examined are neutron-rich fission products. Because the matrix in which the IND is detonated does note have any bearing on fission-product inventory, it is expected that the beta-emitting species expected near gound-zero and their activities will be the same for any U-fueled IND. Once again, with the exception of ^{90}Sr, these beta-emitting nuclides should be analyzed within the first few days to months following a detonation due to their relatively short half-lives. Interference concerns and sample preparation considerations when measuring these nuclides remain the same.

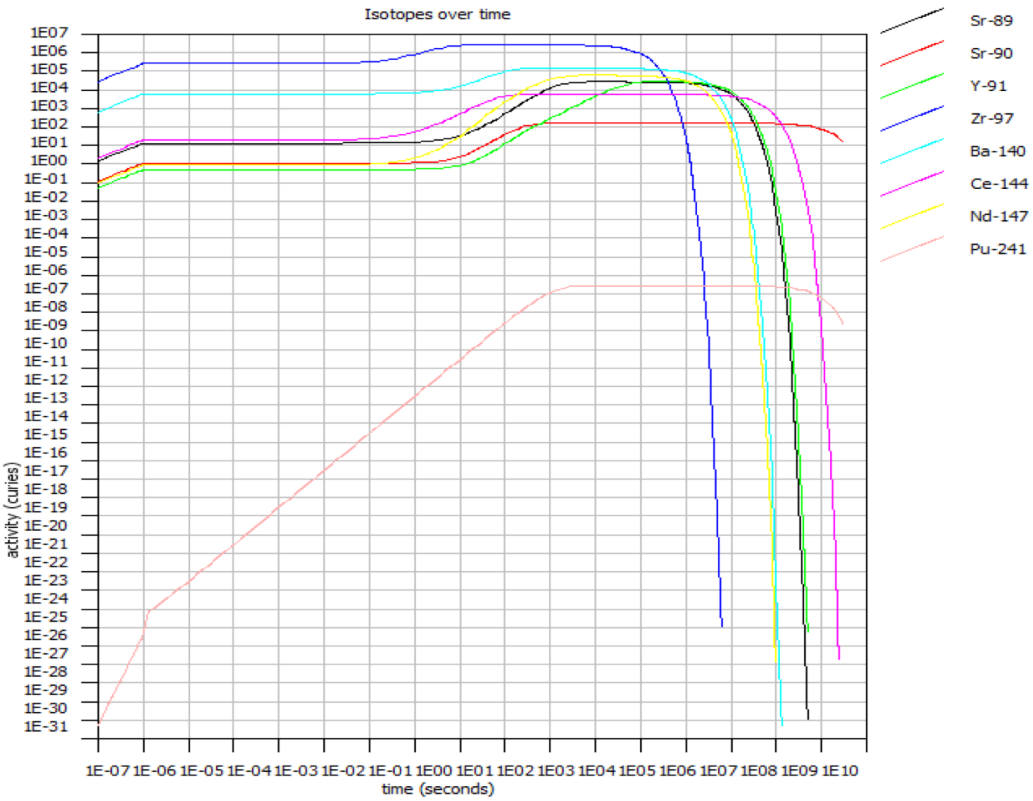


Figure 4.80: Activity of β-emitting radionuclides for a notional U-fueled IND in an NYC matrix expected to be found near ground-zero

The activity over time of beta-emitting radionuclides generated by the detonation of a notional U-fueled IND in an NYC matrix can be seen in Figure: 4.81. Unlike the alpha-emitting radionuclides and the beta-emitters expected near ground-zero, the activity over time for the beta-emitters found way from ground-zero are nearly, but not identical to what is seen in the STF matrix. Again, this is because the beta emitters are fission products, and the matrix in which the modeled detonation takes place will have no bearing on fission product inventories. The exception to this ^{24}Na which is an activation product. The modeled NYC matrix has twice as much Na as the STF matrix and thus twice the ^{24}Na activity. Though this is the only appreciable difference in activity levels, the short half-life of ^{24} makes this point moot after several days.

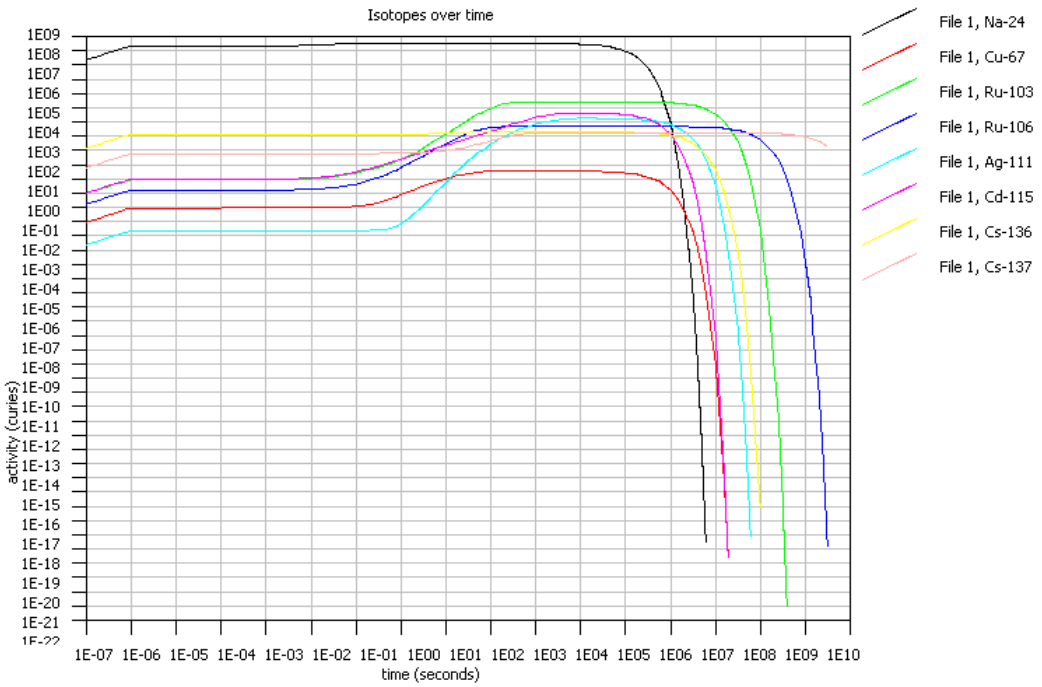


Figure 4.81: Activity of β-emitting radionuclides for a notional U-fueled IND in an NYC matrix expected to be found away from ground-zero

When comparing the activity over time for gamma-emitting radionuclides expected to be found away from ground zero, the STF and NYC matrices yield similar results when exposed via modeling to a notional U-fueled IND. ^{60}Co, ^{137}Cs, ^{152}Eu, and ^{Pb} inventories (and thus activity) are identical for the STF and NYC matrices. The only difference observed in the model, is the behavior of ^{133}Ba. Unlike in the STF matrix where it only contributes tens of pCi to the total activity inventory, ^{133}Ba inventories are twelve orders of magnitude larger for the NYC matrix. The tens of Ci of activity generated makes ^{133}Ba the second largest contributor to total activity of these gamma-emitting radionuclides several minutes after detonation. The drastic increase in the presence of ^{133}Ba is a direct result of the presence of Ba in the NYC matrix, and lack thereof in the STF matrix. The increased activity levels of Ba have no forensic value beyond the ability to back-calculate the neutron-flux of the IND. Sampling and analysis concerns and considerations are the same as those for similar gamma-emitting nuclides generated in the STF matrix. Activity levels over time

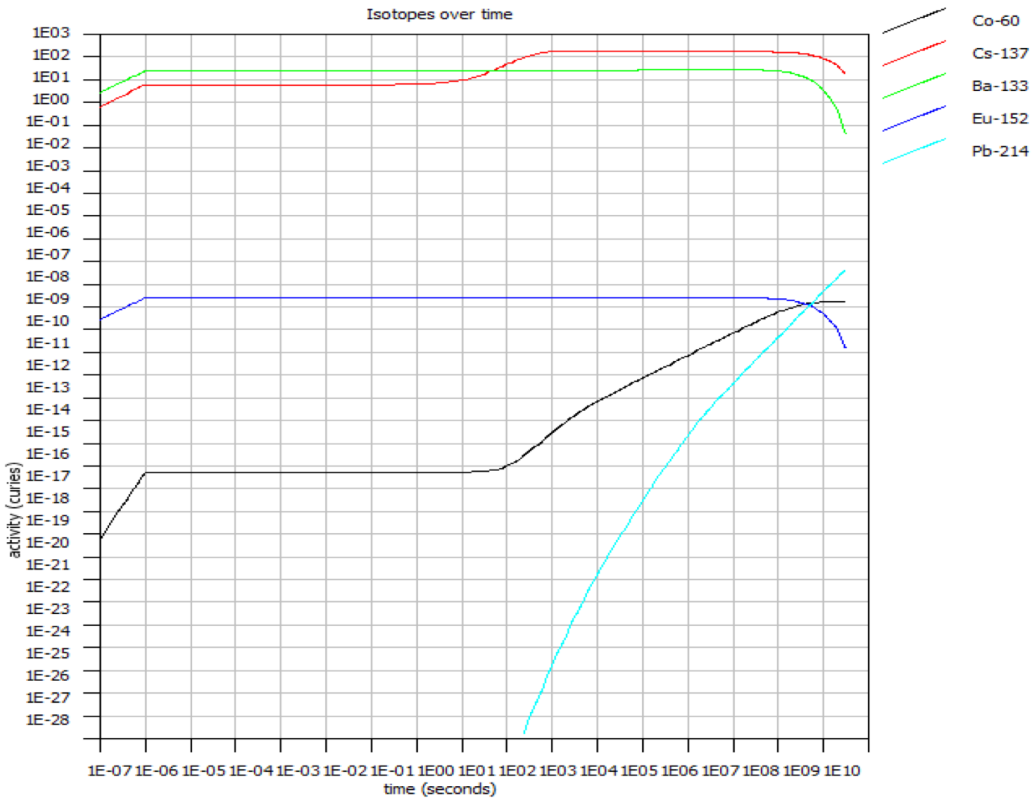


Figure 4.82: Activity of γ-emitting radionuclides for a notional U-fueled IND in an NYC matrix expected to be found near ground-zero

for gamma-emitting radionuclides generated by a notional U-fueled IND in an NYC matrix that are expected to be found near ground-zero can be seen in Figure: 4.82.

Figure: 4.83 shows the activity over time of gamma-emitting nuclides expected to be found in particulate melt glass in locations away from ground-zero. The nuclides examined, were all modeled as being generated from the detonation of a notional U-fueled IND detonated in an NYC matrix. As with the STF matrix, the nuclides generated during detonation produce several MCi of activity for the first few days following the notional event. After that, the contribute to the overall activity in the range of kCi for a few years. The nuclides present and their activity levels over time are identical to those found in the STF matrix when examined with a notional U-fueled IND. These results are not surprising as the nuclides examined are all fission-products,

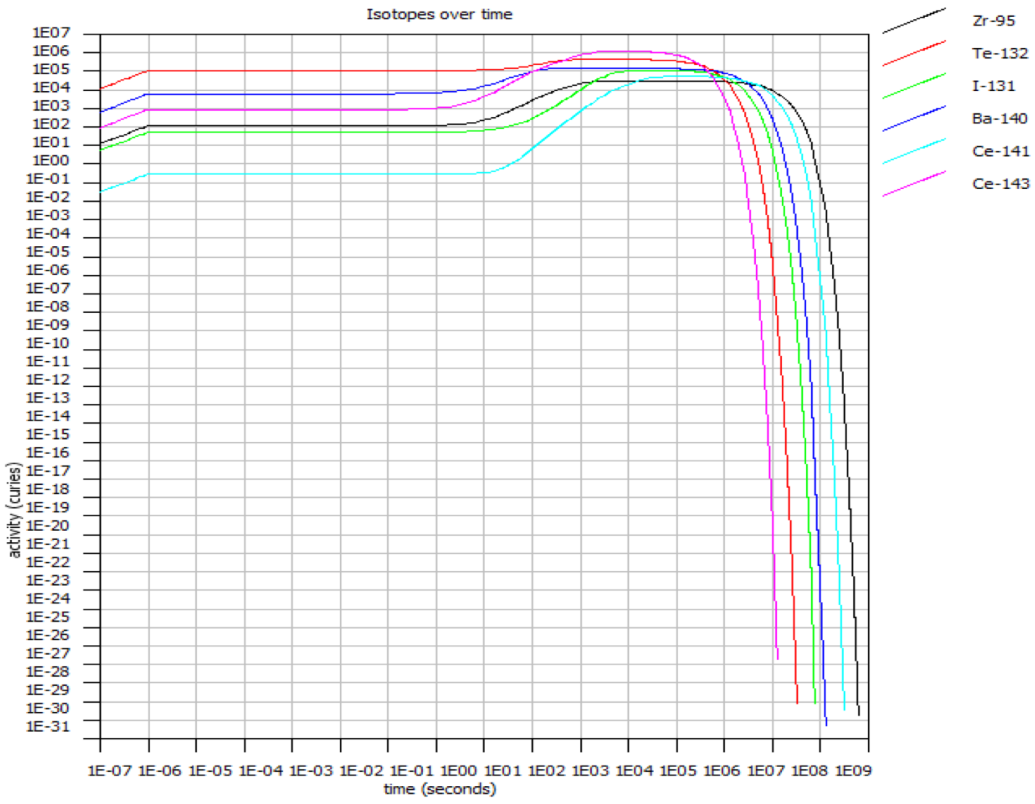


Figure 4.83: Activity of γ-emitting radionuclides for a notional U-fueled IND in an NYC matrix expected to be found away from ground-zero

and thus their inventories are not sensitive to the matrix in which the notional device is detonated.

4.3.7 Pu-Fueled IND in the NYC matrix

The activity of alpha-emitting radionuclides for an notional Pu-fueled IND in a NYC matrix can be seen in Figure: 4.84. Like the STF and NYC matrices for the U-fueled IND, the STF and NYC matrices yielded identical results for the expected alpha-emitters. The reasons for the identical results are the same as those previously mentioned for the U-fueled IND. Again, ideal times for analysis and preparation concerns are the same as those for the alpha-emitters generated from a notional Pu-fueled IND in the STF matrix.

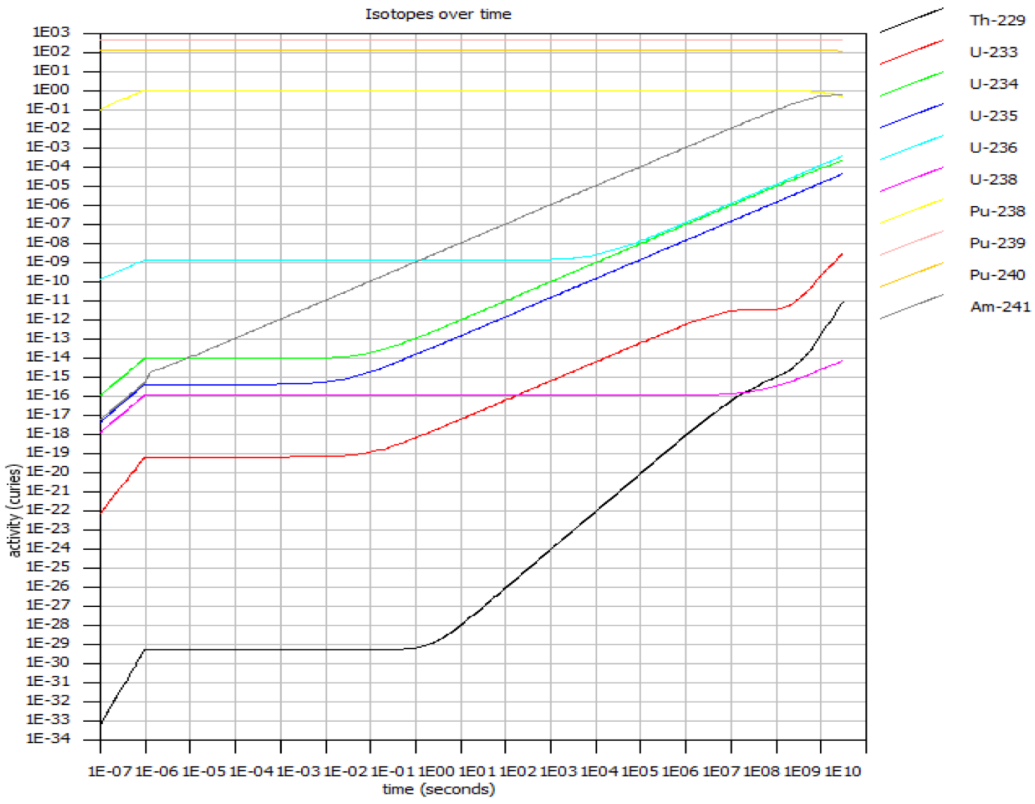


Figure 4.84: Activity of α-emitting radionuclides for an notional Pu-fueled IND in a NYC matrix

Figure: 4.85 shows the activity inventory over time for various beta-emitting radionuclides generated from the modeled detonation of a notional Pu-fueled IND in an NYC matrix that are expected to be found in bulk melt glass near ground-zero. As seen in the STF matrix, ^{97}Zr contributes several MCi of activity for the first three months post-detonation before giving way to ^{140}Ba. The remaining activity levels and radionuclides present are identical to what was seen for the modeled detonation of a notional Pu-fueled IND in an NYC matrix. The reasons for the similarity are the same as those for the notional U-fueled device. Because the inventories of these beta-emitting nuclides are dictated primarily by fission products, the matrix in which the detonation of an IND is modeled has no bearing on the radionuclides examined. Analysis and sample preparation consideration, in addition to ideal sampling times, remain the same as those outlined for the STF matrix.

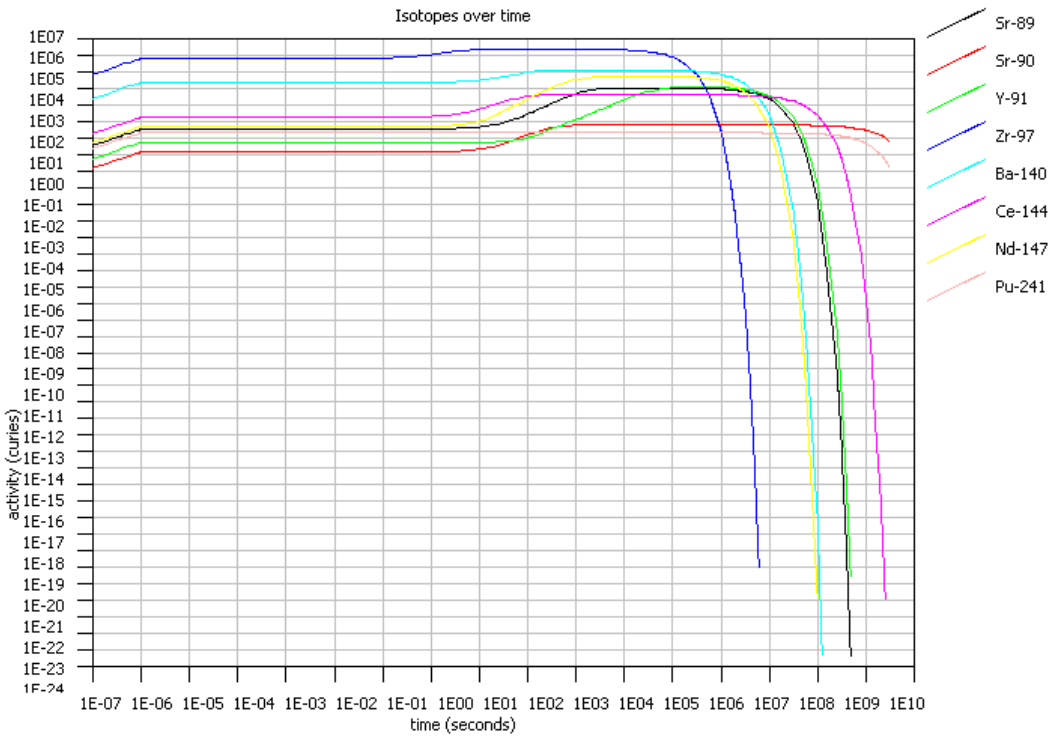


Figure 4.85: Activity of β-emitting radionuclides for a notional Pu-fueled IND in an NYC matrix expected to be found in areas near ground-zero

Activity contributions over time for the beta-emitting radionuclides expected to be found in particulate nuclear melt glass in areas away from ground-zero, and formed from a Pu-fueled IND in a an area similar to that modeled by the NYC matrix can be seen in Figure: 4.86. The total activity contribution from these beta-emitting nuclides is almost six orders of magnitude less than the contribution from the beta-emitting radionuclides expected to be found near ground-zero, the same relationship that was seen in the STF matrix. Activity levels and behaviors of the examined beta-emitting nuclides from areas away from ground-zero is the same as those seen for the STF matrix. Because of this, the optimal time for collection and analysis would be from a few days to a few months post-event.

Figure: 4.87 shows the activity contributions over time for the gamma-emitting radionuclides expected to be found at ground-zero in bulk nuclear melt glass formed from a notional Pu-fueled IND detonated in an area with elemental composition

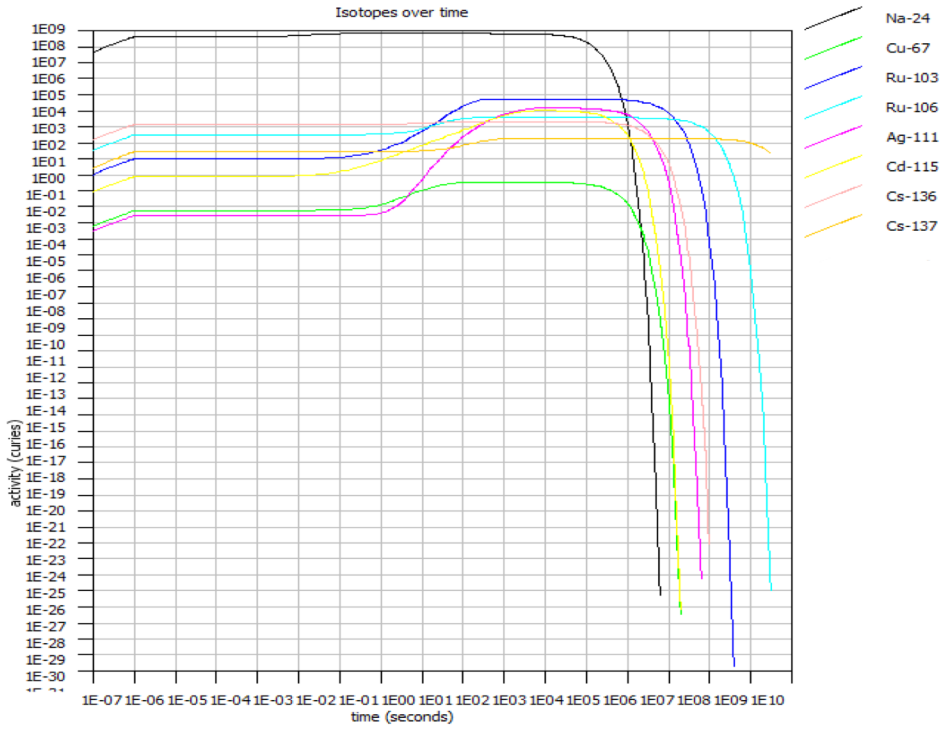


Figure 4.86: Activity of β-emitting radionuclides for a notional Pu-fueled IND in an NYC matrix expected to be found in areas away from ground-zero

similar to that modeled in the NYC matrix. With the exception of ^{133}Ba, all of the nuclides examined exhibit the same behavior as that seen in the model of a Pu-fueled IND in an STF matrix. ^{133}Ba activity shows an increase of approximately nine orders of magnitude when comparing the NYC to the STF matrix. This increase can be attributed to the fact that the STF matrix contains no Ba, and ^{133}Ba is an activation product. The presence of Ba in the NYC matrix allows for the generation of ^{133}Ba via neutron capture when the detonation of the IND is modeled.

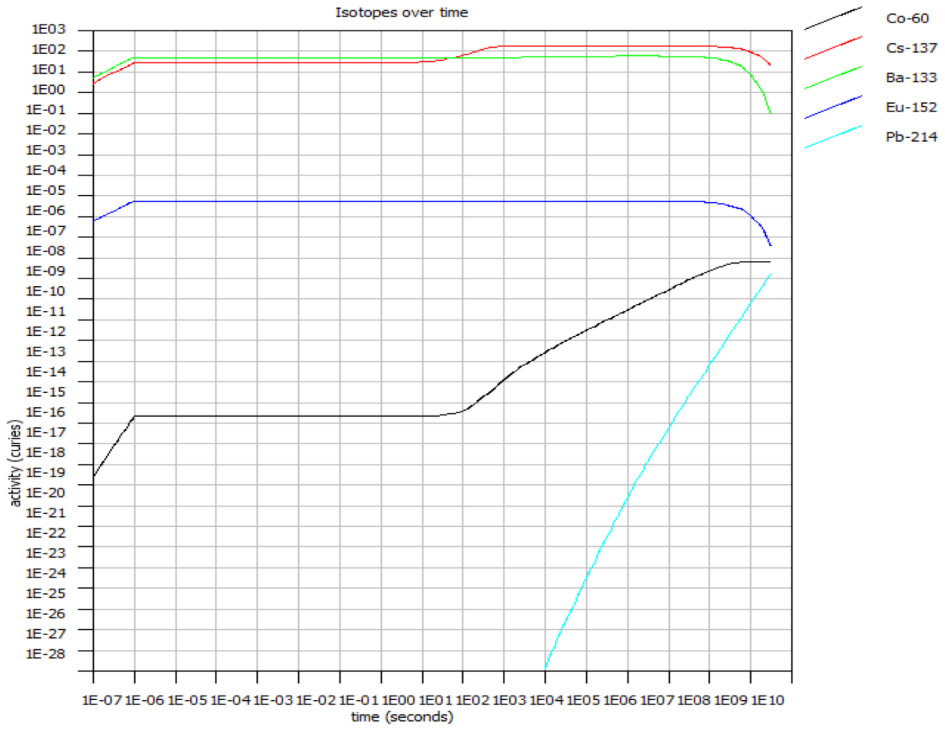


Figure 4.87: Activity of γ-emitting radionuclides for a notional Pu-fueled IND in an NYC matrix expected to be found in areas away from ground-zero

The activity over time for gamma-emitting radionuclides found away from ground-zero in particulate melt glass generated by a notional Pu-fueled IND detonated in an area with similar elemental composition to that found in the NYC matrix can be seen in Figure: 4.88. As with the STF matrix and the U-fueled IND models, all of the these gamma-emitting nuclides (with the exception of ^{132}Te) show a significant ingrowth before rapidly decaying away. Unsurprisingly, contribution to total activity in the model and behavior of the radionuclides over time of the nuclides is the same as that seen in the STF matrix for a Pu-fueled IND. The gamma-emitting radionuclides found away from ground zero that have been examined in this study are all fission products, and thus independent of the matrix in which the IND detonation is modeled.

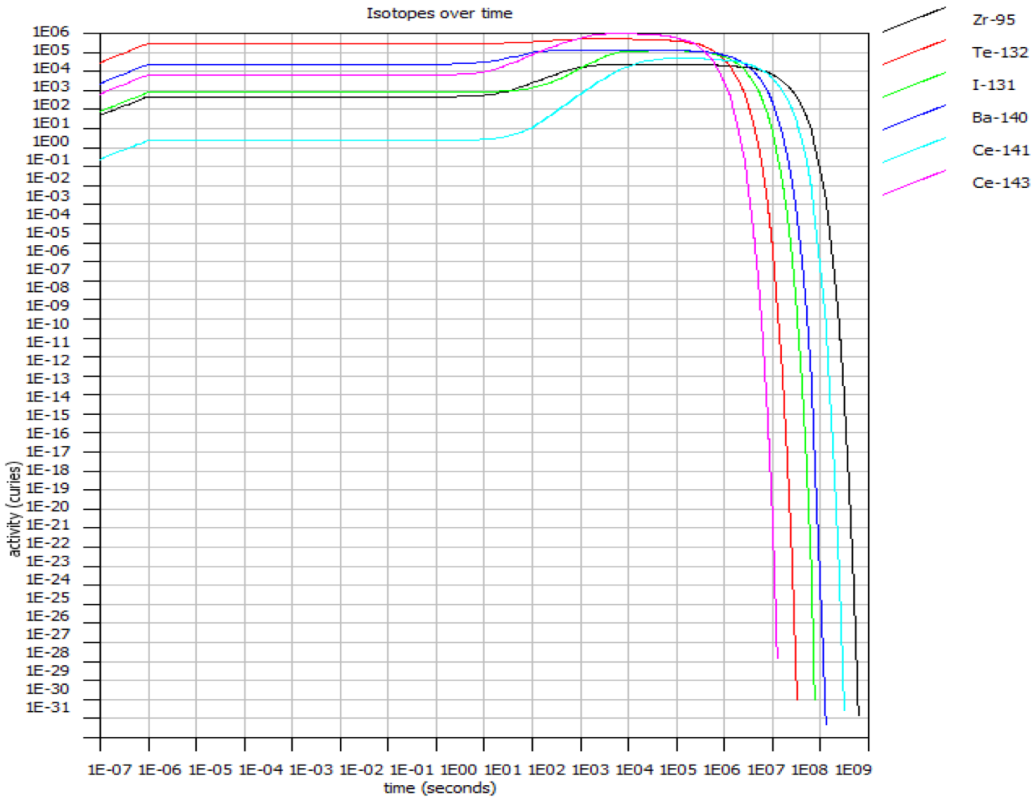


Figure 4.88: Activity of γ-emitting radionuclides for a notional Pu-fueled IND in an NYC matrix near ground-zero

4.3.8 U-Fueled IND in the HOU matrix

The modeled activity over time of alpha-emitting radionuclides created by the detonation of a notional U-fueled IND an area similar to that modeled by the HOU matrix can be seen in Figure: 4.89. Unsurprisingly, the results are identical to those for the alpha-emitters generated by a U-fueled IND in both the STF and NYC matrices. As previously stated, the results are identical because the alpha-emitting nuclides examined can only come from one of three sources: 1) unburned fuel, 2) neutron capture reactions during the fission process, and 3) daughter products of either of the previous two sources. Because the same notional IND was used for all U-fueled IND scenarios, the results are expected. Again, all considerations for sampling and analysis remain the same.

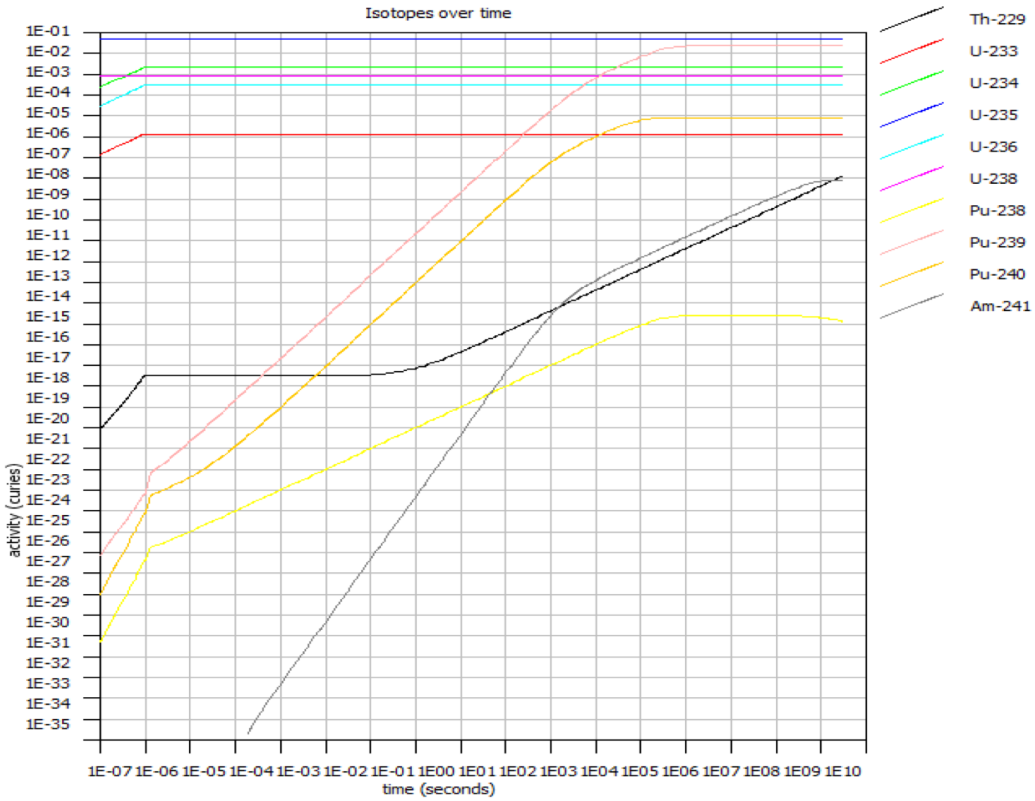


Figure 4.89: Activity of α-emitting radionuclides for an notional U-fueled IND in a HOU matrix

Figure: 4.92 shows the activity over time for beta-emitting radionuclides found near ground-zero in bulk nuclear melt glass generated by a notional U-fueled IND in a HOU matrix. Expectedly, the radionuclides present and their activities over time are identical to those generated by a notional U-fueled IND in the STF and NYC matrices. The same considerations identified for the STF and NYC matrices should be taken when considering the optimal time for sample collection and how to overcome the challenges associated with analysis.

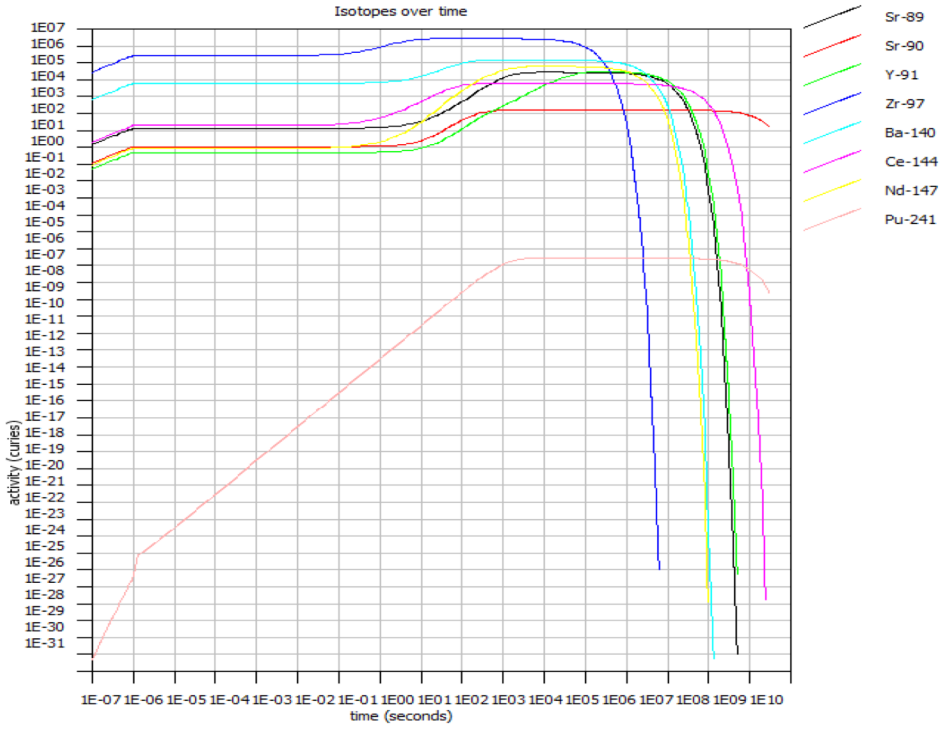


Figure 4.90: Activity of β-emitting radionuclides for a notional U-fueled IND in a HOU matrix expected to be found in the vicinity of ground-zero

The activity over time of beta-emitting radionuclides expected to be found in areas away from ground-zero in particulate nuclear melt glass generated by the detonation of a notional U-fueled IND in a HOU matrix can be seen in Figure: 4.91. ^{24}Na again has only difference difference in activity levels, at about three-quarters that which is seen for the STF matrix. Other than ^{24}Na, activity levels over time for these beta-emitting nuclides are identical to those of the STF and NYC matrices.

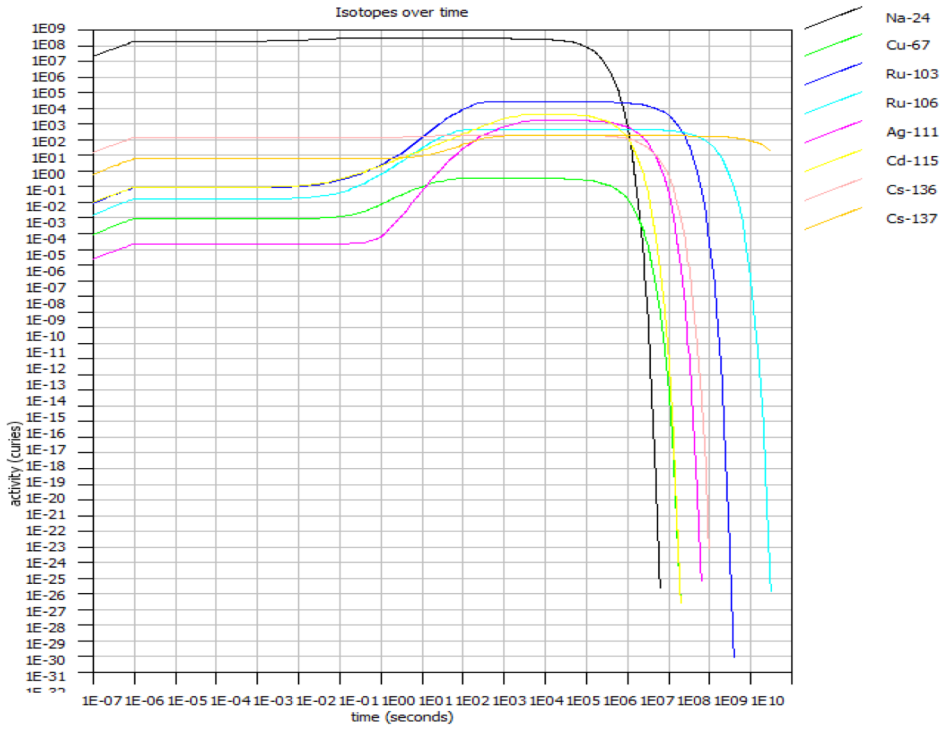


Figure 4.91: Activity of β-emitting radionuclides for a notional U-fueled IND in a HOU matrix expected to be found in areas away from ground-zero

Activity over time for gamma-emitting radionuclides produced by the detonation of a notional U-fueled IND in a HOU matrix and found in areas near ground-zero can be seen in Figure: 4.92. Like the NYC matrix, the HOU matrix shows a larger quantity of ^{133}Ba than the STF matrix. The reason for this higher level activity is again the presence of Ba in the matrix, and the status of ^{133}Ba as an activation product. Activity levels over time are identical to the STF and HOU matrices for the other radionuclides examined. Considerations for sample collection and analysis remain the same as those for the STF and NYC matrices.

Figure: 4.93 shows the activity over time for gamma-emitting nuclides found in particulate nuclear melt glass in areas away from ground zero, and generated by the detonation of a notional U-fueled IND detonated in a HOU matrix. Like the STF and NYC matrices, several MCi of activity are present in the first few days post event.

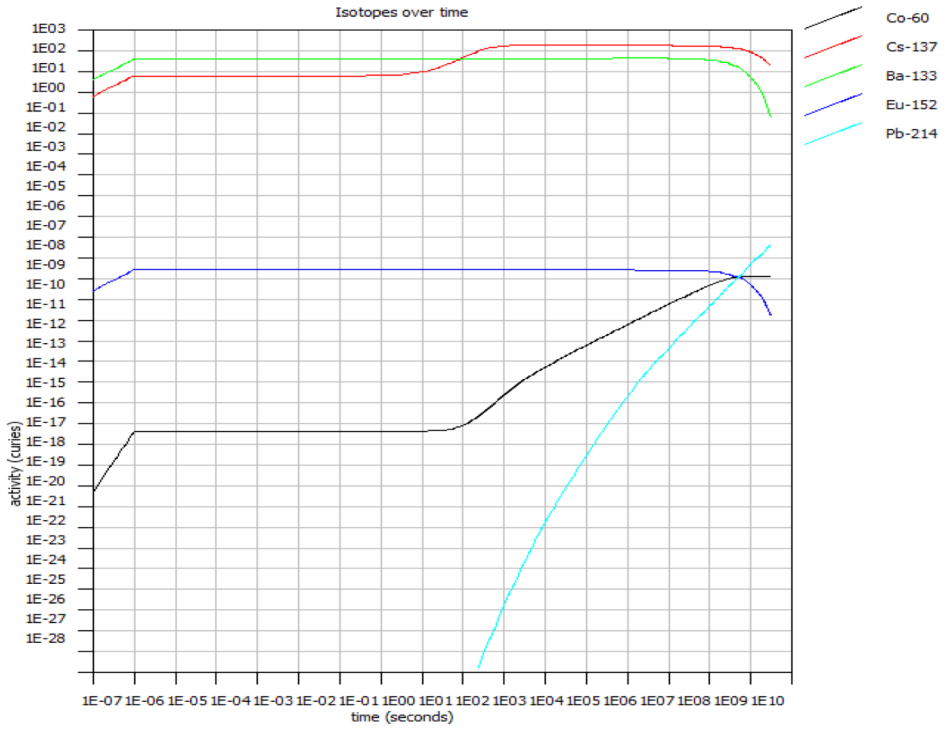


Figure 4.92: Activity of γ-emitting radionuclides expected to be found near ground zero after the detonation of a notional U-fueled IND in a HOU matrix

Once the shorter lived fission products decay, activity produced by these gamma-emitting nuclides is on the order of tens of kCi. As expected, both activity levels and generated nuclides are identical to those produced in the STF and NUC matrices by the detonation of a notional U-fueled IND.

4.3.9 Pu-Fueled IND in the HOU matrix

The activity of alpha-emitting radionuclides for an notional Pu-fueled IND in a HOU matrix can be seen in Figure: 4.94. As expected, the results are identical to the results from the STF and NYC matrices. The reasons for the identical results and the suggested sampling windows and analysis concerns remain the same.

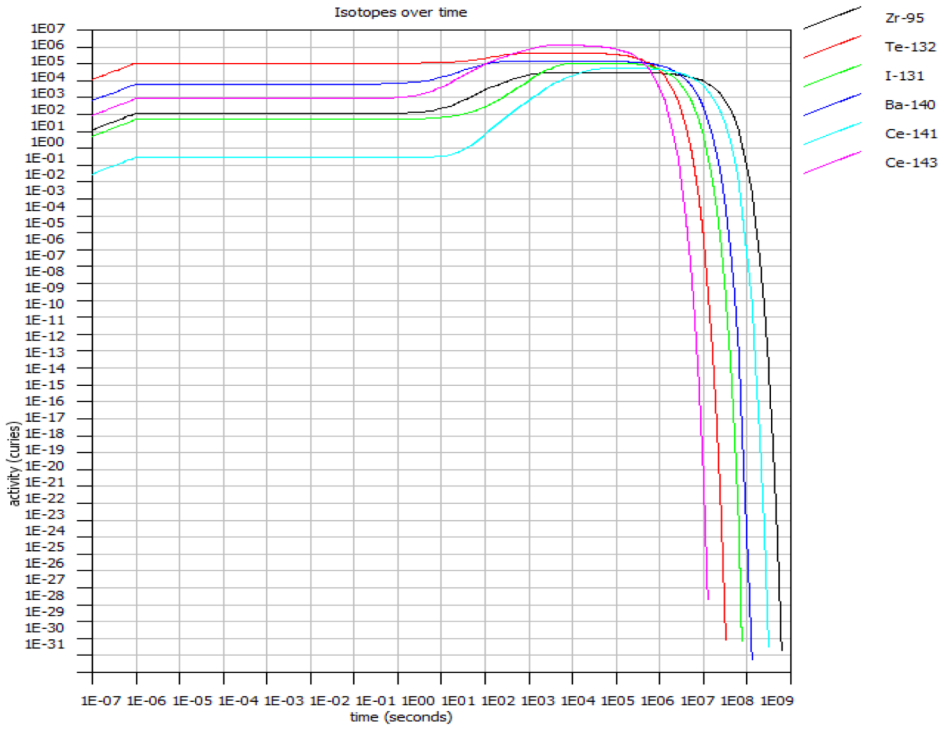


Figure 4.93: Activity of γ-emitting radionuclides for a notional U-fueled IND in a HOU matrix that are expected to be found in areas away from ground-zero

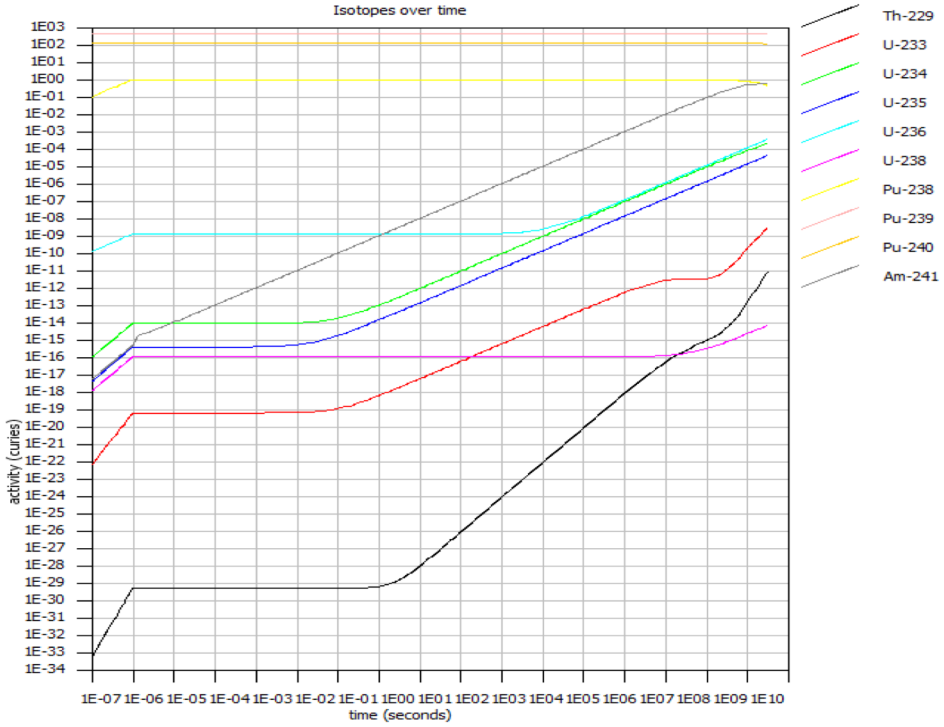


Figure 4.94: Activity of α-emitting radionuclides for an notional Pu-fueled IND in a HOU matrix

Figure: 4.95 shows the activity inventory over time for various beta-emitting radionuclides found near ground-zero in bulk melt glass generated from the modeled detonation of a notional Pu-fueled IND in a HOU matrix. Like what was seen in Figure: 4.85, the modeling results for the HOU matrix are identical in both activity levels and inventory of the beta-emitting nuclides present.

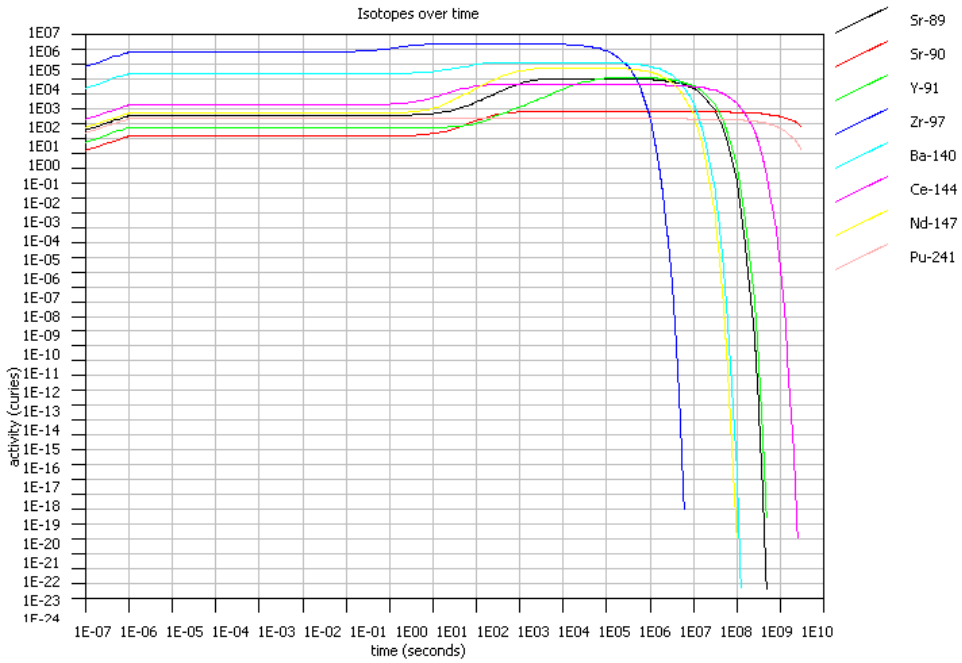


Figure 4.95: Activity of β-emitting radionuclides for a notional Pu-fueled IND in a HOU matrix expected to be found in areas away from ground zero

Activity contributions over time for the beta-emitting radionuclides expected to be found near ground-zero in bulk nuclear melt glass formed from a Pu-fueled IND in a an area similar to that modeled by the HOU matrix can be seen in Figure: 4.95. Unexpectedly, the behavior of the radionuclides examined are identical to those of the beta-emitting nuclides of the STF and NYC matrices in terms of level of activity over time. Both the rationale for these results and the recommendations/concerns regarding optimal sampling times and analysis techniques remain the same.

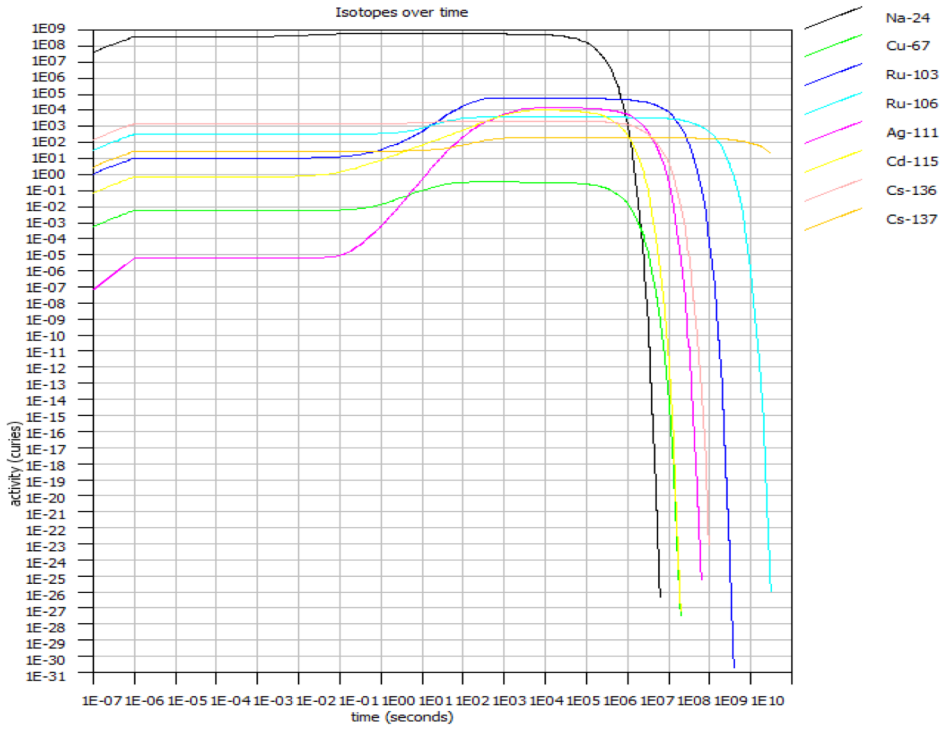


Figure 4.96: Activity of β-emitting radionuclides for a notional Pu-fueled IND in a HOU matrix expected to be found in areas away from ground-zero

As expected, the activity levels of gamma-emitting nuclides expected to be found away from ground-zero in particulate nuclear melt glass generated by a Pu-fueled IND in the HOU matrix are extremely similar. The only difference seen in activity levels is for ^{133}Ba. The activity of ^{133}Ba is 1.5-times higher for the HOU matrix than that seen in the NYC matrix. This difference is the difference in the percentage of BaO in the matrices. The activity levels of the nuclides and their intensity over time are shown in Figure: 4.97.

Figure: 4.98 shows the activity contributions over time for the gamma-emitting radionuclides expected to be found in areas away from ground-zero in particulate nuclear melt glass formed from a Pu-fueled IND detonated in a an area similar to that modeled by the HOU matrix. As with the NYC matrix, activity contribution over time for these gamma-emitting radionuclides is identical to that of the STF

matrix. Again, this is because the nuclides examined are fission products, and thus their yields are independent of that matrix in which the IND detonation is modeled.

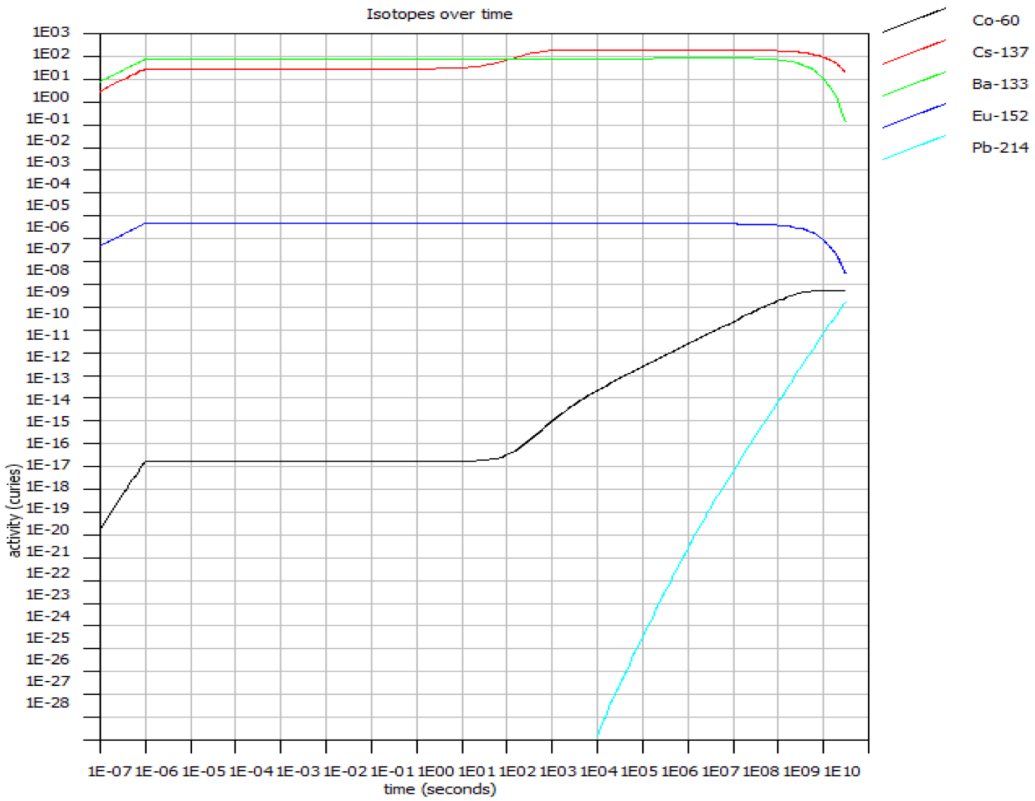


Figure 4.97: Activity of γ-emitting radionuclides generated by a notional Pu-fueled IND in a HOU matrix that are expected to be found in areas near ground-zero

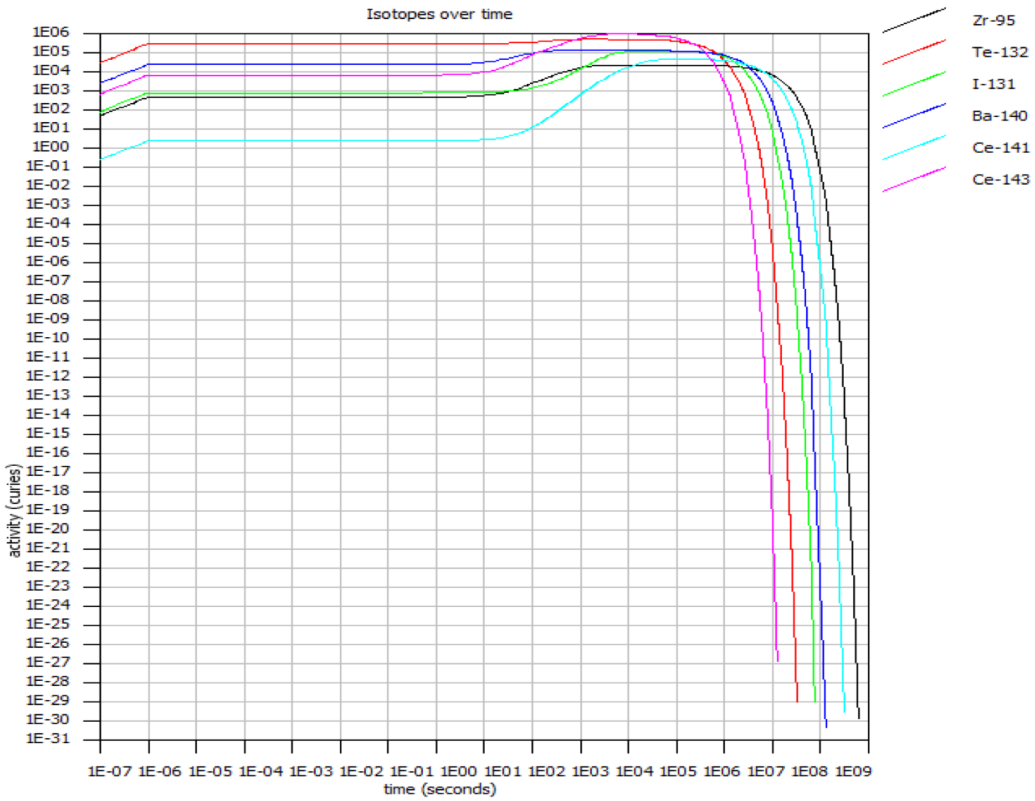


Figure 4.98: Activity of γ-emitting radionuclides generated by a notional Pu-fueled IND in a HOU matrix, and expected to be found in areas away from ground-zero

Chapter 5

Conclusions

The analysis of the surrogates produced in this work has shown that the methods and techniques demonstrated are able to produce urban and particulate surrogate nuclear melt glass. While processes and analytical optimization is still needed, these methods and techniques will be able to meet academic, training, and research needs for surrogate post-detonation nuclear melt glass.

The mathematical model developed to determine elemental compositions of the precursor matrices was successfully implemented, and three unique precursor matrices were developed. These matrices were for the Trinity site in Alamogordo, New Mexico; New York City; and Houston, Texas. The three matrices all had differing, unique elemental compositions. All three matrices were synthesized in a laboratory setting using the oxide forms of the elements in appropriate ratios. A combination of SEM/EDS, P-XRD, and ICP-TOF-MS analyses showed that the three matrices were, in fact, different from one another, showing that the mathematical model developed can indeed be used for the development of precursor matrices for a variety of different scenarios. Beads of surrogate bulk nuclear melt glass were synthesized and analyzed. Optical analysis of the beads revealed that different precursor matrices yielded beads of differing colors, reflecting the differences in their elemental composition. SEM/EDS analysis of the surface of the beads revealed slightly differing morphology for the beads

made from different precursors. Analysis of polished thin sections showed that the beads of all three matrices contained similar features. These feature included small voids, cracks, and regions of granularity. P-XRD analysis showed differing crystalline species between the three precursor matrices. After heat-treatment however, all three beads showed a loss of crystallinity, with the only crystalline species remaining being cristobalite. Due to contamination concerns and ineffective dissolution techniques, no quantitative result could be obtained from the ICP-TOF-MS analysis. From a qualitative standpoint, concentrations of Na, Mg, Mn, U, Ba, and Ti were all present in all three matrices in appropriate relative concentrations. The results showed that while further refinement of the analytical techniques are in order, it is indeed possible to produce a viable surrogate urban bulk melt glass.

Surrogate particulate melt glass was produced for the Trinity and New York matrices. SEM/EDS analysis revealed that heat treatment of the precursor material using a plasma spray coater fused some of the silia-bearing material in the precursor. Additionally, small spheres were found in the heat-treated product from both matrices. The discovery of these features marks the first time that surrogate particulate melt glass has been successfully produced. P-XRD revealed very little crystallinity in the heat-treated material. The predominant crystalline phase identified was alumina. The material created using the New York matrix was extremely amorphous in nature compared to the material generated using the Trinity matrix. As with the result from the bulk melt glass, ICP-TOF-MS results for the particulate were only useful from a qualitative standpoint. Na, Ca, and Fe ratios were found in appropriate relative concentrations between the two matrix types.

Radiological modeling of uranium and plutonium fueled INDs for each matrix revealed many similarities. The largest contributors to alpha-activity were found to be unburned fuel and its subsequent daughter products. Activation products are the primary drivers for all types of activity shortly after detonation, but they tend to quickly decay due to their highly unstable nature. Over time, medium and long-lived fission products are the primary contributors to activity. The biggest contributor to

differences in the nuclides present was the type of fuel used in the weapon. Further analysis is needed to determine what effect trace elements in the environment will have on the radiological profile of these materials.

The study shows that it is possible to use the highlighted techniques to produce both bulk and particulate surrogate nuclear melt glass in appreciable quantities. Further work is needed in order to determine the cause of some of the anomalies found in the data, and to optimize the production routines.

Chapter 6

Future Work

6.0.1 Determining Causes of Anomalies in the ICP-TOF-MS data

The ICP-MS-TOF data showed many anomalies, specifically the discrepancy in the concentration of Al in the bulk melt glass samples. A study of the synthesis of the beads is needed in order to determine where the sources of these discrepancies come from, and if they can be consistently accounted for. This will allow for higher accuracy during analysis, and thus the better development of analytical techniques in the future.

6.0.2 Improvement of Dissolution Techniques

The dissolution techniques used in this study were not as effective as the surveyed literature indicated. Better dissolution techniques are needed in order to thoroughly examine the analytes of interest. Alkaline flux methods ($NaOH/NaNO_3$ for example) could prove useful. Additionally, with the exception of ^{24}Na for neutron flux estimations, sodium is not a useful forensic indicator. Because of this, the Na introduced by the flux method would not be a cause for concern.

6.0.3 Further Analysis of Surrogates via LIBS

While EDS analysis provides an average value for chemical composition over an area, a technique such as laser-induced break-down spectroscopy (LIBS) would be able to provide a high precision map of the elements present in a sample. Unfortunately, as with any analytical technique, matrix effects can interfere with measurements. By using a set of standards and comparing them to melt glass beads, it would be possible to determine what matrix effects are present. Once matrix interferences are determined, it would be possible to quantitatively determine what elements are present in the melt glass bead, along with their locations. This would aid in the study of the melt glass formation process, allow for the determination of sample heterogeneity, and allow for a better understanding of speciation a post-detonation scenario.

6.0.4 Optimization of Particulate Precursor Preparation

Observations of the spray-dried particulate melt glass precursor revealed inconsistent sizes of the powdered oxides used in preparation, most noticeably that the silica was significantly larger than the other constituents. Inconsistent sizes in the precursor will lead to different heat treatments for the different constituents. In future campaigns, it is recommended that a smaller sized silica gel (in the hundreds of nm to μm range) be used to achieve a more consistent size distribution in the precursor, thus allowing for more consistent heat treatment.

6.0.5 Optimization of Torch Operational Conditions

Though it has been shown that the production of particulate nuclear melt glass surrogates is possible, the initial experiments discussed serve only as a proof of concept. Further work is needed in order to determine the optimal carrier gas flow rates, and the appropriate mix of Ar and H_2 used in the torch. Additionally, it is

recommended that historically collected particulate debris be used as a benchmark for this study. This will allow for the production of more realistic particulate surrogates.

6.0.6 Irradiation Campaigns

Radiologically cold surrogates are able to provide a basis for training and the development of new analytical techniques, however certain radiochemical methods cannot be developed with cold surrogates. By irradiating cold samples that have been loaded with U or Pu it will be possible to create highly realistic surrogates for both training and research purposes. One of the challenges for this work is the need for a sufficiently high fast neutron flux to which the samples can be exposed. Facilities such as the Spallation Neutron Source, the University of Missouri Research Reactor, and the National Ignition Facility may be able to provide an adequate neutron source for this work. However, devices to ensure uniform irradiation of the samples and appropriate neutron energy spectra may need to be developed.

6.0.7 Further In-Depth Analysis of Radiological Models

This study only evaluated the historically examined radionuclides that have been found in nuclear melt glass. A further in depth analysis would be useful in helping to identify all of the radionuclides expected to be present after the irradiation campaigns. By studying the trends of decay and ingrowth of these species, an extensive library of radionuclide inventories over time could be compiled. This library would be useful for analysts examining post-detonation debris, and would allow for a quick determination of the analytical techniques and radiochemical separation methods necessary at any given time post-event. This library would also be useful in identifying any species that may cause interference effects during analysis.

6.0.8 Coupling of Atmospheric Chemistry

Atmospheric conditions at the time of a nuclear detonation are expected to have an effect on the chemical formation processes that affect nuclear melt glass. By coupling the plasma spray torch used in these experiments to a particle dispersion chamber, it will be possible to adjust the ambient humidity and introduce atmospheric contaminants such as SO_2 and NO_x, among others. The inclusion of atmospheric impurities will serve to generate more realistic surrogates in addition to providing information about the chemical processes that occur within the fireball immediately post-detonation.

Bibliography

[1] J. J. Molgaard, J. D. Auxier, A. V. Giminaro, C. J. Oldham, M. T. Cook, S. a. Young, and H. L. Hall, "Development of synthetic nuclear melt glass for forensic analysis," *Journal of Radioanalytical and Nuclear Chemistry*, vol. 304, no. 3, pp. 1293–1301, 2015. 1, 8, 10, 32, 47

[2] P. Glasstone, Samuel, Dolan, *Effects of Nuclear Weapons*. United States DOD/DOE, third ed., 1977. 3, 6, 36, 41, 42, 43

[3] C. Ross, "Optical Properties of Glass from Alamogordo, New Mexico," tech. rep., U.S. Geological Survey, 1948. 3, 4, 8, 9, 14, 15

[4] F. Belloni, J. Himbert, O. Marzocchi, and V. Romanello, "Investigating incorporation and distribution of radionuclides in trinitite.," *Journal of environmental radioactivity*, vol. 102, pp. 852–62, sep 2011. 3, 4, 8, 25, 27

[5] R. Hermes and S. W.B., "A new look at Trinitite," *Nucl Weapons J*, no. 2, pp. 2–7, 2005. 3, 8, 9

[6] P. P. Parekh, T. M. Semkow, M. a. Torres, D. K. Haines, J. M. Cooper, P. M. Rosenberg, and M. E. Kitto, "Radioactivity in trinitite six decades later.," *Journal of environmental radioactivity*, vol. 85, pp. 103–20, jan 2006. 4, 22, 23, 25, 26, 27

[7] N. Eby, R. Hermes, N. Charnley, and J. a. Smoliga, "Trinitite-the atomic rock," *Geology Today*, vol. 26, pp. 180–185, sep 2010. 4, 5, 9, 10, 11, 12, 13, 15, 17, 19, 27

[8] G. R. Eppich, K. B. Knight, T. W. Jacomb-Hood, G. D. Spriggs, and I. D. Hutcheon, "Constraints on fallout melt glass formation from a near-surface nuclear test," *Journal of Radioanalytical and Nuclear Chemistry*, vol. 302, pp. 593–609, jul 2014. 5, 11, 12, 19, 20, 27, 28

[9] H. L. Brode, "Review of nuclear weapons effects," *Annual Review of Nuclear Science*, 1968. 5, 6, 7, 8

[10] K. Bainbridge, *Trinity*. 1976. 5, 6, 23

[11] J. J. Bellucci, C. Wallace, E. C. Koeman, A. Simonetti, P. C. Burns, J. Kieser, E. Port, and T. Walczak, "Distribution and behavior of some radionuclides associated with the Trinity nuclear test," *Journal of Radioanalytical and Nuclear Chemistry*, vol. 295, pp. 2049–2057, sep 2012. 8, 25

[12] A. B. Kersting and D. K. Smith, "Observations of Nuclear Explosive Melt Glass Textures and Surface Areas," tech. rep., Lawrence Livermore National Laboratory, Livermore, CA, 2006. 8

[13] E. C. Koeman, A. Simonetti, W. Chen, and P. C. Burns, "Oxygen isotope composition of trinitite post detonation materials," *Analytical chemistry*, vol. 85, pp. 11913–9, 2013. 9, 14, 15, 17

[14] C. Wallace, J. J. Bellucci, A. Simonetti, T. Hainley, E. C. Koeman, and P. C. Burns, "A multi-method approach for determination of radionuclide distribution in trinitite," *Journal of Radioanalytical and Nuclear Chemistry*, vol. 298, pp. 993–1003, apr 2013. 10, 17, 31

[15] I. Y. Borg, "Radioactivity trapped in melt produced by a nuclear explosion," *Nuclear Technology*, vol. 26, pp. 88–100, 1974. 10

[16] T. Matsunami, A. Fujita, and K. Yoshikawa, "Radionuclide fractionation in fallout particles from a land surface burst," *Journal of Geophysical Research*, vol. 74, no. 6, pp. 1374–1387, 1969. 10, 20, 27

[17] T. Mamuro, T. Matsunami, and A. Fujita, "Radionuclide fractionation in fallout particles from an air burst," *Health Physics*, vol. 14, no. 3, pp. 223–239, 1968. 10

[18] C. Adams, N. Farlow, and W. Schell, "The compositions , structures and origins of radioactive fall-out particles," *Geochimica et Cosmochemica Acta*, vol. 18Adams, C, pp. 42–56, 1960. 11, 27

[19] P. Benson, C. Gleit, and L. Leventhal, "Physical characteristics of single particles from high-yield air bursts," *second ceonference*. 11, 29, 30, 31

[20] J. J. Bellucci, A. Simonetti, E. C. Koeman, C. Wallace, and P. C. Burns, "A detailed geochemical investigation of post-nuclear detonation trinitite glass at high spatial resolution: Delineating anthropogenic vs. natural components," *Chemical Geology*, vol. 365, pp. 69–86, 2014. 13, 14, 16

[21] A. J. Fahey, C. J. Zeissler, D. E. Newbury, J. Davis, and R. M. Lindstrom, "Postdetonation nuclear debris for attribution.," *Proceedings of the National Academy of Sciences of the United States of America*, vol. 107, pp. 20207–12, nov 2010. 13, 17, 22

[22] G. F. Eaton and D. K. Smith, "Aged nuclear explosive melt glass : Radiography and scanning electron microscope analyses documenting radionuclide distribution and glass alteration," *Journal of Radioanalytical and Nuclear Chemistry*, vol. 248, no. 3, pp. 543–547, 2001. 13, 22

[23] A. V. Giminaro, S. A. Stratz, J. a. Gill, J. P. Auxier, C. J. Oldham, M. T. Cook, J. D. Auxier, J. J. Molgaard, and H. L. Hall, "Compositional planning for development of synthetic urban nuclear melt glass," *Journal of Radioanalytical and Nuclear Chemistry*, vol. 306, no. 1, pp. 175–181, 2015. 14, 32

[24] P. H. Donohue, A. Simonetti, E. C. Koeman, S. Mana, and P. C. Burns, "Nuclear forensic applications involving high spatial resolution analysis of Trinitite cross-sections," *Journal of Radioanalytical and Nuclear Chemistry*, 2015. 14, 17, 18

[25] J. J. Bellucci and A. Simonetti, "Nuclear forensics: searching for nuclear device debris in trinitite-hosted inclusions," *Journal of Radioanalytical and Nuclear Chemistry*, vol. 293, pp. 313–319, feb 2012. 15, 17

[26] E. C. Koeman, A. Simonetti, and P. C. Burns, "Sourcing of Copper and Lead within Red Inclusions from Trinitite Postdetonation Material," *Analytical Chemistry*, vol. 87, pp. 5380–5386, 2015. 16

[27] J. J. Bellucci, A. Simonetti, C. Wallace, E. C. Koeman, and P. C. Burns, "Lead isotopic composition of trinitite melt glass: Evidence for the presence of Canadian industrial lead in the first atomic weapon test," *Analytical Chemistry*, vol. 85, pp. 7588–7593, 2013. 17

[28] L. Evans, "The use of chelating reagents and alkaline solutions in soil organic-matter extraction," *Journal of Soil Science*, vol. 10, 1959. 19

[29] T. T. Chao, "Use of partial dissolution techniques in geochemical-exploration," *Journal of Geochemical Exploration*, vol. 20, no. 2, pp. 101–135, 1984. 19

[30] S. Gatehouse, D. Russell, and C. Van Moort, J, "Sequential Soil Analysis in Exploration Geochemistry," *Journal of Cheochemical Exploration*, vol. 8, pp. 483–494, 1977. 19

[31] J. A. Gill, *Rapid Dissolution for Destructive Assay of Nuclear Melt Glass*. PhD thesis, University of Tennessee, 2015. 20

[32] D. Lariviere and A. Milliard, "New and Rapid Method for the Dissolution of Actinides by Automated Fusion Designed for ICP Analysis," in *MARC X American Nuclear Society Inernational Topical Conference*, p. 39, 2015. 20

[33] S. L. Maxwell, B. K. Culligan, and J. B. Hutchison, "Rapid determination of actinides in asphalt samples," *Journal of Radioanalytical and Nuclear Chemistry*, vol. 299, pp. 1891–1901, jan 2014. 20

[34] P. Benson, C. Gleit, and L. Leventhal, "Radiochemical fractionation characteristics of singl particles from high-yield air bursts," *The second Conference*. 20

[35] E. C. Freiling, "Fractionation in Surface Bursts," in *Conference on Radioactive Fallout from Nuclear Weapons Tests*, United States Atomic Energy Commission Divison of Technical Information, 1961. 20, 27, 28

[36] T. A. Gibson Jr., "Observed fractionation in ground level fallout from three nuclear cratering detonations," tech. rep., Lawrence Radiation Laboratory, University of California, Livermore, CA, 1968. 20

[37] T. Mamuro, K. Yoshikawa, and N. Maki, "Radionuclide fractionation in fallout particles," *Health Physics*, vol. 11, no. 3, pp. 199–209, 1965. 20

[38] V. J. Jodoin, R. W. Lee, D. E. Peplow, and J. P. Lefebvre, "Application of the ORIGEN Fallout Analysis Tool and the DELFIC Fallout Planning Tool to National Technical Nuclear Forensics," in *ANS EPRRSD -11th Emergency Preparedness and Response*, (Knoxville, TN), 2011. 21

[39] S. M. Bowman, "Scale 6: Comprehensive nuclear safety analysis code system," *Nuclear Technology*, vol. 174, no. 2, pp. 126–148, 2011. 21

[40] D. Pittauerova, W. Kolb, C. Jon, and W. Helmut, "Radioactivity in Trinitite - a review and new measurements," pp. 1–10. 22, 25, 26, 27

[41] D. Schlauf, "Trinitite redux: Comment on Determining the yield of the Trinity nuclear device via gamma-ray spectroscopy, by David Atkatz and Christopher Bragg [Am. J. Phys. 63 (5), 411413 (1995)]," *American Journal of Physics*, vol. 65, no. 11, pp. 411–413, 1997. 22, 25, 26

[42] K. J. Moody, I. D. Hutcheon, and P. M. Grant, *Nuclear Forensic Analysis*. Boca Raton, Fl: Taylor & Francis Group, 1 ed., 2005. 23

[43] T. M. Semkow, P. P. Parekh, and D. K. Haines, "Modeling the Effects of the Trinity Test," *Applied Modeling and Computations in Nuclear Science*, vol. 945, pp. 142–159, 2007. 23, 26, 27

[44] D. Pittauerová, W. M. Kolb, J. C. Rosenstiel, and H. W. Fischer, "Radioactivity in Trinitite," tech. rep., Institute of Environmental Physics, University of Bremen, 2006. 25

[45] Cook, Matthew T., Auxier II, John D., Giminaro, Andrew V., Molgaard, Joshua J., Hall, Howard L, "A Comparison of Gamma Spectra from Trinitite vs Irradiated Synthetic Nuclear Melt Glass," 2015. 25

[46] C. F. Miller, "SMALL BOY SHOT FALLOUT RESEARCH PROGRAM," 27

[47] E. a. Martell, "The size distribution and interaction of radioactive and natural aerosols in the stratosphere," *Tellus A*, vol. 18, no. 2-3, 1966. 28

[48] S. D. Harvey, M. Liezers, K. C. Antolick, B. J. Garcia, L. E. Sweet, A. J. Carman, and G. C. Eiden, "Porous chromatographic materials as substrates for preparing synthetic nuclear explosion debris particles," *Journal of Radioanalytical and Nuclear Chemistry*, vol. 298, pp. 1885–1898, 2013. 33

[49] M. Liezers, A. J. Carman, and G. C. Eiden, "The preparation of non-radioactive glassy surrogate nuclear explosion debris (SNED) loaded with isotopically altered Xe," *Journal of Radioanalytical and Nuclear Chemistry*, vol. 306, pp. 1811–1817, 2015. 33, 34

[50] D. B. Smith, W. Cannon, L. Woodruff, and F. Solano, "Geochemical and mineralogical data for soils of the conterminous United States," *U.S. Geological Survey Data Series*, vol. 801, no. 19, 2013. 35, 44

[51] K. Cochran, T. Townsend, D. Reinhart, and H. Heck, "Estimation of regional building-related debris generation and composition: Case study for Florida, US," *Waste Management*, vol. 27, pp. 921–931, jan 2007. 37

[52] L. W. Cheah, *Cars on a Diet : The Material and Energy Impacts of Passenger Vehicle Weight Reduction in the U . S . by.* Ph.d. dissertation, Massachusettes Institute for Technology, 2010. 39, 40

[53] J. J. Molgaard, *Production of Nuclear Debris Surrogates for Forensic Methods Development.* PhD thesis, University of Tennessee, 2014. 44, 45, 189, 190, 191, 192, 193

[54] IAEA, *IAEA Safegaurds Glossery.* Vienna, Austria: International Atomic Energy Agency, first ed., 2001. 44

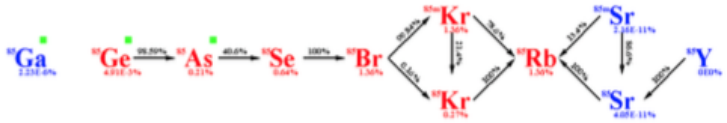
[55] A. Fluegel, "Modeling of Glass Liquidus Temperatures using Disconnected Peak Functions," 2007. 47

Appendix

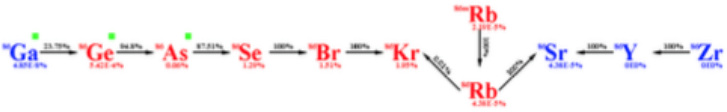
Appendix A

Fractionation Mass Chains

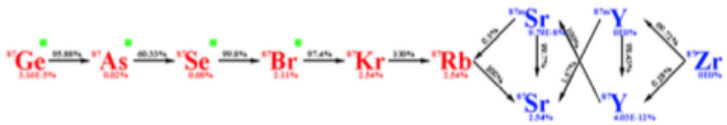
Figures: A.1-A.5 show the mass chains for some fission products of ^{235}U. Elements that are typically found in the vicinity of ground-zero are shown in red, while those found away from ground-zero are shown in blue.



(a) Mass Chain 85



(b) Mass Chain 86



(c) Mass Chain 87



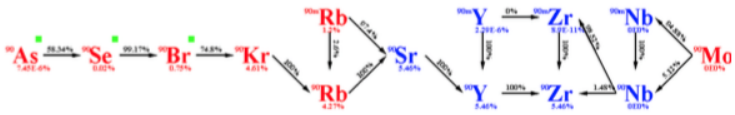
(d) Mass Chain 88

Figure A.1: Mass chains 85-88

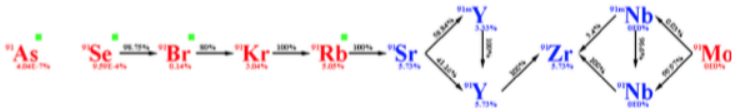
(53)



(a) Mass Chain 89



(b) Mass Chain 90



(c) Mass Chain 91



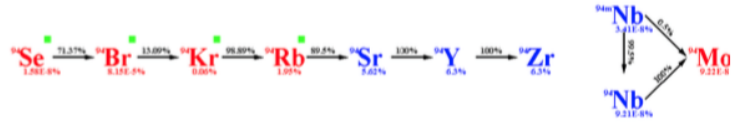
(d) Mass Chain 92

Figure A.2: Mass chains 89-92

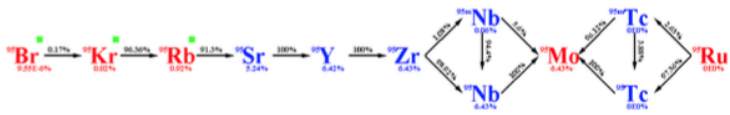
(53)



(a) Mass Chain 93



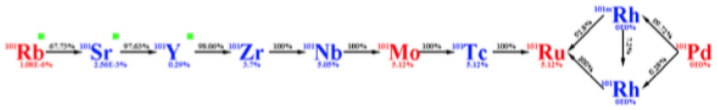
(b) Mass Chain 94



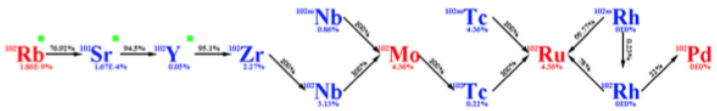
(c) Mass Chain 95

Figure A.3: Mass chains 93-95

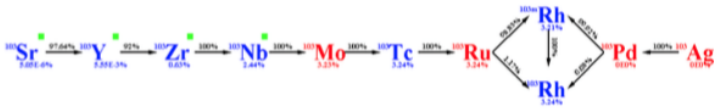
(53)



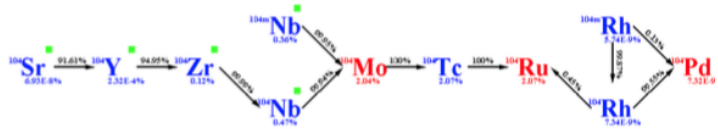
(a) Mass Chain 101



(b) Mass Chain 102



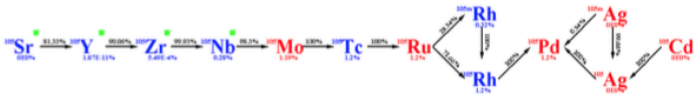
(c) Mass Chain 103



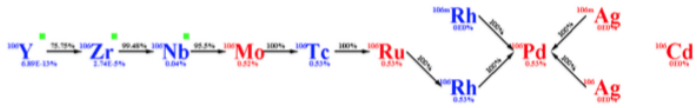
(d) Mass Chain 104

Figure A.4: Mass chains 101-104

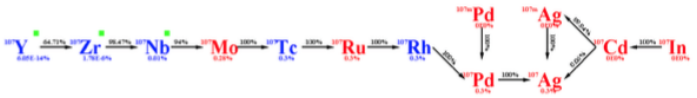
(53)



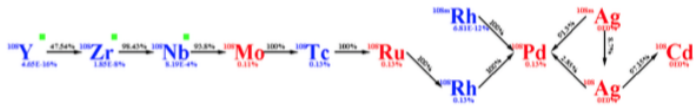
(a) Mass Chain 105



(b) Mass Chain 106



(c) Mass Chain 107



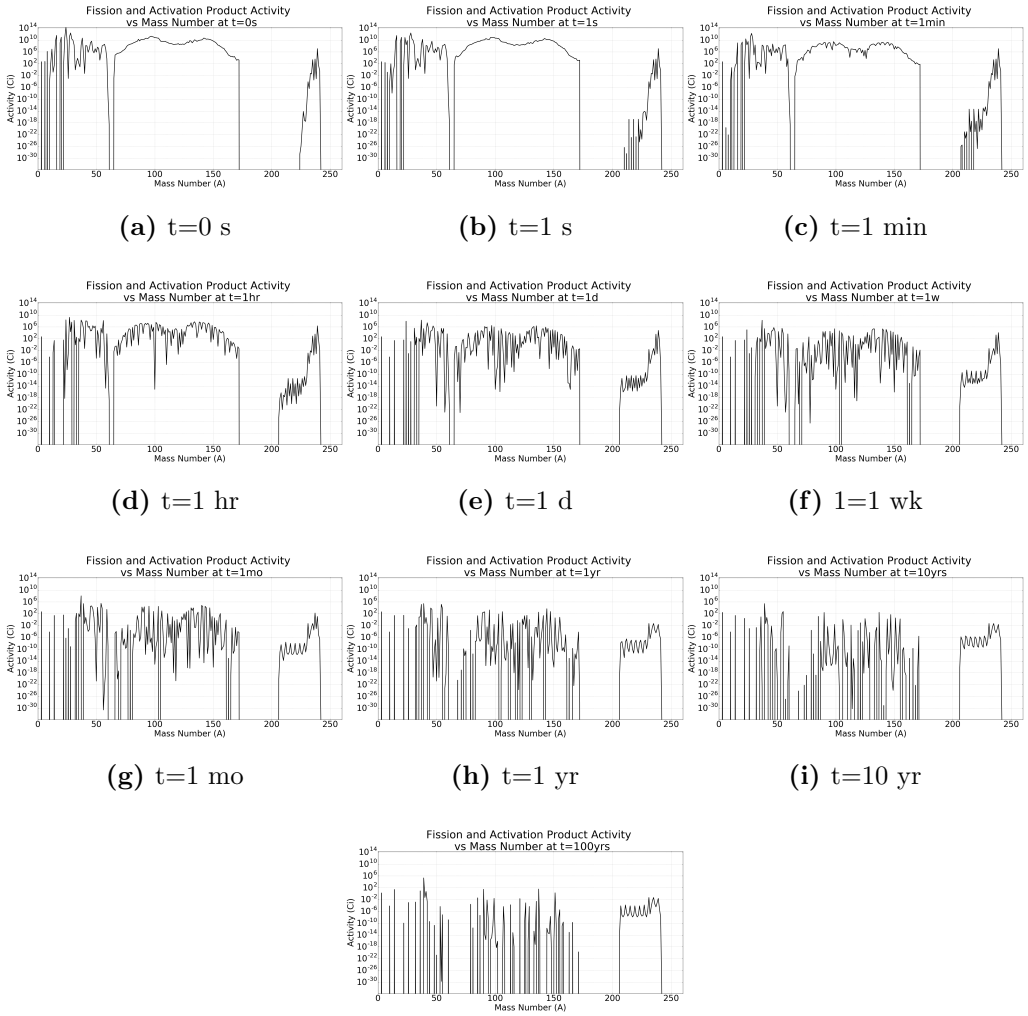
(d) Mass Chain 108

Figure A.5: Mass chains 105-108

(53)

Appendix B

Activity Contributions Over Time



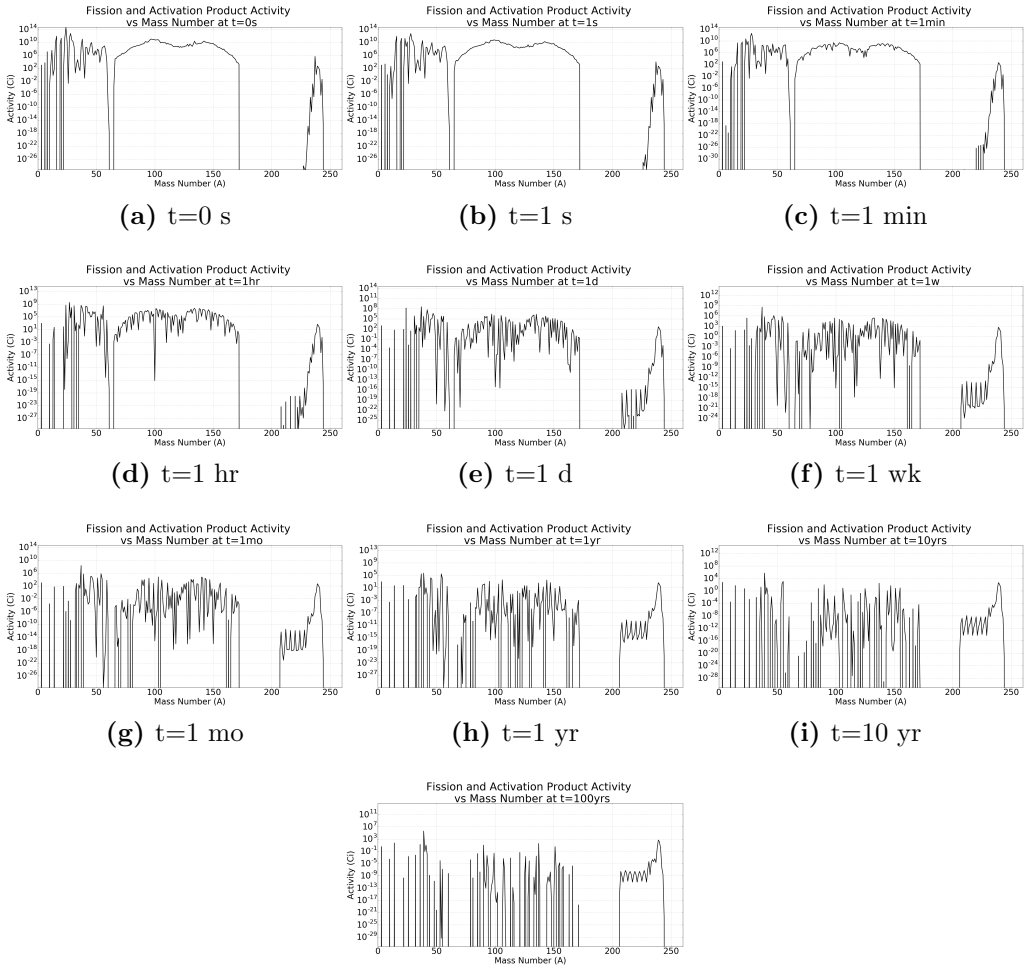
(a) t=0 s **(b)** t=1 s **(c)** t=1 min

(d) t=1 hr **(e)** t=1 d **(f)** 1=1 wk

(g) t=1 mo **(h)** t=1 yr **(i)** t=10 yr

(j) t=100 yr

Figure B.1: Activity contribution by mass number (A) over time for a modeled notional U-fueled IND detonation



(a) t=0 s **(b)** t=1 s **(c)** t=1 min

(d) t=1 hr **(e)** t=1 d **(f)** t=1 wk

(g) t=1 mo **(h)** t=1 yr **(i)** t=10 yr

(j) t=100 yr

Figure B.2: Activity contribution by mass number (A) over time for a modeled notional Pu-fueled IND detonation in a STF matrix

Vita

Andrew Giminaro was born in East Meadow, New York to Vincent Giminaro and Ruth Ferington. Andrew was quite the precocious child, and could frequently be found tinkering with and deconstructing anything mechanical or electronic in his household. His involvement in the Boy Scouts of America (specifically the atomic energy merit badge) peaked in him, an interest in the nuclear sciences. After graduating from Heritage High School/Central Virginia Governors School, Andrew enrolled in the University of Tennessees Department of Nuclear Engineering. He was awarded his Bachelors degree in 2012, and immediately started his graduate studies the following week. Andrew began his graduate research by investigating the effects of liquid alkali eutectics on welds found on steam generator header plates. After many small fires and run-ins with corrosive substances (not to mention earning a Masters degree) he decided to focus his research on nuclear security. Andrews PhD research focused heavily on surrogate nuclear melt glass modeling and development of synthesis methods for said surrogates. He has also conducted research in the areas of advanced radiochemical separations and radiation detection. Andrew earned his Doctorate in 2016 and is currently pursuing a career in nuclear security, safeguards, and forensics.